

# UC San Diego

## UC San Diego Electronic Theses and Dissertations

### Title

Enhancing Electrochemical Performance of Electrode Materials for Li-ion Batteries and Na-ion Batteries via Thermodynamic Surface/Interface Control

### Permalink

<https://escholarship.org/uc/item/2cq4w61p>

### Author

Huang, Jiajia

### Publication Date

2017

Peer reviewed|Thesis/dissertation

UNIVERSITY OF CALIFORNIA, SAN DIEGO

Enhancing Electrochemical Performance of Electrode Materials for Li-ion  
Batteries and Na-ion Batteries via Thermodynamic Surface/Interface Control

A dissertation submitted in partial satisfaction of the  
requirements for the degree Doctor of Philosophy

in

Materials Science and Engineering

by

Jiajia Huang

Committee in charge:

Professor Jian Luo, Chair  
Professor Ying Shirley Meng  
Professor Shyue Ping Ong  
Professor Yu Qiao  
Professor Kesong Yang

2017

Copyright

Jiajia Huang, 2017

All rights reserved.

The Dissertation of Jiajia Huang is approved, and it is acceptable in quality and form for publication on microfilm and electronically:

---

---

---

---

---

Chair

University of California, San Diego

2017

## **DEDICATION**

To my wife Yanfang

## TABLE OF CONTENTS

SIGNATURE PAGE.....	iii
DEDICATION .....	iv
TABLE OF CONTENTS .....	v
LIST OF FIGURES .....	ix
LIST OF TABLES .....	xv
ACKNOWLEDGEMENTS.....	xvi
VITA.....	xx
ABSTRACT OF THE DISSERTATION.....	xxii
Chapter 1. Introduction .....	1
1.1. The Introduction of Thermodynamic Models .....	1
1.1.1 Surface amorphous films .....	1
1.1.2. The Surface adsorption/segregation, Wulff construction, and anisotropic surface segregation .....	4
1.2. The Motivation and Overview .....	5
References.....	10
Chapter 2. A Facile and Generic Method to Improve Cathode Materials for Lithium-Ion Batteries via Utilizing Nanoscale Surface Amorphous Films of Self-regulating Thickness .....	14
2.1. Introduction .....	14
2.2. Thermodynamic Model and Theoretical Analysis .....	19
2.3. Experimental .....	23
2.3.1. Materials synthesis.....	23
2.3.2. Material characterization .....	24
2.3.3. Electrochemical measurement.....	25
2.4. Results and Discussion .....	27
2.4.1. $\text{Li}_3\text{PO}_4$ -based equilibrium-thickness SAFs on $\text{LiCoO}_2$ .....	27
2.4.2. $\text{Li}_3\text{PO}_4$ -based equilibrium-thickness SAFs on $\text{LiMn}_{1.5}\text{Ni}_{0.5}\text{O}_4$ .....	32
2.5. Conclusions.....	36

References.....	54
Chapter 3. Enhancing the Electrochemical Performance of $\text{LiMn}_{1.5}\text{Ni}_{0.5}\text{O}_4$ through $\text{WO}_3$ Doping and Altering the Particle Wulff Shape via Anisotropic Surface Segregation.....	61
3.1. Introduction .....	61
3.2. Experimental .....	64
3.2.1. Materials synthesis.....	64
3.2.2. Material characterization .....	65
3.2.3. Electrochemical measurement.....	67
3.3. Results .....	68
3.3.1. Surface areas and particle morphologies.....	68
3.3.2. Anisotropic surface segregation.....	69
3.3.3. Electrochemical performances.....	71
3.3.4. Surface and bulk $\text{Mn}^{3+}$ concentrations .....	73
3.3.5. Neutron diffraction.....	74
3.4. Discussion.....	75
3.4.1. The change in particle morphology and anisotropic surface segregation of W.....	75
3.4.2. Mechanisms of the improved rate capability .....	76
3.4.3. Mechanisms of the increased discharge capacity and cycling stability .....	77
3.5. Conclusions.....	79
References.....	93
Chapter 4. Enhancing the Electrochemical Performance of Li-rich Layered Oxide $\text{Li}_{1.13}\text{Ni}_{0.3}\text{Mn}_{0.57}\text{O}_2$ via $\text{WO}_3$ Doping and Surface Segregation .....	100
4.1. Introduction .....	100
4.2. Experimental .....	102
4.2.1. Materials synthesis.....	102
4.2.2. Material characterization .....	103
4.2.3. Electrochemical measurement.....	104
4.3. Results .....	105

4.4. Discussion.....	108
4.5. Conclusions.....	111
References.....	120
Chapter 5. Low-cost Si Anode with Enhanced Cycling Performance via Sn Doping by High Energy Ball Milling and Post Annealing .....	124
5.1. Introduction .....	124
5.2. Experimental .....	126
5.2.1. Materials synthesis.....	126
5.2.2. Material characterization .....	127
5.2.3. Electrochemical measurement.....	127
5.3. Results .....	128
5.4. Discussion.....	131
5.5. Conclusions.....	134
References.....	141
Chapter 6. Effects of Secondary Structure Morphology and Surface Nitridation on TiO <sub>2</sub> Anode Materials of Sodium-ion Batteries .....	143
6.1. Introduction .....	143
6.2. Experimental .....	144
6.3. Results .....	146
6.4. Discussion.....	148
6.5. Conclusions.....	150
References.....	158
Chapter 7. Composites of Sodium Manganese Oxides with Enhanced Electrochemical Performance for Sodium-ion Batteries: Tailoring Properties via Controlling Microstructure.....	159
7.1. Introduction .....	159
7.2. Experimental .....	161
7.3. Results and Discussion .....	163
7.4. Conclusions.....	170
References.....	178

Chapter 8. Future Work and Preliminary Results: Cold Sintering of Solid State Electrolyte for the All-solid-state Lithium-ion Batteries .....	180
8.1. Introduction .....	180
8.2. Experimental .....	181
8.3. Results and Discussion .....	183
8.4. Conclusions.....	184
8.5. Future work .....	185
References.....	189

## LIST OF FIGURES

Figure 1.1 Schematic illustration of the thermodynamic principle for stabilizing a nanometer-thick SAF (being treated as an undercooled quasi-liquid film) below the bulk solidus line.....	9
Figure 2.1 XRD patterns of the $\text{LiCoO}_2$ and $\text{LiCoO}_2 + 2 \text{ vol. } \% \text{Li}_3\text{PO}_4$ specimens that were milled and subsequently annealed at $600 \text{ }^\circ\text{C}$ for 4 h. ....	40
Figure 2.2 Representative SEM images of the (a) $\text{LiCoO}_2$ and (b) $\text{LiCoO}_2 + 2 \text{ vol. } \% \text{Li}_3\text{PO}_4$ specimens that were milled and subsequently annealed at $600 \text{ }^\circ\text{C}$ for 4 h. ....	40
Figure 2.3 HRTEM images of the particle surfaces in (a) uncoated and (b) 2 vol. % $\text{Li}_3\text{PO}_4$ coated $\text{LiCoO}_2$ specimens equilibrated at $600 \text{ }^\circ\text{C}$ . (c) Measured film thickness vs. volume percentage of $\text{Li}_3\text{PO}_4$ added in $\text{LiCoO}_2$ for specimens equilibrated at $600 \text{ }^\circ\text{C}$ .....	41
Figure 2.4 Measured rate performance of uncoated and coated $\text{LiCoO}_2$ at the electrolyte concentration of (a) 1M and (b) 0.1M, respectively .....	42
Figure 2.5 (a) Measured electrochemical impedance spectra of the $\text{LiCoO}_2$ specimens with and without $\text{Li}_3\text{PO}_4$ -based SAFs, respectively, tested in 1 M and 0.1 M electrolytes, respectively. (b) an equivalent circuit model .....	43
Figure 2.6 Cycling stability of $\text{LiCoO}_2$ specimens with and without $\text{Li}_3\text{PO}_4$ -based SAFs that were cycled between 3 V and 4.5 V (vs. $\text{Li}/\text{Li}^+$ ) at the charge/discharge rate of 1C at room temperature.....	44
Figure 2.7 Comparison of cyclic voltammograms of the $\text{LiCoO}_2$ specimens with and without $\text{Li}_3\text{PO}_4$ -based SAFs after (a) 1 cycle, (b) 10 cycles, (c) 50 cycles, and (d) 100 cycles.....	45
Figure 2.8 XRD patterns of various $\text{LiMn}_{1.5}\text{Ni}_{0.5}\text{O}_4$ specimens. Minor amounts of a secondary crystalline phase of $\text{Li}_x\text{Ni}_{1-x}\text{O}$ were detected in the milled and annealed specimens. ....	46
Figure 2.9 Representative SEM images of (a) the as-received $\text{LiMn}_{1.5}\text{Ni}_{0.5}\text{O}_4$ specimen and (b) the reference $\text{LiMn}_{1.5}\text{Ni}_{0.5}\text{O}_4$ specimen annealed at $800 \text{ }^\circ\text{C}$ (without ball milling), as well as the (c) $\text{LiMn}_{1.5}\text{Ni}_{0.5}\text{O}_4$ and (d) $\text{LiMn}_{1.5}\text{Ni}_{0.5}\text{O}_4 + 2 \text{ vol. } \% \text{Li}_3\text{PO}_4$ specimens.....	47
Figure 2.10 HRTEM images of the particle surfaces in the (a) $\text{LiMn}_{1.5}\text{Ni}_{0.5}\text{O}_4$ and (b) $\text{LiMn}_{1.5}\text{Ni}_{0.5}\text{O}_4 + 2 \text{ vol. } \% \text{Li}_3\text{PO}_4$ specimens. (c) The corresponding distributions of measured thicknesses of the surface carbonate layers or $\text{Li}_3\text{PO}_4$ -based SAFs for these two specimens..	48

Figure 2.11 Comparisons of discharge curves of $\text{LiMn}_{1.5}\text{Ni}_{0.5}\text{O}_4$ specimens without and with $\text{Li}_3\text{PO}_4$ -based SAFs. . . . .	49
Figure 2.12 Comparison of the cycling stabilities of five $\text{LiMn}_{1.5}\text{Ni}_{0.5}\text{O}_4$ specimens without $\text{Li}_3\text{PO}_4$ -based SAFs and five $\text{LiMn}_{1.5}\text{Ni}_{0.5}\text{O}_4$ specimens with $\text{Li}_3\text{PO}_4$ -based SAFs. . . . .	50
Figure 2.13 The cycling performances of the as-received $\text{LiMn}_{1.5}\text{Ni}_{0.5}\text{O}_4$ specimen and the reference $\text{LiMn}_{1.5}\text{Ni}_{0.5}\text{O}_4$ specimen annealed at $800\text{ }^\circ\text{C}$ without ball milling, along with the two means of the specimens. ....	51
Figure 2.14 Electrochemical impedance spectra of $\text{LiMn}_{1.5}\text{Ni}_{0.5}\text{O}_4$ specimens with and without $\text{Li}_3\text{PO}_4$ -based SAFs. Specimens were firstly charged and discharged at 1C for 10 cycles at room temperature followed by charging and discharging at 1C for 50 cycles at $55\text{ }^\circ\text{C}$ . . . . .	52
Figure 3.1 Representative SEM images of the (a) undoped and (b) 1 vol. % $\text{WO}_3$ doped $\text{LiMn}_{1.5}\text{Ni}_{0.5}\text{O}_4$ specimens, where were prepared by annealing high-energy ball milled powders at $800\text{ }^\circ\text{C}$ for 4 h. . . . .	81
Figure 3.2 Wulff shapes of the (a) undoped and (b) $\text{WO}_3$ doped $\text{LiMn}_{1.5}\text{Ni}_{0.5}\text{O}_4$ that matched the experimentally observed particle morphologies shown in Figure 3.1 and schematics of the Li ion diffusion channels on (c) $\{110\}$ , (d) $\{111\}$ and (e) $\{100\}$ facets, respectively . . . . .	82
Figure 3.3 Atomic ratios of W/Mn and Ni/Mn vs. sputtering time curves measured from XPS. . . . .	83
Figure 3.4 Atomic ratios of W to Mn vs. sputtering time curves measured by AES on three different surface facets of $\{110\}$ , $\{100\}$ and $\{111\}$ . The $\{110\}$ facet has the highest level of W segregation . . . . .	84
Figure 3.5 (a) Comparison of rate performance of undoped and $\text{WO}_3$ doped $\text{LiMn}_{1.5}\text{Ni}_{0.5}\text{O}_4$ specimens and discharge curves of (b) undoped specimen and (c) $\text{WO}_3$ doped $\text{LiMn}_{1.5}\text{Ni}_{0.5}\text{O}_4$ specimens . . . . .	85
Figure 3.6 Measured EIS spectra of the undoped and $\text{WO}_3$ doped (red circles) $\text{LiMn}_{1.5}\text{Ni}_{0.5}\text{O}_4$ specimens. The inset is an equivalent circuit . . . . .	86
Figure 3.7 Measured charge/discharge curves for the undoped and $\text{WO}_3$ doped $\text{LiMn}_{1.5}\text{Ni}_{0.5}\text{O}_4$ specimens. Both specimens were charged and discharged at a low rate of 0.1C at room temperature. . . . .	87
Figure 3.8 Measured CV curves of the undoped and $\text{WO}_3$ -doped $\text{LiMn}_{1.5}\text{Ni}_{0.5}\text{O}_4$ specimens. . . . .	88
Figure 3.9 Cycling stability results of the undoped and $\text{WO}_3$ -doped $\text{LiMn}_{1.5}\text{Ni}_{0.5}\text{O}_4$ specimens tested at an elevated temperature of $55\text{ }^\circ\text{C}$	

with a relatively high charge and discharge rate of 1C as an accelerated test .....	89
Figure 3.10 XPS results of (a) Mn, (b) W, and (c) Ni binding energy shifts after sputtering for different times (labeled in the graphs) for the 1 vol. % WO <sub>3</sub> doped LiMn <sub>1.5</sub> Ni <sub>0.5</sub> O <sub>4</sub> specimen.....	90
Figure 3.11 Neutron powder diffraction patterns of the (a) undoped and (b) 1 vol. % WO <sub>3</sub> doped LiMn <sub>1.5</sub> Ni <sub>0.5</sub> O <sub>4</sub> specimens .....	91
Figure 4.1 SEM micrographs of particle morphologies of (a, b) undoped and (c, d) WO <sub>3</sub> doped Li <sub>1.13</sub> Ni <sub>0.3</sub> Mn <sub>0.57</sub> O <sub>2</sub> .....	113
Figure 4.2 X-ray diffraction pattern of (a) undoped and (b) WO <sub>3</sub> doped Li <sub>1.13</sub> Ni <sub>0.3</sub> Mn <sub>0.57</sub> O <sub>2</sub> . .....	114
Figure 4.3 The rate performance of undoped and doped specimens. Charge/discharge curves of (a) undoped and (b) WO <sub>3</sub> doped Li <sub>1.13</sub> Ni <sub>0.3</sub> Mn <sub>0.57</sub> O <sub>2</sub> at various rates. (c) Rate capabilities of undoped and WO <sub>3</sub> doped Li <sub>1.13</sub> Ni <sub>0.3</sub> Mn <sub>0.57</sub> O <sub>2</sub> .....	115
Figure 4.4 The cycling performances of undoped and WO <sub>3</sub> doped Li <sub>1.13</sub> Ni <sub>0.3</sub> Mn <sub>0.57</sub> O <sub>2</sub> specimens. (a) The specific capacity vs. cycle number curves. (b) Average voltage fading and (c) energy density vs. cycle number curves.....	116
Figure 4.5 X-ray photoelectron spectrum of (a) W4d <sub>5/2</sub> before sputtering and (b) W 4f of doped specimen. (c) Ni/Mn and W/Mn atomic ratios vs. sputtering time for undoped and WO <sub>3</sub> doped Li <sub>1.13</sub> Ni <sub>0.3</sub> Mn <sub>0.57</sub> O <sub>2</sub> . ..	117
Figure 4.6 X-ray photoelectron spectrum of (a, b) undoped and (c, d) WO <sub>3</sub> doped Li <sub>1.13</sub> Ni <sub>0.3</sub> Mn <sub>0.57</sub> O <sub>2</sub> , where the binding energies represent (a, c) Mn 3p, (b, d) Ni 2p. ....	118
Figure 4.7 HRTEM images of (a) undoped and (b, c) WO <sub>3</sub> doped Li <sub>1.13</sub> Ni <sub>0.3</sub> Mn <sub>0.57</sub> O <sub>2</sub> .....	119
Figure 5.1 The particle morphology of Si <sub>1-x</sub> Sn <sub>x</sub> with x of (a) (e) 0.05, (b) (f) 0.10, (c) (g) 0.15 and (d) (h) 0.20. Specifically, (a), (b), (c), and (c) is for ball milled specimens without annealing and (e), (f), (g), and (h) for with annealing at 750 °C for 20 h, respectively. ....	136
Figure 5.2 (a) XRD of high-energy ball milled Si <sub>1-x</sub> Sn <sub>x</sub> without annealing. (b) calculated particle size of Si and Sn from (a). (c) XRD of high-energy ball milled Si <sub>0.90</sub> Sn <sub>0.10</sub> annealed at various temperatures. (d) Calculated particle size of Si and Sn from (c).....	137

Figure 5.3 The cycling performance of (a) $\text{Si}_{1-x}\text{Sn}_x$ after high energy ball milling 20 h with x of 0, 0.05, 0.10, 0.15, and 0.20 annealed at 750 C for 20 h; (b) high-energy ball milled $\text{Si}_{0.90}\text{Sn}_{0.10}$ annealed at 650, 750 and 850 °C for 20 h .....	138
Figure 5.4 The cyclic voltammetry (CV) of (a) $\text{Si}_{1-x}\text{Sn}_x$ after high energy ball milling 20 h with x of 0.05, 0.10, and 0.15. All specimens were annealed at 750 C for 20 h; (b) high-energy ball milled $\text{Si}_{0.90}\text{Sn}_{0.10}$ annealed at 650 and 750 °C for 20 h, respectively .....	138
Figure 5.5 The secondary particle and cross section of high-energy ball milled $\text{Si}_{0.90}\text{Sn}_{0.10}$ (a-c) without annealing and (d-f) annealed at 750 °C for 20 h. ....	139
Figure 5.6 EDX of cross section of high-energy ball milled $\text{Si}_{0.90}\text{Sn}_{0.10}$ (a-d) without annealing and (e-h) annealed at 750 °C for 20 h. ....	139
Figure 5.7 HRTEM images of (a) high-energy ball milled $\text{Si}_{0.90}\text{Sn}_{0.10}$ without annealing and (b) annealed at 750 °C for 20 h.....	140
Figure 6.1 The particle morphology of four $\text{TiO}_2$ specimens: (a) and (e) as received; high-energy ball milled followed with annealing (b) and (f) at 600 °C, (c) and (g) at 700 °C, (d) and (f) at 800 °C, respectively. ....	151
Figure 6.2 The X-ray diffraction results of as received specimen (black), and specimens high-energy ball milled following with annealed at 600 (red), 700 (blue) and 800 °C (green), respectively. The main phase was anatase with minor rutile phase labeled with black dots .....	151
Figure 6.3 (a) Rate performance of $\text{TiO}_2$ specimens as received, and high-energy ball milled following with annealed at 600, 700 and 800 °C, respectively. (b) cycling stability of as-received and high-energy ball milled following with annealed at 600 °C .....	152
Figure 6.4 SEM images of $\text{TiO}_2$ (a) after high-energy ball milling and (b) 600 °C annealing without high-energy ball milling.....	152
Figure 6.5 Rate performance of as-received $\text{TiO}_2$ , ball milled $\text{TiO}_2$ and ball milled $\text{TiO}_2$ followed with annealing at 600 °C. The specimens were charged and discharged at the rates of 0.02C, 0.1C, 0.2C, 0.5C, 1C and 0.02C at room temperature .....	153
Figure 6.6 X-ray diffraction results of anatase $\text{TiO}_2$ for rutile phase change influenced by high-energy ball milling. (a) Specimens annealed at 600 °C with or without high-energy ball milling; (b) specimens annealed at 700 °C with or without high-energy ball milling .....	154

Figure 6.7 Morphology of nitrated TiO <sub>2</sub> . The specimen was firstly fabricated by high-energy ball milling as-received TiO <sub>2</sub> following by annealing at 600 °C for 10 h in air. The product was cooled down and transferred into tube furnace for annealing in NH <sub>3</sub> gas at 600 °C for 1 h. ....	154
Figure 6.8 The X-ray diffraction results of undoped and 1 h nitridation specimens. All specimens were high-energy ball milled followed by 600 °C for 10 h before nitridation in NH <sub>3</sub> gas for 1 h. The main phase was anatase. Rutile phase was labeled with black dots. ....	155
Figure 6.9 (a) Rate performance of nitrated TiO <sub>2</sub> specimens for 1 h under NH <sub>3</sub> gas flow at 600 °C. (b) Cycling stability of nitrated specimen for 1 h was tested at charge and discharge rate of 1C and room temperature for 50 cycles. ....	156
Figure 7.1 SEM images of (a and a') Specimen A and (b and b') Specimen B. Panels (a') and (b') are SEM images taken at a high magnification to show the detailed "meatball-like" and "irregular rods" microstructures, respectively. ....	172
Figure 7.2 XRD patterns of the Na <sub>x</sub> MnO <sub>2</sub> composites of (a) Specimen A and (b) Specimen B. The peaks for the layered Na <sub>0.7</sub> MnO <sub>2.05</sub> and Na <sub>0.91</sub> MnO <sub>2</sub> phases are represented by the symbol * and ◇, respectively. In both cases, Na <sub>0.44</sub> MnO <sub>2</sub> is the dominating phase. ....	173
Figure 7.3 Cycling performance of (a) Specimen A (hierarchical porous microstructure with primary and secondary particles) and (b) Specimen B (irregular rods). Both specimens were charged and discharged at a constant rate of 0.1C at room temperature. ....	174
Figure 7.4 Electrochemical impedance spectra of the Na <sub>0.7</sub> MnO <sub>2</sub> of specimen A and specimen B. Dots are experimental data and solid lines represent fitting curves using the equivalent circuit model shown in the inset. ....	175
Figure 7.5 Comparison of cyclic voltammograms of the 5 <sup>th</sup> cyclic sweep of (a) Specimen A and (b) Specimen B. The a <sub>1</sub> -a <sub>5</sub> peaks represent the redox reactions from the Na <sub>0.44</sub> MnO <sub>2</sub> phase, while the b <sub>1</sub> -b <sub>3</sub> peaks represent the redox reactions from layered phases ....	176
Figure 7.6 The rate performances of (a) Specimen A and (b) Specimen B .....	177
Figure 8.1 SEM images of Li <sub>6.4</sub> Ga <sub>0.2</sub> La <sub>3</sub> Zr <sub>2</sub> O <sub>12</sub> (a) powder synthesized at 1150 °C for 2 h; (b) and (c) pellet of cold sintered at 200 °C for 1 h under pressure of 1.2 GPa. ....	186
Figure 8.2 XRD patterns of Li <sub>6.4</sub> Ga <sub>0.2</sub> La <sub>3</sub> Zr <sub>2</sub> O <sub>12</sub> (a) sintered at 1100 °C for 2 h without cold sintering; (b) cold sintered at 200 °C for 1 h under	

pressure of 1.2 GPa; (c) cold sintering at 200 °C for 1 h under pressure of 1.2 GPa followed by sintering at 1100 °C for 2 h..... 187

Figure 8.3 Cycling performance of (a) Specimen A (hierarchical porous microstructure with primary and secondary particles) and (b) Specimen B (irregular rods). Both specimens were charged and discharged at a constant rate of 0.1C at room temperature. .... 188

## LIST OF TABLES

Table 2.1 Surface film resistance ( $R_f$ , which includes possible contributions from the SEI and SAFs) and charge transfer resistance ( $R_{ct}$ ) of $\text{LiCoO}_2$ specimens tested at the electrolyte concentration of 1M and 0.1M. 53	53
Table 2.2 Measured discharge capacities of the $\text{LiMn}_{1.5}\text{Ni}_{0.5}\text{O}_4$ specimens with and without $\text{Li}_3\text{PO}_4$ -based SAFs (which were subjected to the same milling and annealing treatment), along with the “annealed only” specimen without milling as an additional reference point..... 53	53
Table 3.1 Relative surface energies of the undoped and $\text{WO}_3$ -doped $\text{LiMn}_{1.5}\text{Ni}_{0.5}\text{O}_4$ specimens that matched the experimentally observed Wulff shapes ..... 92	92
Table 3.2 Fitted surface film and charge transfer resistances from EIS ..... 92	92
Table 6.1 Anatase phase percentage and primary particle size ..... 157	157

## ACKNOWLEDGEMENTS

The dissertation I am writing now is a consequence of great and continuous efforts from tens of people, but not only myself. First and foremost, I wish to thank my supervisor, Professor Jian Luo, for his precious time, financial supports, great guidance and all supplied opportunities. He aimed at training me with enormous patience on the capability of innovation, critical thinking and logical thinking, and expression ability, from which I absorb power and nutrition to complete this work. I was inspired deeply by his creative and erupted ideas, strict logic and upright academic attitude through each discussion and communication. I sincerely honored to meet and work with him. I would also like to extend my deepest gratitude to my thesis committee: Dr. Ying Shirley Meng, Dr. Kesong Yang, Dr. Shyue Ping Ong, and Dr. Yu Qiao for their precious time, guidance and great support.

Secondly, I would like to acknowledge my collaborators and co-authors Dr. Haodong Liu, Dr. Naixie Zhou, Dr. Tao Hu, and Archana Kayyar, with whom I learned many experimental skills and had a lot of useful and stimulating discussions. I am also thankful to my other co-authors Dr. Mojtaba Samiee, Dr. Danna Qian, Dr. Sunny Hy, Chenchen Fang, and Dr. Ke An.

I'm also grateful to my group members, Dr. Bing Jiang, Jiuyuan Nie, Xiaolong Xu, Andrew Wright, Haoyang Leng and Sheng Zhao who I worked together on those same projects. I also thank other group members, Dr. Yuanyao Zhang, Dr. Jaeil Jung, Dr. Matt Williams, Dr. Shengfeng Yang, Jiuyuan Nie,

Mingde Qin and Joshua Gild, Sicong Jiang, Dr. Yingfeng Li and Dr. Rongxia Huang, who shared a great time with me. I would also thank group members from Dr. Shirley Meng's group for their kind help and understanding.

I obtained some great training experience of equipment, helped by several excellent masters. I really appreciate Dr. Haijun Qian, who trained me and helped me a lot to use the HRTEM in Clemson University to characterize the nanosized surface amorphous films on the cathodes. Dr. Ilkeun Lee in University of California Riverside did prompt favor twice on the XPS characterization, which was very helpful to acquire depth profiles to prove the phenomenon of W cation surface segregation. Dr. Chuck Hitzman in Stanford University gave me a very helpful training of AES and generously shared his experience of how to reduce the equipment error and tips on reducing charging influence, which was very powerful and armed me with the ability to clarify the W cation anisotropic surface segregation on various crystalline facets for the first time. Thanks to Dr. Jeff Wu in Nano3 in University of California San Diego, I could use the FIB/SEM to originally character the unique cross section morphology of the Si-Sn alloy with an interesting Sn distribution.

I would also like to express my sincere gratitude to Wayne Neilson, and Sabine Foulhaber, and Dr. Steve Horvath in Department of NanoEngineering for their selfless technical support on my various unexpected requests. Ryan Anderson in Nano3 facility supplied a lot of help on SEM training and trouble shooting skills at University of California San Diego. I am also grateful to the staffs, Satomi Saito, Anna Shonle, Ji Song, and Dana Jimenez in NanoEngineering, and

Katie Hamilton in Program of Materials Science and Engineering, for their integral support and great help.

During the hardest time of my Ph.D. study, my friend Dr. Yong Zhang, who was also the supervisor of my master study in Tsinghua University, visited me from China and gave an enormous emotional support. The short time we spent together at San Diego has become a permanent memory and treasure all my life.

For the last but not least, my deepest gratitude goes to my parents Zhenhai Huang and Zhenru Liu, and my young brothers, for their never-ending love. At last, I specially thank to my wife, Yanfang Fan, for her endless encouragement and support.

**Chapter 2**, in part, is a reprint of the material “A Facile and Generic Method to Improve Cathode Materials for Lithium-Ion Batteries via Utilizing Nanoscale Surface Amorphous Films of Self-Regulating Thickness” as it appears in the Physical Chemistry Chemical Physics, Jiajia Huang and Jian Luo, 2014, 16, 7786-7798.

**Chapter 3**, in part, is a reprint of the material “Enhancing the Electrochemical Performance of  $\text{LiMn}_{1.5}\text{Ni}_{0.5}\text{O}_4$  through  $\text{WO}_3$  Doping and Changing the Particle Wulff Shape via Anisotropic Surface Segregation” in preparation, Jiajia Huang, Haodong Liu, Naixie Zhou, Ke An, Ying S. Meng and Jian Luo. Neutron diffraction was carried out by Dr. Haodong Liu and Dr. Ke An in Oak Ridge National Laboratory. Dr. Naixie Zhou gave a lot valuable opinions on the thermodynamic model.

**Chapter 4**, in part, is a reprint of the manuscript “Enhancing the Electrochemical Performance of Li-rich Layered Oxide  $\text{Li}_{1.13}\text{Ni}_{0.3}\text{Mn}_{0.57}\text{O}_2$  via  $\text{WO}_3$  Doping and Surface Segregation” in preparation, Jiajia Huang, Haodong Liu, Tao Hu, Ying S. Meng and Jian Luo.  $\text{Li}_{1.13}\text{Ni}_{0.3}\text{Mn}_{0.57}\text{O}_2$  was synthesized by Dr. Haodong Liu. HRTEM observation was done by Dr. Tao Hu at University of California Los Angeles.

**Chapter 5**, in part, is a reprint of the manuscript “Intergranular Films and Secondary Structures on Cycling Stability of  $\text{Si}_{1-x}\text{Sn}_x$  Anode for Lithium Ion Batteries” in preparation, Jiajia Huang, Bing Jiang, Tao Hu, J. Luo. Part of specimens were prepared by Dr. Bing Jiang. HRTEM images were taken by Dr. Tao Hu.

**Chapter 7**, in part, is a reprint of the material “Composites of Sodium Manganese Oxides with Enhanced Electrochemical Performance for Sodium-ion Batteries: Tailoring Properties via Controlling Microstructure” as it appears in the Science China Technological Sciences, Jiajia Huang and Jian Luo, 2016, 59, 1042.

## VITA

2005	Bachelor of Science	Yanshan University
2009	Master of Science	Tsinghua University
2009	Research Associate	Tsinghua University
2017	Doctor of Philosophy	University of California, San Diego

## PUBLICATIONS

1. **J. Huang**, J. Luo, “Composites of Sodium Manganese Oxides with Enhanced Electrochemical Performance for Sodium-ion Batteries: Tailoring Properties via Controlling Microstructure”, *Science China Technological Sciences*, 2016, 59, 1042.
2. H. Liu, **J. Huang**, D. Qian, S. Hy, C. Fang, J. Luo, Y. S. Meng, “Communication—Enhancing the Electrochemical Performance of Lithium-Excess Layered Oxide  $\text{Li}_{1.13}\text{Ni}_{0.3}\text{Mn}_{0.57}\text{O}_2$  via a Facile Nanoscale Surface Modification”, *Journal of The Electrochemical Society*, 2016, 163, A971.
3. N. Zhou, T. Hu, **J. Huang**, J. Luo, “Stabilization of Nanocrystalline Alloys at High Temperatures via Utilizing High-entropy Grain Boundary Complexions”, *Scripta Materialia*, 2016, 124, 160.
4. **J. Huang**, J. Luo, “A facile and Generic Method to Improve Cathode Materials for Lithium-ion Batteries via Utilizing Nanoscale Surface Amorphous Films of Self-Regulating Thickness”, *Physical Chemistry Chemical Physics*, 2014, 16, 7786.
5. A. Kayyar, **J. Huang**, M. Samiee, J. Luo, “Construction and Testing of Coin Cells of Lithium Ion Batteries”, *Journal of Visualized Experiments*, 2012, 66, 4104.

6. **J. Huang**, H. Liu, N. Zhou, K. An, Y. S. Meng, J. Luo, “Enhancing the Electrochemical Performance of  $\text{LiMn}_{1.5}\text{Ni}_{0.5}\text{O}_4$  through  $\text{WO}_3$  Doping and Changing the Particle Wulff Shape via Anisotropic Surface Segregation”, Chemistry of Materials, 2017 (in preparation).
7. **J. Huang**, H. Liu, T. Hu, Y. S. Meng, J. Luo, “Enhancing the Electrochemical Performance of Li-rich Layered Oxide  $\text{Li}_{1.13}\text{Ni}_{0.3}\text{Mn}_{0.57}\text{O}_2$  via  $\text{WO}_3$  Doping and Surface Segregation”, (in preparation).
8. **J. Huang**, B. Jiang, T. Hu, J. Luo, “Intergranular Films and Secondary Structures on Cycling Stability of  $\text{Si}_{1-x}\text{Sn}_x$  Anode for Lithium Ion Batteries”, (in preparation).

## **ABSTRACT OF THE DISSERTATION**

Enhancing Electrochemical Performance of Electrode Materials for Li-ion Batteries and Na-ion Batteries via Thermodynamic Surface/Interface Control

by

Jiajia Huang

Doctor of Philosophy in Materials Science and Engineering

University of California, San Diego, 2017

Professor Jian Luo, Chair

A facile and low-cost route based on thermodynamic principles of surface amorphous films (SAFs), intergranular films (IGFs), and cation surface segregation benefits electrochemical performances of electrode materials for lithium-ion batteries and sodium-ion batteries.

SAFs as a facile and generic surface modification method is utilized to significantly improve the rate performance and cycling stability of cathode materials for lithium-ion batteries. A thermodynamic framework of SAFs is

proposed. These nanoscale SAFs form spontaneously and uniformly upon mixing and annealing at a thermodynamic equilibrium, and they exhibit a self-regulating or “equilibrium” thickness due to a balance of attractive and repulsive interfacial interactions acting on the films. Specially, spontaneous formation of nanoscale  $\text{Li}_3\text{PO}_4$ -based SAFs has been demonstrated in two proof-of-concept systems  $\text{LiCoO}_2$  and  $\text{LiNi}_{0.5}\text{Mn}_{1.5}\text{O}_4$ . Furthermore, SAFs also facilitate electrochemical performance of  $\text{TiO}_2$  by surface nitridation as an anode material for sodium-ion batteries.

Similarly, IGFs are also found and benefit electrochemical performance in the system of Sn doped Si anode for lithium-ion batteries. The coexistence of IGFs and porous secondary structure (characterized by FIB/SEM on the cross section) results in an enhanced performance. Both SAFs and IGFs can be used to guide future experiments of other material systems.

Utilizing cation surface segregation to thermodynamically control the particle morphology and the surface composition is another economic, facile, and effective method to significantly improve the electrochemical performance of battery electrodes.  $\text{WO}_3$  doping and anisotropic surface segregation can change the facet relative surface energy to tailor the particle Wulff shape of  $\text{LiMn}_{1.5}\text{Ni}_{0.5}\text{O}_4$  spinel materials and the surface Mn/Ni ratio and benefits performances.

W cation surface segregation are also effective on Li-rich layered oxide  $\text{Li}_{1.13}\text{Ni}_{0.3}\text{Mn}_{0.57}\text{O}_2$  cathode material improving its reversible capacity and rate capability. X-ray photoelectron spectroscopy in conjunction with ion sputtering has shown that W segregates to the particle surfaces and decreases the surface Ni/Mn

atomic ratio; high-resolution transmission electron microscopy has further suggested that the segregation of W increases the structural disorder at the particle surfaces, which may also benefit the rate performance.

## Chapter 1. Introduction

### 1.1. The Introduction of Thermodynamic Models

#### 1.1.1 Surface amorphous films

A film will spontaneously “coat” on the surface of crystalline electrode particle if replacing a “clean” crystal-vapor surface of the electrode ( $\gamma_{cv}^{(0)}$ ) with a film-vapor surface ( $\gamma_{fv}$ ) and a crystal-film interface ( $\gamma_{cf}$ ) lowers the free energy:

$$\gamma_{cf} + \gamma_{fv} < \gamma_{cv}^{(0)}. \quad 1.1$$

Eq. 1.1 suggests that we should select a coating material with a lower surface energy than that of the electrode material ( $\gamma_{fv} < \gamma_{cv}^{(0)}$ ) in order to form uniform coatings spontaneously. Moreover, the film-electrode interfacial energy ( $\gamma_{cf}$ ) should be small; consequently, it is easier to make structurally-disordered coatings than crystalline coatings because the incoherent crystal-crystal interfacial energy is typically great. In the following text, we only consider structurally-disordered surface films; thermodynamically, we treat them as an undercooled quasi-liquid; thus, we replace all “f” with “l” in the subscripts (*i.e.*, we rename  $\gamma_{lv} = \gamma_{fv}$  and  $\gamma_{cl} = \gamma_{cf}$ ) in the following text.

We should recognize three important nanoscale wetting phenomena, as follows. First, as schematically illustrated in Figure 1.1(a), a nanometer-thick undercooled liquid film of thickness  $h$  can be thermodynamically stabilized on a surface below the bulk solidus line if

$$-\Delta\gamma \equiv \gamma_{cv}^{(0)} - (\gamma_{cl} + \gamma_{lv}) > \Delta G_{\text{amorph}}^{(\text{vol})} \cdot h, \quad 1.2$$

where  $\Delta G_{\text{amorph}}^{(\text{vol})}$  is the volumetric free-energy penalty for amorphization to form the undercooled liquid. The stabilization of impurity-based, quasi-liquid SAFs below the bulk solidus line is analogous to the well-known phenomenon of premelting (or surface melting) in unary systems<sup>1-3</sup> as well as the prewetting in Cahn's critical point wetting model<sup>4-6</sup>.

Second, when the quasi-liquid film is nanometer-thick, the abutting crystal will inevitably impose significant partial structural order into the film.<sup>7,8</sup> Thus, these SAFs are not fully liquid/amorphous, despite that they were named as surface "amorphous" films.<sup>8</sup> Interestingly, recent experimental and theoretical studies suggesting that such partial structural order near the crystal-glass interfaces can promote ion transport to achieve higher ionic conductivity than both bulk crystal and glass phases.<sup>9,10</sup>

Third, when the film thickness is in the nanometer range, short-range, van der Waals (vdW) London dispersion, electrostatic, and other interfacial interactions will arise. Thus, the excess surface free energy can be written as:

$$G^x(h) = (\gamma_{cl} + \gamma_{lv}) + \Delta G_{\text{amorph}}^{(\text{vol})} \cdot h + \sigma_{\text{short-range}}(h) + \sigma_{\text{vdW}}(h) + \sigma_{\text{elec}}(h) + \dots, \quad 1.3$$

where all interfacial interactions is defined so that  $\sigma(h = +\infty) = 0$  for consistence. The SAF will adopt an "equilibrium" thickness ( $h_{\text{eq}}$ ) that minimizes the excess film free energy ( $dG^x/dh|_{h=h_{\text{eq}}} = 0$ ), which represents a balance among attractive or repulsive pressures ( $d\sigma(h)/dh$ ) acting on the film (Figure 1.1(b)). Such a pressure-balance model was first proposed by Clarke to explain the equilibrium

thickness of IGFs<sup>11-13</sup> and later adapted to model SAFs.<sup>6,8,14,15</sup> Cannon proposed that these impurity-based equilibrium-thickness IGFs and SAFs can be alternatively (and equivalently) interpreted as a special class of structurally-disordered multilayer adsorbates.<sup>16</sup> It is important to note that the two interfaces are no longer independent and become one crystal-vapor surface thermodynamically under the condition that an equilibrium thickness is achieved,<sup>17</sup> where equilibrium surface energy corresponds to the minimum of Eq. 1.3:

$$\gamma_{cv}^{(eq)} = \gamma_{SAF} = \min\{G^x(h)\} = G^x(h_{eq}) \leq \gamma_{cv}^{(0)} \equiv G^x(0). \quad 1.4$$

The sum of the total interfacial pressure ( $\sum_i d\sigma_i(h)/dh$ ) is the well-known Deryaguin disjoining pressure. Quantifying all interfacial interactions in Eq. 1.3 for an oxide or phosphate system is infeasible. Alternatively, we can define a dimensionless interfacial coefficient ( $f(h)$ ) based on the following equation:

$$-\Delta\gamma \cdot [1 - f(h)] = \sum_i \sigma_i(h). \quad 1.5$$

Then, Eq. 1.3 can be simplified to:

$$G^x(h) - \gamma_{cv}^{(0)} = \Delta\gamma \cdot f(h) + \Delta G_{amorph}^{(vol)} \cdot h, \quad 1.6$$

which is schematically plotted in Figure 1.1(b). Since the SAF formation should reduce the total surface excess free energy (*i.e.*,  $G^x(h_{eq}) < \gamma_{cv}^{(0)}$ ), Eq. 1.2 can be refined to a more rigorous inequality:

$$-\Delta\gamma \cdot f(h_{eq}) > \Delta G_{amorph}^{(vol)} \cdot h_{eq}. \quad 1.7$$

By definitions, the dimensionless interfacial coefficient changes from zero to one as the film thickness is varied from zero to infinity, *i.e.*,  $f(0) = 0$  and  $f(+\infty) = 1$ .

### **1.1.2. The Surface adsorption/segregation, Wulff construction, and anisotropic surface segregation**

The surface energy can be changed (reduced) with adsorption/segregation of cation according to the well-known Gibbs adsorption equation:

$$\frac{d\gamma}{d\mu} = -\Gamma, \quad 1.8$$

where  $\gamma$  is the surface energy, and  $\mu$  and  $\Gamma$ , respectively, are the chemical potential and surface excess (total adsorption amount per unit area) of the adsorbing specie, respectively.

According to the well-established Wulff construction theory, a crystalline particle for a given volume at thermodynamic equilibrium status is of the lowest sum of anisotropic surface energy of various surface facets, which implies that the facets with lower surface energy should contribute to larger fraction of crystalline surface area; the decrease of surface area of certain facets indicates an increased surface energy corresponding to those facets.

Hence, by combining the Gibbs adsorption and Wulff theory, the morphology of crystal could be controlled by tailing facet surface energy resulting from cation surface segregation. Furthermore, the surface segregation of cation

could prefer to occur on the facets with higher relative surface energy to minimize the system Gibbs free energy.

## 1.2. The Motivation and Overview

Upgrading the electric energy storage capability can promote the renewable energy synchronization with power grid, expedite the distributed energy storage for high efficient utilization of traditional energy, and boom the electric automotive. Lithium-ion batteries, sodium-ion batteries as energy storage devices aims at higher energy density, higher rate capability, longer battery life, and lower cost to meet the application requirements. The electrode materials of both cathode and anode for lithium-ion batteries and sodium-ion batteries are the most important factors to improve the electrochemical performances.

It is a promising route that apply the thermodynamic principles based on surface amorphous films and cation surface segregation, combined with facile and low-cost synthesis method of high-energy ball milling with post annealing, to modify cathode and anode materials for enhanced electrochemical performances. Nanoscale coatings are widely used to improve the performance of electrode materials for lithium-ion batteries. In an ideal scenario, one wishes that such coatings form spontaneously via a facile treatment, have self-regulating and highly-uniform thickness, and help to significantly improve the performance of electrode materials.<sup>18-44</sup> This study demonstrates an approach to make such “dream coatings” through a facile “mixing and annealing” route via utilizing a unique class of equilibrium-thickness surface amorphous films (SAFs), which are essentially two-

dimensional surface “phases” (also called “complexions” based on an argument that they are not “phases” rigorously according to the Gibbs definition). In **chapter 1** and **chapter 2**, a thermodynamic framework of Surface amorphous films (SAFs) is proposed, which can be used to guide future experiments of other material systems. SAFs as a facile and generic surface modification method is utilized to significantly improve the rate performance and cycling stability of cathode materials for lithium-ion batteries. These nanoscale SAFs form spontaneously and uniformly upon mixing and annealing at a thermodynamic equilibrium, and they exhibit a self-regulating or “equilibrium” thickness due to a balance of attractive and repulsive interfacial interactions acting on the films. Furthermore, the formation of these SAFs improves the rate capability and cycling stability of both cathode materials significantly. Such SAFs can be utilized to improve the performance of many cathode as well as anode materials via a facile treatment. A potentially-transformative concept is to utilize surface phases (complexions) to achieve superior properties unattainable by conventional bulk phases or nanomaterials.

In **chapter 3**, utilizing anisotropic surface segregation to thermodynamically control the particle morphology is another economic, facile, and effective method to significantly improve the electrochemical performance of battery electrodes that can be applied to other materials.  $\text{WO}_3$  doping and anisotropic surface segregation can change the particle Wulff shape of  $\text{LiMn}_{1.5}\text{Ni}_{0.5}\text{O}_4$  spinel materials and the surface Mn/Ni ratio. The anisotropic surface segregation of W changes relative surface energies, increasing the areas of  $\{110\}$  and  $\{111\}$  facets with open

channels for fast lithium-ion diffusion. The rate capability is improved significantly by  $\text{WO}_3$  doping.

In **chapter 4**, the  $\text{WO}_3$  anisotropic surface segregation can also improve Co-free Li-rich layered oxide  $\text{Li}_{1.13}\text{Ni}_{0.3}\text{Mn}_{0.57}\text{O}_2$  cathode material with enhanced discharge capacity, rate capability, and cycling stability. X-ray photoelectron spectroscopy in conjunction with ion sputtering has shown that W segregates to the particle surfaces and decreases the surface Ni/Mn atomic ratio; high-resolution transmission electron microscopy has further suggested that the segregation of W increases the structural disorder at the particle surfaces, which may also benefit the rate performance.

In **chapter 5** for the anode material of lithium-ion batteries, the amorphous intergranular films (IGFs) is found on the surface region of Sn doped Si anode with improved cycling stability. The coexistence of amorphous intergranular films and porous secondary structure (characterized by FIB/SEM on the cross section) could be resulted in the enhanced cycling stability.

In **chapter 6**, beyond lithium-ion batteries, surface amorphous films (SAFs) can also improve the rate performance and cycling stability of electrode materials for sodium-ion batteries. A modified  $\text{TiO}_2$  with spherical secondary structure for via facile method of high energy ball milling following with annealing and surface nitridation.

In **chapter 7**, the feasibility of tailoring the electrochemical performance of electrode materials by simply changing their microstructures via facile ball milling and heat treatments can be particularly useful for optimizing composite electrodes

for sodium-ion batteries. Composites of  $\text{Na}_{0.44}\text{MnO}_2$ ,  $\text{Na}_{0.7}\text{MnO}_{2.05}$ , and  $\text{Na}_{0.91}\text{MnO}_2$  as cathode materials for sodium-ion batteries are synthesized by facile solid-state reaction, ball milling, and annealing methods. Two different composites of identical overall composition but drastically different morphologies and microstructures are synthesized.

**Chapter 1**, in part, is a reprint of the material “A Facile and Generic Method to Improve Cathode Materials for Lithium-Ion Batteries via Utilizing Nanoscale Surface Amorphous Films of Self-Regulating Thickness” as it appears in the Physical Chemistry Chemical Physics, Jiajia Huang and Jian Luo, 2014, 16, 7786-7798. **Chapter 1**, in part, is a reprint of the material “Composites of sodium manganese oxides with enhanced electrochemical performance for sodium-ion batteries: Tailoring properties via controlling microstructure” as it appears in the Science China Technological Sciences, Jiajia Huang and Jian Luo, 2016, 59, 1042-1047.

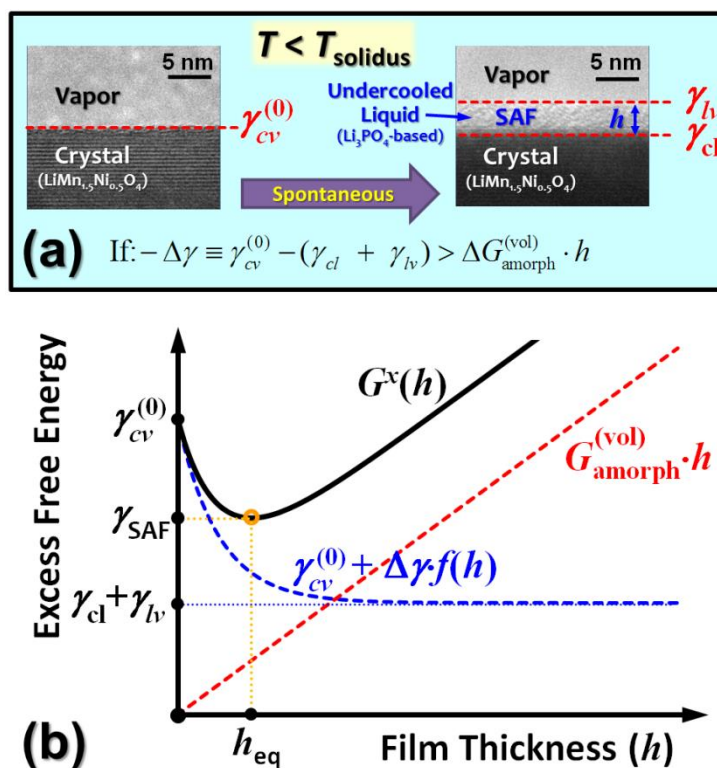


Figure 1.1 Schematic illustration of the thermodynamic principle for stabilizing a nanometer-thick SAF (being treated as an undercooled quasi-liquid film) below the bulk solidus line. The two micrographs used in this schematic illustration are actual HRTEM images of the  $\text{LiMn}_{1.5}\text{Ni}_{0.5}\text{O}_4$  specimens with and without a  $\text{Li}_3\text{PO}_4$ -based SAF. (b) Schematic illustration of an excess free energy vs. film thickness curve. The equilibrium thickness ( $h_{\text{eq}}$ ) corresponds to the minimum in  $G^x(h)$ , which is determined by a trade-off between the reduction of surface energy as the thermodynamic driving force ( $\Delta\gamma \cdot f(h)$ ) and the free-energy penalty for forming the undercooled liquid ( $\Delta G_{\text{amorph}}^{(\text{vol})} \cdot h$ ).

## References

- (1) Dash, J. G.; Wettlaufer, J. S. Classical Rotational Inertia of Solid He-4. *Physical Review Letters* **2005**, *94*, 235301.
- (2) Dash, J. G. Surface Melting. *Contemporary Physics* **1989**, *30*, 89-100.
- (3) van der Veen, J. F.; Pluis, B.; Denier, A. W.: Surface Melting. In *Chemistry and Physics of Solid Surfaces*; Vanselow, R., Howe, R. F., Eds.; Berlin Springer, 1988; Vol. 7; pp 455-467.
- (4) Cahn, J. W. Critical Point Wetting. *Journal of Chemical Physics* **1977**, *66*, 3667-3672.
- (5) Tang, M.; Carter, W. C.; Cannon, R. M. Grain Boundary Transitions in Binary Alloys. *Physical Review Letters* **2006**, *97*, 075502.
- (6) Luo, J.; Tang, M.; Cannon, R. M.; Carter, W. C.; Chiang, Y.-M. Pressure-Balance and Diffuse-Interface Models for Surficial Amorphous Films. *Materials Science and Engineering A* **2006**, *422*, 19-28.
- (7) Kaplan, W. D.; Kauffmann, Y. Structural Order in Liquids Induced by Interfaces with Crystals. *Annual Review of Materials Research* **2006**, *36*, 1-48.
- (8) Luo, J.; Chiang, Y.-M. Wetting and Prewetting on Ceramic Surfaces. *Annual Review of Materials Research* **2008**, *38*, 227-249.
- (9) Li, C.; Gu, L.; Maier, J. Enhancement of the Li Conductivity in  $\text{LiF}$  by Introducing Glass/Crystal Interfaces. *Advanced Functional Materials* **2012**, *22*, 1145-1149.
- (10) Schirmeisen, A.; Taskiran, A.; Fuchs, H.; Bracht, H.; Murugavel, S.; Roling, B. Fast Interfacial Ionic Conduction in Nanostructured Glass Ceramics. *Physical Review Letters* **2007**, *98*, 225901.
- (11) Clarke, D. R. On the Equilibrium Thickness of Intergranular Glass Phases in Ceramic Materials. *Journal of the American Ceramic Society* **1987**, *70*, 15-22.
- (12) Clarke, D. R.; Shaw, T. M.; Philipse, A. P.; Horn, R. G. Possible Electrical Double-Layer Contribution to the Equilibrium Thickness of Intergranular Glass Films in Polycrystalline Ceramics. *Journal of the American Ceramic Society* **1993**, *76*, 1201-1204.
- (13) Bobeth, M.; Clarke, D. R.; Pompe, W. Diffuse Interface Description of Intergranular Films in Polycrystalline Ceramics. *Journal of the American Ceramic Society* **1999**, *82*, 1537-1546.
- (14) Luo, J.; Chiang, Y.-M. Existence and Stability of Nanometer-Thick Disordered Films on Oxide Surfaces. *Acta Materialia* **2000**, *48*, 4501-4515.

- (15) Luo, J.; Chiang, Y.-M. Equilibrium-Thickness Amorphous Films on {11-20} Surfaces of Bi<sub>2</sub>O<sub>3</sub>-Doped ZnO. *Journal of the European Ceramic Society* **1999**, *19*, 697-701.
- (16) Cannon, R. M.; Rühle, M.; Hoffmann, M. J.; French, R. H.; Gu, H.; Tomsia, A. P.; Saiz, E. Adsorption and Wetting Mechanisms at Ceramic Grain Boundaries. *Ceramic Transactions (Grain Boundary Engineering in Ceramics)* **2000**, *118*, 427-444.
- (17) Baram, M.; Chatain, D.; Kaplan, W. D. Nanometer-Thick Equilibrium Films: The Interface between Thermodynamics and Atomistics. *Science* **2011**, *332*, 206-209.
- (18) Meng, X.; Yang, X.-Q.; Sun, X. Emerging Applications of Atomic Layer Deposition for Lithium-Ion Battery Studies. *Advanced Materials* **2012**, *24*, 3589-3615.
- (19) Riley, L. A.; Van Ana, S.; Cavanagh, A. S.; Yan, Y.; George, S. M.; Liu, P.; Dillon, A. C.; Lee, S.-H. Electrochemical Effects of Al<sub>2</sub>O<sub>3</sub> Surface Modification on Combustion Synthesized LiNi<sub>1/3</sub>Mn<sub>1/3</sub>Co<sub>1/3</sub>O<sub>2</sub> as a Layered-Cathode Material. *Journal of Power Sources* **2011**, *196*, 3317-3324.
- (20) Jung, Y. S.; Cavanagh, A. S.; Dillon, A. C.; Groner, M. D.; George, S. M.; Lee, S.-H. Enhanced Stability of LiCoO<sub>2</sub> Cathodes in Lithium-Ion Batteries Using Surface Modification by Atomic Layer Deposition. *Journal of the Electrochemical Society* **2010**, *157*, A75-A81.
- (21) Scott, I. D.; Jung, Y. S.; Cavanagh, A. S.; An, Y.; Dillon, A. C.; George, S. M.; Lee, S.-H. Ultrathin Coatings on Nano-LiCoO<sub>2</sub> for Li-Ion Vehicular Applications. *Nano Letters* **2011**, *11*, 414-418.
- (22) Guan, D.; Jeevarajan, J. A.; Wang, Y. Enhanced Cycleability of LiMn<sub>2</sub>O<sub>4</sub> Cathodes by Atomic Layer Deposition of Nanosized-Thin Al<sub>2</sub>O<sub>3</sub> Coatings. *Nanoscale* **2011**, *3*, 1465-1469.
- (23) Zhao, J.; Wang, Y. Ultrathin Surface Coatings for Improved Electrochemical Performance of Lithium Ion Battery Electrodes at Elevated Temperature. *Journal of Physical Chemistry C* **2012**, *116*, 11867-11876.
- (24) Zhao, J.; Wang, Y. Surface Modifications of Li-Ion Battery Electrodes with Various Ultrathin Amphoteric Oxide Coatings for Enhanced Cycleability. *Journal of Solid State Electrochemistry* **2013**, *17*, 1049-1058.
- (25) Zhao, J.; Wang, Y. Atomic Layer Deposition of Epitaxial ZrO<sub>2</sub> Coating on LiMn<sub>2</sub>O<sub>4</sub> Nanoparticles for High-Rate Lithium Ion Batteries at Elevated Temperature. *Nano Energy* **2013**, *2*, 882-889.
- (26) Li, C.; Zhang, H. P.; Fu, L. J.; Liu, H.; Wu, Y. P.; Ram, E.; Holze, R.; Wu, H. Q. Cathode Materials Modified by Surface Coating for Lithium Ion Batteries. *Electrochimica Acta* **2006**, *51*, 3872-3883.

(27) Fu, L. J.; Liu, H.; Li, C.; Wu, Y. P.; Rahm, E.; Holze, R.; Wu, H. Q. Surface Modifications of Electrode Materials for Lithium Ion Batteries. *Solid State Sciences* **2006**, *8*, 113-128.

(28) Liu, J.; Manthiram, A. Kinetics Study of the 5 V Spinel Cathode  $\text{Li}_{1.5}\text{Ni}_{0.5}\text{O}_4$  before and after Surface Modifications. *Journal of the Electrochemical Society* **2009**, *156*, A833-A838.

(29) Liu, J.; Manthiram, A. Understanding the Improved Electrochemical Performances of Fe-Substituted 5 V Spinel Cathode  $\text{Li}_{1.5}\text{Ni}_{0.5}\text{O}_4$ . *Journal of Physical Chemistry C* **2009**, *113*, 15073-15079.

(30) Wang, Q. Y.; Liu, J.; Murugan, A. V.; Manthiram, A. High Capacity Double-Layer Surface Modified  $\text{Li}[\text{Li}_{0.2}\text{Mn}_{0.54}\text{Ni}_{0.13}\text{Co}_{0.13}]\text{O}_2$  Cathode with Improved Rate Capability. *Journal of Materials Chemistry* **2009**, *19*, 4965-4972.

(31) Liu, J.; Manthiram, A. Understanding the Improvement in the Electrochemical Properties of Surface Modified 5 V  $\text{Li}_{1.42}\text{Ni}_{0.42}\text{Co}_{0.16}\text{O}_4$  Spinel Cathodes in Lithium-Ion Cells. *Chemistry of Materials* **2009**, *21*, 1695-1707.

(32) Wu, Y.; Manthiram, A. Effect of Surface Modifications on the Layered Solid Solution Cathodes (1-Z)  $\text{Li}[\text{Li}_{1/3}\text{Mn}_{2/3}]\text{O}_2$ -(Z)  $\text{Li}[\text{Mn}_{0.5}\text{Y}_{0.5}\text{Co}_{2y}]\text{O}_2$ . *Solid State Ionics* **2009**, *180*, 50-56.

(33) Liu, J.; Manthiram, A. Improved Electrochemical Performance of the 5 V Spinel Cathode  $\text{Li}_{1.5}\text{Ni}_{0.42}\text{Zn}_{0.08}\text{O}_4$  by Surface Modification. *Journal of the Electrochemical Society* **2009**, *156*, A66-A72.

(34) Wu, Y.; Murugan, A. V.; Manthiram, A. Surface Modification of High Capacity Layered  $\text{Li}[\text{Li}_{0.2}\text{Mn}_{0.54}\text{Ni}_{0.13}\text{Co}_{0.13}]\text{O}_2$  Cathodes by  $\text{Al}_2\text{O}_3$ . *Journal of the Electrochemical Society* **2008**, *155*, A635-A641.

(35) Wu, Y.; Manthiram, A. High Capacity, Surface-Modified Layered  $\text{Li}[\text{Li}(1-X)/3\text{Mn}(2-X)/3\text{Ni}_x/3\text{Co}_x/3]\text{O}_2$  Cathodes with Low Irreversible Capacity Loss. *Electrochemical and Solid State Letters* **2006**, *9*, A221-A224.

(36) Kannan, A. M.; Rabenberg, L.; Manthiram, A. High Capacity Surface-Modified  $\text{LiCoO}_2$  Cathodes for Lithium-Ion Batteries. *Electrochemical and Solid State Letters* **2003**, *6*, A16-A18.

(37) Kannan, A. M.; Manthiram, A. Surface/Chemically Modified  $\text{LiMn}_2\text{O}_4$  Cathodes for Lithium-Ion Batteries. *Electrochemical and Solid State Letters* **2002**, *5*, A167-A169.

(38) Cho, J.; Kim, Y. J.; Park, B. Novel  $\text{LiCoO}_2$  Cathode Material with  $\text{Al}_2\text{O}_3$  Coating for a Li Ion Cell. *Chemistry of Materials* **2000**, *12*, 3788-3791.

(39) Sun, K.; Dillon, S. J. A Mechanism for the Improved Rate Capability of Cathodes by Lithium Phosphate Surficial Films. *Electrochemistry Communications* **2011**, *13*, 200-202.

(40) Chong, J.; Xun, S. D.; Song, X. Y.; Liu, G.; Battaglia, V. S. Surface Stabilized  $\text{Li}_{1.5}\text{Mn}_{1.5}\text{O}_4$  Cathode Materials with High-Rate Capability and Long Cycle Life for Lithium Ion Batteries. *Nano Energy* **2013**, *2*, 283-293.

(41) Yi, T. F.; Li, X. Y.; Liu, H. P.; Shu, J.; Zhu, Y. R.; Zhu, R. S. Recent Developments in the Doping and Surface Modification of  $\text{LiFePO}_4$  as Cathode Material for Power Lithium Ion Battery. *Ionics* **2012**, *18*, 529-539.

(42) Li, X. W.; Yang, R.; Cheng, B.; Hao, Q.; Xu, H. Y.; Yang, J.; Qian, Y. T. Enhanced Electrochemical Properties of Nano- $\text{Li}_3\text{PO}_4$  Coated on the  $\text{LiMn}_2\text{O}_4$  Cathode Material for Lithium Ion Battery at 55 Degrees C. *Materials Letters* **2012**, *66*, 168-171.

(43) Lee, K. T.; Jeong, S.; Cho, J. Roles of Surface Chemistry on Safety and Electrochemistry in Lithium Ion Batteries. *Accounts of Chemical Research* **2013**, *46*, 1161-1170.

(44) Yi, T. F.; Zhu, Y. R.; Zhu, X. D.; Shu, J.; Yue, C. B.; Zhou, A. N. A Review of Recent Developments in the Surface Modification of  $\text{LiMn}_2\text{O}_4$  as Cathode Material of Power Lithium-Ion Battery. *Ionics* **2009**, *15*, 779-784.

## **Chapter 2. A Facile and Generic Method to Improve Cathode Materials for Lithium-Ion Batteries via Utilizing Nanoscale Surface Amorphous Films of Self-regulating Thickness**

### **2.1. Introduction**

Surface coatings and modifications are widely used to improve the performance of electrode materials for lithium-ion batteries. Notably, a series of recent studies have demonstrated that nanoscale surface oxide coatings made by atomic layer deposition (ALD) can improve the cycling stability and other performance properties of cathode materials.<sup>1-8</sup> Although ALD can be used to make uniform nanoscale oxide coatings with high levels of controls, this technique requires special equipment. Alternatively, numerous prior studies attempted to “coat” battery materials by mixing the active materials with coating materials by wet chemistry methods or simply dry mixing, where the specimens were typically subjected to subsequent annealing.<sup>9-27</sup> It is hoped that uniform nanoscale surface coatings might form, which were not always guaranteed. Consequently, substantial trials and errors were required and the success of such an approach largely depended on luck.

This study aims to establish an innovative coating strategy through a facile “mixing and annealing” route via utilizing a unique class of equilibrium-thickness surface amorphous films (SAFs). Compared with conventional approaches, these nanoscale SAFs form spontaneously with self-regulating and uniform thickness. Using  $\text{LiCoO}_2$  and  $\text{LiNi}_{0.5}\text{Mn}_{1.5}\text{O}_4$  as two proof-of-concept systems, we have

demonstrated that nanoscale  $\text{Li}_3\text{PO}_4$ -based SAFs can form these spontaneously and uniformly at thermodynamic equilibria, which have subsequently improved the rate performance and cycling stability of the two cathode materials via reducing the interfacial charge transfer resistance and suppressing the growth of the solid-electrolyte interphase (SEI).

The study was primarily motivated by the discovery of the thermodynamic stabilization of nanoscale SAFs in a variety of oxide systems.<sup>28-36</sup> These SAFs are free-surface counterparts to a class of equilibrium-thickness intergranular films (IGFs) that have been widely observed at ceramic grain boundaries and metal-oxide interfaces.<sup>35-40</sup> Thermodynamically, these equilibrium-thickness SAFs (or IGFs) can be considered as two-dimensional surface (or interfacial) “phases,” which have been named as “complexions” by Tang, Carter and Cannon based on arguments that they are not “phases” according to the rigorous Gibbs definition and they cannot exist without abutting bulk phases.<sup>35,41-46</sup> These SAFs (and analogous IGFs) have several distinct characteristics. First, they form spontaneously by mixing and annealing at a thermodynamic equilibrium. Second, they adopt a self-regulating or “equilibrium” thicknesses on the order of 1 nm. Third, they are neither fully crystalline nor completely amorphous (despite being called “amorphous” films). Forth, they can possess structures and compositions that are neither found nor stable as bulk phases (*e.g.*, the average film composition can lie in a bulk miscibility gap). Fifth, they can form at a thermodynamic equilibrium when the corresponding bulk liquid or glass phase is no longer stable. Thus, they can be utilized to achieve superior properties

unattainable by conventional bulk phases or nanomaterials.<sup>28</sup>

In 2005, Li and Garofalini<sup>47</sup> first suggested that such nanoscale “amorphous” interfacial films can act as rapid Li ion transport pathway via molecular dynamics simulations of  $V_2O_5$ . In 2008, De Jonghe and co-workers showed that the formation of 1-4 nm thick, impurity-based IGFs in lanthanum phosphate solid-state electrolytes increased the proton conductivity by more than an order of magnitude.<sup>48</sup> Later, nanoscale, phosphate-based IGFs, along with SAFs of similar character, have also been observed in partially-sintered  $LiFePO_4$  and  $LiMn_{1.5}Ni_{0.5}O_4$  electrodes.<sup>29,49,50</sup> In 2009, Tang, Chiang and Carter suggested that nanoscale SAFs can form in  $LiMPO_4$  ( $M = Fe, Mn, Co, Ni$ ) olivines and critically affect the phase transformation during electrochemical cycling via a diffuse-interface (phase-field) model.<sup>51</sup> In the same month, Kang and Ceder reported that the formation of a glassy  $Li_4P_2O_7$ -like “fast ion-conducting surface phase” (<5 nm) in “off-stoichiometric”  $LiFePO_4$  can help to achieve ultrafast discharging.<sup>52</sup> Although this report<sup>52</sup> led to great excitement, it too resulted in a debate.<sup>53,54</sup> A technical comment<sup>53</sup> suggested: “There is no reason to believe that  $Li_4P_2O_7$  impurity will coat the particles. Instead, impurities usually form nanoparticles that stick on the surfaces.” The follow-up study by Kayyar *et al.*<sup>29</sup> showed that such coatings can form and they are likely equilibrium-thickness SAFs. In 2012, Chong *et al.* carefully re-examined Kang and Ceder’s material and benchmarked it with carbon-coated  $LiFePO_4$ ; their study confirmed the effects of  $Li_4P_2O_7$ -based “fast ion-conducting surface phase” in improving the rate performance despite that the electronic conductivity was not increased.<sup>49</sup>

It is also worth noting that a series of prior studies coated amorphous oxides (such as  $\text{Al}_2\text{O}_3$ ,  $\text{ZnO}$ ,  $\text{Bi}_2\text{O}_3$ ,  $\text{AlPO}_4$ ,  $\text{MgO}$ ,  $\text{CoPO}_4$ ,  $\text{CeO}_2$ ,  $\text{ZrO}_2$ , and  $\text{SiO}_2$ ) on a variety of cathode particles to improve cycling and rate performances.<sup>11-20</sup> These coatings were made by a special solution-based sol-gel coating method. Some of these coatings remained uniform and amorphous after subsequent annealing at 400-600 °C, so that they must be at least metastable. However, it is unknown whether they are true equilibrium SAFs; in fact, many of these systems are unlikely equilibrium SAFs because of the high surface energies of the film-forming oxides (as discussed in the next section). Thus, these surface coatings were likely kinetically stabilized (*a.k.a.* they were not the equilibrium SAFs that would form spontaneously with self-regulating thickness upon annealing). Nonetheless, this series of studies<sup>11-20</sup> demonstrated the great potential of using nanoscale amorphous coatings to improve the performance of cathode materials.

Three more recent studies attempted to coat lithium phosphates on the surfaces of various cathode materials with some successes. In 2011, Sun and Dillon showed that  $\text{Li}_3\text{PO}_4$ -based surficial films could form on  $\text{LiCoO}_2$  in specimens annealed and quenched from 850 °C, which improved the rate performance; however, the authors noted that the surficial films formed at that specific condition were “not necessarily continuous or constant thickness” and were thicker (~10 nm) where they were present.<sup>22</sup> In 2012, Li *et al.* coated “nano- $\text{Li}_3\text{PO}_4$ ” on  $\text{LiMn}_2\text{O}_4$  to enhance the cycling stability at an evaluated temperature;<sup>25</sup> in their work, the specimens were calcined at a lower temperature of 450 °C, which resulted in ~ 10 nm thick crystalline nano- $\text{Li}_3\text{PO}_4$  phase

(presumably not uniform films) on  $\text{LiMn}_2\text{O}_4$ . In 2013, Chong *et al.* reported “surface stabilized  $\text{LiMn}_{1.5}\text{Ni}_{0.5}\text{O}_4$ ” by  $\text{Li}_4\text{P}_2\text{O}_7$ -based coatings with improved rate capability and cycling stability at room temperature;<sup>50</sup> in this study, the surface coatings appear to be uniform and thicker (8-10 nm), which the authors referred to as “a coating layer of  $\text{Li}_4\text{P}_2\text{O}_7$  crystallite coexisting with a little  $\text{Li}_3\text{PO}_4$ ”. It appeared that these phosphate-based coatings obtained at the specific processing conditions used in the three above-mentioned studies were not fully equilibrium SAFs that would form continuously with nearly constant thickness in a typical range of 0.5-5 nm.<sup>28</sup>

The assembly of the above-discussed recent studies motivated us to use  $\text{Li}_3\text{PO}_4$ -based SAFs on  $\text{LiCoO}_2$  and  $\text{LiNi}_{0.5}\text{Mn}_{1.5}\text{O}_4$  as two proof-of-concept systems to conduct a systematic and definite study, where we successfully found the processing conditions to form SAFs with self-regulating (equilibrium) thickness of ~2.9 nm and ~2.5 nm, respectively. It is imperative to conduct careful statistic measurements to prove the formation of uniform SAFs with nearly constant (equilibrium) thickness and then demonstrate that such SAFs can be utilized to improve the rate performance and cycling stability; such a critical and definite study has never been conducted before, which warrant the current work.

A further objective of this study is to investigate the underlying mechanisms of how such surface films/phases (regardless they are equilibrium or not) improve the performance of cathode materials. Kang and Ceder proposed that  $\text{Li}_4\text{P}_2\text{O}_7$ -like “fast ion-conducting surface phase” can serve as a “beltway” to

effectively improve ion transport because of the one-dimensional lithium ion conduction in  $\text{LiFePO}_4$ .<sup>52</sup> Sun and Dillon showed that  $\text{Li}_3\text{PO}_4$ -based surficial films, although they were not continuous with a constant thickness, significantly improved the rate performance of a more isotropic material,  $\text{LiCoO}_2$ , with two-dimensional ion conduction; thus, they suggested that these films might enhance the rate capability by reducing concentration polarization at the participle surfaces.<sup>22</sup> In this study, we found the processing conditions to form significantly more uniform  $\text{Li}_3\text{PO}_4$ -based SAFs on  $\text{LiCoO}_2$  with an equilibrium thickness of  $\sim 2.9$  nm. Furthermore, we adopted a special technique developed by Creager and co-workers<sup>55</sup> to show that the enhanced rate capability is not due to reduction in the concentration polarization; further impedance measurements suggested that these nanoscale SAFs may enhance the rate performance by reducing the interfacial charge transfer resistance. We further demonstrated that  $\text{Li}_3\text{PO}_4$ -based SAFs can enhance the rate performance of an even more isotropic material, spinel  $\text{LiNi}_{0.5}\text{Mn}_{1.5}\text{O}_4$ , as well as significantly improving its cycling stability at an elevated temperature by protecting the electrode surfaces and suppressing the SEI growth.

## 2.2. Thermodynamic Model and Theoretical Analysis

Here, we first present a thermodynamic model<sup>28</sup> to assess the stabilization of  $\text{Li}_3\text{PO}_4$ -based SAFs in the two proof-of-concept systems and to explain origin of the equilibrium thickness based on the discussion in **chapter 1.1.1**. This model can also be used to analyze and forecast the formation and stability of

equilibrium-thickness SAFs in other battery materials in future studies.

we can use the above framework to assess the possible stabilization of  $\text{Li}_3\text{PO}_4$ -based, equilibrium-thickness SAFs on  $\text{LiCoO}_2$  and  $\text{LiNi}_{0.5}\text{Mn}_{1.5}\text{O}_4$ , the two proof-of-concept systems adopted for this study. On one hand, the reduction in the interfacial energy (represented by  $\Delta\gamma f(h)$ , which should be negative for SAF formation,) is the thermodynamic driving force to form an SAF. In the current case, first-principle calculations estimated the  $\gamma_{\text{cv}}^{(0)}$  to be  $\sim 1\text{-}3 \text{ J/m}^2$  for  $\text{LiCoO}_2$  (Ref. <sup>56</sup>) and  $\sim 1.7\text{-}3.1 \text{ J/m}^2$  for  $\text{LiNi}_{0.5}\text{Mn}_{1.5}\text{O}_4$  (Ref. <sup>57</sup>), respectively. Thus, we adopt a median value of  $\gamma_{\text{cv}}^{(0)} \approx 2 \text{ J/m}^2$  for our estimation. In comparison, the crystalline  $\text{Li}_3\text{PO}_4$  surface energy was calculated to be  $\sim 0.6\text{-}1.2 \text{ J/m}^2$  by first-principle calculations,<sup>58</sup> and the liquid/amorphous  $\gamma_{\text{lv}}$  for  $\text{Li}_3\text{PO}_4$  should be less because some broken bonds can be satisfied by more relaxation; thus, we adopt the lower end value of the computed crystalline  $\text{Li}_3\text{PO}_4$  surface energy for the liquid/amorphous surface energy:  $\gamma_{\text{lv}} \approx 0.6 \text{ J/m}^2$ . Since we know that  $0 < -\Delta\gamma < (\gamma_{\text{cv}}^{(0)} - \gamma_{\text{lv}}) \approx 1.4 \text{ J/m}^2$  for SAF formation, we adopt a median value of  $\Delta\gamma \approx -0.7 \text{ J/m}^2$  as a rough estimation for the driving force for stabilizing an SAF in our systems.

On the other hand, there are two major attractive interactions that act to thin (diminish) the SAF. First, an attractive vdW London dispersion force is believed to restrain SAFs and IGFs from thickening above the bulk solidus line.<sup>28,30,37,39,40</sup> In the current cases, the specific refractive indices and dielectric constants are not available for estimating the sign and strength of the dispersion

force; however, the refractive index of the  $\text{LiPO}_3$  glass ( $n \approx 1.5$ ) is less than those of transition metal oxides ( $n > 2$  for  $\text{MnO}$  and  $\text{NiO}$ )<sup>59</sup>, so the dispersion force is likely to be repulsive and insignificant for the current case.<sup>60,61</sup> More importantly, we aimed to form SAFs well below the corresponding bulk solidus lines and prior studies suggested that the dispersion force is typically overwhelmed by the other (second) most common attractive interaction resulted from the  $\Delta G_{\text{amorph}}^{(\text{vol})} \cdot h$  term.<sup>28,62</sup> Under such conditions, we can safely neglect the dispersion interaction. Then, we can introduce a thermodynamic parameter ( $\lambda$ ) to represent the thermodynamic tendency to stabilize a nanoscale SAF well below the bulk solidus line, as follows:<sup>63-65</sup>

$$\lambda \equiv \frac{-\Delta\gamma}{\Delta G_{\text{amorph}}^{(\text{vol})}} \quad 2.1$$

The computed  $\lambda$  scales the actual film thickness. In the current case, where the  $\Delta G_{\text{amorph}}^{(\text{vol})} \cdot h$  term is the dominant term that controls the film thickness well below the bulk solidus line,  $\lambda$  can be used as a first-order estimate of the film thickness. More details about the derivation and justifications of this model and estimation method can be found in earlier studies of analogous subsolidus IGFs in metallic alloys,<sup>63-67</sup> where the basic interfacial thermodynamic model and analysis methods are applicable to the current case.

To quantify  $\Delta G_{\text{amorph}}^{(\text{vol})}$  and accurately estimate the film thickness, we need full thermodynamic functions (typically from CALPHAD data) for the multicomponent systems involved,<sup>63-67</sup> which are not available for the current

case. However, we can roughly estimate this term by using a one-component equation,  $\Delta G_{\text{amorph}}^{(\text{vol})} \approx \Delta S_{\text{fusion}}^{(\text{vol})} \cdot \Delta T$ , where  $\Delta S_{\text{fusion}}^{(\text{vol})}$  is the volumetric fusion entropy and  $\Delta T$  is the effective undercooling. There is no reported fusion entropy for  $\text{Li}_3\text{PO}_4$ . The fusion entropy is  $\sim 23$  J/mol·K for  $\text{K}_3\text{PO}_4$ ,  $\sim 33$  J/mol·K for  $\text{H}_3\text{PO}_4$ , and  $\sim 17$  J/mol·K for  $\text{NaPO}_3$  (Ref. <sup>68</sup>); thus, we estimate the fusion entropy for  $\text{Li}_3\text{PO}_4$  to be  $\sim 15$ - $35$  J/mol·K, resulting in  $\Delta S_{\text{fusion}}^{(\text{vol})} \approx \sim 3$ - $7 \times 10^5$  J/m<sup>3</sup>·K. The melting temperature for  $\text{Li}_3\text{PO}_4$  is  $1205$  °C (Refs. <sup>69,70</sup>). We select annealing temperatures of  $600$ - $800$  °C to form SAFs so that the effective  $\Delta T \approx 400$ - $600$  K since there is no known intermediate compound or eutectic reaction in either binary system. Subsequently,  $\Delta G_{\text{amorph}}^{(\text{vol})}$  is estimated to be  $\sim 1$ - $4 \times 10^8$  J/m<sup>3</sup>, which is equivalent to an attractive pressure of  $100$ - $400$  MPa that acts to thin the SAF; this estimate also further justifies that dispersion forces, which are typically on the order of  $1$ - $10$  MPa for similar cases<sup>28,62</sup>, can be safely neglected for the current cases. The actual effective  $\Delta T$  and  $\Delta G_{\text{amorph}}^{(\text{vol})}$  can be reduced somewhat if there are some solubilities of other oxide components in the  $\text{Li}_3\text{PO}_4$ -based liquid or SAFs.

Eq. 1.2, Eq. 1.7 and Figure 1.1(b) show that  $\Delta G_{\text{amorph}}^{(\text{vol})} \cdot h$  is the free-energy penalty to form an SAF, which adds  $0.1$ - $0.4$  J/m<sup>2</sup> per nanometer (of the SAF thickness) to the total excess surface energy in Eq. 1.3 or Eq. 1.6. The analysis above estimates the median value of  $\Delta\gamma$  to  $-0.7$  J/m<sup>2</sup>, which provides the thermodynamic driving force that is significant enough for stabilizing an SAF (Figure 1.1(b)). Combining the estimations of driving force and penalty, Eq. 1.8

produces an estimated  $\lambda$  value of ~2-7 nm (which may be somewhat greater if the actual effective  $\Delta T$  is less). Furthermore, comparing Eq. 1.7 and Eq. 1.8 produces:  $h_{\text{eq}} < \lambda \cdot f(h_{\text{eq}})$ ; thus, it is reasonable to estimate the actual equilibrium thickness to be in the low end of estimated range of 2-7 nm. In the experiments that will be presented subsequently, we have observed the formation of SAFs with equilibrium thicknesses of ~2.9 nm and ~2.5 nm, respectively, for the two proof-of-concept systems, which are well consistent with the model prediction.

## **2.3. Experimental**

### **2.3.1. Materials synthesis**

To prepare  $\text{Li}_3\text{PO}_4$ -coated  $\text{LiCoO}_2$ , 2 or 5 vol. % of  $\text{Li}_3\text{PO}_4$  powder was added to 5 g of as-received  $\text{LiCoO}_2$  (Alfa Aesar, 99.5%) and dispersed in 10 ml acetone; the mixture was placed in a silicon nitride grinding vial with two silicon nitride balls. Before sealing the jar, corprene gasket was taped by Teflon to prevent it from acetone corrosion and precursor contamination. High energy ball milling was carried out using a SPEX 8000D mill for a duration of 10 min followed by a 15 min resting interval, and this milling process was repeated for 3 times. The mixture was dried in a vacuum oven. The dried powder was placed in a covered alumina crucible, isothermally annealed at 600 °C for 4 h in a box furnace with a heating rate of 5 °C/min, and air quenched. As a reference, controlled specimens of uncoated  $\text{LiCoO}_2$  were prepared with exactly the same ball milling and annealing procedure described above without the addition of  $\text{Li}_3\text{PO}_4$ .

LiMn<sub>1.5</sub>Ni<sub>0.5</sub>O<sub>4</sub>-based specimens were prepared with a similar procedure. To prepare the reference uncoated specimens, as-received LiMn<sub>1.5</sub>Ni<sub>0.5</sub>O<sub>4</sub> (Sigma-Aldrich, >99%) was ball milled for 60 min, isothermally annealed at 800 °C for 8h (with 5 °C/min heating rate), and quickly cooled down in the furnace with power shut down. Li<sub>3</sub>PO<sub>4</sub>-coated LiMn<sub>1.5</sub>Ni<sub>0.5</sub>O<sub>4</sub> specimens were prepared by mixing 2 vol. % Li<sub>3</sub>PO<sub>4</sub> with the pristine LiMn<sub>1.5</sub>Ni<sub>0.5</sub>O<sub>4</sub>, which were subsequently subjected to the exact same ball milling and heat treatment procedures. Since the as-received LiMn<sub>1.5</sub>Ni<sub>0.5</sub>O<sub>4</sub> are non-uniform in particle size distribution and agglomerated, an additional reference LiMn<sub>1.5</sub>Ni<sub>0.5</sub>O<sub>4</sub> specimen was prepared by annealing as-received LiMn<sub>1.5</sub>Ni<sub>0.5</sub>O<sub>4</sub> at 800 °C for 8h without prior ball milling.

### **2.3.2. Material characterization**

X-ray diffraction (XRD) was carried out on a Scintag 2000 diffractometer using Cu K<sub>α</sub> radiation ( $\lambda = 1.5418 \text{ \AA}$ ) operating at 40 kV and 35 mA with a step size of 0.02° and a step time of 1 s. Particle sizes and morphologies were characterized using a Hitachi 4800 scanning electron microscope (SEM). Particle surfaces were characterized by high-resolution transmission electron microscopy (HRTEM) using a Hitachi 9500 microscope. HRTEM specimens were prepared by dispersing powders ultrasonically in acetone and dropping a small amount of the suspension onto carbon coated copper grids; the specimens were then dried overnight in a desiccator. Minimum exposure was used during HRTEM to reduce electron beam damages. A large number of images of randomly-selected particle surfaces were recorded for each specimen for a fair statistical analysis.

### 2.3.3. Electrochemical measurement

To prepare cathodes, 80 wt. % active materials, 15 wt. % carbon black (MTI), 5 wt. % PVDF (MTI), and appropriate amount of NMP (Alfa Aesar, anhydrous, 99.5 %) were mixed in a glass vial by a vibrating mixer, followed by further ultrasonic dispersion. The mixture was coated on an aluminum foil, which was subsequently dried in a vacuum oven at 120 °C for 12 h. Cathode electrodes with a diameter of 10 mm were punched out, pressed at ~187 MPa, and transferred into an Ar-filled glovebox for battery construction. Half cells were made with a cathode electrode, a metal Li chip (MTI, 99.9 %) as the anode, 1M LiPF<sub>6</sub> electrolyte, C480 separator (Celgard), and 2032 coin cell cases (SS304, MTI). The detailed procedure of assembling coin cells can be found in Ref. <sup>71</sup>. To make the electrolyte, EC/DEC/DMC (1:1:1 vol., BASF) solvent was used for LiCoO<sub>2</sub> batteries that were charged up to 4.3 V, and EC/DMC (1:1 vol., BASF) solvent was used for LiCoO<sub>2</sub> batteries that were charged up to 4.5 V and LiMn<sub>1.5</sub>Ni<sub>0.5</sub>O<sub>4</sub> batteries that were charged to 5.0 V. To probe whether the interfacial polarization of the electrolyte near the particle surfaces is the rate control step in LiCoO<sub>2</sub>-based cathodes, we also prepared and tested coin cells with 0.1M LiPF<sub>6</sub> electrolyte following a procedure developed by Creager and co-workers.<sup>55</sup>

Electrochemical cycling tests were carried out on an Arbin 2143 tester. The rate capabilities of LiCoO<sub>2</sub> were tested at charge and discharge rate of C/5 for 4 cycles, followed by discharging at 1C, 2C, 5C, 10C, and 25C sequentially (2

cycles at each discharge rate) while keeping the charge rate at C/5. An external pressure of ~40 MPa was added on coin cells during rate performance tests to reduce internal contact resistance. The rate performance of  $\text{LiMn}_{1.5}\text{Ni}_{0.5}\text{O}_4$  specimens was tested at the discharge rates of C/5, 1C, 5C, 25C, 45C, 65C, and 85C sequentially (1 cycle at each discharge rate) with a constant charge rate of C/5. Before the rate performance test, all fresh  $\text{LiCoO}_2$  cells were charged and discharged at C/10 for 1 cycle and C/5 for 10 cycles to allow cells reaching a steady state. The cycling stability test of  $\text{LiCoO}_2$  was performed between 3.0 V and 4.5 V at a rate of 1C and room temperature after charging and discharging from 3 V to 4.2 V at a rate of C/10 for 1 cycle. The cycling stability of  $\text{LiMn}_{1.5}\text{Ni}_{0.5}\text{O}_4$  specimens were measured at charge and discharge rate of 1C between 3.2 V and 5.0 V at an elevated temperature of  $55 \pm 3$  °C in an isothermal dry oven after first idling at  $55 \pm 3$  °C for 2 h.

Cyclic voltammetry (CV) and electrochemical impedance spectroscopy (EIS) were performed using a Solartron 1287A/1255B analyzer. CV of  $\text{LiCoO}_2$  was performed between 3.3 V and 4.5 V at a scan rate of  $0.1 \text{ mV s}^{-1}$ . Electrochemical impedance was measured from 1 MHz to 0.05 Hz at 10 mV. Fresh cells of  $\text{LiCoO}_2$  with Li metal as the counter electrodes were cycled for 4 cycles at rate of C/5 and finally charged to 4.2 V before the impedance measurements. Impedance measurements were also conducted for  $\text{LiMn}_{1.5}\text{Ni}_{0.5}\text{O}_4$  cells that were cycled at room temperature for 10 cycles (before the first measurement) and then cycled at  $55 \pm 3$  °C for 50 additional cycles

(before the second measurement). All cells for impedance measurements were kept for more than 10 h after the charging to reach steady states.

## 2.4. Results and Discussion

### 2.4.1. $\text{Li}_3\text{PO}_4$ -based equilibrium-thickness SAFs on $\text{LiCoO}_2$

XRD revealed only  $\text{LiCoO}_2$  peaks in both uncoated and 2 vol. %  $\text{Li}_3\text{PO}_4$  coated  $\text{LiCoO}_2$  specimens (Figure 2.1); some crystalline  $\text{Li}_3\text{PO}_4$  phase might exist in the coated specimens as the secondary phase, but the amount and crystallinity were below the detection limit of XRD. SEM characterization showed that uncoated and 2 vol. %  $\text{Li}_3\text{PO}_4$  coated  $\text{LiCoO}_2$  specimens have similar particle sizes on the order of  $\sim 1\ \mu\text{m}$  (Figure 2.2).

Thin layers were found on the surfaces of uncoated  $\text{LiCoO}_2$  particles, which were presumably  $\text{Li}_2\text{CO}_3$  formed during annealing (that was commonly seen in prior studies<sup>29,72</sup>). As shown in Figure 2.3, thicker and more uniform amorphous films were observed to form on particle surfaces of  $\text{Li}_3\text{PO}_4$  added  $\text{LiCoO}_2$  specimens, in comparison with the reference uncoated  $\text{LiCoO}_2$  that has been subjected to the exactly the same milling and annealing conditions. The observed surface films in  $\text{Li}_3\text{PO}_4$ -coated  $\text{LiCoO}_2$  specimens appeared to be largely “amorphous” in HRTEM imaging (Figure 2.3(b)), despite the equilibrium temperature ( $600\ \text{°C}$ ) was likely well below the solidus temperature ( $T_{\text{melt}} = 1205\ \text{°C}$  for  $\text{Li}_3\text{PO}_4$  according to Refs.<sup>69,70</sup> and there is no known deep eutectic reaction between  $\text{Li}_3\text{PO}_4$  and  $\text{LiCoO}_2$ ). As discussed in §2, the stabilization of the “amorphous” or quasi-liquid surface films with large structural disorder was likely

driven by the  $-\Delta\gamma$  term as the formation of crystalline surface films was frustrated by the high crystal-crystal interfacial energy that would occur.

To determine whether the observed SAFs have an equilibrium thickness, a large number of HRTEM images were recorded for randomly selected particle surfaces in three specimens (uncoated, 2 vol. % and 5 vol. %  $\text{Li}_3\text{PO}_4$ -coated  $\text{LiCoO}_2$ ) that were equilibrated at and quenched from 600 °C, and careful statistical analysis was performed subsequently. The key results were summarized in Figure 2.3(c). In the uncoated  $\text{LiCoO}_2$  specimen, and surface (carbonate) films ( $> \sim 0.3$  nm thick to be clearly discerned by HRTEM) were found on  $\sim 78\%$  particle surfaces among 18 surfaces characterized. The mean film thickness was measured to be 0.88 nm with a large relative standard deviation of 0.75 nm; this specimen was referred to as “uncoated  $\text{LiCoO}_2$ ” or “ $\text{LiCoO}_2$  without SAFs” interchangeably despite of the presence of thin carbonate layers. Discernable SAFs were observed on 62 out of 64 ( $\sim 97\%$ ) independent particle surfaces in the  $\text{Li}_3\text{PO}_4$ -coated  $\text{LiCoO}_2$  specimens. In the 2 vol. %  $\text{Li}_3\text{PO}_4$  added  $\text{LiCoO}_2$  specimen, the mean film thickness was measured to be 2.90 nm with a standard deviation of 2.17 nm from a population of 35 independent particle surfaces characterized. When the addition of  $\text{Li}_3\text{PO}_4$  was increased to 5 vol. %, the mean measured film thickness remained at 2.97 nm with a standard deviation of 2.00 nm (measured from 29 independent particle surfaces). The fact that the mean and distribution of the measured film thickness was independent of the extra amount of added  $\text{Li}_3\text{PO}_4$  (2 vs. 5 vol. %) after reaching equilibration (Figure 2.3(c)) unequivocally proved that these  $\text{Li}_3\text{PO}_4$ -based SAFs exhibited a self-

limiting (equilibrium) thickness of  $\sim 2.9$  nm, which was thermodynamically-determined (as discussed in §2).

As shown in Figure 2.4(a),  $\text{Li}_3\text{PO}_4$ -based SAFs appreciably improved the rate performance of  $\text{LiCoO}_2$  for specimens tested in the normal 1M electrolyte. At 25°C, the average discharge capacity was measured to be 25.0 mAh/g for the  $\text{LiCoO}_2$  specimen without SAFs, which was increased by  $\sim 130$  % to 56.1 mAh/g in the 2 vol. %  $\text{Li}_3\text{PO}_4$ -coated  $\text{LiCoO}_2$  specimen with  $\sim 2.9$  nm thick SAFs. Since the SEM measurements showed that both specimens have comparable particles sizes (Figure 2.2), the comparison of rate performances was fair. Interestingly, the average discharge capacity was measured to be 37.0 mAh/g for the 5 vol. %  $\text{Li}_3\text{PO}_4$  added  $\text{LiCoO}_2$  specimen, which represented only a  $\sim 50$  % increase from the uncoated specimen. This result suggested that adding extra amount of  $\text{Li}_3\text{PO}_4$  beyond that was needed for forming equilibrium-thickness SAFs provided no additional benefits; in fact, the extra  $\text{Li}_3\text{PO}_4$  existed as a secondary phase, which might cause detrimental sintering and agglomeration effects during the 600 °C annealing. The substantial improvement of the rate performance was consistent with Sun and Dillon's prior results obtained in specimens quenched from 800 °C with thicker and non-uniform surficial films.<sup>22</sup>

Kang and Ceder proposed that  $\text{Li}_4\text{P}_2\text{O}_7$ -based surface phase improved the rate performance of one-dimensional ionic conducting  $\text{LiFePO}_4$  by enhancing fast surface ion conduction around the particle.<sup>52</sup> Since  $\text{LiCoO}_2$  is a more isotropic two-dimensional ion conductor, Sun and Dillon suspected that the enhanced rate performance was achieved by reducing concentration polarization of the

electrolyte at the participle surfaces.<sup>22</sup> In a recent work, Creager and co-workers<sup>55</sup> suggested that if the interfacial concentration polarization was the rate limiting step, the benefit would be increased after intentionally lowering the concentration of the electrolyte. Following this idea, we tested our specimens with and without SAFs in the 0.1 M LiPF<sub>6</sub> electrolyte for a mechanistic study. As shown in Figure 2.4(b), the SAFs became detrimental and lowered the discharge capacity at all rates. This result suggested that the concentration polarization of the electrolyte at the interface was not the rate limiting step for the current case according to Creager and co-workers' theory,<sup>55</sup> though we should recognize that Sun and Dillon's specimens had thicker (but non-uniform) surficial films, which might exhibit more ability to reduce the concentration polarization of the electrolyte by creating a through-thickness lithium gradient in the film (that was ~10 nm or ~3X thicker, according to their HRTEM images) as they suspected.<sup>22</sup>

EIS measurements were carried out to further understand how SAFs improve the rate performance. The measured spectra were shown in Figure 2.5(a) and fitted to an equivalent circuit shown in Figure 2.5(b) that was proposed and tested by Liu and Manthiram.<sup>14</sup> In this model (Figure 2.5(b)),  $R_o$  refers to Ohmic resistance arising from electrolyte, internal contact of different cell parts, separator, and cell cases;  $R_f$  and  $C_f$  refer to film resistance and capacitance of SEI and SAFs, which produce the high-frequency semicircle in the spectra;  $R_{ct}$  and  $C_{dl}$  represent the charge transfer resistance and capacitance of double layer, which produce the middle-frequency semicircle. The fitted  $R_f$  and  $R_{ct}$  values were summarized in Table 2.1. It was found that the sum resistance of  $R_f$  and  $R_{ct}$

inversely correlated with the measured discharge capacities at 25C (by comparing the last two columns in Table 2.1), with the following order (decreasing rate performance or increasing  $R_f + R_{ct}$ ): the coated cathode in the 1 M electrolyte > the uncoated cathode in the 1 M electrolyte > the uncoated cathode in the 0.1 M electrolyte > the coated sample cathode in the 1 M electrolyte, which suggested that ( $R_f + R_{ct}$ ) might control the rate performance. If this was true, the EIS measurements suggested that the formation of SAFs (at ~97% of surfaces with an average thickness of 2.9 nm) improved rate performance (at the normal electrolyte concentration of 1 M) largely by reducing interfacial charge transfer resistance ( $R_{ct}$ ), as shown in Table 2.1.

It is well known that  $\text{LiCoO}_2$  exhibits good cycling stability at room temperature when it charged up to 4.2V, but the capacity fades when it is charged to a higher voltage (with the occurrence of a hexagonal-monoclinic-hexagonal phase transition accompanying anisotropic lattice distortion<sup>73</sup> along with possibly more significant Co dissolution and HF corrosion). To investigate the effects of SAFs on capacity fading, we measured cycling performances of the  $\text{LiCoO}_2$  specimens with and without  $\text{Li}_3\text{PO}_4$ -based SAFs by charging and discharging between 3.0 and 4.5 V for 200 cycles. The measured results suggested that SAFs did appreciably reduce the capacity decaying (Figure 2.6). It was presumed that SAFs protected the electrode by reducing HF attack and Co dissolution. In the current case, phase transitions and associated strains and fractures likely make significant contributions to the capacity fading,<sup>74</sup> which are

presumably less effected by SAFs; this is partially confirmed by CV studies of cycling stability mechanism described below.

As shown in Figure 2.7(a), CV curves of  $\text{LiCoO}_2$  specimens with and without  $\text{Li}_3\text{PO}_4$ -based SAFs after the first cycle indicates that both materials underwent similar Li ion extraction/insertion and phase transition. Specifically, the peaks at 4.20/4.16 V corresponded to the phase transition with large lattice expansion,<sup>73</sup> and Figure 2.7(a) illustrated that  $\text{Li}_3\text{PO}_4$ -based SAFs had no effect on suppressing this phase transition. Figure 2.7(b)-(d) displayed the CV results of these two materials after 10, 50 and 100 cycles, respectively. It was evident that the peak current of  $\text{LiCoO}_2$  with  $\text{Li}_3\text{PO}_4$ -based SAFs was higher than that of the reference  $\text{LiCoO}_2$  specimen without  $\text{Li}_3\text{PO}_4$ -based SAFs at all cycles, suggesting a protection effect from the SAFs; these CV results were consistent with cycling stability performance shown in Figure 2.6. Furthermore, the peak currents of both coated and uncoated  $\text{LiCoO}_2$  decreased with increasing number of cycles, indicating the performance decaying in both specimens; this was presumably due to the strain accumulation and possible micro-fractures for which SAFs would have little protection effect; these results were also consistent with the gradual decaying of discharge capacities for both materials (Figure 2.6). Consequently, we conducted a more thorough study to examine the effects of  $\text{Li}_3\text{PO}_4$ -based SAFs on protecting  $\text{LiMn}_{1.5}\text{Ni}_{0.5}\text{O}_4$  at an elevated temperature, where HF attack and Mn dissolution is the major concern (so SAF formation is more beneficial), which was described in the next section.

#### **2.4.2. $\text{Li}_3\text{PO}_4$ -based equilibrium-thickness SAFs on $\text{LiMn}_{1.5}\text{Ni}_{0.5}\text{O}_4$**

XRD characterization of  $\text{LiMn}_{1.5}\text{Ni}_{0.5}\text{O}_4$  specimens revealed the presence of minor impurities of  $\text{Li}_x\text{Ni}_{1-x}\text{O}$  in the milled and annealed specimens (Figure 2.8), the formation of which was reported in literature for specimens annealed at similar conditions.<sup>75</sup>  $\text{LiMn}_{1.5}\text{Ni}_{0.5}\text{O}_4$  was the majority phase (while the amount of  $\text{Li}_x\text{Ni}_{1-x}\text{O}$  was fairly minor) and no other impurity phase was detected by XRD (Figure 2.8). Again, minor secondary crystalline phase of  $\text{Li}_3\text{PO}_4$  might be present in the  $\text{Li}_3\text{PO}_4$  added specimens, but below the detection limit of XRD. SEM characterization showed that the particles were well dispersed with comparable and normal distributions of particle sizes (both about 1  $\mu\text{m}$ ) for uncoated and coated specimens after milling and annealing, even if the starting powder has a non-uniform particle size distribution and was agglomerated (Figure 2.9).

HRTEM showed the formation of nanoscale  $\text{Li}_3\text{PO}_4$ -based SAFs in the 2 vol. %  $\text{Li}_3\text{PO}_4$  added specimen, which appeared to be largely “amorphous” in HRTEM imaging (Figure 2.10(b)); this was again consistent with the thermodynamic model presented in §2. The statistical results of the film thickness measurements were displayed in Figure 2.10(c). On one hand, ultrathin surface layers were identified on 17 out of 19 particle surfaces in the reference uncoated specimen; the mean thickness was measured to be 0.44 nm with a standard deviation of 0.26 nm, which was significantly thinner than the case of uncoated  $\text{LiCoO}_2$ . Again, this specimen is referred to as “uncoated  $\text{LiMn}_{1.5}\text{Ni}_{0.5}\text{O}_4$ ” or “ $\text{LiMn}_{1.5}\text{Ni}_{0.5}\text{O}_4$  without SAFs” in the following text despite of the presence of thin layers of presumably carbonate. On the other hand, discernable SAFs were

observed on 28 out of 29 (~97%) independent particle surfaces in the 2 vol. %  $\text{Li}_3\text{PO}_4$  added  $\text{LiCoO}_2$  specimen that was milled and annealed at the identical conditions. The mean film thickness was measured to be 2.53 nm with a standard deviation of 1.31 nm. The relative narrow distribution of the measured film thicknesses for  $\text{Li}_3\text{PO}_4$ -coated  $\text{LiCoO}_2$  specimen was an indication that an equilibrium (constant) thickness was achieved for the  $\text{Li}_3\text{PO}_4$ -based SAFs.

The rate performances of  $\text{LiMn}_{1.5}\text{Ni}_{0.5}\text{O}_4$  specimens with and without  $\text{Li}_3\text{PO}_4$ -based SAFs, which were subjected to identical milling and annealing conditions and have comparable particle sizes of  $\sim 1 \mu\text{m}$ , were summarized in Table 2.2. Representative discharging curves were displayed in Figure 2.11. Similar to the case of  $\text{LiCoO}_2$ ,  $\text{Li}_3\text{PO}_4$ -based SAFs appreciably improved the rate performance of  $\text{LiMn}_{1.5}\text{Ni}_{0.5}\text{O}_4$  at all rates. The increases were  $\sim 5\text{-}6\%$  at 0.2-5C,  $\sim 40\%$  at 25C, and  $\sim 360\%$  at 45C, respectively, which were presumably due to the formation of  $\sim 2.5$  nm thick  $\text{Li}_3\text{PO}_4$ -based SAFs. Small (but non-zero) discharge capacities of  $\sim 15.4$  mAh/g at 65C and  $\sim 7.3$  mAh/g at 85C were measured for the specimen with SAFs, while the capacity almost vanished for the specimen without SAFs at the same rates. At the same nominal rate of 25C, the achieved discharge capacity with SAFs was  $\sim 70.7$  mAh/g for the  $\text{LiMn}_{1.5}\text{Ni}_{0.5}\text{O}_4$  specimen with  $\sim 2.5$  nm thick  $\text{Li}_3\text{PO}_4$ -based SAFs, which was greater than the discharge capacity of 56.1 mAh/g for the  $\text{LiCoO}_2$  specimen with  $\sim 2.9$  nm thick  $\text{Li}_3\text{PO}_4$ -based SAFs, although the percentage increase was less ( $\sim 40\%$  for  $\text{LiMn}_{1.5}\text{Ni}_{0.5}\text{O}_4$  vs.  $\sim 130\%$  for  $\text{LiCoO}_2$  with the SAF formation).  $\text{LiMn}_{1.5}\text{Ni}_{0.5}\text{O}_4$  has a cubic spinel structure, which is even more isotropic than the layered  $\text{LiCoO}_2$ .

The SAFs still enhanced the rate performance, suggesting that anisotropic ion conduction was not a necessary condition for SAFs to improve the rate performance.<sup>22,52</sup>

It is well-known that the high-voltage materials  $\text{LiMn}_{1.5}\text{Ni}_{0.5}\text{O}_4$  is prone to capacity fading due to Mn dissolution and unstable SEI, particularly at elevated temperatures.<sup>76-78</sup> We have measured the cycling stability at an elevated temperature of 55 °C (with a relatively high charge/discharge rate of 1C) for five cells of  $\text{LiMn}_{1.5}\text{Ni}_{0.5}\text{O}_4$  specimens without  $\text{Li}_3\text{PO}_4$ -based SAFs and five cells of  $\text{LiMn}_{1.5}\text{Ni}_{0.5}\text{O}_4$  specimens with  $\text{Li}_3\text{PO}_4$ -based SAFs, respectively; the results clearly showed that the formation of  $\text{Li}_3\text{PO}_4$ -based SAFs reduced the capacity fading at 55 °C and improved cycling stability and consistency substantially. As shown in Figure 2.12, all five cells of  $\text{LiMn}_{1.5}\text{Ni}_{0.5}\text{O}_4$  with  $\text{Li}_3\text{PO}_4$ -based SAFs produced very consistent and stable cycling behaviors. In contrast, the cycling behaviors of the  $\text{LiMn}_{1.5}\text{Ni}_{0.5}\text{O}_4$  specimens without  $\text{Li}_3\text{PO}_4$ -based SAFs (that was subjected to identical milling and annealing processes) showed large variations in their capacities and capacity fading rates. Two cells of the uncoated  $\text{LiMn}_{1.5}\text{Ni}_{0.5}\text{O}_4$  died after ~150 and ~250 cycles, respectively; other cells also exhibited lower capacities and greater capacity fading rates. Figure 2.12 clearly showed that all five  $\text{LiMn}_{1.5}\text{Ni}_{0.5}\text{O}_4$  specimens with  $\text{Li}_3\text{PO}_4$ -based SAFs consistently exhibited more superior cycling stability than the five reference specimens without  $\text{Li}_3\text{PO}_4$ -based SAFs. Notably, the  $\text{LiMn}_{1.5}\text{Ni}_{0.5}\text{O}_4$  specimen with ~ 2.5 nm thick SAFs retained ~90 mAh/g or ~80% of the initial capacity after 350 cycles at an elevated temperature of 55 °C and relatively high

charge/discharge rate of 1C, which was an exceptional performance. Figure 2.13 further showed that  $\text{LiMn}_{1.5}\text{Ni}_{0.5}\text{O}_4$  with  $\sim 2.5$  nm thick SAFs also performed better than the as-received  $\text{LiMn}_{1.5}\text{Ni}_{0.5}\text{O}_4$  and an additional reference specimen that was annealed at 800 °C without prior ball milling.

We further conducted EIS measurements to investigate how SAFs improved the cycling stability. Four electrochemical impedance spectra for the specimens with and without SAFs, respectively, after 10 cycles at room temperature (as the start point before raising the temperature) and after 50 additional cycles at an elevated temperature of 55 °C, respectively, were collected and shown in Figure 2.14. The semicircles in the spectra represented the responses from the film resistance, which were mainly contributed from the SEI formed during the cycling. While the film resistance should always increase with cycling due to the SEI formation, it was clearly evident from Figure 2.14 that  $\text{Li}_3\text{PO}_4$ -based SAFs suppressed the growth of SEI, which was likely related to the improvement of the cycling stability at 55 °C; presumably, this was because the  $\text{Li}_3\text{PO}_4$ -based SAFs protected the electrode surfaces from HF attacks and reduced Mn dissolution, which resulted in more stable SEI that grew slower with the high-temperature cycling.

## 2.5. Conclusions

This study unequivocally demonstrated that equilibrium-thickness SAFs can form spontaneously via a facile mixing and annealing method in selected systems and processing conditions that satisfy certain thermodynamic criteria. A

thermodynamic framework is presented, which can be used to forecast the formation and stability of such nanoscale equilibrium-thickness SAFs in a broad range of battery electrode-coating systems if the relevant thermodynamic data are available or can be estimated. Using  $\text{Li}_3\text{PO}_4$ -based SAFs on  $\text{LiCoO}_2$  and  $\text{LiMn}_{1.5}\text{Ni}_{0.5}\text{O}_4$  as two proof-of-concept systems, we demonstrated that in each system/equilibrium condition, the spontaneously-formed SAFs formed uniformly (on ~ 97% of surfaces) with rather a narrow distribution of film thicknesses (around the corresponding thermodynamically-determined “equilibrium” thickness). Adding extra film-forming materials beyond that was needed for forming equilibrium-thickness SAFs did not change the mean and distribution of the measured film thicknesses, which definitely proved that these SAFs have self-limiting (equilibrium) thickness.

The formation of SAFs significantly improved the rate performance and cycling stability of both  $\text{LiCoO}_2$  and  $\text{LiMn}_{1.5}\text{Ni}_{0.5}\text{O}_4$ . At a high rate of 25C, SAF formation improved the discharge capacity by ~130% for  $\text{LiCoO}_2$  and by ~40 % for  $\text{LiMn}_{1.5}\text{Ni}_{0.5}\text{O}_4$ , respectively. A specially-designed mechanistic study suggested that interfacial polarization of the electrolyte was not the rate-limiting step for  $\text{LiCoO}_2$  specimens, and EIS measurements further suggested that SAFs improved the rate performance of  $\text{LiCoO}_2$  by facilitating interfacial charge transfer.  $\text{Li}_3\text{PO}_4$ -based SAFs also significantly improved the cycling stability of both cathodes. With the formation of ~2.5 nm thick equilibrium-thickness SAFs on the high-voltage material  $\text{LiMn}_{1.5}\text{Ni}_{0.5}\text{O}_4$ , a discharge capacity of ~90 mAh/g has been successfully retained after 350 cycles at an elevated temperature 55 °C

and a relatively high charge/discharge rate of 1C. EIS measurements suggested that  $\text{Li}_3\text{PO}_4$ -based SAFs reduced the capacity fading and improved the cycling stability and consistence by suppressing the SEI growth.

This study established a facile and generic surface modification method via an innovative use of equilibrium-thickness SAFs (*a.k.a.* a type of equilibrium surface “phases”) to improve the performance of battery electrodes, and this method can be readily applied to many other cathode as well as anode materials. The key idea is to let thermodynamics make the uniform nanoscale coating for us. On the top of this, a potentially-transformative concept is to utilize surface “phases” or complexions (equilibrium-thickness SAFs as only one example) to achieve superior structures and properties that are unattainable by using conventional bulk phases or normal materials fabrication methods. It is interesting to note that there was spot evidence in recent literature showing that facile heat treatments in controlled chemical environments can sometimes substantially improve the performance of both cathode<sup>79-81</sup> and anode<sup>82-85</sup> materials for lithium-ion batteries via the formation of surface defects or disordered structures including segregation or adsorption of impurity or doping species<sup>80,81,85</sup> (and similar surface “phases” can also be utilized to improved other properties, *e.g.*, catalytic and photocatalytic activities<sup>31,32,86,87</sup>), though it was unknown whether equilibrium surface “phases” or complexions truly formed (and if so, what were their particular types and characters) in those cases. The success of current study called for systematic and in-depth studies to explore the

innovative concept of utilizing surface “phases” or complexions to achieve distinct surface structures with superior properties that may be unattainable otherwise.

**Chapter 2**, in part, is a reprint of the material “A Facile and Generic Method to Improve Cathode Materials for Lithium-Ion Batteries via Utilizing Nanoscale Surface Amorphous Films of Self-Regulating Thickness” as it appears in the Physical Chemistry Chemical Physics, Jijia Huang and Jian Luo, 2014, 16, 7786-7798.

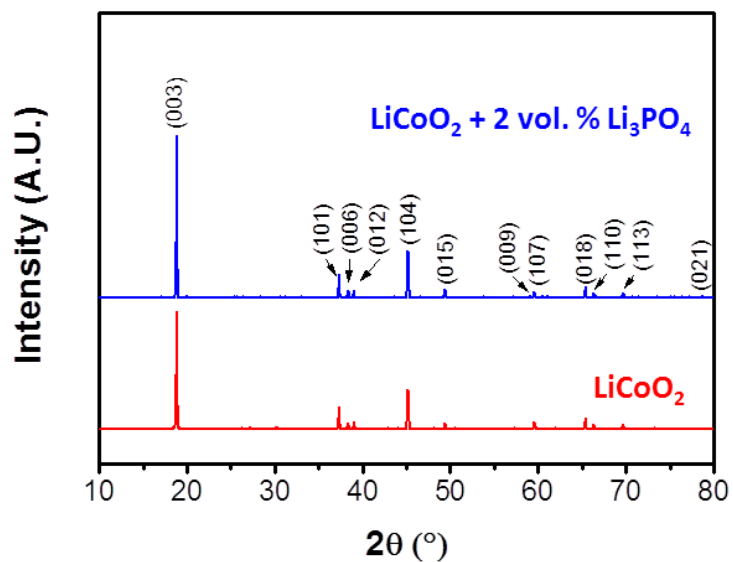


Figure 2.1 XRD patterns of the  $\text{LiCoO}_2$  and  $\text{LiCoO}_2 + 2 \text{ vol. } \% \text{Li}_3\text{PO}_4$  specimens that were milled and subsequently annealed at  $600^\circ\text{C}$  for 4 h.

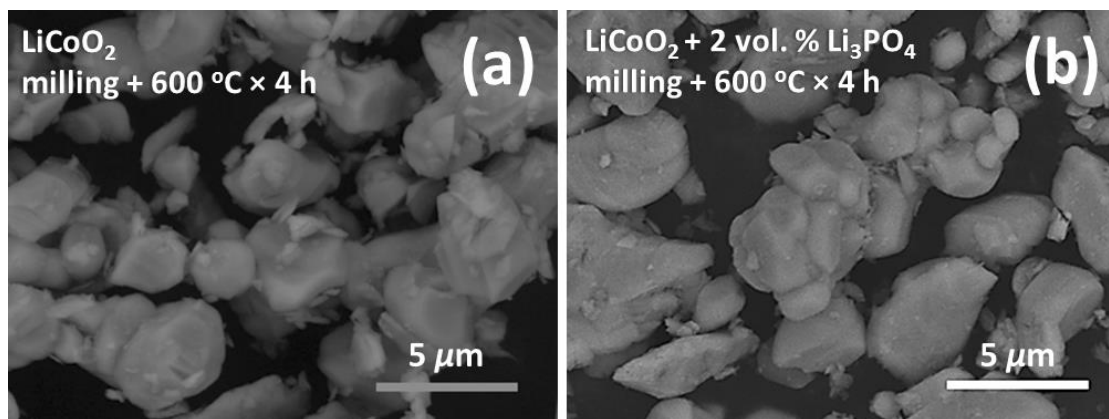


Figure 2.2 Representative SEM images of the (a)  $\text{LiCoO}_2$  and (b)  $\text{LiCoO}_2 + 2 \text{ vol. } \% \text{Li}_3\text{PO}_4$  specimens that were milled and subsequently annealed at  $600^\circ\text{C}$  for 4 h.

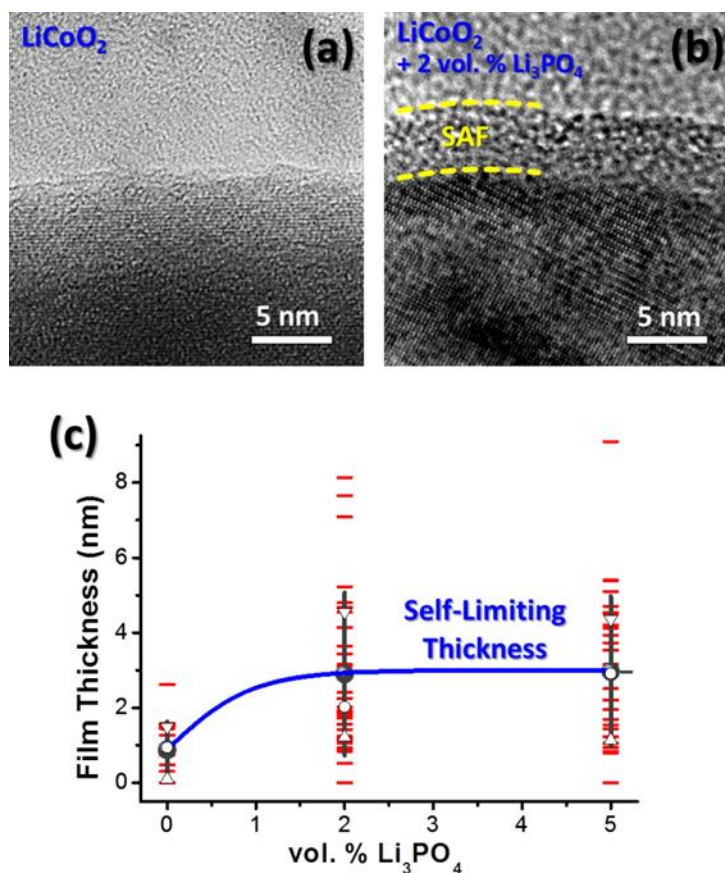


Figure 2.3 Representative HRTEM images of the particle surfaces in (a) uncoated and (b) 2 vol. %  $\text{Li}_3\text{PO}_4$  coated  $\text{LiCoO}_2$  specimens equilibrated at 600 °C. (c) Measured film thickness vs. volume percentage of  $\text{Li}_3\text{PO}_4$  added in  $\text{LiCoO}_2$  for specimens equilibrated at 600 °C. Each horizontal bar represents the average thickness of an SAF formed on the surface of one particle (measured at multiple points around the particles and averaged). Each solid dot represents the measured mean thickness for the SAFs on all particle surfaces in a specimen and the connecting vertical bar represents  $\pm$  one standard deviation. Open circles, upper triangles and lower triangles, respectively, represent the medians, lower quartiles and upper quartiles, respectively. These SAFs exhibit a self-limiting thickness that is independent of the excess volume fraction of  $\text{Li}_3\text{PO}_4$ , after an equilibration is achieved, which unequivocally proved the existence of a thermodynamically-determined equilibrium thickness.

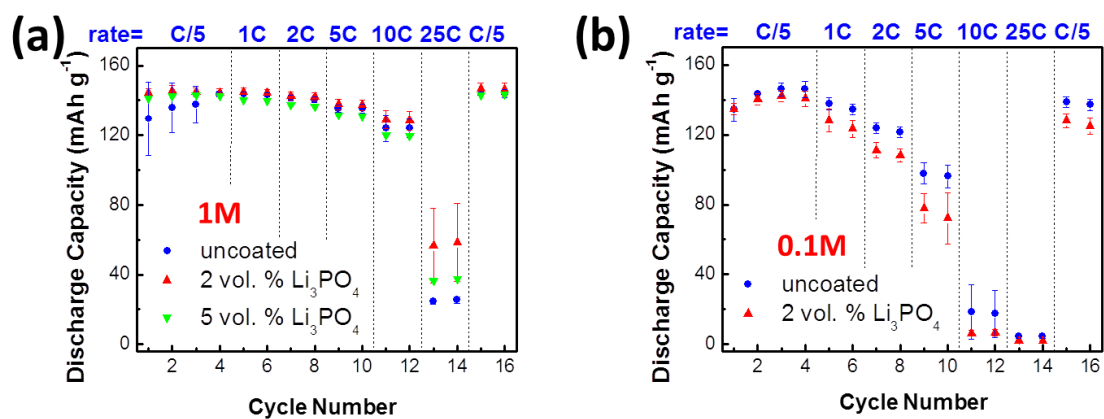


Figure 2.4 Measured rate performance of uncoated and coated  $\text{LiCoO}_2$  at the electrolyte concentration of (a) 1M and (b) 0.1M, respectively. Three coin cells were made and tested for each condition; the means are presented in the graphs and error bars represent  $\pm$  one standard deviations. All cells were charged at C/5 and discharged at various rates (labeled in the graphs) at room temperature.

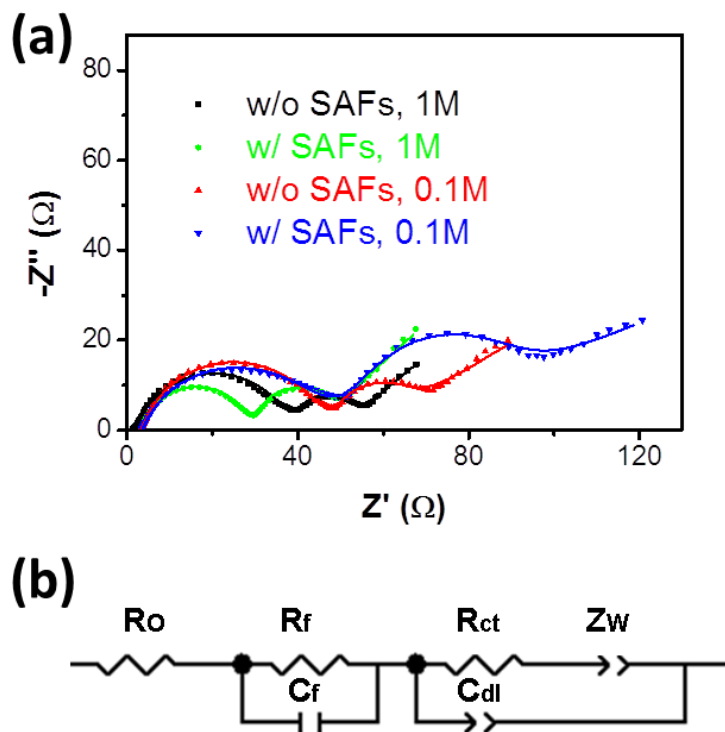


Figure 2.5 (a) Measured electrochemical impedance spectra of the  $\text{LiCoO}_2$  specimens with and without  $\text{Li}_3\text{PO}_4$ -based SAFs, respectively, tested in 1 M and 0.1 M electrolytes, respectively. Dots represent experimental data and solid lines represent fitting curves using (b) an equivalent circuit model that was proposed by Liu and Manthiram.<sup>14</sup>

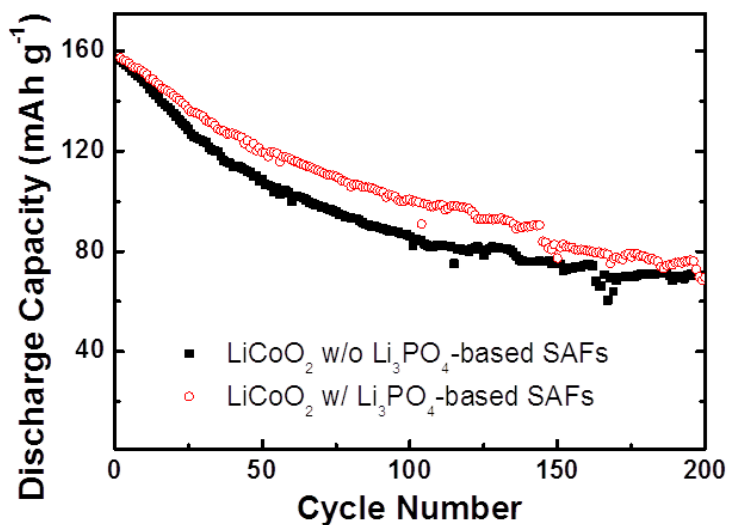


Figure 2.6 Cycling stability of LiCoO<sub>2</sub> specimens with and without Li<sub>3</sub>PO<sub>4</sub>-based SAFs that were cycled between 3 V and 4.5 V (vs. Li/Li<sup>+</sup>) at the charge/discharge rate of 1C at room temperature. The capacity fading is appreciably lower in the specimen with ~ 2.5 nm thick SAFs. It is possible that the SAFs disintegrated after ~140 cycles due to the strain accumulation resulted from cycling at the extended voltage range of 3 V to 4.5 V.

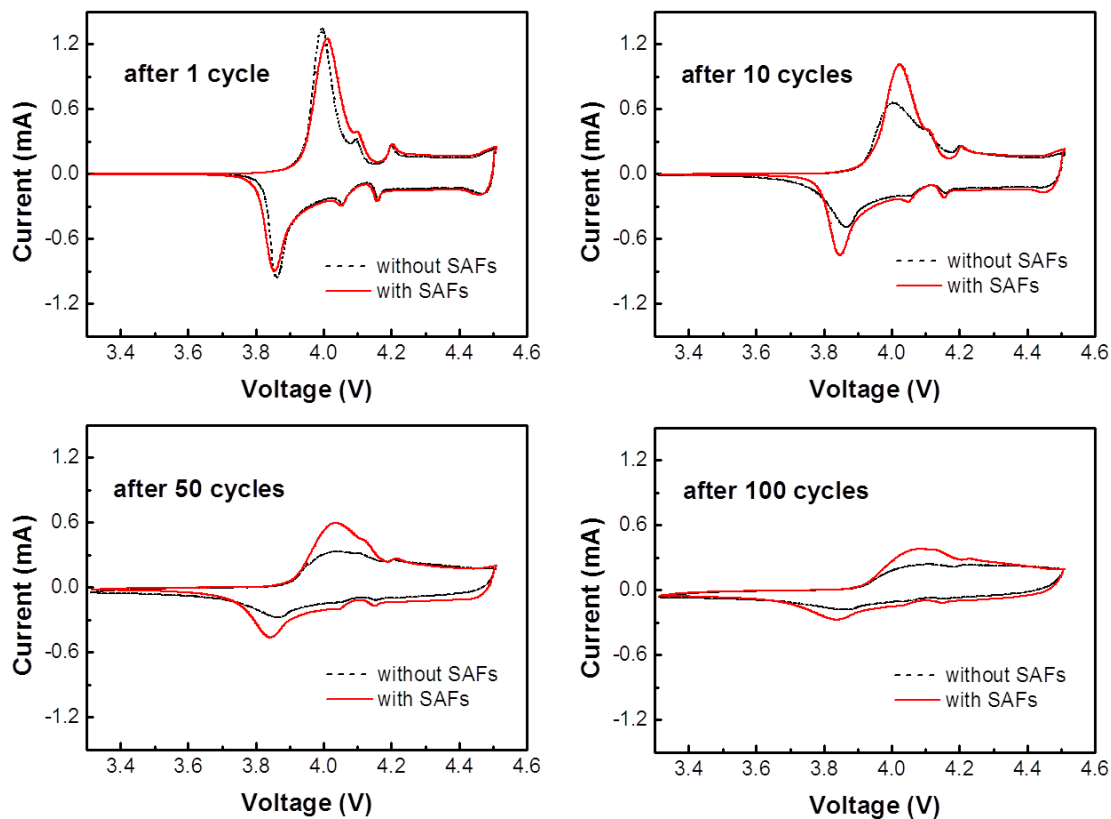


Figure 2.7 Comparison of cyclic voltammograms of the  $\text{LiCoO}_2$  specimens with and without  $\text{Li}_3\text{PO}_4$ -based SAFs after (a) 1 cycle, (b) 10 cycles, (c) 50 cycles, and (d) 100 cycles, which were measured at a scan rate of  $0.1 \text{ mV s}^{-1}$  from 3.3 V to 4.5 V. The first charge-discharge cycle was conducted from 3 V to 4.2 V at C/10, and the subsequent cycles were all conducted from 3 V to 4.5 V at 1C.

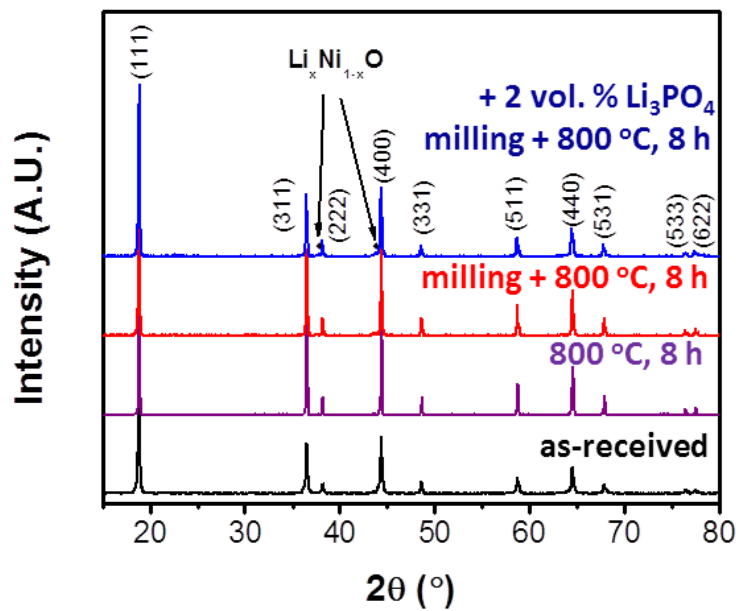


Figure 2.8 XRD patterns of various  $\text{LiMn}_{1.5}\text{Ni}_{0.5}\text{O}_4$  specimens. Minor amounts of a secondary crystalline phase of  $\text{Li}_x\text{Ni}_{1-x}\text{O}$  were detected in the milled and annealed specimens.

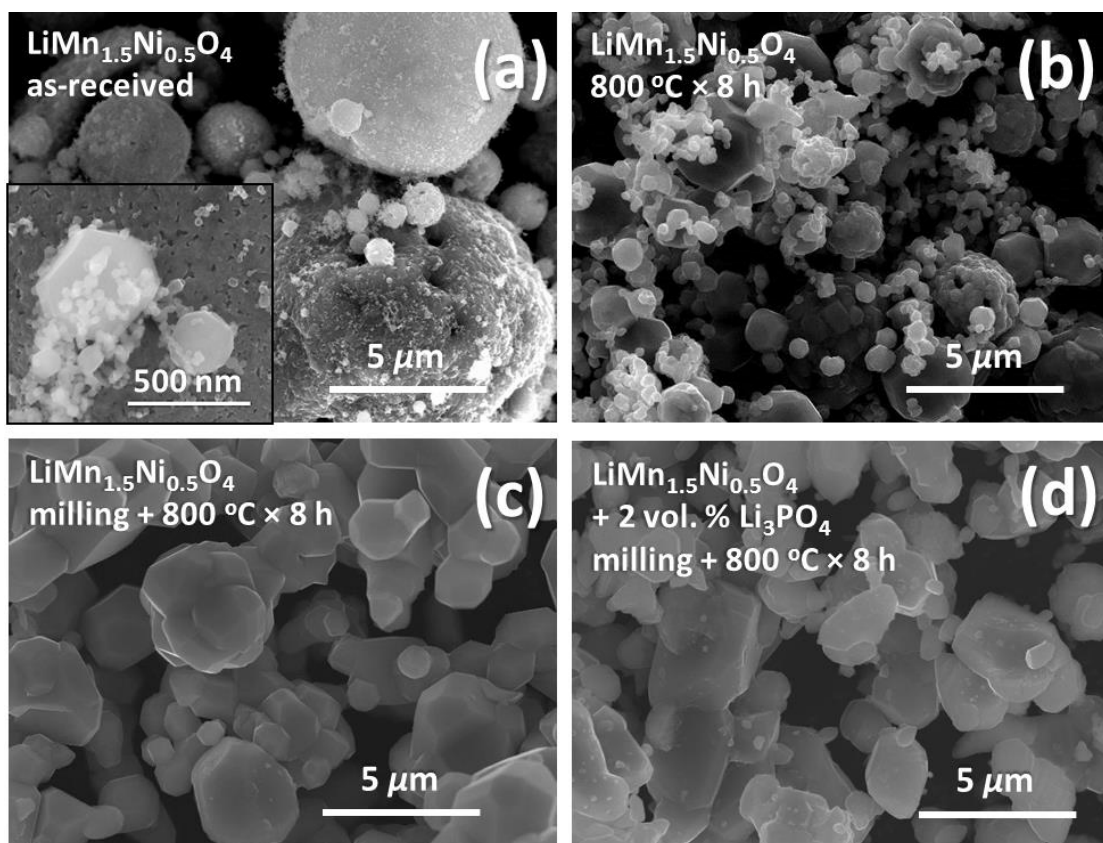


Figure 2.9 Representative SEM images of (a) the as-received  $\text{LiMn}_{1.5}\text{Ni}_{0.5}\text{O}_4$  specimen and (b) the reference  $\text{LiMn}_{1.5}\text{Ni}_{0.5}\text{O}_4$  specimen annealed at 800  $^\circ\text{C}$  (without ball milling), as well as the (c)  $\text{LiMn}_{1.5}\text{Ni}_{0.5}\text{O}_4$  and (d)  $\text{LiMn}_{1.5}\text{Ni}_{0.5}\text{O}_4$  + 2 vol. %  $\text{Li}_3\text{PO}_4$  specimens that were milled and subsequently annealed at 800  $^\circ\text{C}$  for 8 h.

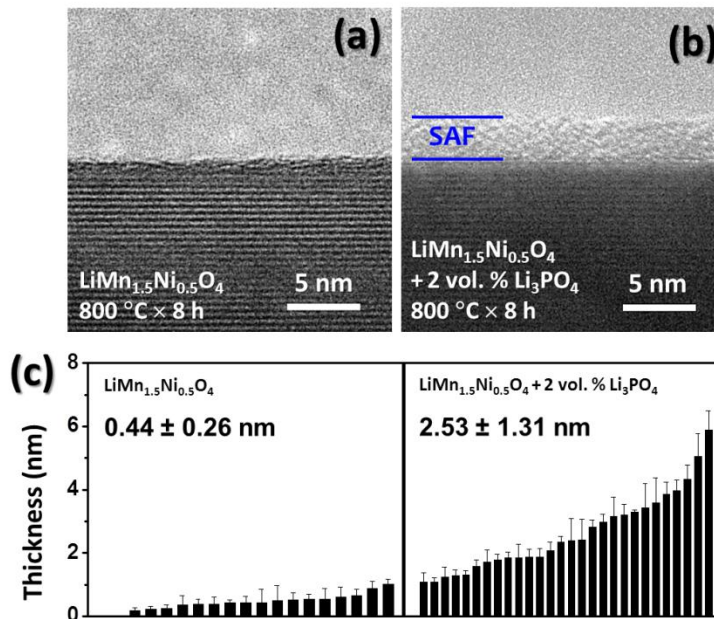


Figure 2.10 Representative HRTEM images of the particle surfaces in the (a)  $\text{LiMn}_{1.5}\text{Ni}_{0.5}\text{O}_4$  and (b)  $\text{LiMn}_{1.5}\text{Ni}_{0.5}\text{O}_4 + 2 \text{ vol. } \% \text{Li}_3\text{PO}_4$  specimens that were ball milled and subsequently annealed at 800 °C for 8h. (c) The corresponding distributions of measured thicknesses of the surface carbonate layers or  $\text{Li}_3\text{PO}_4$ -based SAFs for these two specimens, where each bar represents to an average thickness measured from multiple points of one particle surface (and each error bar represents + one standard deviation of those multiple measurements, which signifies the uniformity of the surface film).

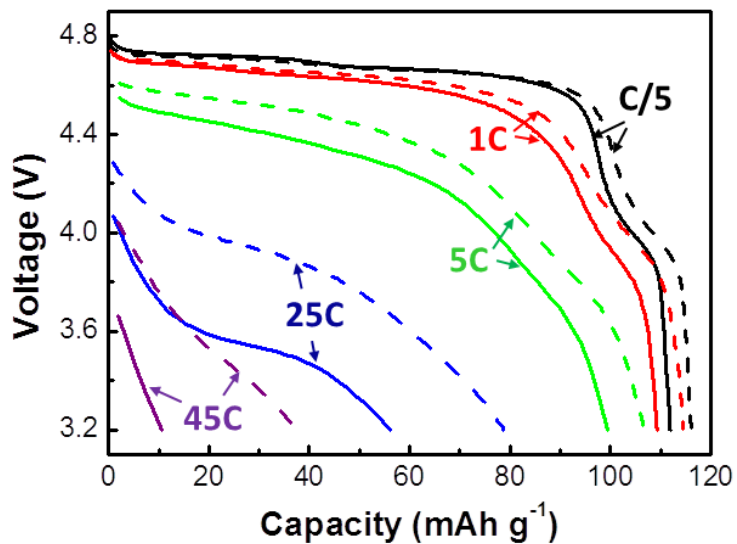


Figure 2.11 Comparisons of discharge curves of  $\text{LiMn}_{1.5}\text{Ni}_{0.5}\text{O}_4$  specimens without (solid lines) and with (dash lines)  $\text{Li}_3\text{PO}_4$ -based SAFs. All cells were first charged and discharged at C/10 for 1 cycle and C/5 for 10 cycles to reach steady states before testing at the various discharge rates labeled in the graph.

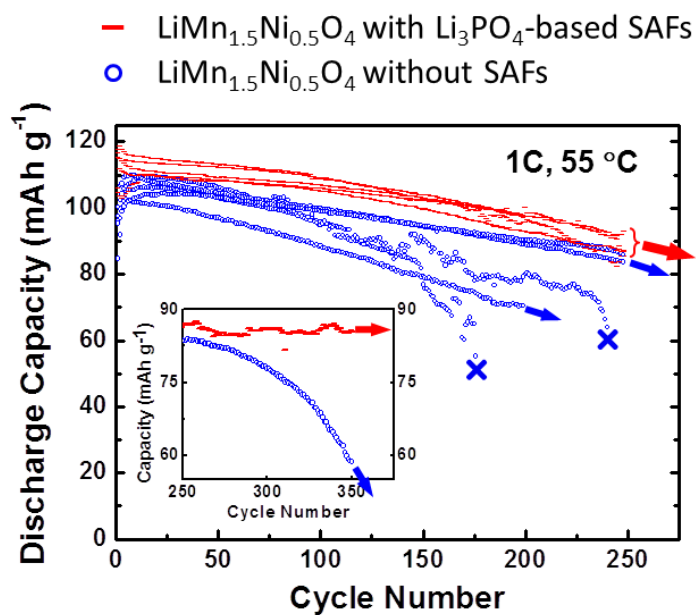


Figure 2.12 Comparison of the cycling stabilities of five  $\text{LiMn}_{1.5}\text{Ni}_{0.5}\text{O}_4$  specimens without  $\text{Li}_3\text{PO}_4$ -based SAFs and five  $\text{LiMn}_{1.5}\text{Ni}_{0.5}\text{O}_4$  specimens with  $\text{Li}_3\text{PO}_4$ -based SAFs; all ten specimens were ball milled and subsequently annealed at 800 °C for 8 h. All fresh cells were charged and discharged at 1C at 55 °C. "X" indicates that the battery died at that point.

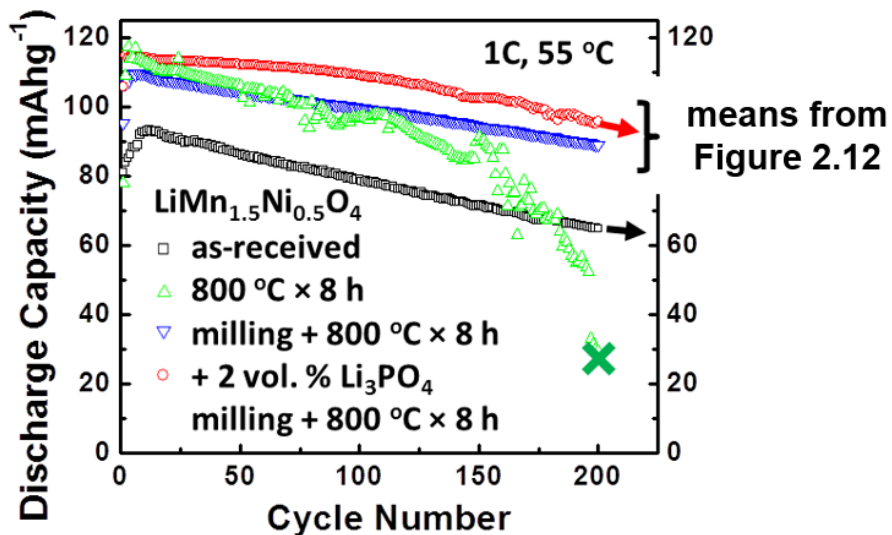


Figure 2.13 Comparison of the cycling performances of the as-received  $\text{LiMn}_{1.5}\text{Ni}_{0.5}\text{O}_4$  specimen and the reference  $\text{LiMn}_{1.5}\text{Ni}_{0.5}\text{O}_4$  specimen annealed at  $800\text{ }^\circ\text{C}$  without ball milling, along with the two means of the  $\text{LiMn}_{1.5}\text{Ni}_{0.5}\text{O}_4$  specimens with and without  $\text{Li}_3\text{PO}_4$ -based SAFs that were milled and annealed at  $800\text{ }^\circ\text{C}$ , which were averaged from the data shown in Figure 2.12 (noting that those uncoated specimens that failed before 200 cycles were excluded for obtaining the mean). All fresh cells were charged and discharged at 1C at  $55\text{ }^\circ\text{C}$ . “X” indicates that the battery died.

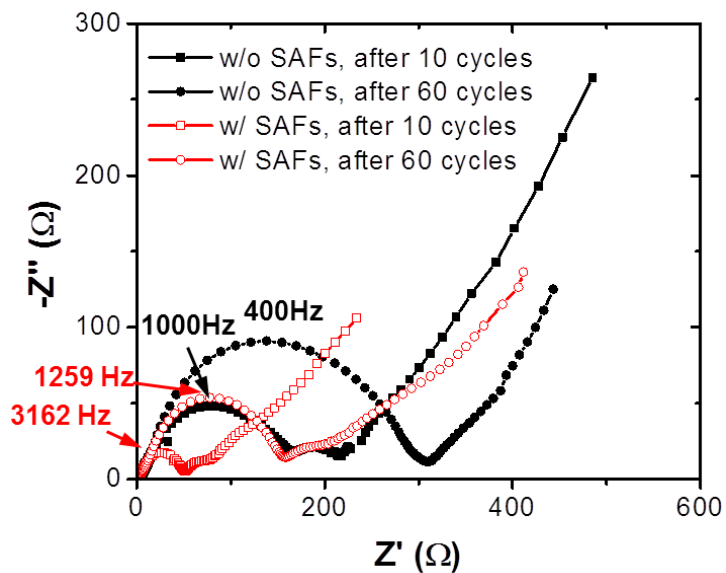


Figure 2.14 Electrochemical impedance spectra of  $\text{LiMn}_{1.5}\text{Ni}_{0.5}\text{O}_4$  specimens with and without  $\text{Li}_3\text{PO}_4$ -based SAFs. Specimens were firstly charged and discharged at 1C for 10 cycles at room temperature followed by charging and discharging at 1C for 50 cycles at 55 °C.

Table 2.1 Surface film resistance ( $R_f$ , which includes possible contributions from the SEI and SAFs) and charge transfer resistance ( $R_{ct}$ ) of  $\text{LiCoO}_2$  specimens tested at the electrolyte concentration of 1M and 0.1M. The average measured discharge capacities at 25C from Figure 2.4 are also listed for comparison. The entries are sorted according to increasing total resistance ( $R_f + R_{ct}$ ), which is correlated with decreasing discharge capacity at 25C.

Specimen	Electrolyte Concentration	$R_f$ ( $\Omega$ )	$R_{ct}$ ( $\Omega$ )	$R_f + R_{ct}$ ( $\Omega$ )	Discharge Capacity at 25C (mAh/g)
$\text{LiCoO}_2$ with SAFs	1M	$14.0 \pm 0.5$	$26.0 \pm 0.2$	39.9	57.6
$\text{LiCoO}_2$ without SAFs	1M	$11.0 \pm 1.2$	$37.0 \pm 0.5$	48.1	25.0
$\text{LiCoO}_2$ without SAFs	0.1M	$12.1 \pm 0.9$	$42.2 \pm 0.5$	54.3	4.3
$\text{LiCoO}_2$ with SAFs	0.1M	$24.4 \pm 0.7$	$38.8 \pm 0.7$	63.2	2.0

Table 2.2 Measured discharge capacities of the  $\text{LiMn}_{1.5}\text{Ni}_{0.5}\text{O}_4$  specimens with and without  $\text{Li}_3\text{PO}_4$ -based SAFs (which were subjected to the same milling and annealing treatment), along with the “annealed only” specimen without milling as an additional reference point.

Rate	Discharge Capacity (mAh/g)			Increased Percentage with SAFs
	annealed only	without SAFs	with SAFs	
C/5	$116.9 \pm 0.6$	$110.5 \pm 0.1$	$116.3 \pm 3.1$	5.2 %
1C	$115.5 \pm 1.0$	109.2	$114.5 \pm 3.3$	4.8 %
5C	$99.6 \pm 8.4$	$96.9 \pm 2.4$	$102.6 \pm 6.1$	5.9 %
25C	$58.3 \pm 6.0$	$50.1 \pm 6.1$	$70.7 \pm 7.1$	41 %
45C	$8.7 \pm 5.7$	$7.9 \pm 2.7$	$36.3 \pm 7.9$	~360 %
65C	$3.0 \pm 2.9$	$2.2 \pm 1.0$	$15.4 \pm 3.8$	~600 %
85C	$1.3 \pm 1.3$	~0.2	$7.3 \pm 2.0$	--
C/5	$118.6 \pm 1.1$	112.4	$118.1 \pm 2.3$	5.1 %

## References

- (1) Meng, X.; Yang, X.-Q.; Sun, X. Emerging Applications of Atomic Layer Deposition for Lithium-Ion Battery Studies. *Advanced Materials* **2012**, *24*, 3589-3615.
- (2) Riley, L. A.; Van Ana, S.; Cavanagh, A. S.; Yan, Y.; George, S. M.; Liu, P.; Dillon, A. C.; Lee, S.-H. Electrochemical Effects of Al<sub>2</sub>O<sub>3</sub> Surface Modification on Combustion Synthesized Li<sub>1/3</sub>Mn<sub>1/3</sub>Co<sub>1/3</sub>O<sub>2</sub> as a Layered-Cathode Material. *Journal of Power Sources* **2011**, *196*, 3317-3324.
- (3) Jung, Y. S.; Cavanagh, A. S.; Dillon, A. C.; Groner, M. D.; George, S. M.; Lee, S.-H. Enhanced Stability of LiCoO<sub>2</sub> Cathodes in Lithium-Ion Batteries Using Surface Modification by Atomic Layer Deposition. *Journal of the Electrochemical Society* **2010**, *157*, A75-A81.
- (4) Scott, I. D.; Jung, Y. S.; Cavanagh, A. S.; An, Y.; Dillon, A. C.; George, S. M.; Lee, S.-H. Ultrathin Coatings on Nano-LiCoO<sub>2</sub> for Li-Ion Vehicular Applications. *Nano Letters* **2011**, *11*, 414-418.
- (5) Guan, D.; Jeevarajan, J. A.; Wang, Y. Enhanced Cycleability of LiMn<sub>2</sub>O<sub>4</sub> Cathodes by Atomic Layer Deposition of Nanosized-Thin Al<sub>2</sub>O<sub>3</sub> Coatings. *Nanoscale* **2011**, *3*, 1465-1469.
- (6) Zhao, J.; Wang, Y. Ultrathin Surface Coatings for Improved Electrochemical Performance of Lithium Ion Battery Electrodes at Elevated Temperature. *Journal of Physical Chemistry C* **2012**, *116*, 11867-11876.
- (7) Zhao, J.; Wang, Y. Surface Modifications of Li-Ion Battery Electrodes with Various Ultrathin Amphoteric Oxide Coatings for Enhanced Cycleability. *Journal of Solid State Electrochemistry* **2013**, *17*, 1049-1058.
- (8) Zhao, J.; Wang, Y. Atomic Layer Deposition of Epitaxial ZrO<sub>2</sub> Coating on LiMn<sub>2</sub>O<sub>4</sub> Nanoparticles for High-Rate Lithium Ion Batteries at Elevated Temperature. *Nano Energy* **2013**, *2*, 882-889.
- (9) Li, C.; Zhang, H. P.; Fu, L. J.; Liu, H.; Wu, Y. P.; Ram, E.; Holze, R.; Wu, H. Q. Cathode Materials Modified by Surface Coating for Lithium Ion Batteries. *Electrochimica Acta* **2006**, *51*, 3872-3883.
- (10) Fu, L. J.; Liu, H.; Li, C.; Wu, Y. P.; Ram, E.; Holze, R.; Wu, H. Q. Surface Modifications of Electrode Materials for Lithium Ion Batteries. *Solid State Sciences* **2006**, *8*, 113-128.
- (11) Liu, J.; Manthiram, A. Kinetics Study of the 5 V Spinel Cathode LiMn<sub>1.5</sub>Ni<sub>0.5</sub>O<sub>4</sub> before and after Surface Modifications. *Journal of the Electrochemical Society* **2009**, *156*, A833-A838.

- (12) Liu, J.; Manthiram, A. Understanding the Improved Electrochemical Performances of Fe-Substituted 5 V Spinel Cathode  $\text{Li}_{1.5}\text{Ni}_{0.5}\text{O}_4$ . *Journal of Physical Chemistry C* **2009**, *113*, 15073-15079.
- (13) Wang, Q. Y.; Liu, J.; Murugan, A. V.; Manthiram, A. High Capacity Double-Layer Surface Modified  $\text{Li}[\text{Li}_{0.2}\text{Mn}_{0.54}\text{Ni}_{0.13}\text{Co}_{0.13}]\text{O}_2$  Cathode with Improved Rate Capability. *Journal of Materials Chemistry* **2009**, *19*, 4965-4972.
- (14) Liu, J.; Manthiram, A. Understanding the Improvement in the Electrochemical Properties of Surface Modified 5 V  $\text{Li}_{1.42}\text{Ni}_{0.42}\text{Co}_{0.16}\text{O}_4$  Spinel Cathodes in Lithium-Ion Cells. *Chemistry of Materials* **2009**, *21*, 1695-1707.
- (15) Wu, Y.; Manthiram, A. Effect of Surface Modifications on the Layered Solid Solution Cathodes (1-Z)  $\text{Li}[\text{Li}_{1/3}\text{Mn}_{2/3}]\text{O}_2$ -(Z)  $\text{Li}[\text{Mn}_{0.5}\text{Y}_{0.5}\text{Co}_2]\text{O}_2$ . *Solid State Ionics* **2009**, *180*, 50-56.
- (16) Liu, J.; Manthiram, A. Improved Electrochemical Performance of the 5 V Spinel Cathode  $\text{Li}_{1.5}\text{Ni}_{0.42}\text{Zn}_{0.08}\text{O}_4$  by Surface Modification. *Journal of the Electrochemical Society* **2009**, *156*, A66-A72.
- (17) Wu, Y.; Murugan, A. V.; Manthiram, A. Surface Modification of High Capacity Layered  $\text{Li}[\text{Li}_{0.2}\text{Mn}_{0.54}\text{Ni}_{0.13}\text{Co}_{0.13}]\text{O}_2$  Cathodes by  $\text{Al}_2\text{O}_3$ . *Journal of the Electrochemical Society* **2008**, *155*, A635-A641.
- (18) Wu, Y.; Manthiram, A. High Capacity, Surface-Modified Layered  $\text{Li}[\text{Li}_{1-X}/3\text{Mn}_{2-X}/3\text{Ni}_X/3\text{Co}_X/3]\text{O}_2$  Cathodes with Low Irreversible Capacity Loss. *Electrochemical and Solid State Letters* **2006**, *9*, A221-A224.
- (19) Kannan, A. M.; Rabenberg, L.; Manthiram, A. High Capacity Surface-Modified  $\text{LiCoO}_2$  Cathodes for Lithium-Ion Batteries. *Electrochemical and Solid State Letters* **2003**, *6*, A16-A18.
- (20) Kannan, A. M.; Manthiram, A. Surface/Chemically Modified  $\text{LiMn}_2\text{O}_4$  Cathodes for Lithium-Ion Batteries. *Electrochemical and Solid State Letters* **2002**, *5*, A167-A169.
- (21) Cho, J.; Kim, Y. J.; Park, B. Novel  $\text{LiCoO}_2$  Cathode Material with  $\text{Al}_2\text{O}_3$  Coating for a Li Ion Cell. *Chemistry of Materials* **2000**, *12*, 3788-3791.
- (22) Sun, K.; Dillon, S. J. A Mechanism for the Improved Rate Capability of Cathodes by Lithium Phosphate Surficial Films. *Electrochemistry Communications* **2011**, *13*, 200-202.
- (23) Chong, J.; Xun, S. D.; Song, X. Y.; Liu, G.; Battaglia, V. S. Surface Stabilized  $\text{LiNi}_{0.5}\text{Mn}_{1.5}\text{O}_4$  Cathode Materials with High-Rate Capability and Long Cycle Life for Lithium Ion Batteries. *Nano Energy* **2013**, *2*, 283-293.

- (24) Yi, T. F.; Li, X. Y.; Liu, H. P.; Shu, J.; Zhu, Y. R.; Zhu, R. S. Recent Developments in the Doping and Surface Modification of  $\text{LiFePO}_4$  as Cathode Material for Power Lithium Ion Battery. *Ionics* **2012**, *18*, 529-539.
- (25) Li, X. W.; Yang, R.; Cheng, B.; Hao, Q.; Xu, H. Y.; Yang, J.; Qian, Y. T. Enhanced Electrochemical Properties of Nano- $\text{Li}_3\text{PO}_4$  Coated on the  $\text{LiMn}_2\text{O}_4$  Cathode Material for Lithium Ion Battery at 55 Degrees C. *Materials Letters* **2012**, *66*, 168-171.
- (26) Lee, K. T.; Jeong, S.; Cho, J. Roles of Surface Chemistry on Safety and Electrochemistry in Lithium Ion Batteries. *Accounts of Chemical Research* **2013**, *46*, 1161-1170.
- (27) Yi, T. F.; Zhu, Y. R.; Zhu, X. D.; Shu, J.; Yue, C. B.; Zhou, A. N. A Review of Recent Developments in the Surface Modification of  $\text{LiMn}_2\text{O}_4$  as Cathode Material of Power Lithium-Ion Battery. *Ionics* **2009**, *15*, 779-784.
- (28) Luo, J.; Chiang, Y.-M. Wetting and Prewetting on Ceramic Surfaces. *Annual Review of Materials Research* **2008**, *38*, 227-249.
- (29) Kayyar, A.; Qian, H. J.; Luo, J. Surface Adsorption and Disordering in  $\text{LiFePO}_4$  Based Battery Cathodes. *Applied Physics Letters* **2009**, *95*, 221905.
- (30) Qian, H. J.; Luo, J.; Chiang, Y. M. Anisotropic Wetting of  $\text{ZnO}$  by  $\text{Bi}_2\text{O}_3$  with and without Nanometer-Thick Surficial Amorphous Films. *Acta Materialia* **2008**, *56*, 862-873.
- (31) Qian, H.; Luo, J. Nanoscale Surficial Films and a Surface Transition in  $\text{V}_2\text{O}_5$ - $\text{TiO}_2$ -Based Ternary Oxide Systems. *Acta Materialia* **2008**, *56*, 4702-4714.
- (32) Qian, H. J.; Luo, J. Vanadia-Based Equilibrium-Thickness Amorphous Films on Anatase (101) Surfaces. *Applied Physics Letters* **2007**, *91*, 061909.
- (33) Luo, J.; Wang, H.; Chiang, Y.-M. Origin of Solid State Activated Sintering in  $\text{Bi}_2\text{O}_3$ -Doped  $\text{ZnO}$ . *Journal of the American Ceramic Society* **1999**, *82*, 916.
- (34) Luo, J.; Chiang, Y.-M. Equilibrium-Thickness Amorphous Films on {11-20} Surfaces of  $\text{Bi}_2\text{O}_3$ -Doped  $\text{ZnO}$ . *Journal of the European Ceramic Society* **1999**, *19*, 697-701.
- (35) Baram, M.; Chatain, D.; Kaplan, W. D. Nanometer-Thick Equilibrium Films: The Interface between Thermodynamics and Atomistics. *Science* **2011**, *332*, 206-209.
- (36) Baram, M.; Kaplan, W. D. Intergranular Films at Au-Sapphire Interfaces. *Journal of Materials Science* **2006**, *41*, 7775-7784.
- (37) Clarke, D. R. On the Equilibrium Thickness of Intergranular Glass Phases in Ceramic Materials. *Journal of the American Ceramic Society* **1987**, *70*, 15-22.

- (38) Cannon, R. M.; Esposito, L. High Temperature Colloidal Behavior: Particles in Liquid Silicates. *Zeitschrift Fur Metallkunde* **1999**, *90*, 1002-1015.
- (39) Luo, J. Stabilization of Nanoscale Quasi-Liquid Interfacial Films in Inorganic Materials: A Review and Critical Assessment. *Critical Reviews in Solid State and Material Sciences* **2007**, *32*, 67-109.
- (40) Clarke, D. R.; Shaw, T. M.; Philipse, A. P.; Horn, R. G. Possible Electrical Double-Layer Contribution to the Equilibrium Thickness of Intergranular Glass Films in Polycrystalline Ceramics. *Journal of the American Ceramic Society* **1993**, *76*, 1201-1204.
- (41) Harmer, M. P. The Phase Behavior of Interfaces. *Science* **2011**, *332*, 182-183.
- (42) Tang, M.; Carter, W. C.; Cannon, R. M. Diffuse Interface Model for Structural Transitions of Grain Boundaries. *Physical Review B* **2006**, *73*, 024102.
- (43) Kaplan, W. D.; Chatain, D.; Wynblatt, P.; Carter, W. C. A Review of Wetting Versus Adsorption, Complexions, and Related Phenomena: The Rosetta Stone of Wetting *Journal of Materials Science* **2013**, *48*, 5681-5717.
- (44) Cantwell, P. R.; Tang, M.; Dillon, S. J.; Luo, J.; Rohrer, G. S.; Harmer, M. P. Overview No. 152: Grain Boundary Complexions. *Acta Materialia* **2014**, *62*, 1-48.
- (45) Luo, J.; Cheng, H.; Asl, K. M.; Kiely, C. J.; Harmer, M. P. The Role of a Bilayer Interfacial Phase on Liquid Metal Embrittlement. *Science* **2011**, *333*, 1730-1733.
- (46) Dillon, S. J.; Tang, M.; Carter, W. C.; Harmer, M. P. Complexion: A New Concept for Kinetic Engineering in Materials Science. *Acta Materialia* **2007**, *55*, 6208-6218
- (47) Li, W. Q.; Garofalini, S. H. Molecular Dynamics Simulations of Li Insertion in a Nanocrystalline V<sub>2</sub>O<sub>5</sub> Thin Film Cathode. *Journal of the Electrochemical Society* **2005**, *152*, A364-A369.
- (48) Zhang, G. J.; Yu, R.; Vyas, S.; Stettler, J.; Reimer, J. A.; Harley, G.; De Jonghe, L. C. Proton Conduction and Characterization of an La(PO<sub>3</sub>)<sub>3</sub>-Ca(PO<sub>3</sub>)<sub>2</sub> Glass-Ceramic. *Solid State Ionics* **2008**, *178*, 1811-1816.
- (49) Chong, J.; Xun, S. D.; Song, X. Y.; Ridgway, P.; Liu, G.; Battaglia, V. S. Towards the Understanding of Coatings on Rate Performance of LiFePO<sub>4</sub>. *Journal of Power Sources* **2012**, *200*, 67-76.
- (50) Chong, J.; Xun, S.; Song, X.; Liu, G.; Battaglia, V. S. Surface Stabilized LiNi<sub>0.5</sub>Mn<sub>1.5</sub>O<sub>4</sub> Cathode Materials with High-Rate Capability and Long Cycle Life for Lithium Ion Batteries. *Nano Energy* **2013**, *2*, 283-293.
- (51) Tang, M.; Huang, H. Y.; Meethong, N.; Kao, Y. H.; Carter, W. C.; Chiang, Y. M. Model for the Particle Size, Overpotential, and Strain Dependence of Phase Transition

Pathways in Storage Electrodes: Application to Nanoscale Olivines. *Chemistry of Materials* **2009**, *21*, 1557-1571.

(52) Kang, B.; Ceder, G. Battery Materials for Ultrafast Charging and Discharging. *Nature* **2009**, *458*, 190-193.

(53) Zaghbi, K.; Goodenough, J. B.; Mauger, A.; Julien, C. Unsupported Claims of Ultrafast Charging of Lifepo<sub>4</sub> Li-Ion Batteries. *Journal of Power Sources* **2009**, *194*, 1021-1023.

(54) Ceder, G.; Kang, B. Response to "Unsupported Claims of Ultrafast Charging of Li-Ion Batteries". *Journal of Power Sources* **2009**, *194*, 1024-1028.

(55) Oh, J. M.; Geiculescu, O.; DesMarteau, D.; Creager, S. Ionomer Binders Can Improve Discharge Rate Capability in Lithium-Ion Battery Cathodes. *Journal of the Electrochemical Society* **2011**, *158*, A207-A213.

(56) Kramer, D.; Ceder, G. Tailoring the Morphology of Licoo<sub>2</sub>: A First Principles Study. *Chemistry of Materials* **2009**, *21*, 3799-3809.

(57) Lee, E.; Persson, K. A. First-Principles Study of the Nano-Scaling Effect on the Electrochemical Behavior in Lini<sub>0.5</sub>mn<sub>1.5</sub>o<sub>4</sub>. *Nanotechnology* **2013**, *24*, 424007.

(58) Leply, N. D.; Holzwarth, N. A. W.; Du, Y. J. A. Structures, Li<sup>+</sup> Mobilities, and Interfacial Properties of Solid Electrolytes Li<sub>3</sub>ps<sub>4</sub> and Li<sub>3</sub>po<sub>4</sub> from First Principles. *Physical Review B* **2013**, *88*, 104103.

(59) Samsonov, G. V.: *The Oxide Handbook*; 2 ed.; Plenum Data Company: New York, 1982.

(60) French, R. H.; Parsegian, V. A.; Podgornik, R.; Rajter, R. F.; Jagota, A.; Luo, J.; Asthagiri, D.; Chaudhury, M. K.; Chiang, Y. M.; Granick, S.; Kalinin, S.; Kardar, M.; Kjellander, R.; Langreth, D. C.; Lewis, J.; Lustig, S.; Wesolowski, D.; Wettlaufer, J. S.; Ching, W. Y.; Finnis, M.; Houlihan, F.; von Lilienfeld, O. A.; van Oss, C. J.; Zemb, T. Long Range Interactions in Nanoscale Science. *Reviews of Modern Physics* **2010**, *82*, 1887-1944.

(61) French, R. H. Origin and Applications of London Dispersion Forces and Hamaker Constants in Ceramics. *Journal of the American Ceramic Society* **2000**, *83*, 2117-2146

(62) Luo, J.; Chiang, Y.-M. Existence and Stability of Nanometer-Thick Disordered Films on Oxide Surfaces. *Acta Materialia* **2000**, *48*, 4501-4515.

(63) Luo, J. Developing Interfacial Phase Diagrams for Applications in Activated Sintering and Beyond: Current Status and Future Directions. *Journal of the American Ceramic Society* **2012**, *95*, 2358-2371.

- (64) Shi, X.; Luo, J. Developing Grain Boundary Diagrams as a Materials Science Tool: A Case Study of Nickel-Doped Molybdenum. *Physical Review B* **2011**, *84*, 014105.
- (65) Luo, J.; Shi, X. M. Grain Boundary Disorder in Binary Alloys. *Applied Physics Letters* **2008**, *92*, 101901
- (66) Shi, X.; Luo, J. Decreasing the Grain Boundary Diffusivity in Binary Alloys with Increasing Temperature. *Physical Review Letters* **2010**, *105*, 236102.
- (67) Luo, J. Liquid-Like Interface Complexion: From Activated Sintering to Grain Boundary Diagrams. *Current Opinion in Solid State and Materials Science* **2008**, *12*, 81-88.
- (68) Poling, B. E.; Thomson, G. H.; Friend, D. G.; Rowley, R. L.; Wilding, W. V.: *Perry's Chemical Engineers' Handbook*; The McGraw-Hill Companies, 2008.
- (69) Ji, L. N.; Li, J. B.; Chen, Y. Q.; Luo, J.; Liang, J. K.; Rao, G. H. Subsolidus Phase Relations of the Zn-Li<sub>2</sub>O-P<sub>2</sub>O<sub>5</sub> System. *Journal of Alloys and Compounds* **2009**, *486*, 352-356.
- (70) Nakano, J.; Yamada, T.; Miyazawa, S. Phase-Diagram for a Portion of the System Li<sub>2</sub>O-Nd<sub>2</sub>O<sub>3</sub>-P<sub>2</sub>O<sub>5</sub>. *Journal of the American Ceramic Society* **1979**, *62*, 465-467.
- (71) Kayyar, A.; Huang, J.; Samiee, M.; Luo, J. Construction and Testing of Coin Cells of Lithium Ion Batteries. *Journal of visualized experiments : JoVE* **2012**, e4104-e4104.
- (72) Aurbach, D.; Markovsky, B.; Levi, M. D.; Levi, E.; Schechter, A.; Moshkovich, M.; Cohen, Y. New Insights into the Interactions between Electrode Materials and Electrolyte Solutions for Advanced Nonaqueous Batteries. *Journal of Power Sources* **1999**, *81*, 95-111.
- (73) Reimers, J. N.; Dahn, J. R. Electrochemical and Insitu X-Ray-Diffraction Studies of Lithium Intercalation in LiCoO<sub>2</sub>. *Journal of the Electrochemical Society* **1992**, *139*, 2091-2097.
- (74) Wang, H. F.; Jang, Y. I.; Huang, B. Y.; Sadoway, D. R.; Chiang, Y. M. Tem Study of Electrochemical Cycling-Induced Damage and Disorder in LiCoO<sub>2</sub> Cathodes for Rechargeable Lithium Batteries. *Journal of the Electrochemical Society* **1999**, *146*, 473-480.
- (75) Ooms, F. G. B.; Kelder, E. M.; Schoonman, J.; Wagemaker, M.; Mulder, F. M. High-Voltage Limg Delta Ni<sub>0.5</sub>-Delta Mn<sub>1.5</sub>O<sub>4</sub> Spinels for Li-Ion Batteries. *Solid State Ionics* **2002**, *152*, 143-153.
- (76) Choi, W.; Manthiram, A. Comparison of Metal Ion Dissolutions from Lithium Ion Battery Cathodes. *Journal of the Electrochemical Society* **2006**, *153*, A1760-A1764.

- (77) Yi, T. F.; Xie, Y.; Ye, M. F.; Jiang, L. J.; Zhu, R. S.; Zhu, Y. R. Recent Developments in the Doping of  $\text{Li}_{0.5}\text{Mn}_{1.5}\text{O}_4$  Cathode Material for 5 V Lithium-Ion Batteries. *Ionics* **2011**, *17*, 383-389.
- (78) Liu, D.; Zhu, W.; Trottier, J.; Gagnon, C.; Barray, F.; Guerfi, A.; Mauger, A.; Groult, H.; Julien, C. M.; Goodenough, J. B.; Zaghi, K. Spinel Materials for High-Voltage Cathodes in Li-Ion Batteries. *Rsc Advances* **2014**, *4*, 154-167.
- (79) Liu, D. W.; Liu, Y. Y.; Pan, A. Q.; Nagle, K. P.; Seidler, G. T.; Jeong, Y. H.; Cao, G. Z. Enhanced Lithium-Ion Intercalation Properties of  $\text{V}_2\text{O}_5$  Xerogel Electrodes with Surface Defects. *Journal of Physical Chemistry C* **2011**, *115*, 4959-4965.
- (80) Shin, D. W.; Bridges, C. A.; Huq, A.; Paranthaman, M. P.; Manthiram, A. Role of Cation Ordering and Surface Segregation in High-Voltage Spinel  $\text{Li}_{1-x}\text{M}_x\text{Ni}_{0.5}\text{O}_4$  (M = Cr, Fe, and Ga) Cathodes for Lithium-Ion Batteries. *Chemistry of Materials* **2012**, *24*, 3720-3731.
- (81) Shin, D. W.; Manthiram, A. Surface-Segregated, High-Voltage Spinel  $\text{Li}_{1-x}\text{M}_x\text{Ni}_{0.42}\text{Ga}_{0.08}\text{O}_4$  Cathodes with Superior High-Temperature Cyclability for Lithium-Ion Batteries. *Electrochemistry Communications* **2011**, *13*, 1213-1216.
- (82) Park, K.-S.; Benayad, A.; Kang, D.-J.; Doo, S.-G. Nitridation-Driven Conductive  $\text{Li}_4\text{Ti}_5\text{O}_{12}$  for Lithium Ion Batteries. *Journal of the American Chemical Society* **2008**, *130*, 14930-14931.
- (83) Han, K. S.; Lee, J. W.; Kang, Y. M.; Lee, J. Y.; Kang, J. K. Nature of Atomic and Molecular Nitrogen Configurations in  $\text{TiO}_2$ -X<sub>n</sub> Nanotubes and Tailored Energy-Storage Performance on Selective Doping of Atomic N States. *Small* **2008**, *4*, 1682-1686.
- (84) Han, H.; Song, T.; Bae, J.-Y.; Nazar, L. F.; Kim, H.; Paik, U. Nitridated  $\text{TiO}_2$  Hollow Nanofibers as an Anode Material for High Power Lithium Ion Batteries. *Energy & Environmental Science* **2011**, *4*, 4532-4536.
- (85) Samiee, M.; Luo, J. A Facile Nitridation Method to Improve the Rate Capability of  $\text{TiO}_2$  for Lithium-Ion Batteries. *Journal of Power Sources* **2014**, *245*, 594-598.
- (86) Chen, X. B.; Liu, L.; Yu, P. Y.; Mao, S. S. Increasing Solar Absorption for Photocatalysis with Black Hydrogenated Titanium Dioxide Nanocrystals. *Science* **2011**, *331*, 746-750.
- (87) Samiee, M.; Luo, J. Enhancing the Visible-Light Photocatalytic Activity of  $\text{TiO}_2$  by Heat Treatments in Reducing Environments. *Materials Letters* **2013**, *98*, 205-208.

## Chapter 3. Enhancing the Electrochemical Performance of $\text{LiMn}_{1.5}\text{Ni}_{0.5}\text{O}_4$ through $\text{WO}_3$ Doping and Altering the Particle Wulff Shape via Anisotropic Surface Segregation

### 3.1. Introduction

High-voltage  $\text{LiMn}_{1.5}\text{Ni}_{0.5}\text{O}_4$  spinel is one of the most promising candidates for next-generation cathode materials of lithium-ion batteries for electric vehicles and other high-energy density applications due to its high operating voltage  $\sim 4.7$  V, low cost, and environmental friendliness. Prior studies investigated the effects of Mn and Ni cation disordering,<sup>1-6</sup>  $\text{Mn}^{3+}$  concentration,<sup>3, 7, 8</sup> oxygen vacancies,<sup>1, 9, 10</sup> cation doping<sup>6, 11-22</sup>, impurities<sup>5, 23</sup> and surface coating<sup>24, 25</sup> on improving the electrochemical performance of  $\text{LiMn}_{1.5}\text{Ni}_{0.5}\text{O}_4$ . Specifically, several recent studies suggested that the crystalline orientations on the particle surfaces can have significant influences on the electrochemical properties.<sup>26-34</sup> In most experiments, different crystalline facets were found to coexist at the surfaces of  $\text{LiMn}_{1.5}\text{Ni}_{0.5}\text{O}_4$  particles.<sup>28-34</sup>  $\{111\}$  and  $\{100\}$  surface facets were most frequently observed, followed by a smaller fraction of  $\{110\}$  facets that exhibit the most open channels for fast lithium diffusion but appear to have a higher surface energy.<sup>35</sup> Thermodynamically,  $\{111\}$  and  $\{100\}$  facets tend to coexist due to their similar (low) surface energies, while eliminating  $\{100\}$  facets appears to benefit rate capability and cycling stability.<sup>29</sup> Notably, Chemelewski *et al.* synthesized  $\text{LiMn}_{1.5}\text{Ni}_{0.5}\text{O}_4$  particles with dominating  $\{111\}$  surface facets (by an improved co-precipitation method to kinetically control the particle morphology to eliminate

{100} facets), which achieved an improved rate performance comparing to that of particles with coexisting {100} surface facets synthesized by a traditional co-precipitation method.<sup>29</sup> Interestingly, a prior study also showed that Fe doping could promote the formation of {111} surface facets of  $\text{LiMn}_{1.5}\text{Ni}_{0.5}\text{O}_4$  particles (synthesized by a traditional co-precipitation method),<sup>29</sup> though its underlying mechanism remained unclear.

Here, we have proposed and successfully realized a novel strategy to increase the fraction of the most favorite {110} facets thermodynamically to improve the rate capabilities via anisotropic surface segregation of  $\text{WO}_3$ , along with enhancing the cycling stability via improving the surface stability. Moreover, we have conducted a combination of neutron diffraction, X-ray photoelectron spectroscopy, Auger electron spectroscopy and various other systematic characterizations to verify our hypothesis and reveal the underlying mechanisms at multiple length scales.

Furthermore, prior reports already suggested that the surface segregation of dopants can influence the electrochemical performance of  $\text{LiMn}_{1.5}\text{Ni}_{0.5}\text{O}_4$ .<sup>6,36,37</sup> Though surface segregation appears to be related to the particle morphology change,<sup>37</sup> the relation between the two phenomena has not been investigated (and, in fact, it was often believed that particle morphology was mostly determined by the synthesis method and different dopants; and the influence surface segregation is unimportant<sup>38</sup>). Here, we demonstrated, for the first time to our knowledge, that the anisotropic segregation of W preferably on the {110} surface facets of  $\text{LiMn}_{1.5}\text{Ni}_{0.5}\text{O}_4$  can stabilize the most favorite {110} facets with

the most open channels for fast lithium diffusion, in accord with the well-established Gibbs and Wulff theories. Consequently, the surface segregation and associated particle morphological changes contribute to significant improvements of both rate capabilities and cycling stabilities of the high-voltage  $\text{LiMn}_{1.5}\text{Ni}_{0.5}\text{O}_4$  cathode.

It should be noted that aliovalent doping can also change the  $\text{Mn}^{3+}$  concentration, which can influence the formation of oxygen vacancies and cation disordering (both inside the bulk phase and at/near the surface). On one hand, the existence of  $\text{Mn}^{3+}$  cations benefits the rate capability by increasing both of the lithium ion bulk diffusion rate and the electronic conductivity and it contributes an extra amount of discharge capacity from  $\text{Mn}^{3+}/\text{Mn}^{4+}$  redox at the voltage plateau of  $\sim 4$  V.<sup>3,7</sup> On the other hand, the presence of  $\text{Mn}^{3+}$  cations decreases cycling stability by promoting the formation of  $\text{Mn}^{2+}$  on surface and subsequently dissolution of  $\text{Mn}^{2+}$  in the electrolyte.<sup>15,39</sup> Notably, a prior study also demonstrated that surface segregation of Fe, Cr and Ga in  $\text{LiMn}_{1.5}\text{Ni}_{0.5}\text{O}_4$  particles could inhibit the  $\text{Mn}^{2+}$  dissolution in electrolyte to subsequently improve the cycling stability.<sup>6</sup>

Specifically, in this study, we added 1 vol. % of  $\text{WO}_3$ , which is a well-known “supported oxide catalyst” that would spontaneously spread (adsorb) on the surfaces of inert oxides (typically  $\text{Al}_2\text{O}_3$  and  $\text{TiO}_2$  nanoparticles) upon annealing due to its low surface energy,<sup>40-42</sup> to  $\text{LiMn}_{1.5}\text{Ni}_{0.5}\text{O}_4$ , which spontaneously adsorbed (segregated) on the particle surfaces upon a facile and cost-effective “mixing and annealing” process. We further demonstrated that  $\text{WO}_3$  dissolved into the  $\text{LiMn}_{1.5}\text{Ni}_{0.5}\text{O}_4$  bulk phase and anisotropically adsorbed (a.k.a.

segregated) on the surfaces of  $\text{LiMn}_{1.5}\text{Ni}_{0.5}\text{O}_4$  particles to increase the fraction of the most favorite  $\{110\}$  facets.<sup>31</sup> The combination effects of bulk doping, surface segregation, and anisotropic-segregation induced morphological changes improved not only rate capabilities substantially (e.g., an ~500% increase in the discharge capacity at 25C) but also the cycling stability (e.g., >25% increase in the discharge capacity at 55 °C after 200 cycles at 1C).

## **3.2. Experimental**

### **3.2.1. Materials synthesis**

To prepare 1 vol. %  $\text{WO}_3$  doped  $\text{LiMn}_{1.5}\text{Ni}_{0.5}\text{O}_4$  (a nominal volumetric percentage calculated using the molar volumes of individual compounds, corresponding to an overall W/Mn atomic ratio of ~0.06),  $(\text{NH}_4)_2\text{WO}_4$  (precursor for  $\text{WO}_3$ ) was added to as-received  $\text{LiMn}_{1.5}\text{Ni}_{0.5}\text{O}_4$  (Sigma-Aldrich, >99%) and dispersed in 4 ml of acetone. The mixture was placed in a silicon nitride grinding vial with two silicon nitride balls. Before sealing the jar, the corprene gasket was taped by Teflon to prevent it from acetone corrosion and precursor contamination. High-energy ball milling was carried out using a SPEX 8000D mill for a duration of 10 min, followed by a 15-min resting interval; this milling process was repeated for 3 times. The mixture was dried isothermally in an oven around 70 °C. The dried powder was placed in a covered alumina crucible, isothermally annealed at 800 °C for 4 h in a box furnace with a heating rate of 5 °C/min and subsequently cooled in the furnace (with power being shut down) after the isothermal annealing. As a reference, controlled specimens of undoped

LiMn<sub>1.5</sub>Ni<sub>0.5</sub>O<sub>4</sub> were prepared with exactly the same ball milling and annealing procedure described above, but without the addition of the WO<sub>3</sub> precursor ((NH<sub>4</sub>)<sub>2</sub>WO<sub>4</sub>).

### 3.2.2. Material characterization

Particle sizes and morphologies were characterized using a FEI XL30 scanning electron microscope (SEM). Specific surface area was measured on a Micromeritics ASAP-2000 Gas Adsorption Analyzer.

The surface composition and depth profile of WO<sub>3</sub> doped LiMn<sub>1.5</sub>Ni<sub>0.5</sub>O<sub>4</sub> particles were characterized by both X-ray photoelectron spectroscopy (XPS) and Auger electron spectroscopy (AES). XPS was carried out by using a Kratos AXIS ULTRA DLD XPS system equipped with an Al K $\alpha$  monochromated X-ray source and a 165 mm mean radius electron energy hemispherical analyzer with a step size of 0.1 eV. A 4 keV Ar ion beam was used for sputtering. Binding energies were corrected using C 1s peak 284.6 eV. The sample current was set to be ~4  $\mu$ A. Depth profile data were collected after sputtering time of 10 s, 30 s, 60 s, 120 s and 240 s. The measured XPS depth profiles represent averages of many different particles and crystalline facets. The XPS data were fitted with the XPSPEAK41 software.

AES surface analysis, in conjunction with depth profiling using ion sputtering, was carried out by a PHI 700 scanning Auger nanoprobe with a nanoscale spatial resolution to obtain surface compositions of individual crystalline facets. Au foils were used as substrates to eliminate charging effects.

A multiplex mode survey was used to acquire accurate quantitative results of various elements on surface. The signals from O, Mn, Ni, and W, respectively, were scanned in ranges of 496.4 – 532.0 eV, 557.8 – 611 eV, 811 – 871 eV and 1692.5 – 1758.8 eV respectively, and subsequently analyzed in ranges of 502.7 – 526.5 eV, 563.9 – 604.5 eV, 824.1 – 863.0 eV and 1713.0 – 1748.9 eV, respectively. Each test was carried out with 40 sweeps and 1 eV per step. 10 cycles of measurements were conducted for obtain high-quality signals, in which process the acquisition area was corrected after each point test to avoid beam drift and ensure that data was acquired in the same location. The Mn<sub>2</sub> signal at 536 eV was selected since there is an overlap of the Mn<sub>1</sub> (519 eV) and O (510 eV) signals. Elemental compositions on the facets of (100), (110), and (111) of W doped and undoped LiMn<sub>1.5</sub>Ni<sub>0.5</sub>O<sub>4</sub> specimens were investigated. At least two points were taken on each facet. A beam energy of 20 kV was used to get a smaller beam size with a spatial resolution of about 8 – 10 nm. The sputtering source was neutralized Ar of 1 kV beam energy and with a 30° incident angle with the sample. The target emission current was 15 mA. The sputtering area was 1 mm by 1 mm. The sputter time was 30 s (between collecting two data points) with a delay of 3 s. The specimen position was recalibrated after each spot was measured. The AES data were fitted with the MultiPak software.

Neutron diffraction characterization data were collected on the VULCAN beamline at the Spallation Neutron Sources (SNS) in the Oak Ridge National Laboratory (ORNL). An incident beam (5 mm × 12 mm) of 0.7 to 3.5 Å bandwidth, allowing 0.5 - 2.5 Å *d*-space in diffracted patterns in the  $\theta \pm 90^\circ$  detector banks,

was selected using the double-disk choppers at a 30 Hz speed. The high-resolution mode was employed with  $\Delta d / d \approx 0.25\%$ . The SNS power was at 1100 KW nominally. Neutron diffraction data were collected for a duration of 3 h<sup>43,44</sup> at room temperature and were reduced by the VDRIVE software.<sup>45,46</sup> A full-pattern Rietveld refinement was performed using the GSAS programs with the EXPGUI interface.<sup>47,48</sup>

### 3.2.3. Electrochemical measurement

To prepare cathodes, 80 wt. % active materials, 15 wt. % carbon black (MTI), 5 wt. % PVDF (MTI), and an appropriate amount of NMP (Alfa Aesar, anhydrous, 99.5 %) were mixed in a glass vial by a vibrating mixer, followed by ultrasonic dispersion. The mixture was coated on an aluminum foil, which was subsequently dried in a vacuum oven at 90 °C for 6 h. Cathode electrodes with a diameter of 10 mm were punched out, pressed at ~187 MPa, and dried in a vacuum oven at 120 °C for 8 h before transferring into an Ar-filled glovebox for battery construction. The density of dried electrode coating was ~3.2 mg cm<sup>-2</sup>. Half cells were made with a cathode electrode, a metal Li chip (MTI, 99.9 %) as the anode, 1M LiPF<sub>6</sub> in 1:1 vol. EC/DMC electrolyte (LP 30, BASF), C480 separators (Celgard), and 2032 coin cell cases (SS304, MTI).

Electrochemical cycling tests were carried out on an Arbin 2143 tester. The rate performance of LiMn<sub>1.5</sub>Ni<sub>0.5</sub>O<sub>4</sub> specimens was tested at the discharge rates of C/10, C/5, 1C, 5C, 25C, 45C, 65C, and 85C sequentially (with 4 cycles at C/5 to stabilize the battery and 1 cycle for other discharge rates subsequently;

1C equates to  $150 \text{ mA g}^{-1}$ ) with a constant charge rate of C/5 at room temperature. The cycling stability of  $\text{LiMn}_{1.5}\text{Ni}_{0.5}\text{O}_4$  specimens were measured at charge and discharge rate of 1C between 3.2 V and 5.0 V at an elevated temperature of  $55 \pm 3 \text{ }^\circ\text{C}$  in a dry oven after first idling at  $55 \pm 3 \text{ }^\circ\text{C}$  for 2 h.

The cyclic voltammetry (CV) and electrochemical impedance spectroscopy (EIS) were performed using a Solartron 1287A/1255B analyzer. CV was performed between 3.2 V and 5.0 V at a scan rate of  $0.1 \text{ mV s}^{-1}$ . Electrochemical impedance spectra were measured from 1 MHz to 0.05 Hz at 10 mV. The EIS data were fitted with the ZView software. The cells after rate capability test were charged to a cut-off voltage of 5.0 V at C/10 and kept for 10 h for the subsequent impedance measurements.

### **3.3. Results**

#### **3.3.1. Surface areas and particle morphologies**

The measured BET specific surface areas of the undoped and  $\text{WO}_3$  doped  $\text{LiMn}_{1.5}\text{Ni}_{0.5}\text{O}_4$  specimens prepared using identical ball milling and annealing conditions were  $\sim 1.8 \text{ m}^2/\text{g}$  and  $\sim 1.7 \text{ m}^2/\text{g}$ , respectively; the difference was only  $\sim 6 \%$  and the undoped  $\text{LiMn}_{1.5}\text{Ni}_{0.5}\text{O}_4$  specimen had a slightly larger specific surface area. The comparable BET specific surface areas ensured fair comparisons so that the enhanced rate capability and cycling stability of the  $\text{WO}_3$  doped  $\text{LiMn}_{1.5}\text{Ni}_{0.5}\text{O}_4$  specimen as compared to those of the undoped specimen (that will be discussed subsequently) were not due to different specific surface areas.

The morphologies of the undoped and  $\text{WO}_3$  doped  $\text{LiMn}_{1.5}\text{Ni}_{0.5}\text{O}_4$  particles are shown in Figure 3.1, where some differences are evident. For the undoped  $\text{LiMn}_{1.5}\text{Ni}_{0.5}\text{O}_4$  particles, surface facets of  $\{111\}$ ,  $\{110\}$ ,  $\{100\}$ , and  $\{311\}$  coexisted, with estimated surface area fractions of  $\sim 44\%$ ,  $\sim 18\%$ ,  $\sim 20\%$ , and  $\sim 18\%$ , respectively, which were calculated from Wulff construction simulation of a particle (Figure 3.2(a)) that matched the observation by SEM (Figure 3.1(a)). These observed results are generally consistent with prior density functional theory (DFT) computations.<sup>35</sup> For the  $\text{WO}_3$  doped  $\text{LiMn}_{1.5}\text{Ni}_{0.5}\text{O}_4$  particles, the surface area fraction of the  $\{111\}$  facets increased slightly from  $\sim 44\%$  to  $\sim 56\%$  and the fraction of the  $\{110\}$  facets increased substantially from  $\sim 18\%$  to  $\sim 43\%$ , whereas the fraction of the  $\{100\}$  facets decreased drastically from  $\sim 20\%$  to  $<2\%$  and the  $\{311\}$  facets disappeared completely. The surface area fraction of the  $\{110\}$  facets had the largest increase, being more than doubled with  $\text{WO}_3$  doping.

The simulation of Wulff shapes was done with the software Wulffmaker running in Wolfram CDF Player.<sup>49</sup> The simulated Wulff crystals of the undoped and  $\text{WO}_3$  doped  $\text{LiMn}_{1.5}\text{Ni}_{0.5}\text{O}_4$  that matched the crystal morphologies observed by SEM (Figure 3.1) are shown in Figures 3.2(a) and 3.2(b), respectively, and corresponding relative surface energies are listed in Table 3.1. In comparison with that of the  $\{100\}$  facets, the surface energies of both  $\{111\}$  and  $\{110\}$  facets decreased more rapidly with  $\text{WO}_3$  adsorption.

### 3.3.2. Anisotropic surface segregation

Strong surface segregation of W was clearly evident in the XPS depth profile. As shown in Figure 3.3, the surface atomic ratio of W/Mn was measured by XPS to be  $0.23 \pm 0.01$  based on the fitting results, which decreased rapidly with ion sputtering to  $\sim 0.07$  after 60 s and leveled off at  $\sim 0.03$  after sputtering 240 s (while the overall nominal W/Mn ratio is 0.06). The surface Ni/Mn ratio was measured to be  $0.23 \pm 0.07$ , which was substantially lower than the nominal bulk Ni/Mn ratio of 1/3. After sputtering 60 s, the measured atomic ratio of W/Mn is  $0.33 \pm 0.04$ , approaching to the nominal bulk stoichiometric ratio of 1/3 and stayed roughly a constant. The sputtering rate was calibrated to be about  $30 \text{ nm min}^{-1}$  when a reference  $\text{SiO}_2$  material was sputtered at the same experimental condition.<sup>50</sup>

Furthermore, Auger electron spectroscopy (AES) with a nanoprobe of  $\sim 10 \text{ nm}$  in the beam size was employed to quantitatively analyze the W atomic ratios on various facets to identify anisotropy in surface segregation. The measured depth profiles of W (obtained by ion sputtering) on the facets  $\{110\}$ ,  $\{100\}$  and  $\{111\}$  are shown in Figure 3.4. The atomic ratios of W/Mn on  $\{110\}$ ,  $\{100\}$ , and  $\{111\}$  facets, respectively, before sputtering was 0.28, 0.15, and 0.11, respectively. The surface of the  $\{110\}$  facet had the highest W/Mn atomic ratio of 0.28, which was  $1.8\times$  of that on the  $\{100\}$  facet and  $2.4\times$  of that the  $\{111\}$  facet, respectively. The atomic ratios of W/Mn on all facets decreased with increasing sputtering time and leveled off after sputtering for 90 s. The sputtering rate was calibrated to be  $\sim 5 \text{ nm min}^{-1}$  for a reference material of Si for using 1 kV Ar. Finally, the atomic ratio of W/Mn on various facets all converged to  $\sim 0.05$  after

sputtering for 240 s, close to the XPS result. The AES depth profiles clearly indicate that W prefers to segregate on {110} facets, in comparison with {100} and {111} facets.

### 3.3.3. Electrochemical performances

The rate capability of  $\text{LiMn}_{1.5}\text{Ni}_{0.5}\text{O}_4$  was enhanced significantly by  $\text{WO}_3$  doping, as shown in Figure 3.5. The discharge capacities of the doped specimen were substantially higher than those of the undoped specimen at all rates. Specifically, the difference in the discharge capacities between doped and undoped specimens increased with the increasing rate from 1C to 25C. At the rate of 25C, undoped  $\text{LiMn}_{1.5}\text{Ni}_{0.5}\text{O}_4$  only had an average discharge capacity of  $16.6 \pm 24.3 \text{ mAh g}^{-1}$ ; in contrast, the  $\text{WO}_3$  doped  $\text{LiMn}_{1.5}\text{Ni}_{0.5}\text{O}_4$  maintained an average discharge capacity of  $101.3 \pm 0.4 \text{ mAh g}^{-1}$ , representing an ~500 % increase from the undoped specimen. Furthermore, at rates higher than 25C, the undoped specimen exhibited virtually no discharge capacity ( $< 1 \text{ mAh g}^{-1}$ ), but the  $\text{WO}_3$  doped specimen still retained discharge capacities of  $79.4 \pm 5.6 \text{ mAh g}^{-1}$  at 45C,  $46.9 \pm 16.8 \text{ mAh g}^{-1}$  at 65C, and  $13.8 \pm 2.4 \text{ mAh g}^{-1}$  at 85C, respectively. Though a relatively low mass loading of  $3.2 \text{ mg/cm}^2$  with 80% active material was used in this study, outstanding rate performance could still be achieved by optimizing the carbon content for a thick electrode.

The measured EIS spectra are shown in Figure 3.6 and fitted results are displayed in Table 3.2. Both the surface film and charge transfer resistances

decreased from 156.0 and 47.0  $\Omega$  of the undoped specimen to 56.3 and 19.5  $\Omega$  of the doped specimen, which is consistent with the enhanced rate performance.

Figure 3.7 displays the charge and discharge profiles of the doped and undoped specimens in the first cycle at C/10. The discharge capacity of the doped  $\text{LiMn}_{1.5}\text{Ni}_{0.5}\text{O}_4$  is 132.6  $\text{mAh g}^{-1}$ , which was higher than 116.9  $\text{mAh g}^{-1}$  of the undoped  $\text{LiMn}_{1.5}\text{Ni}_{0.5}\text{O}_4$ . The increase of discharge capacity of  $\sim 16 \text{ mAh g}^{-1}$  in the  $\text{WO}_3$  doped specimen is mainly resulted from the extended  $\text{Ni}^{2+/4+}$  plateau (at  $\sim 4.6$  and  $\sim 4.8 \text{ V}$ ) and  $\text{Mn}^{3+/4+}$  plateau (at  $\sim 4.0 \text{ V}$ ), indicating increased amounts of  $\text{Ni}^{2+/4+}$  and  $\text{Mn}^{3+/4+}$  redox couples.<sup>4,51</sup> This observation is consistent with measured CV results shown in Figure 3.8. Specifically, the discharge capacity contributed by  $\text{Mn}^{3+/4+}$  (3.60 – 4.25 V) and  $\text{Ni}^{2+/4+}$  (4.25 – 4.8 V) in the doped specimen increased by 6.6  $\text{mAh g}^{-1}$  (from 10.4 to 17.0  $\text{mAh g}^{-1}$ ) and 10.8  $\text{mAh g}^{-1}$  (from 104 to 114.8  $\text{mAh g}^{-1}$ ), respectively, in comparison to those of the undoped  $\text{LiMn}_{1.5}\text{Ni}_{0.5}\text{O}_4$ . In addition, the coulombic efficiency of the first cycle was also improved from 78 % to 86 % with  $\text{WO}_3$  doping.

Figure 3.9 shows that the cycling performance was also enhanced by  $\text{WO}_3$  doping. After 200 cycles at an elevated temperature of 55  $^\circ\text{C}$  and a relatively high rate of 1C, the discharge capacities were 111.7  $\text{mAh g}^{-1}$  and 88.9  $\text{mAh g}^{-1}$ , respectively, for the doped and undoped specimens, respectively, corresponding to the capacity retentions of 87 % and 81 %, respectively.

Both the rate capability and cycling stability of the undoped specimen obtained in this work are comparable with those previously reported with the same/similar compositions and loading density of the active material.<sup>38</sup>

### 3.3.4. Surface and bulk Mn<sup>3+</sup> concentrations

XPS characterization of the Mn cations of the WO<sub>3</sub> doped specimen as a function of sputtering time (labeled in the graph) are shown in Figure 3.10(a), where a decrease in the binding energy represents a decrease of the cation valence. Specifically, the Mn 2p binding energy shifted from 641.8 eV at the surface to 640.3 eV in the bulk, suggesting that the average Mn valence at the surface is higher. In other words, the Mn<sup>3+</sup> concentration on the surface was likely lower than that in the bulk. This result is different from the reported result of the undoped LiMn<sub>1.5</sub>Ni<sub>0.5</sub>O<sub>4</sub>, where no shift in the Mn 2p binding energy after sputtering implies no change of the Mn valence at the surface.<sup>50</sup>

For W, the distance between the two spin-orbit split doublets, W 4f<sub>5/2</sub> and W 4f<sub>7/2</sub>, is 2.15 eV and the area ratio is 4:3, both of which should be constants (as required by quantum mechanics). As shown in Figure 3.10(b), the W 4f<sub>7/2</sub> peak was at ~34.7 eV in the XPS spectrum before sputtering, and shifted by ~0.2 eV toward higher energies after sputtering. The lower peak energies suggest the presence of some W<sup>5+</sup> on the surface, while the shift to a higher binding energy with sputtering time implies more oxidized states of tungsten (presumably W<sup>6+</sup>) in the bulk phase. The more reduced valence state of W (W<sup>6+</sup> → W<sup>5+</sup>) is likely correlated with more oxidized state Mn (Mn<sup>3+</sup> → Mn<sup>4+</sup>) at the surface, which presumably helps to reduce the dissolution of Mn and improve the cycling stability.

In addition, the Ni2p<sub>3/2</sub> binding energy was ~854.2 eV, which is consistent with that reported in literature,<sup>50,52</sup> and did not change with the sputtering time, indicating that the Ni valence does not change at the surface.

### 3.3.5. Neutron diffraction

Figure 3.11 shows the neutron diffraction patterns for the undoped and WO<sub>3</sub> doped LiMn<sub>1.5</sub>Ni<sub>0.5</sub>O<sub>4</sub> specimens. The Rietveld refinement structure analysis was used to investigate the crystal structure of both samples.<sup>53-56</sup> For long term annealing at 700 °C, LiMn<sub>1.5</sub>Ni<sub>0.5</sub>O<sub>4</sub> intended to become ordered structure, and the ordered structure is disturbed upon further higher heating.<sup>57,58</sup> While these samples were annealed at 800 °C and cooled down quickly, both of them retained the fully disordered structure. Both patterns of undoped and doped specimens did not show any superstructure peaks arising from ordered structure (P4<sub>3</sub>2 space group) and both were successfully refined according to the Fd $\bar{3}$ m space group of a disordered structure; the corresponding reliable factors R<sub>wp</sub> and R<sub>p</sub> are 3.76% and 2.89 % for the undoped specimen, and they were 3.36% and 2.47% for the doped specimen. The lattice constant was 8.1610 ± 0.0003 Å and 8.1662 ± 0.0002 Å, respectively, for the undoped and doped specimens, respectively. An increase in the lattice constant (0.0052 Å) after WO<sub>3</sub> doping was observed.

A secondary phase indexed with a rock-salt structure (Fm $\bar{3}$ m space group) was found in both patterns.<sup>58</sup> The impurity content was 0.82 ± 0.07 wt. % for the undoped specimen, and it was 1.83 ± 0.08 wt. % for the doped specimen.

The influence of such small amounts of the impurity phase on the electrochemical performance may be negligible.  $\text{WO}_3$  doping also decreased the oxygen occupancy from  $100.6 \pm 1.8\%$  to  $97.7 \pm 1.5\%$ , which is consistent with the increased concentration of  $\text{Mn}^{3+}$  in the bulk phase, as well as the slight increase in the lattice constant.

### **3.4. Discussion**

#### **3.4.1. The change in particle morphology and anisotropic surface segregation of W**

Both undoped and doped specimens were prepared via the same procedure using the same  $\text{LiMn}_{1.5}\text{Ni}_{0.5}\text{O}_4$  material and except the addition of  $\text{WO}_3$ . The resultant particle sizes (Figure 3.1) and BET surface areas of undoped and doped specimens were roughly identical within the measurement errors. Hence, it is reasonable to assume that  $\text{WO}_3$  doping led to the change in particle morphology (Figure 3.1 and Figures 3.2(a) and 3.2(b)).

Furthermore, Both XPS and AES have unequivocally demonstrated the surface segregation (adsorption) of W in the doped  $\text{LiMn}_{1.5}\text{Ni}_{0.5}\text{O}_4$  particles. The surface energy can be changed (reduced) with adsorption/segregation of W according to the well-known Gibbs adsorption (Eq. 1.8). AES depth profiles (Figure 3.4) show that W prefers to segregate at the  $\{110\}$  surface facets (with a greater  $\Gamma$ ) that leads to a greater reduction of  $\gamma_{\{110\}}$ , in comparison with other facets. Consequently, the largest reduction in the relative surface energy in  $\gamma_{\{110\}}$  (Table 3.1) leads to an increase in the fraction of the  $\{110\}$  facets according to the

well-established Wulff theory (construction) of the equilibrium crystal shape, which are consistent with experimental observations (Figure 3.1 and Figures 3.2(a) and 3.2(b)). Similarly, anisotropic segregation may also destabilize {311} facets and change the relative ratios of other facets.

### 3.4.2. Mechanisms of the improved rate capability

The increase fraction of the {110} (as well as {111}) facets may enhance the rate capability because {110} (as well as {111}) facets exhibit more open channels for fast diffusion of  $\text{Li}^+$  ions (Figures 3.2(c) - (e)). Though  $\text{LiMn}_{1.5}\text{Ni}_{0.5}\text{O}_4$  is regarded as a 3D lithium diffusion material, the lithium diffusion rates perpendicular to different facets can be different, particularly at high charging and discharging rates. As shown in Figures 3.2(c) – (e), the {110} facets provide the most open path for the lithium diffusion, followed by the {111} facets and then the {100} facets. Since the anisotropic surface segregation of W significantly increased the fraction of the {110} facets (from ~18% to ~43%) and moderately increased the fraction of the {111} facets (from ~44% to ~56%), as shown in Figure 3.1 and Figures 3.2(a) and 3.2(b), it improved the rate performance of the doped specimen (Figure 3.5).

We note that the bulk doping of  $\text{W}^{6+}$  can increase the concentration of  $\text{Mn}^{3+}$  in the bulk phase, which can also improve the rate capability via triggering cation disordering in  $\text{LiMn}_{1-x}\text{Ni}_x\text{O}_4$  (being a possible alternative mechanism for the improved rate performance).<sup>8</sup> However, if the structure is (already) disordered, further increasing the  $\text{Mn}^{3+}$  content in the disordered structure may not further

improve the rate capability.<sup>8</sup> In the current case, refined structures obtained from neutron diffraction (Figure 3.11) suggested both undoped and doped specimens are likely fully disordered. Hence, the increase of the  $\text{Mn}^{3+}$  concentration in the bulk phase of the doped specimen may not play a major role in improving the rate capability in the current case. In other words, the improved rate capability in the current case is mostly likely related to the anisotropic surface segregation of W and the associated particle morphological change of the Wulff shape with increased fractions of the favorite  $\{110\}$ , as well as  $\{111\}$ , facets.

In addition to improving the cycling stability (a subject that will be discussed further in the next section), the improved the chemical stability of the W-segregated surfaces can also improve the rate capability via suppressing the rapid increase of the surface resistance, as evident directly in EIS results (Figure 3.6).

### **3.4.3. Mechanisms of the increased discharge capacity and cycling stability**

The neutron diffraction showed evidence of increased oxygen vacancy concentration, as well as an increased lattice constant, with the W doping, implying an increase of the  $\text{Mn}^{3+}$  concentration in the bulk phase of the  $\text{WO}_3$  doped  $\text{LiMn}_{1.5}\text{Ni}_{0.5}\text{O}_4$  specimen. It is known that an increased  $\text{Mn}^{3+}$  content can contribute to an increasing specific capacity at the voltage plateau  $\sim 4$  V (Figure 3.7).<sup>10</sup>

It is also known that the existence of  $\text{Mn}^{3+}$  on the surface can trigger disproportionation of  $\text{Mn}^{3+}$  cations to  $\text{Mn}^{2+}$  and  $\text{Mn}^{4+}$  cations, which can promote

the dissolution of  $\text{Mn}^{2+}$  in the electrolyte and subsequently capacity losses; subsequently, the  $\text{Mn}^{3+}$  concentration on the surface can increase further during electrochemical cycling, which can further promote the dissolution of  $\text{Mn}^{2+}$ , resulting in poor cycling stability.<sup>59</sup>

However, our cycling stability results (Figure 3.9) clearly show that the doped specimen (that presumably have a high  $\text{Mn}^{3+}$  content) had a better cycling stability than the undoped specimen. It is likely related to the W surface segregation (along with the partial reduction of  $\text{W}^{6+}$  to  $\text{W}^{5+}$  at the surface; Figure 3.10(b)), which likely decreases the  $\text{Mn}^{3+}$  concentration at the surface, thereby enhancing the cycling stability via reducing the disproportionation of  $\text{Mn}^{3+}$  cations and suppressing the  $\text{Mn}^{2+}$  dissolution.

In summary,  $\text{W}^{6+}$  doping in the bulk phase introduces oxygen vacancies and increases the bulk  $\text{Mn}^{3+}$  concentration, which can enhance the specific discharge capacity. The surface segregation and partial reduction of W at surface reduce the surface  $\text{Mn}^{3+}$  concentration, which may increase the cycling stability by suppressing the formation and dissolution of  $\text{Mn}^{2+}$  at the surfaces (along with the possible beneficial effects of the surface segregation of W).

This beneficial surface configuration (with W segregation and partial reduction, along with suppressed  $\text{Mn}^{3+}$  concentration at/near the surface) that spontaneously formed during mixing and annealing in the  $\text{WO}_3$  doped  $\text{LiMn}_{1.5}\text{Ni}_{0.5}\text{O}_4$  specimen (as the thermodynamically equilibrium surface state) is a 2-D surface phase (also called “complexion”<sup>60-62</sup>) that can be considered as naturally-formed surface protective “coatings,” akin to those nanoscale surface

amorphous films<sup>63-66</sup> or nitridated surfaces<sup>67</sup> observed in prior studies that also improved both the rate capabilities<sup>63,64,66,67</sup> and cycling stabilities<sup>63</sup> of a range of battery cathode<sup>63,64,66</sup> and anode<sup>67</sup> materials.

### 3.5. Conclusions

Minor  $\text{WO}_3$  doping, which can be achieved by a facile ball milling and annealing process, can substantially enhance the electrochemical performance of  $\text{LiMn}_{1.5}\text{Ni}_{0.5}\text{O}_4$ . While the  $\text{W}^{6+}$  doping in the bulk phase leads to extra oxygen vacancies and increase of the bulk  $\text{Mn}^{3+}$  concentration, the surface segregation and partial reduction of W reduce the surface  $\text{Mn}^{3+}$  concentration, which improves the cycling stability via reducing the surface disproportionation of  $\text{Mn}^{3+}$  cations and suppressing the subsequent dissolution of  $\text{Mn}^{2+}$  cations. Furthermore, anisotropic surface segregation of W changes the relative surface energies of different crystalline facets and subsequently the Wulff shape of the crystalline particles, which improves the rate capability via increasing the areas of  $\{110\}$  and  $\{111\}$  facets with more open channels for fast lithium ion diffusion. For example, the discharge capacity at 25C can be increased by ~500% by 1 vol. %  $\text{WO}_3$  doping.

In a broader context, this study has demonstrated the anisotropic surface segregation (or formation of 2-D surface phases<sup>63-67</sup> in general) can be utilized as a facile method to control the particle morphology thermodynamically, as well as modify surface properties (i.e., increase the electrochemical stability and surface transport rates in this particular case), to significantly improve the rate capability,

cycling stability, and potentially other properties of battery materials, as well as a broad range of other functional materials for energy-related applications, such as supercapacitors<sup>68</sup> and photocatalysts<sup>69,70</sup>.

**Chapter 3**, in part, is a reprint of the material “Enhancing the Electrochemical Performance of  $\text{LiMn}_{1.5}\text{Ni}_{0.5}\text{O}_4$  through  $\text{WO}_3$  Doping and Changing the Particle Wulff Shape via Anisotropic Surface Segregation” in preparation, Jijia Huang, Haodong Liu, Naixie Zhou, Ke An, Ying S. Meng and Jian Luo. Neutron diffraction was carried out by Dr. Haodong Liu and Dr. Ke An in Oak Ridge National Laboratory. Dr. Naixie Zhou gave a lot valuable opinions on the thermodynamic model.

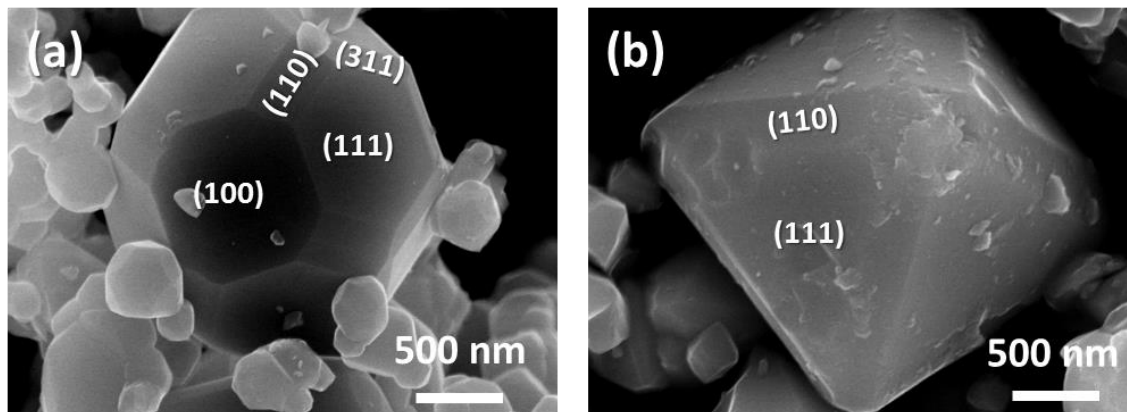


Figure 3.1 Representative SEM images of the (a) undoped and (b) 1 vol. %  $\text{WO}_3$  doped  $\text{LiMn}_{1.5}\text{Ni}_{0.5}\text{O}_4$  specimens, where were prepared by annealing high-energy ball milled powders at 800 °C for 4 h.

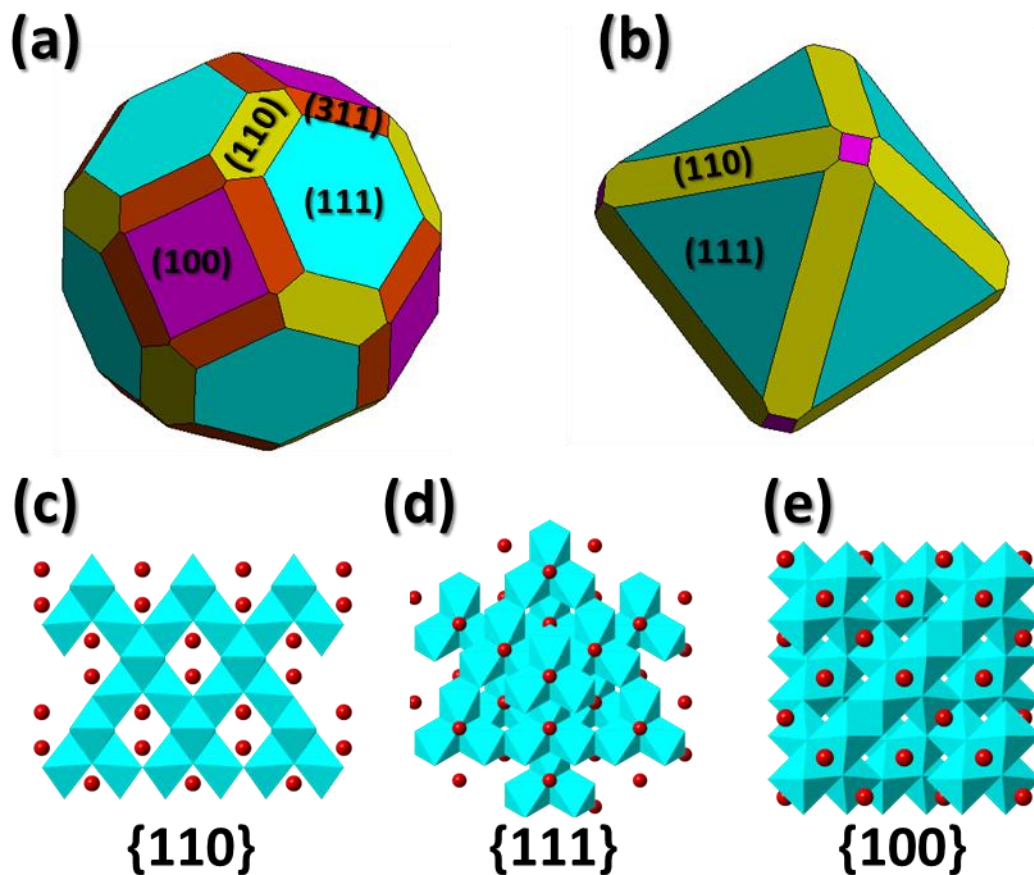


Figure 3.2 Calculated Wulff shapes of the (a) undoped and (b)  $\text{WO}_3$  doped  $\text{LiMn}_{1.5}\text{Ni}_{0.5}\text{O}_4$  that matched the experimentally observed particle morphologies shown in Figure 3.1 and schematics of the Li ion diffusion channels on (c)  $\{110\}$ , (d)  $\{111\}$  and (e)  $\{100\}$  facets, respectively. The relative surface energies that produced these Wulff shapes are listed in Table 3.1.

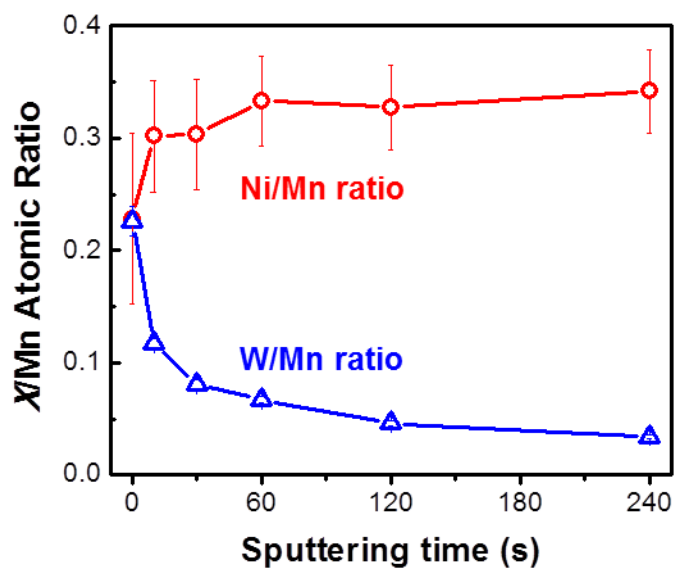


Figure 3.3 Atomic ratios of W/Mn and Ni/Mn vs. sputtering time curves measured from XPS.

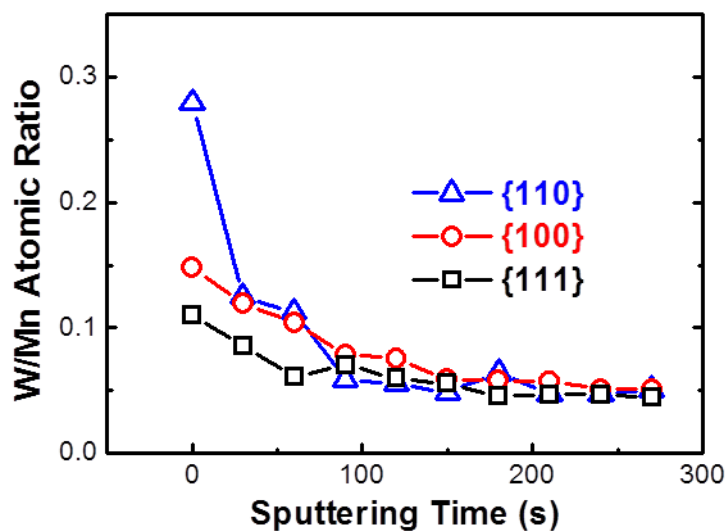


Figure 3.4 Atomic ratios of W to Mn vs. sputtering time curves measured by AES on three different surface facets of {110}, {100} and {111}. The {110} facet has the highest level of W segregation, which is consistent with the observed largest reduction in the relative surface energy in the  $\text{WO}_3$  doped specimen (Table 3.1).

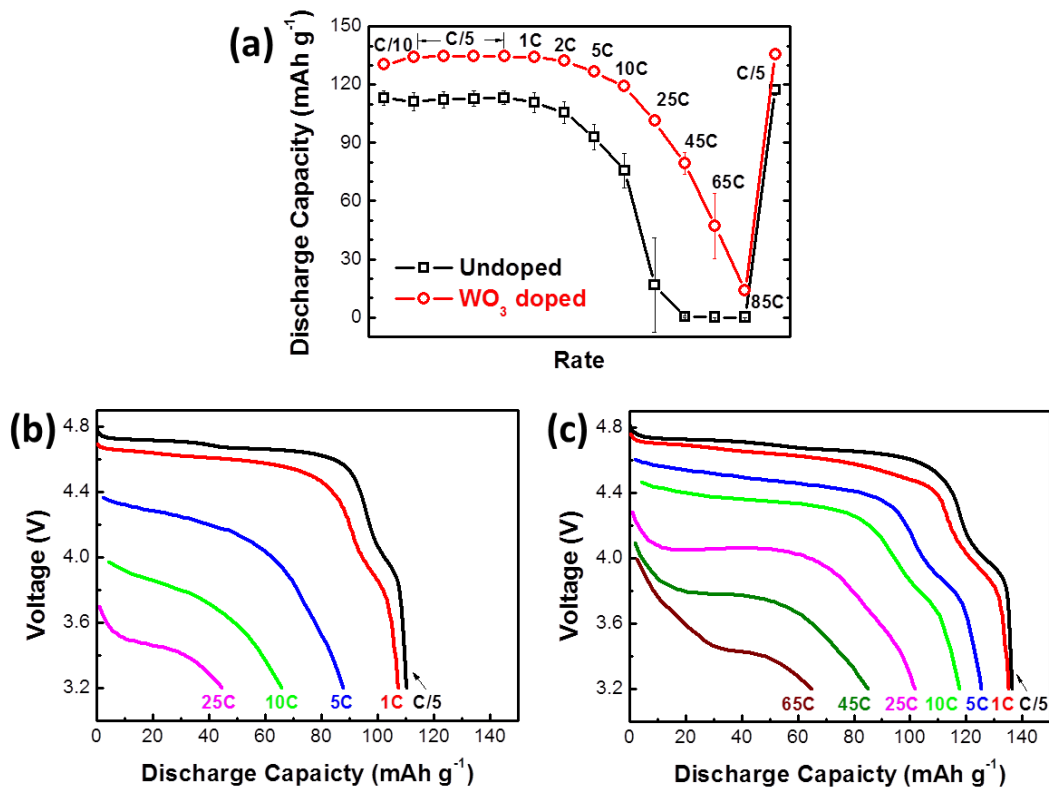


Figure 3.5 (a) Comparison of rate performance of undoped and  $\text{WO}_3$  doped  $\text{LiMn}_{1.5}\text{Ni}_{0.5}\text{O}_4$  specimens and discharge curves of (b) undoped specimen and (c)  $\text{WO}_3$  doped  $\text{LiMn}_{1.5}\text{Ni}_{0.5}\text{O}_4$  specimens. Three coin cells were made and tested for each specimen. The means are presented in the graph and error bars represent  $\pm$  one standard deviations. All cells were first charged and discharged at C/10 for 1 cycle and C/5 for 4 cycles to reach steady states and subsequently charged at C/5 and discharged at various rates (labeled in the graph) at room temperature

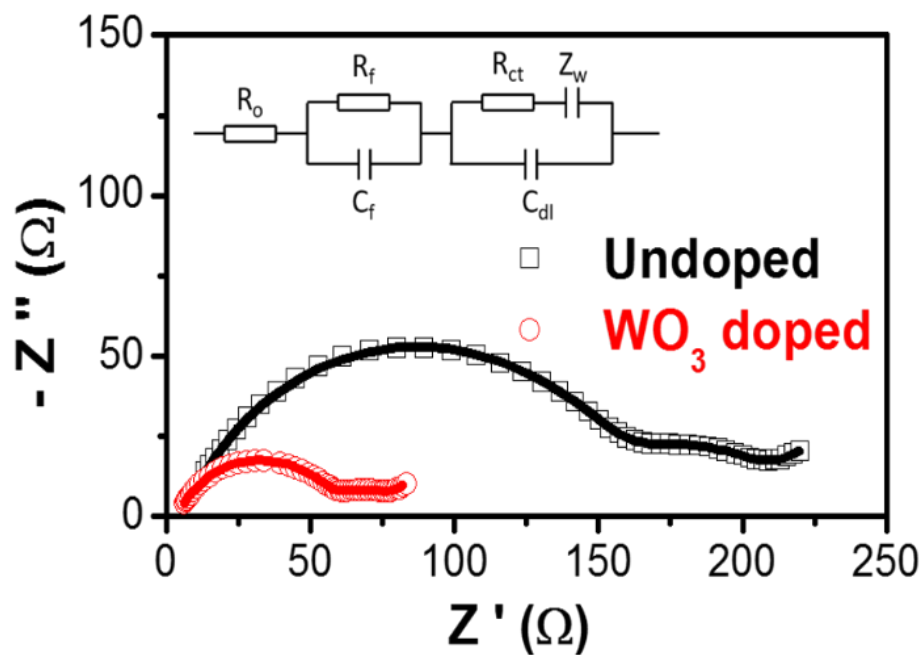


Figure 3.6 Measured EIS spectra of the undoped and  $\text{WO}_3$  doped (red circles)  $\text{LiMn}_{1.5}\text{Ni}_{0.5}\text{O}_4$  specimens. The inset is an equivalent circuit. The fitted surface film and charge transfer resistances are given in Table 3.2

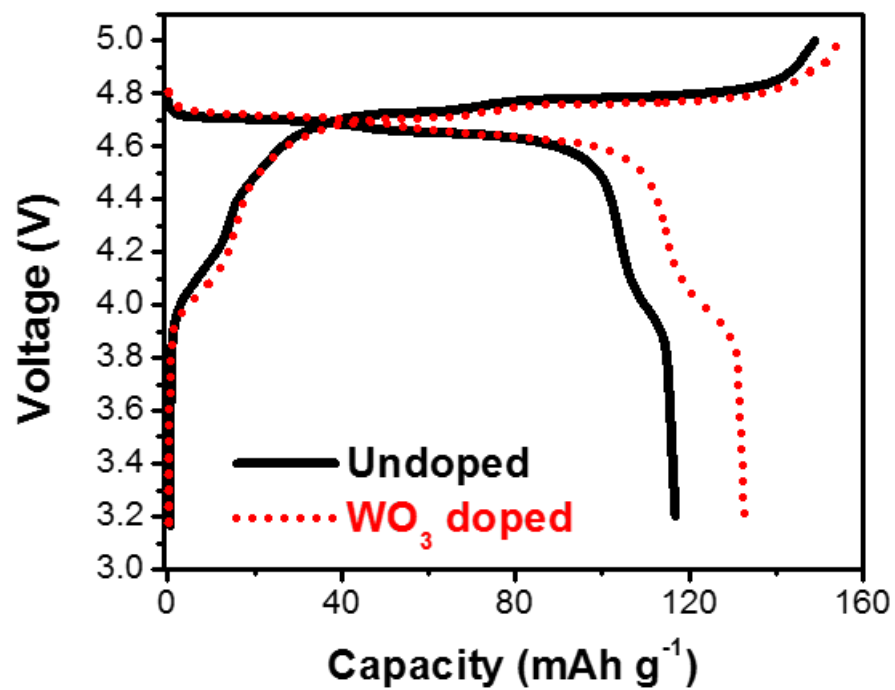


Figure 3.7 Measured charge/discharge curves for the undoped and WO<sub>3</sub> doped LiMn<sub>1.5</sub>Ni<sub>0.5</sub>O<sub>4</sub> specimens. Both specimens were charged and discharged at a low rate of 0.1C at room temperature.

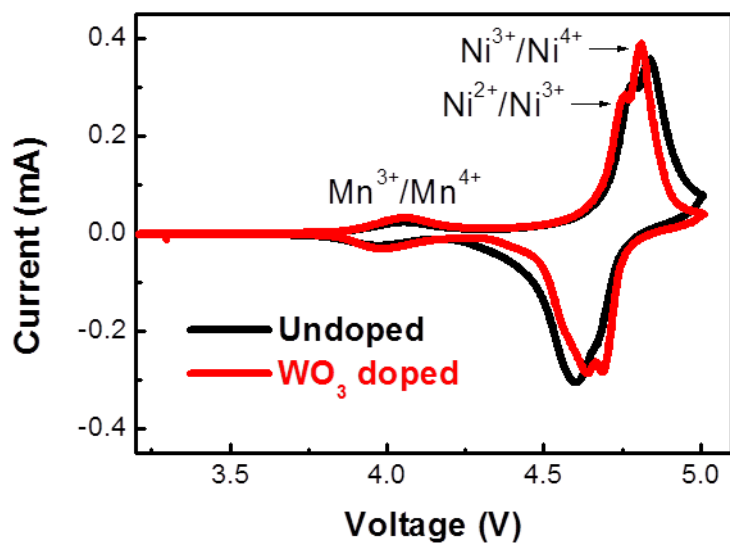


Figure 3.8 Measured CV curves of the undoped and WO<sub>3</sub>-doped LiMn<sub>1.5</sub>Ni<sub>0.5</sub>O<sub>4</sub> specimens.

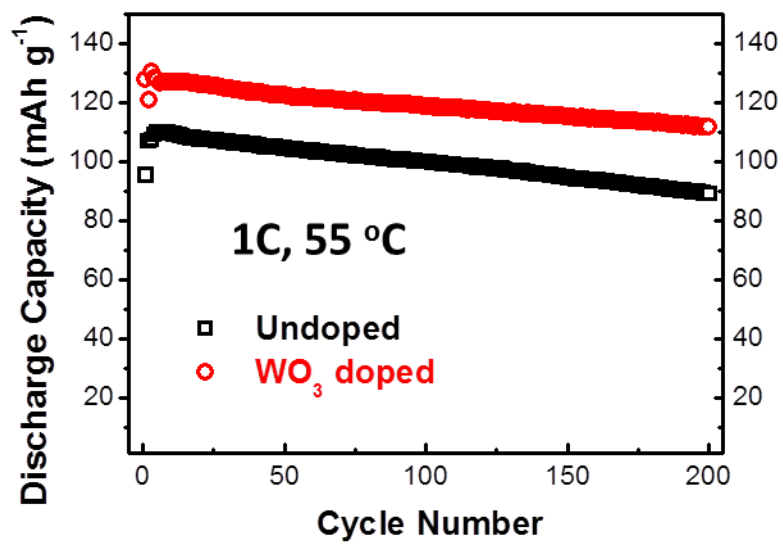


Figure 3.9 Cycling stability results of the undoped and WO<sub>3</sub>-doped doped LiMn<sub>1.5</sub>Ni<sub>0.5</sub>O<sub>4</sub> specimens tested at an elevated temperature of 55 °C with a relatively high charge and discharge rate of 1C as an accelerated test

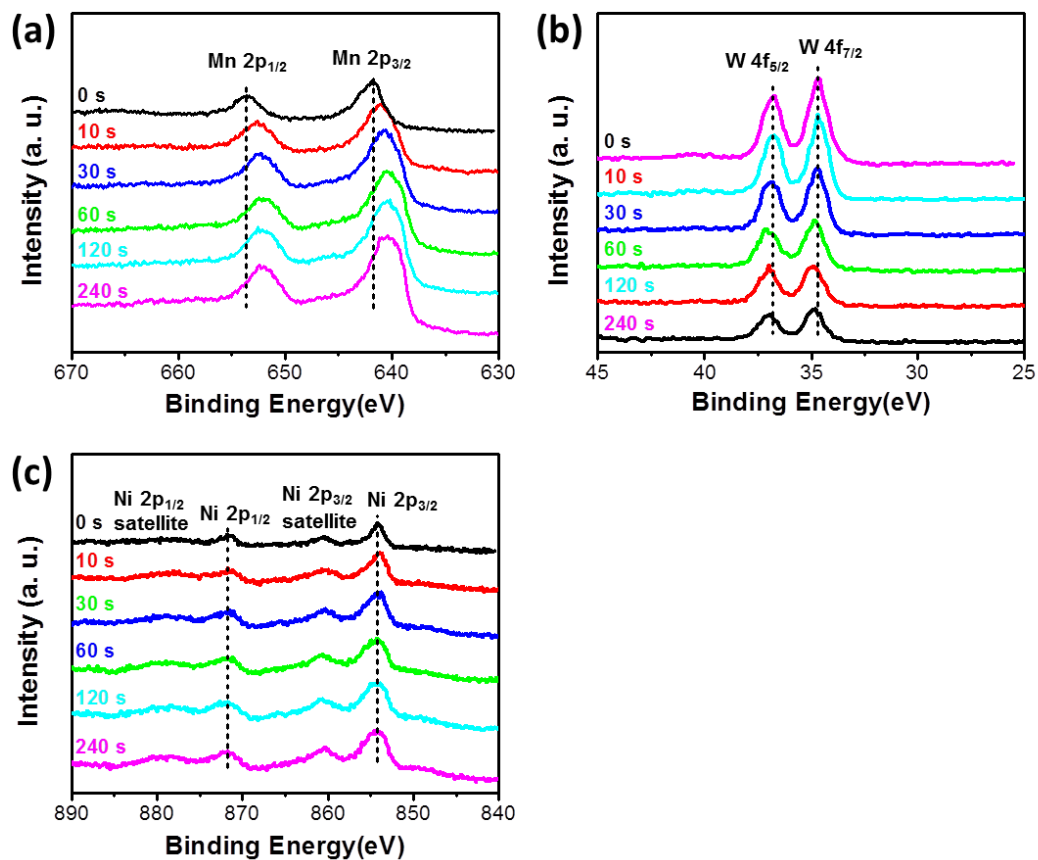


Figure 3.10 XPS results of (a) Mn, (b) W, and (c) Ni binding energy shifts after sputtering for different times (labeled in the graphs) for the 1 vol. %  $\text{WO}_3$  doped  $\text{LiMn}_{1.5}\text{Ni}_{0.5}\text{O}_4$  specimen.

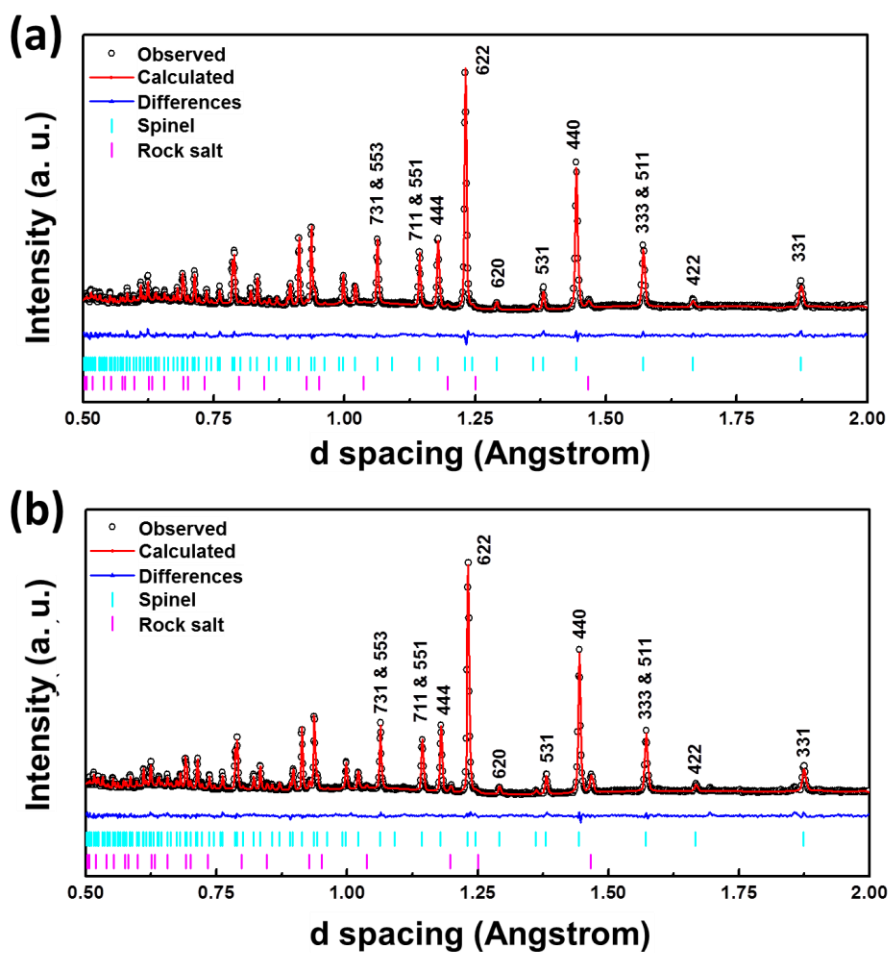


Figure 3.11 Neutron powder diffraction patterns of the (a) undoped and (b) 1 vol. %  $\text{WO}_3$  doped  $\text{LiMn}_{1.5}\text{Ni}_{0.5}\text{O}_4$  specimens

Table 3.1 Relative surface energies of the undoped and WO<sub>3</sub>-doped doped LiMn<sub>1.5</sub>Ni<sub>0.5</sub>O<sub>4</sub> specimens that matched the experimentally observed Wulff shapes

	undoped	WO <sub>3</sub> -doped
$\gamma_{\{111\}}/\gamma_{\{100\}}$	0.94	0.69
$\gamma_{\{110\}}/\gamma_{\{100\}}$	1.04	0.76
$\gamma_{\{311\}}/\gamma_{\{100\}}$	1.05	-

Table 3.2 Fitted surface film and charge transfer resistances from EIS

Specimen	R <sub>f</sub> (Ω)	R <sub>ct</sub> (Ω)
undoped	156.0 ± 0.7	47.0 ± 1.9
WO <sub>3</sub> doped	56.3 ± 0.3	19.5 ± 1.0

## References

- (1) Idemoto, Y.; Narai, H.; Koura, N. Crystal Structure and Cathode Performance Dependence on Oxygen Content of  $\text{Li}_{1.5}\text{Ni}_{0.5}\text{O}_4$  as a Cathode Material for Secondary Lithium Batteries. *Journal of Power Sources* **2003**, *119–121*, 125-129.
- (2) Kim, J. H.; Myung, S. T.; Yoon, C. S.; Kang, S. G.; Sun, Y. K. Comparative Study of  $\text{Li}_{1.5}\text{Mn}_{1.5}\text{O}_4$  and  $\text{Li}_{1.5}\text{Ni}_{0.5}\text{O}_4$  Cathodes Having Two Crystallographic Structures: Fd3M and P4332. *Chemistry of Materials* **2004**, *16*, 906-914.
- (3) Kunduraci, M.; Al-Sharab, J. F.; Amatucci, G. G. High-Power Nanostructured  $\text{Li}_{1-x}\text{Ni}_x\text{O}_4$  High-Voltage Lithium-Ion Battery Electrode Materials: Electrochemical Impact of Electronic Conductivity and Morphology. *Chemistry of Materials* **2006**, *18*, 3585-3592.
- (4) Kunduraci, M.; Amatucci, G. G. The Effect of Particle Size and Morphology on the Rate Capability of 4.7 V  $\text{Li}_{1.5}\text{Ni}_{0.5}\text{O}_4$  Spinel Lithium-Ion Battery Cathodes. *Electrochimica Acta* **2008**, *53*, 4193-4199.
- (5) Cabana, J.; Casas-Cabanas, M.; Omenya, F. O.; Chernova, N. A.; Zeng, D.; Whittingham, M. S.; Grey, C. P. Composition-Structure Relationships in the Li-Ion Battery Electrode Material  $\text{Li}_{1.5}\text{Ni}_{0.5}\text{O}_4$ . *Chemistry of Materials* **2012**, *24*, 2952-2964.
- (6) Shin, D. W.; Bridges, C. A.; Huq, A.; Paranthaman, M. P.; Manthiram, A. Role of Cation Ordering and Surface Segregation in High-Voltage Spinel  $\text{Li}_{1.5}\text{Ni}_{0.5}\text{M}_x\text{O}_4$  (M = Cr, Fe, and Ga) Cathodes for Lithium-Ion Batteries. *Chemistry of Materials* **2012**, *24*, 3720-3731.
- (7) Xiao, J.; Chen, X.; Sushko, P. V.; Sushko, M. L.; Kovarik, L.; Feng, J.; Deng, Z.; Zheng, J.; Graff, G. L.; Nie, Z.; Choi, D.; Liu, J.; Zhang, J.-G.; Whittingham, M. S. High-Performance  $\text{Li}_{1.5}\text{Ni}_{0.5}\text{M}_x\text{O}_4$  Spinel Controlled by  $\text{Mn}^{3+}$  Concentration and Site Disorder. *Advanced Materials* **2012**, *24*, 2109-2116.
- (8) Duncan, H.; Hai, B.; Leskes, M.; Grey, C. P.; Chen, G. Relationships between  $\text{Mn}^{3+}$  Content, Structural Ordering, Phase Transformation, and Kinetic Properties in  $\text{Li}_{1-x}\text{Ni}_x\text{Mn}_{2-x}\text{O}_4$  Cathode Materials. *Chemistry of Materials* **2014**, *26*, 5374-5382.
- (9) Tarascon, J. M.; McKinnon, W. R.; Coowar, F.; Bowmer, T. N.; Amatucci, G.; Guyomard, D. Synthesis Conditions and Oxygen Stoichiometry Effects on Li Insertion into the Spinel  $\text{Li}_{1.5}\text{Ni}_{0.5}\text{O}_4$ . *Journal of the Electrochemical Society* **1994**, *141*, 1421-1431.
- (10) Song, J.; Shin, D. W.; Lu, Y.; Amos, C. D.; Manthiram, A.; Goodenough, J. B. Role of Oxygen Vacancies on the Performance of  $\text{Li}[\text{Ni}_{0.5}\text{Mn}_{1.5}\text{X}]\text{O}_4$  (X = 0, 0.05, and 0.08) Spinel Cathodes for Lithium-Ion Batteries. *Chemistry of Materials* **2012**, *24*, 3101-3109.

- (11) Aklalouch, M.; Rojas, R. M.; Rojo, J. M.; Saadoune, I.; Amarilla, J. M. The Role of Particle Size on the Electrochemical Properties at 25 and at 55 °C of the  $\text{Li}_{0.2}\text{Ni}_{0.4}\text{Mn}_{1.4}\text{O}_4$  Spinel as 5 V-Cathode Materials for Lithium-Ion Batteries. *Electrochimica Acta* **2009**, *54*, 7542-7550.
- (12) Wang, H.; Xia, H.; Lai, M. O.; Lu, L. Enhancements of Rate Capability and Cyclic Performance of Spinel  $\text{Li}_{0.5}\text{Mn}_{1.5}\text{O}_4$  by Trace Ru-Doping. *Electrochemistry Communications* **2009**, *11*, 1539-1542.
- (13) Prabakar, S. J. R.; Han, S. C.; Singh, S. P.; Lee, D. K.; Sohn, K.-S.; Pyo, M. W-Doped  $\text{Li}_{1-x}\text{Ni}_{0.5}\text{Mn}_{1.5-x}\text{O}_4$  Cathodes for the Improvement of High Rate Performances in Li Ion Batteries. *Journal of Power Sources* **2012**, *209*, 57-64.
- (14) Yi, T.-F.; Xie, Y.; Zhu, Y.-R.; Zhu, R.-S.; Ye, M.-F. High Rate Micron-Sized Niobium-Doped  $\text{Li}_{1-x}\text{Ni}_{0.5}\text{O}_4$  as Ultra High Power Positive-Electrode Material for Lithium-Ion Batteries. *Journal of Power Sources* **2012**, *211*, 59-65.
- (15) Zhong, G. B.; Wang, Y. Y.; Zhao, X. J.; Wang, Q. S.; Yu, Y.; Chen, C. H. Structural, Electrochemical and Thermal Stability Investigations on  $\text{Li}_{1-x}\text{Al}_{2x}\text{Mn}_{1.5-x}\text{O}_4$  ( $0 \leq x \leq 1.0$ ) as 5 v Cathode Materials. *Journal of Power Sources* **2012**, *216*, 368-375.
- (16) Sha, O.; Qiao, Z.; Wang, S.; Tang, Z.; Wang, H.; Zhang, X.; Xu, Q. Improvement of Cycle Stability at Elevated Temperature and High Rate for  $\text{Li}_{1-x}\text{Cu}_x\text{Mn}_{1.5}\text{O}_4$  Cathode Material after Cu Substitution. *Materials Research Bulletin* **2013**, *48*, 1606-1611.
- (17) Shiu, J.-J.; Pang, W. K.; Wu, S.-h. Preparation and Characterization of Spinel  $\text{Li}_{1-x}\text{Mg}_x\text{Mn}_{1.5}\text{O}_4$  Cathode Materials Via Spray Pyrolysis Method. *Journal of Power Sources* **2013**, *244*, 35-42.
- (18) Wu, P.; Zeng, X. L.; Zhou, C.; Gu, G. F.; Tong, D. G. Improved Electrochemical Performance of  $\text{Li}_{1-x}\text{Rh}_x\text{Mn}_{1.5}\text{O}_4$  Cathode Materials for 5 V Lithium Ion Batteries Via Rh-Doping. *Materials Chemistry and Physics* **2013**, *138*, 716-723.
- (19) Kim, M. C.; Nam, K.-W.; Hu, E.; Yang, X.-Q.; Kim, H.; Kang, K.; Aravindan, V.; Kim, W.-S.; Lee, Y.-S. Sol-Gel Synthesis of Aliovalent Vanadium-Doped  $\text{Li}_{1-x}\text{Mn}_{1.5}\text{O}_4$  Cathodes with Excellent Performance at High Temperatures. *ChemSusChem* **2014**, *7*, 829-834.
- (20) Mo, M.; Hui, K. S.; Hong, X.; Guo, J.; Ye, C.; Li, A.; Hu, N.; Huang, Z.; Jiang, J.; Liang, J.; Chen, H. Improved Cycling and Rate Performance of Sm-Doped  $\text{Li}_{1-x}\text{Mn}_{1.5}\text{O}_4$  Cathode Materials for 5 V Lithium Ion Batteries. *Applied Surface Science* **2014**, *290*, 412-418.
- (21) Yang, Z.; Jiang, Y.; Kim, J.-H.; Wu, Y.; Li, G.-L.; Huang, Y.-H. The  $\text{Li}_{1-x}\text{Ni}_x\text{Mn}_{1.5}\text{O}_4$  Spinel with Improved High Voltage Stability for Li-Ion Batteries. *Electrochimica Acta* **2014**, *117*, 76-83.

- (22) Yi, T.-F.; Chen, B.; Zhu, Y.-R.; Li, X.-Y.; Zhu, R.-S. Enhanced Rate Performance of Molybdenum-Doped Spinel  $\text{LiNi}_{0.5}\text{Mn}_{1.5}\text{O}_4$  Cathode Materials for Lithium Ion Battery. *Journal of Power Sources* **2014**, *247*, 778-785.
- (23) Zhong, Q.; Bonakdarpour, A.; Zhang, M.; Gao, Y.; Dahn, J. R. Synthesis and Electrochemistry of  $\text{LiNi}_x\text{Mn}_{2-x}\text{O}_4$ . *Journal of the Electrochemical Society* **1997**, *144*, 205-213.
- (24) Chong, J.; Xun, S.; Song, X.; Liu, G.; Battaglia, V. S. Surface Stabilized  $\text{LiNi}_{0.5}\text{Mn}_{1.5}\text{O}_4$  Cathode Materials with High-Rate Capability and Long Cycle Life for Lithium Ion Batteries. *Nano Energy* **2013**, *2*, 283-293.
- (25) Huang, J.; Luo, J. A Facile and Generic Method to Improve Cathode Materials for Lithium-Ion Batteries Via Utilizing Nanoscale Surface Amorphous Films of Self-Regulating Thickness. *Physical Chemistry Chemical Physics* **2014**, *16*, 7786-7798.
- (26) Chen, Z.; Qiu, S.; Cao, Y.; Ai, X.; Xie, K.; Hong, X.; Yang, H. Surface-Oriented and Nanoflake-Stacked  $\text{LiNi}_{0.5}\text{Mn}_{1.5}\text{O}_4$  Spinel for High-Rate and Long-Cycle-Life Lithium Ion Batteries. *Journal of Materials Chemistry* **2012**, *22*, 17768-17772.
- (27) Hai, B.; Shukla, A. K.; Duncan, H.; Chen, G. The Effect of Particle Surface Facets on the Kinetic Properties of  $\text{LiMn}_{1.5}\text{Ni}_{0.5}\text{O}_4$  Cathode Materials. *Journal of Materials Chemistry A* **2013**, *1*, 759-769.
- (28) Chemelewski, K. R.; Lee, E.-S.; Li, W.; Manthiram, A. Factors Influencing the Electrochemical Properties of High-Voltage Spinel Cathodes: Relative Impact of Morphology and Cation Ordering. *Chemistry of Materials* **2013**, *25*, 2890-2897.
- (29) Chemelewski, K. R.; Shin, D. W.; Li, W.; Manthiram, A. Octahedral and Truncated High-Voltage Spinel Cathodes: The Role of Morphology and Surface Planes in Electrochemical Properties. *Journal of Materials Chemistry A* **2013**, *1*, 3347-3354.
- (30) Lin, H. B.; Zhang, Y. M.; Rong, H. B.; Mai, S. W.; Hu, J. N.; Liao, Y. H.; Xing, L. D.; Xu, M. Q.; Li, X. P.; Li, W. S. Crystallographic Facet- and Size-Controllable Synthesis of Spinel  $\text{LiNi}_{0.5}\text{Mn}_{1.5}\text{O}_4$  with Excellent Cyclic Stability as Cathode of High Voltage Lithium Ion Battery. *Journal of Materials Chemistry A* **2014**, *2*, 11987-11995.
- (31) Chen, Z.; Zhao, R.; Du, P.; Hu, H.; Wang, T.; Zhu, L.; Chen, H. Polyhedral  $\text{LiNi}_{0.5}\text{Mn}_{1.5}\text{O}_4$  with Excellent Electrochemical Properties for Lithium-Ion Batteries. *Journal of Materials Chemistry A* **2014**, *2*, 12835-12848.
- (32) Chen, Z.; Zhao, R.; Li, A.; Hu, H.; Liang, G.; Lan, W.; Cao, Z.; Chen, H. Polyhedral Ordered  $\text{LiNi}_{0.5}\text{Mn}_{1.5}\text{O}_4$  Spinel with Excellent Electrochemical Properties in Extreme Conditions. *Journal of Power Sources* **2015**, *274*, 265-273.

- (33) Liu, H.; Kloepsch, R.; Wang, J.; Winter, M.; Li, J. Truncated Octahedral  $\text{LiNi}_{0.5}\text{Mn}_{1.5}\text{O}_4$  Cathode Material for Ultralong-Life Lithium-Ion Battery: Positive (100) Surfaces in High-Voltage Spinel System. *Journal of Power Sources* **2015**, *300*, 430-437.
- (34) Liu, H.; Wang, J.; Zhang, X.; Zhou, D.; Qi, X.; Qiu, B.; Fang, J.; Kloepsch, R.; Schumacher, G.; Liu, Z.; Li, J. Morphological Evolution of High-Voltage Spinel  $\text{LiNi}_{0.5}\text{Mn}_{1.5}\text{O}_4$  Cathode Materials for Lithium-Ion Batteries: The Critical Effects of Surface Orientations and Particle Size. *Acs Applied Materials & Interfaces* **2016**, *8*, 4661-4675.
- (35) Lee, E.; Persson, K. A. First-Principles Study of the Nano-Scaling Effect on the Electrochemical Behavior in  $\text{LiNi}_{0.5}\text{Mn}_{1.5}\text{O}_4$ . *Nanotechnology* **2013**, *24*, 424007.
- (36) Shin, D. W.; Manthiram, A. Surface-Segregated, High-Voltage Spinel  $\text{LiMn}_{1.5}\text{Ni}_{0.42}\text{Ga}_{0.08}\text{O}_4$  Cathodes with Superior High-Temperature Cyclability for Lithium-Ion Batteries. *Electrochemistry Communications* **2011**, *13*, 1213-1216.
- (37) Chemelewski, K. R.; Li, W.; Gutierrez, A.; Manthiram, A. High-Voltage Spinel Cathodes for Lithium-Ion Batteries: Controlling the Growth of Preferred Crystallographic Planes through Cation Doping. *Journal of Materials Chemistry A* **2013**, *1*, 15334-15341.
- (38) Manthiram, A.; Chemelewski, K.; Lee, E.-S. A Perspective on the High-Voltage  $\text{LiMn}_{1.5}\text{Ni}_{0.5}\text{O}_4$  Spinel Cathode for Lithium-Ion Batteries. *Energy & Environmental Science* **2014**, *7*, 1339-1350.
- (39) Amatucci, G.; Tarascon, J.-M. Optimization of Insertion Compounds Such as  $\text{LiMn}_2\text{O}_4$  for Li-Ion Batteries. *Journal of the Electrochemical Society* **2002**, *149*, K31-K46.
- (40) Luo, J.; Chiang, Y. M. Existence and Stability of Nanometer-Thick Disordered Films on Oxide Surfaces. *Acta Materialia* **2000**, *48*, 4501-4515.
- (41) Scheithauer, M.; Grasselli, R. K.; Knözinger, H. Genesis and Structure of  $\text{Wox}/\text{Zro}_2$  Solid Acid Catalysts. *Langmuir* **1998**, *14*, 3019-3029.
- (42) Tae Kwon, Y.; Yong Song, K.; In Lee, W.; Jin Choi, G.; Rag Do, Y. Photocatalytic Behavior of  $\text{W}_3\text{-Loaded TiO}_2$  in an Oxidation Reaction. *Journal of Catalysis* **2000**, *191*, 192-199.
- (43) Qiu, B.; Zhang, M. H.; Wu, L. J.; Wang, J.; Xia, Y. G.; Qian, D. N.; Liu, H. D.; Hy, S.; Chen, Y.; An, K.; Zhu, Y. M.; Liu, Z. P.; Meng, Y. S. Gas-Solid Interfacial Modification of Oxygen Activity in Layered Oxide Cathodes for Lithium-Ion Batteries. *Nature Communications* **2016**, *7*.
- (44) Liu, H. D.; Qian, D. N.; Verde, M. G.; Zhang, M. H.; Baggetto, L.; An, K.; Chen, Y.; Carroll, K. J.; Lau, D.; Chi, M. F.; Veith, G. M.; Meng, Y. S. Understanding the Role of

Nh<sub>4</sub>f and Al<sub>2</sub>O<sub>3</sub> Surface Co-Modification on Lithium-Excess Layered Oxide Li<sub>1.2</sub>ni<sub>0.2</sub>mn<sub>0.6</sub>o<sub>2</sub>. *Acs Applied Materials & Interfaces* **2015**, *7*, 19189-19200.

(45) An, K.; Skorpenske, H. D.; Stoica, A. D.; Ma, D.; Wang, X. L.; Cakmak, E. First in Situ Lattice Strains Measurements under Load at Vulcan. *Metallurgical and Materials Transactions a-Physical Metallurgy and Materials Science* **2011**, *42A*, 95-99.

(46) An, K.; Wang, X. L.; Stoica, A. D.: Vulcan Data Reduction and Interactive Visualization Software. 2012.

(47) Toby, B. H. Expgui, a Graphical User Interface for Gsas. *Journal of Applied Crystallography* **2001**, *34*, 210-213.

(48) Larson, A. C.; Dreele, R. B. V. General Structure Analysis System (Gsas). *Los Alamos National Laboratory Report (LAUR)* **2004**, 86-748.

(49) Zucker, R. V.; Chatain, D.; Dahmen, U.; Hagege, S.; Carter, W. C. New Software Tools for the Calculation and Display of Isolated and Attached Interfacial-Energy Minimizing Particle Shapes. *Journal of Materials Science* **2012**, *47*, 8290-8302.

(50) Liu, J.; Manthiram, A. Understanding the Improved Electrochemical Performances of Fe-Substituted 5 V Spinel Cathode Limn<sub>1.5</sub>ni<sub>0.5</sub>o<sub>4</sub>. *The Journal of Physical Chemistry C* **2009**, *113*, 15073-15079.

(51) Terada, Y.; Yasaka, K.; Nishikawa, F.; Konishi, T.; Yoshio, M.; Nakai, I. In Situ Xafs Analysis of Li(Mn, M)<sub>2</sub>o<sub>4</sub> (M=Cr, Co, Ni) 5v Cathode Materials for Lithium-Ion Secondary Batteries. *Journal of Solid State Chemistry* **2001**, *156*, 286-291.

(52) Amine, K.; Tukamoto, H.; Yasuda, H.; Fujita, Y. Preparation and Electrochemical Investigation of Limn<sub>2</sub> – Xmexo<sub>4</sub> (Me: Ni, Fe, and X = 0.5, 1) Cathode Materials for Secondary Lithium Batteries. *Journal of Power Sources* **1997**, *68*, 604-608.

(53) Trease, N. M.; Seymour, I. D.; Radin, M. D.; Liu, H.; Liu, H.; Hy, S.; Chernova, N.; Parikh, P.; Devaraj, A.; Wiaderek, K. M.; Chupas, P. J.; Chapman, K. W.; Whittingham, M. S.; Meng, Y. S.; Van der Van, A.; Grey, C. P. Identifying the Distribution of Al<sup>3+</sup> in Lini<sub>0.8</sub>co<sub>0.15</sub>al<sub>0.05</sub>o<sub>2</sub>. *Chemistry of Materials* **2016**, *28*, 8170-8180.

(54) Liu, H. D.; Huang, J. J.; Qian, D. N.; Hy, S.; Fang, C. C.; Luo, J.; Meng, Y. S. Communication-Enhancing the Electrochemical Performance of Lithium-Excess Layered Oxide Li<sub>1.13</sub>ni<sub>0.3</sub>mn<sub>0.57</sub>o<sub>2</sub> Via a Facile Nanoscale Surface Modification. *Journal of the Electrochemical Society* **2016**, *163*, A971-A973.

(55) Liu, H. D.; Chen, Y.; Hy, S.; An, K.; Venkatachalam, S.; Qian, D. N.; Zhang, M. H.; Meng, Y. S. Operando Lithium Dynamics in the Li-Rich Layered Oxide Cathode Material Via Neutron Diffraction. *Advanced Energy Materials* **2016**, *6*.

- (56) Liu, H. D.; Fell, C. R.; An, K.; Cai, L.; Meng, Y. S. In-Situ Neutron Diffraction Study of the  $\text{XLi}_2\text{MnO}_3 \cdot (1-X)\text{Li}_2\text{O}$  ( $X=0, 0.5$ ;  $M = \text{Ni, Mn, Co}$ ) Layered Oxide Compounds During Electrochemical Cycling. *Journal of Power Sources* **2013**, *240*, 772-778.
- (57) Chen, Y.; Cheng, Y.; Li, J.; Feyngenson, M.; Heller, W. T.; Liang, C.; An, K. Lattice-Cell Orientation Disorder in Complex Spinel Oxides. *Advanced Energy Materials* **2017**, *7*, 1601950-n/a.
- (58) Cai, L.; Liu, Z.; An, K.; Liang, C. Unraveling Structural Evolution of  $\text{LiNi}_{0.5}\text{Mn}_{1.5}\text{O}_4$  by in Situ Neutron Diffraction. *Journal of Materials Chemistry A* **2013**, *1*, 6908-6914.
- (59) Qiao, R.; Wang, Y.; Olalde-Velasco, P.; Li, H.; Hu, Y.-S.; Yang, W. Direct Evidence of Gradient Mn(II) Evolution at Charged States in  $\text{LiNi}_{0.5}\text{Mn}_{1.5}\text{O}_4$  Electrodes with Capacity Fading. *Journal of Power Sources* **2015**, *273*, 1120-1126.
- (60) Cantwell, P. R.; Tang, M.; Dillon, S. J.; Luo, J.; Rohrer, G. S.; Harmer, M. P. Overview No. 152: Grain Boundary Complexions. *Acta Materialia* **2014**, *62*, 1-48.
- (61) Kaplan, W. D.; Chatain, D.; Wynblatt, P.; Carter, W. C. A Review of Wetting Versus Adsorption, Complexions, and Related Phenomena: The Rosetta Stone of Wetting *Journal of Materials Science* **2013**, *48*, 5681-5717.
- (62) Luo, J. Interfacial Engineering of Solid Electrolytes. *Journal of Materiomics* **2015**, *1*, 22-32.
- (63) Huang, J.; Luo, J. A Facile and Generic Method to Improve Cathode Materials for Lithium-Ion Batteries Via Utilizing Nanoscale Surface Amorphous Films of Self-Regulating Thickness. *Physical Chemistry Chemical Physics* **2014**, *16*, 7786-7798.
- (64) Kayyar, A.; Qian, H. J.; Luo, J. Surface Adsorption and Disorder in  $\text{LiFePO}_4$  Based Battery Cathodes. *Applied Physics Letters* **2009**, *95*, 221905.
- (65) Luo, J.; Chiang, Y.-M. Wetting and Prewetting on Ceramic Surfaces. *Annual Review of Materials Research* **2008**, *38*, 227-249.
- (66) Kang, B.; Ceder, G. Battery Materials for Ultrafast Charging and Discharging. *Nature* **2009**, *458*, 190-193.
- (67) Samiee, M.; Luo, J. A Facile Nitridation Method to Improve the Rate Capability of  $\text{TiO}_2$  for Lithium-Ion Batteries. *Journal of Power Sources* **2014**, *245*, 594-598.
- (68) Samiee, M.; Luo, J. Pseudocapacitive Properties of Two-Dimensional Surface Vanadia Phases Formed Spontaneously on Titania. *Acs Applied Materials & Interfaces* **2016**, *8*, 12871-12880.

(69) Samiee, M.; Luo, J. Enhancing the Visible-Light Photocatalytic Activity of  $\text{TiO}_2$  by Heat Treatments in Reducing Environments. *Materials Letters* **2013**, *98*, 205-208.

(70) Chen, X. B.; Liu, L.; Yu, P. Y.; Mao, S. S. Increasing Solar Absorption for Photocatalysis with Black Hydrogenated Titanium Dioxide Nanocrystals. *Science* **2011**, *331*, 746-750.

## Chapter 4. Enhancing the Electrochemical Performance of Li-rich Layered Oxide $\text{Li}_{1.13}\text{Ni}_{0.3}\text{Mn}_{0.57}\text{O}_2$ via $\text{WO}_3$ Doping and Surface Segregation

### 4.1. Introduction

Li- and Mn-rich layered oxides  $x\text{Li}(\text{Li}_{1/3}\text{Mn}_{2/3})\text{O}_2 \cdot (1-x)\text{LiMO}_2$  (that can alternatively be expressed as  $x\text{Li}_2\text{MnO}_3 \cdot (1-x)\text{LiMO}_2$ ) ( $0 < x < 1$ ;  $M = \text{Mn, Ni, Co}$ ) are promising candidates of next-generation cathode materials for lithium-ion batteries due to their high specific capacity of  $> 280 \text{ mAh g}^{-1}$ ; with an average discharge voltage of  $\sim 3.6 \text{ V}$ , this capacity corresponds to an energy density of  $> 1000 \text{ Wh kg}^{-1}$ .<sup>1-3</sup> The Li-rich layered oxides are also low cost and environmentally friendly due to the reducing of Co content in their composition. However, the practical applications of these layered oxides are still hindered by the irreversible capacity loss in the first cycle, the subsequent poor cycling stability, the low rate capability, and the voltage fading.<sup>4-6</sup>

It is interesting to note that all the above-mentioned challenging electrochemical properties can be highly affected by the surface properties of the Li-rich layered oxides. The significant irreversible capacity loss in the first cycle is believed to be resulted from formation of oxygen vacancies<sup>7,8</sup> and/or the occupation of lithium sites by transition metal ions on the surfaces (when the cathode is charged over  $4.4 \text{ V}$ )<sup>9</sup>, which subsequently triggers an irreversible surface phase transition from the layered structure to a spinel-like structure.<sup>1,9-11</sup> Moreover, the rate capability can also be explained by the above-mentioned surface structure/chemistry changes as the lithium diffusion path could be

partially blocked by the occupancy of lithium layer sites by transition metal cations.<sup>5,6,9,12</sup> Hence, surface modifications could be an effective way to improve electrochemical performance of Li-rich layered cathode materials.

Recently, Sathiya *et al.* reported that Ru(4d) substitution of  $M(3d)$  in  $\text{Li}_2\text{MO}_3$  in the bulk phase can significantly relieve the first-cycle irreversible capacity loss, voltage fade and cycling decay.<sup>13 14 15</sup> A density functional theory calculation suggested that a strong covalent character of the  $M$ -O bond would likely promote reversible high capacity of Li-rich layered oxides, which can be achieved by substituting  $M(3d)$  with  $M(4d, 5d)$  metal cations,<sup>16</sup> because  $M(4d, 5d)$ -O are stronger covalent bonds that enhance the structural stability of  $\text{Li}_2\text{MnO}_3$  and reduce voltage fade during cycling. However, the rate capability of  $M(4d, 5d)$  substituted Li-rich layered oxides are generally poor ( $< 50 \text{ mAh g}^{-1}$  at 5C) and these materials are more expensive due to the use of noble metals. Thus, simultaneous achieving high discharge capacity, stable voltage during cycling, and low cost remains a major challenge.

In this study, we used a small amount of  $\text{WO}_3$  (a 5d transition metal oxide) to “surface dope” a Li-rich layered oxide.  $\text{WO}_3$  is selected because it has a low surface free energy and tend to spread spontaneously (i.e., segregate or adsorb thermodynamically) on the surfaces of other oxides (such as  $\text{TiO}_2$  and  $\text{ZrO}_2$ ) during annealing, following a facile and cost-effective “mixing and annealing” procedure that is employed widely to make so-called “supported oxide catalysts” or “monolayer catalysts” in the petroleum and chemical industries.<sup>17-19</sup> As a result, these  $\text{WO}_3$  doped specimens exhibit improved rate capabilities (e.g.,

retaining a capacity of  $90 \text{ mAh g}^{-1}$  at a high discharge rate of 40C that represent a 200% improvement from the undoped specimens) and cycling stability as well as reduced voltage fading, in comparison with a undoped benchmark specimen prepared using the identical ball milling and annealing procedure. The improvements are attributed to surface segregation and disordering induced by as low as  $\sim 1 \text{ vol. \% WO}_3$  doping.

## 4.2. Experimental

### 4.2.1. Materials synthesis

The Li-rich prepared by coprecipitation method which is described in our previous publications.<sup>4,6</sup> To prepare 1 vol. %  $\text{WO}_3$  doped  $\text{Li}_{1.13}\text{Ni}_{0.3}\text{Mn}_{0.57}\text{O}_2$  (where the volume percentage was calculated based on the molar volumes before mixing and the overall chemical composition is  $0.4\text{Li}(\text{Li}_{1/3}\text{Mn}_{2/3})\text{O}_2 \cdot 0.6\text{LiMn}_{1/2}\text{Ni}_{1/2}\text{O}_2 \cdot 0.04\text{WO}_3$ ), an appropriate amount of  $(\text{NH}_4)_2\text{WO}_4$  (Alfa Aesar, 99.99 %) precursor (that decomposes to  $\text{WO}_3$  upon annealing) was added to 3 g of pristine  $\text{Li}_{1.13}\text{Ni}_{0.3}\text{Mn}_{0.57}\text{O}_2$  and dispersed in 4 ml of acetone. The mixture was placed in a silicon nitride grinding vial with two silicon nitride balls. High-energy ball milling was carried out using a SPEX 8000D mill for a duration of 10 min, followed by a 15-min resting interval; this milling process was repeated for 3 times. The mixture was dried in an oven isothermally at around  $70 \text{ }^\circ\text{C}$ . The dried powder was placed in a covered alumina crucible, isothermally annealed at  $800 \text{ }^\circ\text{C}$  for 4 h in a box furnace with a heating rate of  $5 \text{ }^\circ\text{C}/\text{min}$ ; subsequently, the specimens were furnace quenched. As a reference, a

controlled specimen of undoped  $\text{Li}_{1.13}\text{Ni}_{0.3}\text{Mn}_{0.57}\text{O}_2$  was prepared with the same ball milling and annealing procedure described above without the addition of the  $\text{WO}_3$  precursor.

#### 4.2.2. Material characterization

X-ray diffraction (XRD) was carried out on a Bruker D2 diffractometer using  $\text{Cu K}\alpha$  radiation ( $\lambda = 1.5418 \text{ \AA}$ ) operating at 40 kV and 40 mA with a step size of  $0.02^\circ$  and a step time of 1 s. Particle sizes and morphologies were characterized using a FEI XL30 scanning electron microscope (SEM).

The surface composition and depth profile of the  $\text{WO}_3$  doped  $\text{Li}_{1.13}\text{Ni}_{0.3}\text{Mn}_{0.57}\text{O}_2$  particles were characterized by X-ray photoelectron spectroscopy (XPS). XPS was carried out by using a Kratos AXIS ULTRA DLD XPS system equipped with an  $\text{Al K}\alpha$  monochromated X-ray source and a 165 mm mean radius electron energy hemispherical analyzer. 4 keV Ar ion beam was used for sputtering. The sample current was  $\sim 4 \mu\text{A}$ . Depth profile data were collected after sputtering time of 2 s, 5 s, 10 s, 30 s, and 90 s. The XPS characterization provided the overall surface composition and depth profiles that are averages of many different particles and crystalline facets. XPS was also carried out by using a Kratos Ultra DLD XPS. All XPS measurements were collected with a 300 mm  $\times$  700 mm spot size using a charge neutralizer during acquisition. Survey scans were collected with a 1.0 eV step size, and were followed by high resolution scans with a step size of 0.05 eV for Mn 3p, Ni 2p, and W 4d region. Bonding Energies were calibrated using C 1s peak of 284.6 eV.

Particle surfaces were characterized by high-resolution transmission electron microscopy (HRTEM) using a FEI Titan 80-300 microscope at 300 kV. HRTEM specimens were prepared by dispersing powders ultrasonically in acetone and dropping a small amount of the suspension onto carbon coated copper grids; the specimens were then dried overnight in a desiccator. Minimum exposure was used during HRTEM to reduce electron beam damage.

#### **4.2.3. Electrochemical measurement**

To prepare cathodes, 80 wt. % active materials, 15 wt. % carbon black (MTI), 5 wt. % PVDF (MTI), and an appropriate amount of NMP (Alfa Aesar, anhydrous, 99.5 %) were mixed in a glass vial by a vibrating mixer, followed by ultrasonic dispersion. The mixture was coated on an aluminum foil, which was subsequently dried in a vacuum oven at 90 °C for 6 h. Cathode electrodes with a diameter of 10 mm were punched out, pressed at ~187 MPa, and dried in a vacuum oven at 120 °C for 8 h before transferring into an Ar-filled glovebox for battery construction. The area density of dried electrode coating is ~2.5 mg cm<sup>-2</sup>. Half cells were made with a cathode electrode, a metal Li chip (MTI, 99.9 %) as the anode, 1M LiPF<sub>6</sub> in EC/DMC 1:1 vol. electrolyte LP 30, BASF), C480 separator (Celgard), and 2032 coin cell cases (SS304, MTI).

Electrochemical cycling tests were carried out on an Arbin 2143 tester. The rate performance of LiMn<sub>1.5</sub>Ni<sub>0.5</sub>O<sub>4</sub> specimens was tested at the discharge rates of C/20, C/10, C/2, 1C, 2C, 5C, 10C, 20C, 40C, 60C, 80C, 100C, and C/10 sequentially (1C equates to 250 mA h g<sup>-1</sup>; 1 cycle at each discharge rate) with a

constant charge rate of C/10 at room temperature. The cycling stability of  $\text{Li}_{1.13}\text{Ni}_{0.3}\text{Mn}_{0.57}\text{O}_2$  specimens were measured at a constant charge and discharge rate of 1C between 2.0 V and 4.8 V at room temperature. Electrochemical impedance spectroscopy (EIS) was performed using a Solartron 1287A/1255B analyzer measured from 1 MHz to 0.05 Hz at 10 mV. Cells after the testing were charged to 4.8 at C/10 and kept for 10 h for subsequent impedance measurements.

### 4.3. Results

No obvious difference of particle morphology between undoped and  $\text{WO}_3$  doped  $\text{Li}_{1.13}\text{Ni}_{0.3}\text{Mn}_{0.57}\text{O}_2$  was observed, as shown in Figure 4.1. Both specimens have similar agglomerated secondary particles (Figure 4.1(a) and (c)). The measured primary particle sizes are  $89.8 \pm 36.9$  nm for undoped specimen and  $88.2 \pm 30.5$  nm for  $\text{WO}_3$  doped specimen, respectively, and the representative SEM images are shown in Figure 4.1(b) and (d). The difference in the measured particle sizes is within the range of measurement errors and negligible.

Moreover, the primary particles of both undoped and doped specimens have similar round morphology without observed faceting. Hence, a fair comparison study of electrochemical performance between undoped and doped specimens can be conducted without significant effects of the particle size and morphology.

XRD results reveal only  $\text{Li}_{1.13}\text{Ni}_{0.3}\text{Mn}_{0.57}\text{O}_2$  peaks in both undoped and  $\text{WO}_3$  doped specimens, as shown in Figure S4.2. All peaks are indexed to the  $R\bar{3}m$  space group that corresponds to the  $\text{LiMO}_2$  structure, except for the

superstructure peaks between 20–30° which are associated with a honeycomb ordering of Li, Ni, and Mn in the TM layers.<sup>9</sup> The XRD patterns were refined by the Rietveld method. The lattice constants of the undoped  $\text{Li}_{1.13}\text{Ni}_{0.3}\text{Mn}_{0.57}\text{O}_2$  were obtained as:  $a = 2.8654(2)$  and  $c = 14.257(2)$  Å, while the  $\text{WO}_3$  doped  $\text{Li}_{1.13}\text{Ni}_{0.3}\text{Mn}_{0.57}\text{O}_2$  has lattice constants of  $a = 2.8667(2)$  Å and  $c = 14.262(2)$  Å. The slight increases in the lattice parameters of the  $\text{WO}_3$  doped specimen indicates the W is successfully doped into the Li-rich.

A comparison of Figure 4.3(a) and Figure 4.3(b) shows that the  $\text{WO}_3$  doped specimen has a higher initial discharge capacity tested at C/20 and room temperature. On one hand, the first-cycle charge and discharge capacities for the undoped specimen are 363 and 251 mAh g<sup>-1</sup>, respectively, with a coulombic efficiency of 69%, which are consistent with the typical values reported in prior studies.<sup>10,20,21</sup> On the other hand, the  $\text{WO}_3$  doped specimen has charge and discharge capacities of 350 and 284 mAh g<sup>-1</sup>, respectively, with an improved coulombic efficiency of 81% (representing a 12% increase from that of the undoped specimen). Correspondingly, the reversible discharge capacity is increased by 33 mAh g<sup>-1</sup> or 13% with as low as 1 vol. %  $\text{WO}_3$  doping, in comparison with that of the undoped specimen.

The  $\text{WO}_3$  doping improves the rate capability significantly. With  $\text{WO}_3$  doping, the discharge capacity is increased from 164 to 198 mAh g<sup>-1</sup> (by ~21 %) at 5C, and from 30 to 90 mAh g<sup>-1</sup> (by ~200 %) at 40C on an average as shown in Figure 1(c). The cells after the rate performance test were characterized by electrochemical impedance spectroscopy (EIS) and the spectra are shown in

Figure. 4.3(d). The EIS results have revealed that the  $\text{WO}_3$  doped specimen has smaller total resistance than that of the undoped specimen. After  $\text{WO}_3$  doping, the charge transfer resistance decreases from  $66.6 \Omega$  to  $18.9 \Omega$ , while the surface film resistance in fact increases from  $3.5 \Omega$  to  $13.3 \Omega$ ; thus, the total resistance decreases from  $70.1 \Omega$  to  $32.2 \Omega$  by 54 % with  $\text{WO}_3$  doping.

The cycling stability is also enhanced by  $\text{WO}_3$  doping, as shown in Figure 4.4. The  $\text{WO}_3$  doped specimen maintains a discharge capacity of  $188 \text{ mAh g}^{-1}$  after 100 cycles at a relatively high charge and discharge rate of 1C, which is about 27 % higher than that of the undoped specimen (Figure 4.4(a)). This improved cycling stability is comparable with some of the best reported performance in literature.<sup>12,20</sup> Furthermore, the voltage fading is also mitigated significantly by minor  $\text{WO}_3$  doping, which is in Figure 4.4(b). Consequently, an energy density of  $\sim 664.6 \text{ Wh kg}^{-1}$  is achieved after 100 cycles at 1C, which represent an  $\sim 30$  % improvement from the undoped specimen (Figure 4.4(c)).

Figure 4.5 and Figure 4.6 shows XPS results of the undoped and doped specimens. XPS spectra were collected before ion sputtering and after sputtering for 2 s, 5 s, 10 s, 30 s and 90 s. The sputtering rate was calibrated to be about  $30 \text{ nm min}^{-1}$  using a  $\text{SiO}_2$  reference specimen sputtered at the same experimental condition.<sup>22</sup>

The observed  $\text{W } 4d_{5/2}$  peak before sputtering in Figure 4.5(a) suggests that most W cations at the surfaces are  $\text{W}^{5+}$  in doped  $\text{Li}_{1.13}\text{Ni}_{0.3}\text{Mn}_{0.57}\text{O}_2$  instead of the more stable  $\text{W}^{6+}$  in  $\text{WO}_3$ . The binding energies of the  $\text{W}^{6+}$ ,  $\text{W}^{5+}$ , and  $\text{W}^{4+}$  cations, respectively, correspond to are 248.2, 245.7 and 243.5 eV,

respectively;<sup>23</sup> the brown, blue, and green lines, respectively, are the fitted peaks for the  $W^{6+}$ ,  $W^{5+}$ , and  $W^{4+}$  cations, respectively. Specifically,  $W^{5+}$  has the highest atomic ratio of 73 %, in comparison with 16 % of  $W^{6+}$  and 11 % of  $W^{4+}$ .

Furthermore, the binding energy of W  $4f_{7/2}$  shifts from 35.1 eV to 35.3 eV after sputtering (Fig 4.5(b)),<sup>24</sup> which indicates that W valence increases with sputtering time; in other words,  $W^{6+}$  cations (representing the most stable valent of W in bulk phase like  $WO_3$ ) likely dominate in the bulk phase, while  $W^{5+}$  cations could dominate at the surfaces. In summary, the majority W cations are reduced from  $W^{6+}$  (in the bulk phase) to  $W^{5+}$  at the surface.

For both undoped and doped specimens, the binding energy of Mn 3p peak before sputtering is ~49.7 eV, which shifted to ~48.2 eV after sputtering 90 s (Figures 4.6(a) and 4.6(c)); the decrease of binding energy with the sputtering time represents a decrease of Mn valence, which indicates an increase of  $Mn^{3+}$  concentration from surface to bulk, though  $Mn^{4+}$  still dominates in bulk.<sup>25,26</sup> Figure 4.6(b) and Figure 4.6(d) also show that the binding energy of Ni peaks do not change with sputtering time for both specimens.

XPS in conjunction with sputtering also shows the surface segregation (enrichment) of W (Figure 4.5(c)), while W is also present inside the bulk phase. Furthermore, the surface segregation of W leads to a decrease of Ni/Mn ratio on the surface; interestingly, the surface of the undoped specimen is enriched with Ni, whereas the surface of the  $WO_3$  doped specimen is enriched of Mn.

#### **4.4. Discussion**

Summarizing the results shown in Figure 4.5, we know that (1) Ni segregates at the surfaces in the undoped specimen; (2) W segregates at the surfaces with a surface reduction ( $W^{6+}$  in bulk vs. predominately  $W^{5+}$  at the surfaces), and (3) the surface segregation of W suppresses the surface segregation of Ni to increase the relative surface concentration of Mn. Furthermore, HRTEM images (Figure 4.7) show that the surfaces of  $WO_3$  doped specimen is more disordered than that of the undoped specimen.

Such a unique surface configuration in the  $WO_3$  doped  $Li_{1.13}Ni_{0.3}Mn_{0.57}O_2$ , which formed spontaneously (during annealing) as the equilibrium surface thermodynamic state and has its own distinct chemistry (composition and valence states; Figure 4.5) and structure (more disordered; Figure 4.7) that are markedly different from those of the underneath bulk phase, can be considered as a 2-D surface phase (or complexion<sup>27-29</sup>), akin to those nanoscale surface amorphous films (SAFs)<sup>30-33</sup> and other surface complexions<sup>34</sup> previously observed in various battery materials, which can also improve the rate capabilities<sup>30,31,33-35</sup> and cycling stabilities<sup>30</sup>. In contrast to the prior cases of phosphate-based, nanometer-thick SAFs that are discrete in HRTEM, the 2-D surface phase observed in the  $WO_3$  doped  $Li_{1.13}Ni_{0.3}Mn_{0.57}O_2$  appears to have more gradually-varying profiles of composition and structures (Figure. 4.5 and 4.7). Nonetheless, this the 2-D surface phase observed in the  $WO_3$  doped  $Li_{1.13}Ni_{0.3}Mn_{0.57}O_2$  in this study can also contribute to improved rate capability and cycling stability as well as reduced charge transfer and voltage fading (similar to

other types of 2-D surface phases<sup>30,31,33-35</sup>). Specifically, several possible benefits of this 2-D surface can be discussed.

In the first charge, the region below ~4.4 V is usually attributed to a reversible  $\text{Ni}^{2+}/\text{Ni}^{4+}$  oxidation, corresponding to the lithium extraction from the lithium layer.<sup>5</sup> The plateau above 4.4 V is attributed to a partially reversible anionic  $\text{O}^{2-}/\text{O}^{2-x}$  and irreversible oxygen loss, corresponding to the lithium extraction from the lithium layer and transition metal layer with oxygen vacancy formation, which will inevitably lead to the migration of transition metal cations from the transition metal layer to the lithium layer.<sup>3,12,36</sup> Consequently, there is always a high irreversible capacity observed in the first cycle of Li-rich. A prior study showed that in the  $\text{Li}_2\text{Ru}_x\text{Mn}_{1-x}\text{O}_3$  with Ru partial substitution of Mn, a  $\text{Ru}^{5+}/\text{Ru}^{4+}$  redox was accompanied by the  $\text{O}^{2-}/\text{O}^-$  redox processes.<sup>15</sup> It is also suggested that  $M(4d, 5d)\text{-O}$  bonds are stronger than those of  $M(3d)\text{-O}$  and can enhance the M-O covalency and structural stability of  $\text{Li}_2\text{MO}_3$ .<sup>16</sup> Likewise, W doping in  $\text{Li}_{1.13}\text{Ni}_{0.3}\text{Mn}_{0.57}\text{O}_2$  phase (as well as on its surface with an enhanced effect due to segregation) may also have similar stabilization effects as those of Ru. Specifically, W has a higher formation enthalpy of W-O (~598 – 632 kJ mol<sup>-1</sup>) than that of Mn-O (~402 kJ mol<sup>-1</sup>) and Ni-O (391.6 kJ mol<sup>-1</sup>), which may strengthen the M-O covalency and reduce oxygen release from breaking M-O bonds (via promoting reversible  $\text{M-O}^{2-}/\text{M-O}^{2-x}$  redox instead of oxygen loss from lattice structure).<sup>13</sup> In this work, the first cycle irreversible capacity of Li-rich is significantly reduced from 112 mAh g<sup>-1</sup> to 66 mAh g<sup>-1</sup> by W doping. At the same time, the reversible discharge capacity of W doped specimen shows 33 mAh g<sup>-1</sup>

enhancement than the undoped specimen. All these facts indicate that the W doping suppresses the irreversible oxygen loss and facilitates the reversible  $O^{2-}/O^-$  redox processes, which helps to maintain the structural stability of Li-rich and further improve the cycling performance.

The low oxidation state cation ( $Ni^{2+}$ ) migration to the lithium layer blocks the lithium diffusion during electrochemical charge and discharge, which leads to poor rate capability. The existence of oxygen vacancy facilitates this cation migration.<sup>7</sup> In this work,  $WO_3$  doping and surface segregation not only mitigates the oxygen vacancy formation, but also decreases the Ni content at the surface. As a consequence, the transition metal migration is suppressed, results in an improved rate performance of Li-rich.<sup>3</sup>

#### **4.5. Conclusions**

Minor 1 vol. %  $WO_3$  doping can simultaneously enhance the reversible capacity in the first cycle, the rate capability, and the cycling stability, as well as reduce voltage fading, of the  $Li_{1.13}Ni_{0.3}Mn_{0.57}O_2$  cathode material. XPS (with depth profiling) and HRTEM characterizations showed that W segregates at the particle surfaces, occurring concurrently with a surface reduction of W, a change of surface Ni/Mn ratio, and surface structural disordering. Consequently, a stable surface structure forms, which can be considered as a spontaneously-formed 2-D surface phase, which benefits both cycling stability and rate capability. It is further suggested that the stronger covalent character of the W-O bond could alleviate oxygen loss on the surface and the migration of the transition metal

cations. This work provides a new strategy of improving the performance of Li-rich layered oxide cathode materials significantly via a facile and cost-effective “mixing and annealing” procedure for uses in the next generation lithium-ion batteries with high energy densities.

**Chapter 4**, in part, is a reprint of the manuscript “Enhancing the Electrochemical Performance of Li-rich Layered Oxide  $\text{Li}_{1.13}\text{Ni}_{0.3}\text{Mn}_{0.57}\text{O}_2$  via  $\text{WO}_3$  Doping and Surface Segregation” in preparation, Jiajia Huang, Haodong Liu, Tao Hu, Ying S. Meng and Jian Luo.  $\text{Li}_{1.13}\text{Ni}_{0.3}\text{Mn}_{0.57}\text{O}_2$  was synthesized by Dr. Haodong Liu. HRTEM observation was done by Dr. Tao Hu at University of California Los Angeles.

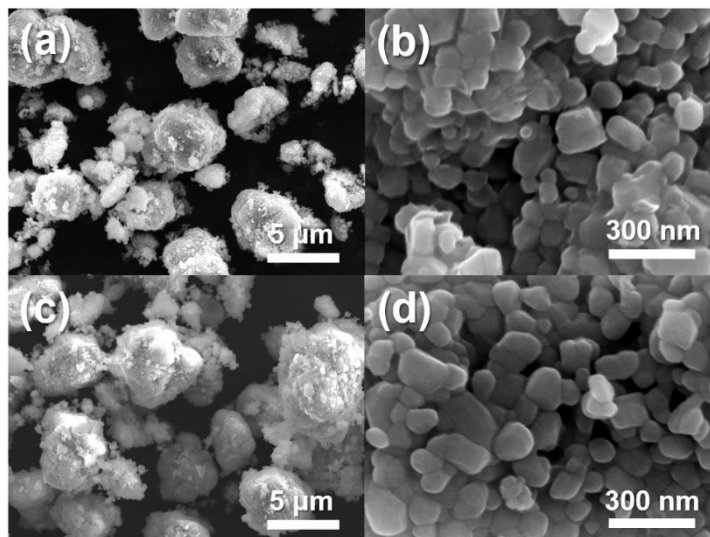


Figure 4.1 SEM micrographs of particle morphologies of (a, b) undoped and (c, d)  $\text{WO}_3$  doped  $\text{Li}_{1.13}\text{Ni}_{0.3}\text{Mn}_{0.57}\text{O}_2$ .

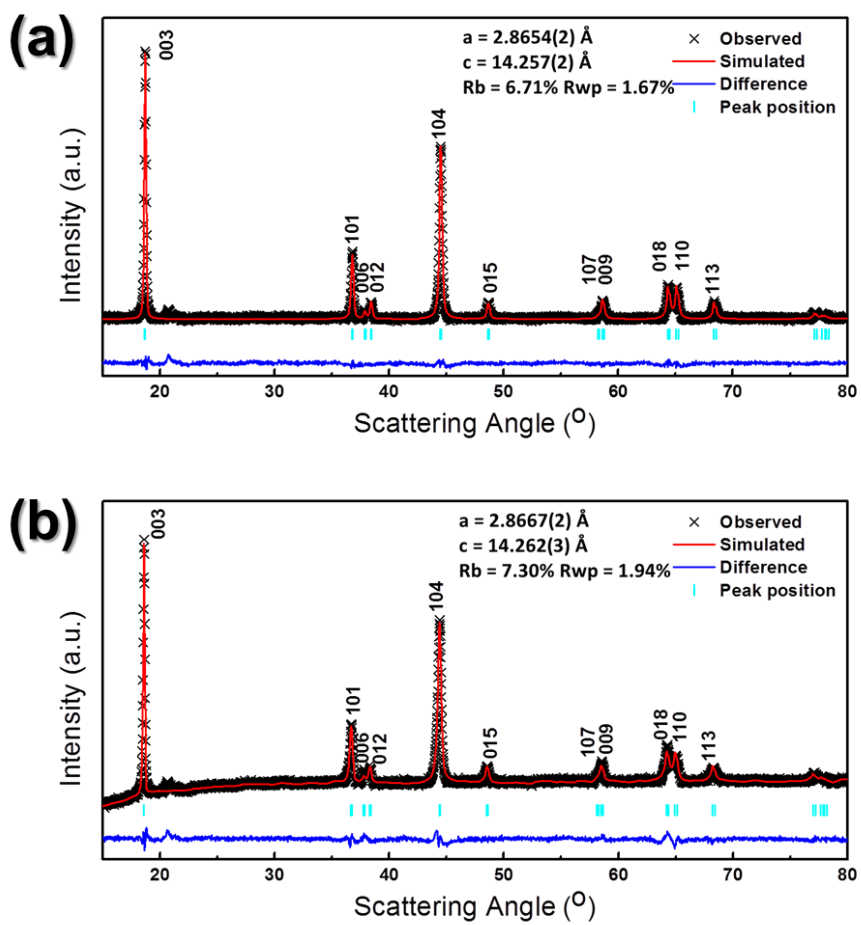


Figure 4.2 X-ray diffraction pattern of (a) undoped and (b)  $\text{WO}_3$  doped  $\text{Li}_{1.13}\text{Ni}_{0.3}\text{Mn}_{0.57}\text{O}_2$ .

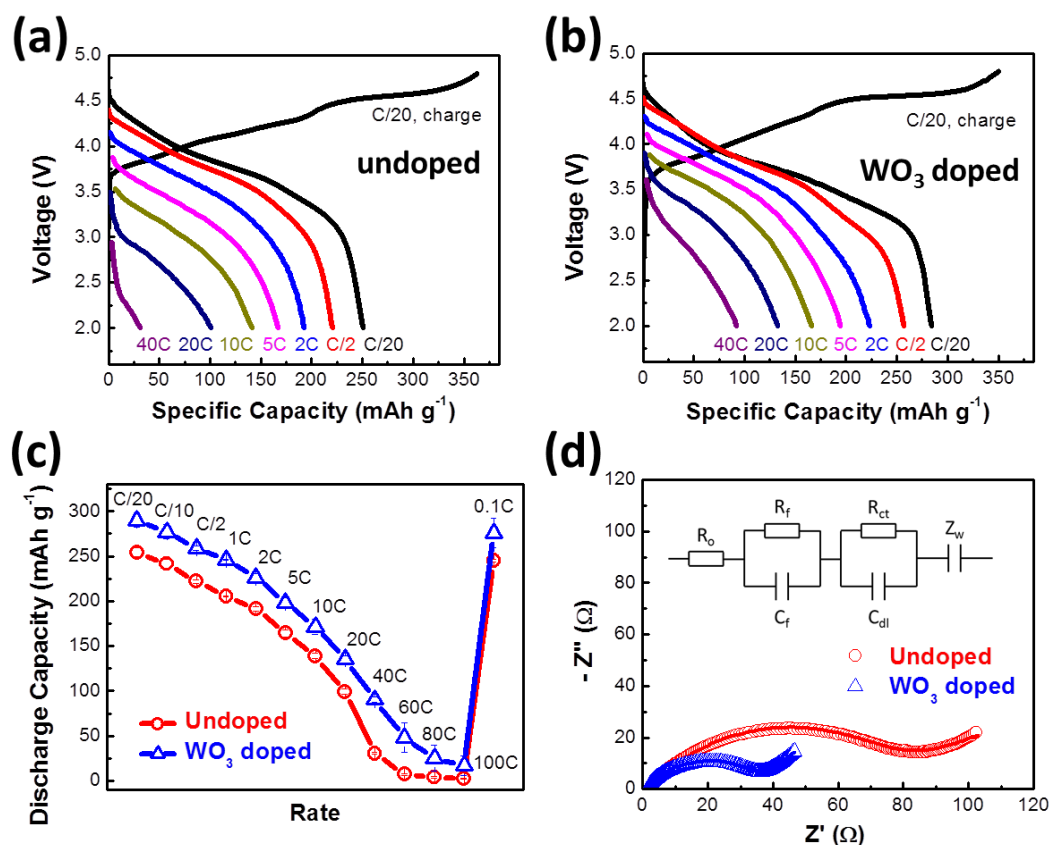


Figure 4.3 The rate performance of undoped and doped specimens. Charge/discharge curves of (a) undoped and (b)  $\text{WO}_3$  doped  $\text{Li}_{1.13}\text{Ni}_{0.3}\text{Mn}_{0.57}\text{O}_2$  at various rates. The black lines represent the initial charge/discharge curves tested at  $C/20$  ( $1C = 250 \text{ mAh g}^{-1}$ ) and color lines show subsequent discharge curves at various rates labeled in the graph (with a constant charge rate of  $C/5$ ). (c) Rate capabilities of undoped (red circles) and  $\text{WO}_3$  doped (blue triangles)  $\text{Li}_{1.13}\text{Ni}_{0.3}\text{Mn}_{0.57}\text{O}_2$ . Three coin cells were made and tested for each specimen. The means are presented and error bars represent  $\pm$  one standard deviations. (d) Electrochemical impedance spectra of undoped (red circles) and  $\text{WO}_3$  doped (blue triangles)  $\text{Li}_{1.13}\text{Ni}_{0.3}\text{Mn}_{0.57}\text{O}_2$ . The fittings were based on the equivalent circuit shown in the inset. All tests were performed at room temperature in a voltage window of 2.0 – 4.8 V

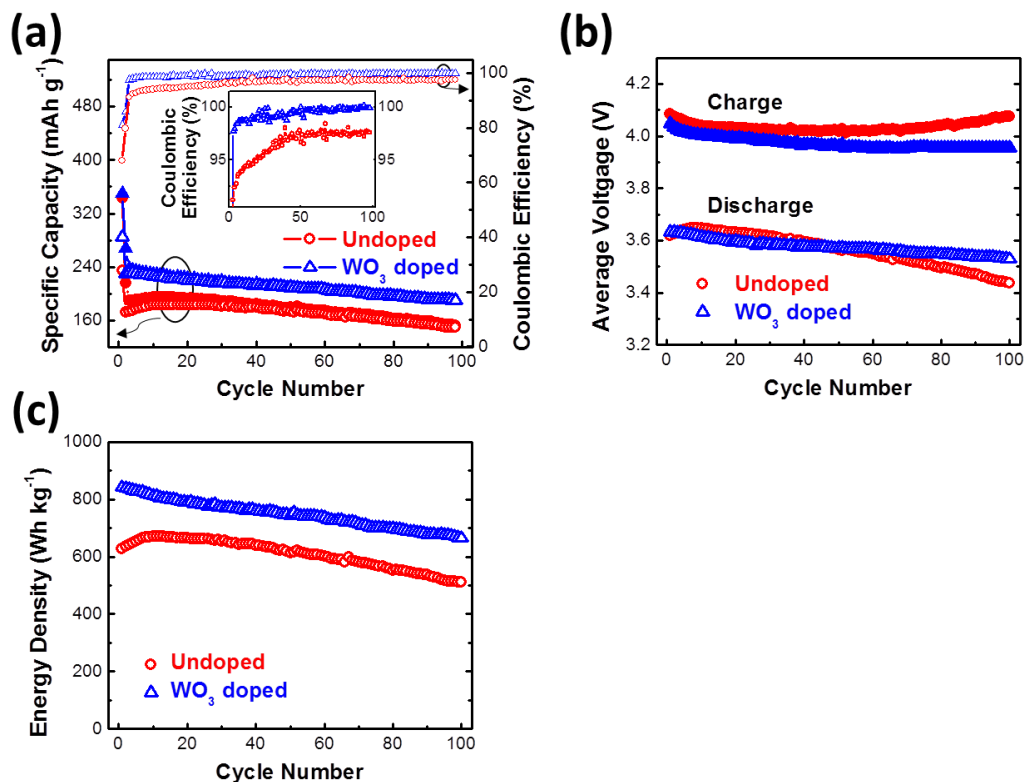


Figure 4.4 The cycling performances of undoped (red circles) and  $\text{WO}_3$  doped (blue triangles)  $\text{Li}_{1.13}\text{Ni}_{0.3}\text{Mn}_{0.57}\text{O}_2$  specimens, where the solid and hollow symbols represent charge and discharge performances, respectively. (a) The specific capacity vs. cycle number curves, where Coulombic efficiencies are also plotted using smaller symbols. Insert is the replotted Coulombic efficiency in a smaller range of 90% - 101%. (b) Average voltage fading and (c) energy density vs. cycle number curves. Both undoped and doped specimens were cycled at a charge/discharge rate of 1C at room temperature in the voltage window of 2.0 – 4.8 V.

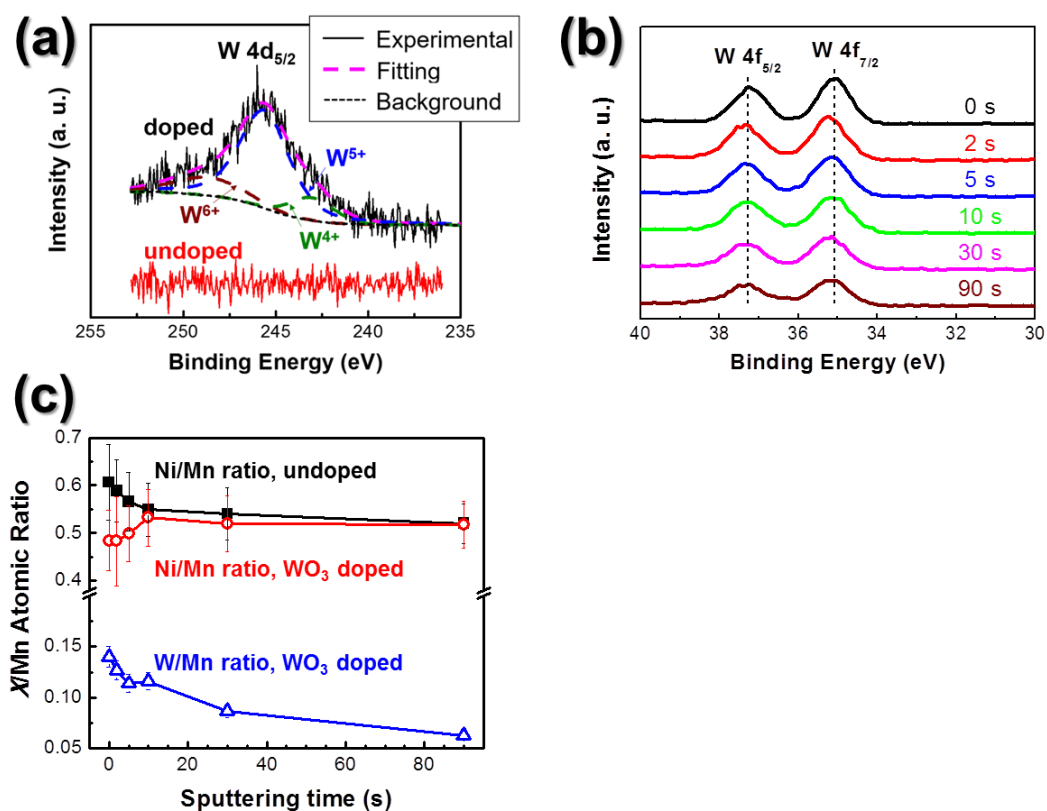


Figure 4.5 X-ray photoelectron spectrum of (a) W4d<sub>5/2</sub> before sputtering and (b) W 4f of doped specimen. (c) Ni/Mn and W/Mn atomic ratios vs. sputtering time for undoped and WO<sub>3</sub> doped Li<sub>1.13</sub>Ni<sub>0.3</sub>Mn<sub>0.57</sub>O<sub>2</sub>.

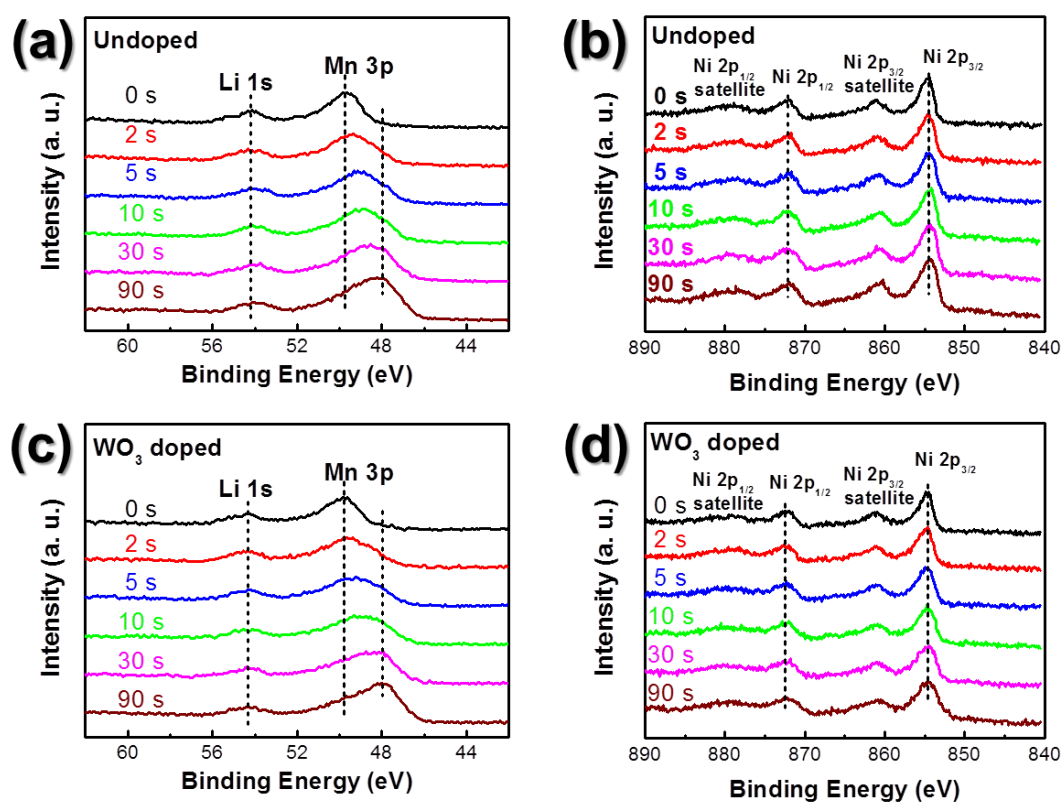


Figure 4.6 X-ray photoelectron spectrum of (a, b) undoped and (c, d) WO<sub>3</sub> doped Li<sub>1.13</sub>Ni<sub>0.3</sub>Mn<sub>0.57</sub>O<sub>2</sub>, where the binding energies represent (a, c) Mn 3p, (b, d) Ni 2p.

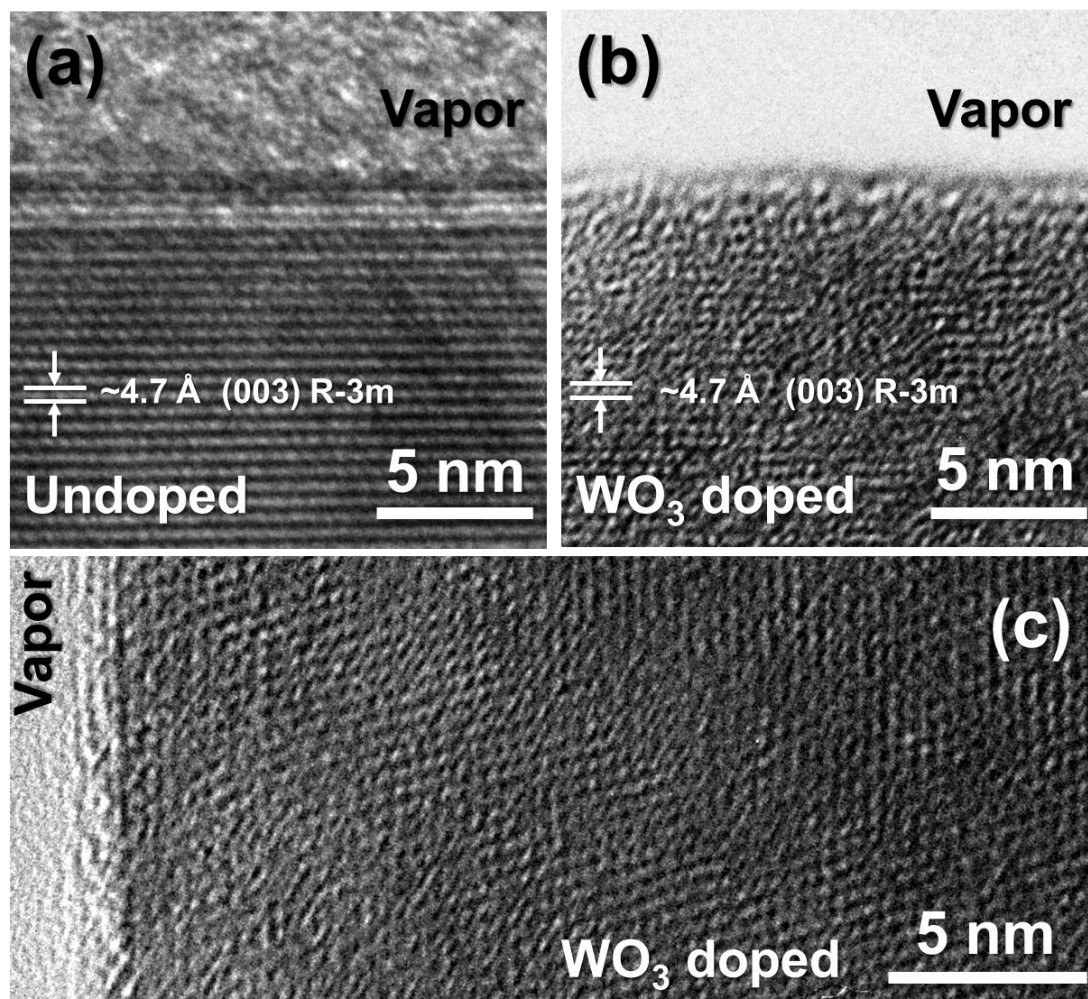


Figure 4.7 HRTEM images of (a) undoped and (b, c)  $\text{WO}_3$  doped  $\text{Li}_{1.13}\text{Ni}_{0.3}\text{Mn}_{0.57}\text{O}_2$ . Both undoped and doped specimens were fabricated via an identical procedure by ball milling and subsequently annealed at  $800 \text{ }^\circ\text{C}$  for 4 h. The “vapor” shown in the pictures means that the specimen was exposed in a vacuum environment during the observation. The region above specimen in Figure 4(a) was amorphous carbon on the grid since the sample was prepared on a copper grid with carbon film coating.

## References

- (1) Erickson, E. M.; Schipper, F.; Penki, T. R.; Shin, J.-Y.; Erk, C.; Chesneau, F.-F.; Markovsky, B.; Aurbach, D. Review—Recent Advances and Remaining Challenges for Lithium Ion Battery Cathodes: Ii. Lithium-Rich,  $\text{Li}_{2-x}\text{MnO}_3 \cdot (1-x)\text{LiNiCoMnO}_2$ . *Journal of the Electrochemical Society* **2017**, *164*, A6341-A6348.
- (2) Thackeray, M. M.; Kang, S.-H.; Johnson, C. S.; Vaughey, J. T.; Benedek, R.; Hackney, S. A.  $\text{Li}_2\text{MnO}_3$ -Stabilized  $\text{LiMO}_2$  (M = Mn, Ni, Co) Electrodes for Lithium-Ion Batteries. *Journal of Materials Chemistry* **2007**, *17*, 3112-3125.
- (3) Hy, S.; Liu, H. D.; Zhang, M. H.; Qian, D. N.; Hwang, B. J.; Meng, Y. S. Performance and Design Considerations for Lithium Excess Layered Oxide Positive Electrode Materials for Lithium Ion Batteries. *Energy & Environmental Science* **2016**, *9*, 1931-1954.
- (4) Verde, M. G.; Liu, H. D.; Carroll, K. J.; Baggetto, L.; Veith, G. M.; Meng, Y. S. Effect of Morphology and Manganese Valence on the Voltage Fade and Capacity Retention of  $\text{Li}[\text{Li}_{1/2}\text{Ni}_{1/2}\text{Mn}_{1/2}]\text{O}_2$ . *ACS Applied Materials & Interfaces* **2014**, *6*, 18868-18877.
- (5) Liu, H. D.; Chen, Y.; Hy, S.; An, K.; Venkatachalam, S.; Qian, D. N.; Zhang, M. H.; Meng, Y. S. Operando Lithium Dynamics in the Li-Rich Layered Oxide Cathode Material Via Neutron Diffraction. *Advanced Energy Materials* **2016**, *6*.
- (6) Liu, H. D.; Fell, C. R.; An, K.; Cai, L.; Meng, Y. S. In-Situ Neutron Diffraction Study of the  $\text{Li}_2\text{MnO}_3 \cdot (1-x)\text{LiMO}_2$  (X=0, 0.5; M = Ni, Mn, Co) Layered Oxide Compounds During Electrochemical Cycling. *Journal of Power Sources* **2013**, *240*, 772-778.
- (7) Qian, D.; Xu, B.; Chi, M.; Meng, Y. S. Uncovering the Roles of Oxygen Vacancies in Cation Migration in Lithium Excess Layered Oxides. *Physical Chemistry Chemical Physics* **2014**, *16*, 14665-14668.
- (8) Yan, P.; Xiao, L.; Zheng, J.; Zhou, Y.; He, Y.; Zu, X.; Mao, S. X.; Xiao, J.; Gao, F.; Zhang, J.-G.; Wang, C.-M. Probing the Degradation Mechanism of  $\text{Li}_2\text{MnO}_3$  Cathode for Li-Ion Batteries. *Chemistry of Materials* **2015**, *27*, 975-982.
- (9) Xu, B.; Fell, C. R.; Chi, M.; Meng, Y. S. Identifying Surface Structural Changes in Layered Li-Excess Nickel Manganese Oxides in High Voltage Lithium Ion Batteries: A Joint Experimental and Theoretical Study. *Energy & Environmental Science* **2011**, *4*, 2223-2233.
- (10) Armstrong, A. R.; Holzapfel, M.; Novák, P.; Johnson, C. S.; Kang, S.-H.; Thackeray, M. M.; Bruce, P. G. Demonstrating Oxygen Loss and Associated Structural Reorganization in the Lithium Battery Cathode  $\text{Li}[\text{Ni}_{0.2}\text{Li}_{0.2}\text{Mn}_{0.6}]\text{O}_2$ . *Journal of the American Chemical Society* **2006**, *128*, 8694-8698.

- (11) Boulineau, A.; Simonin, L.; Colin, J.-F.; Bourbon, C.; Patoux, S. First Evidence of Manganese–Nickel Segregation and Densification Upon Cycling in Li-Rich Layered Oxides for Lithium Batteries. *Nano Letters* **2013**, *13*, 3857-3863.
- (12) Yu, X.; Lyu, Y.; Gu, L.; Wu, H.; Bak, S.-M.; Zhou, Y.; Amine, K.; Ehrlich, S. N.; Li, H.; Nam, K.-W.; Yang, X.-Q. Understanding the Rate Capability of High-Energy-Density Li-Rich Layered  $\text{Li}_{1.2}\text{Ni}_{0.15}\text{Co}_{0.1}\text{Mn}_{0.55}\text{O}_2$  Cathode Materials. *Advanced Energy Materials* **2014**, *4*, 1300950.
- (13) Sathiya, M.; Rouse, G.; Ramesha, K.; Laisa, C. P.; Vezin, H.; Sougrati, M. T.; Doublet, M. L.; Foix, D.; Gonbeau, D.; Walker, W.; Prakash, A. S.; Ben Hassine, M.; Dupont, L.; Tarascon, J. M. Reversible Anionic Redox Chemistry in High-Capacity Layered-Oxide Electrodes. *Nat Mater* **2013**, *12*, 827-835.
- (14) Sathiya, M.; Abakumov, A. M.; Foix, D.; Rouse, G.; Ramesha, K.; Saubanère, M.; Doublet, M. L.; Vezin, H.; Laisa, C. P.; Prakash, A. S.; Gonbeau, D.; VanTendeloo, G.; Tarascon, J. M. Origin of Voltage Decay in High-Capacity Layered Oxide Electrodes. *Nat Mater* **2015**, *14*, 230-238.
- (15) Sathiya, M.; Ramesha, K.; Rouse, G.; Foix, D.; Gonbeau, D.; Prakash, A. S.; Doublet, M. L.; Hemalatha, K.; Tarascon, J. M. High Performance  $\text{Li}_2\text{Ru}_1 - \text{Ymnyo}_3$  ( $0.2 \leq Y \leq 0.8$ ) Cathode Materials for Rechargeable Lithium-Ion Batteries: Their Understanding. *Chemistry of Materials* **2013**, *25*, 1121-1131.
- (16) Xie, Y.; Saubanere, M.; Doublet, M. L. Requirements for Reversible Extra-Capacity in Li-Rich Layered Oxides for Li-Ion Batteries. *Energy & Environmental Science* **2017**, *10*, 266-274.
- (17) Luo, J.; Chiang, Y. M. Existence and Stability of Nanometer-Thick Disordered Films on Oxide Surfaces. *Acta Materialia* **2000**, *48*, 4501-4515.
- (18) Scheithauer, M.; Grasselli, R. K.; Knözinger, H. Genesis and Structure of  $\text{Wox}/\text{Zro}_2$  Solid Acid Catalysts. *Langmuir* **1998**, *14*, 3019-3029.
- (19) Tae Kwon, Y.; Yong Song, K.; In Lee, W.; Jin Choi, G.; Rag Do, Y. Photocatalytic Behavior of  $\text{Wo}_3$ -Loaded  $\text{Tio}_2$  in an Oxidation Reaction. *Journal of Catalysis* **2000**, *191*, 192-199.
- (20) Wang, D.; Belharouak, I.; Zhou, G.; Amine, K. Nanoarchitecture Multi-Structural Cathode Materials for High Capacity Lithium Batteries. *Advanced Functional Materials* **2013**, *23*, 1070-1075.
- (21) Manthiram, A.; Fu, Y.; Chung, S.-H.; Zu, C.; Su, Y.-S. Rechargeable Lithium–Sulfur Batteries. *Chemical Reviews* **2014**, *114*, 11751-11787.

(22) Liu, J.; Manthiram, A. Understanding the Improved Electrochemical Performances of Fe-Substituted 5 V Spinel Cathode  $\text{Li}_{1.5}\text{Ni}_{0.5}\text{O}_4$ . *The Journal of Physical Chemistry C* **2009**, *113*, 15073-15079.

(23) Romanyuk, A.; Steiner, R.; Marot, L.; Oelhafen, P. Temperature-Induced Metal–Semiconductor Transition in W-Doped  $\text{VO}_2$  Films Studied by Photoelectron Spectroscopy. *Solar Energy Materials and Solar Cells* **2007**, *91*, 1831-1835.

(24) Ho, S. F.; Contarini, S.; Rabalais, J. W. Ion-Beam-Induced Chemical Changes in the Oxyanions (Moyn-) and Oxides (Mox) Where M = Chromium, Molybdenum, Tungsten, Vanadium, Niobium and Tantalum. *The Journal of Physical Chemistry* **1987**, *91*, 4779-4788.

(25) Baggetto, L.; Dudney, N. J.; Veith, G. M. Surface Chemistry of Metal Oxide Coated Lithium Manganese Nickel Oxide Thin Film Cathodes Studied by Xps. *Electrochimica Acta* **2013**, *90*, 135-147.

(26) Liu, H.; Qian, D.; Verde, M. G.; Zhang, M.; Baggetto, L.; An, K.; Chen, Y.; Carroll, K. J.; Lau, D.; Chi, M.; Veith, G. M.; Meng, Y. S. Understanding the Role of  $\text{Ni}^{4f}$  and  $\text{Al}_2\text{O}_3$  Surface Co-Modification on Lithium-Excess Layered Oxide  $\text{Li}_{1.2}\text{Ni}_{0.2}\text{Mn}_{0.6}\text{O}_2$ . *ACS Applied Materials & Interfaces* **2015**, *7*, 19189-19200.

(27) Cantwell, P. R.; Tang, M.; Dillon, S. J.; Luo, J.; Rohrer, G. S.; Harmer, M. P. Overview No. 152: Grain Boundary Complexions. *Acta Materialia* **2014**, *62*, 1-48.

(28) Kaplan, W. D.; Chatain, D.; Wynblatt, P.; Carter, W. C. A Review of Wetting Versus Adsorption, Complexions, and Related Phenomena: The Rosetta Stone of Wetting *Journal of Materials Science* **2013**, *48*, 5681-5717.

(29) Luo, J. Interfacial Engineering of Solid Electrolytes. *Journal of Materiomics* **2015**, *1*, 22-32.

(30) Huang, J.; Luo, J. A Facile and Generic Method to Improve Cathode Materials for Lithium-Ion Batteries Via Utilizing Nanoscale Surface Amorphous Films of Self-Regulating Thickness. *Physical Chemistry Chemical Physics* **2014**, *16*, 7786-7798.

(31) Kayyar, A.; Qian, H. J.; Luo, J. Surface Adsorption and Disorder in  $\text{LiFePO}_4$  Based Battery Cathodes. *Applied Physics Letters* **2009**, *95*, 221905.

(32) Luo, J.; Chiang, Y.-M. Wetting and Prewetting on Ceramic Surfaces. *Annual Review of Materials Research* **2008**, *38*, 227-249.

(33) Kang, B.; Ceder, G. Battery Materials for Ultrafast Charging and Discharging. *Nature* **2009**, *458*, 190-193.

(34) Samiee, M.; Luo, J. A Facile Nitridation Method to Improve the Rate Capability of  $\text{TiO}_2$  for Lithium-Ion Batteries. *Journal of Power Sources* **2014**, *245*, 594-598.

(35) Liu, H.; Huang, J.; Qian, D.; Hy, S.; Fang, C.; Luo, J.; Meng, Y. S. Communication—Enhancing the Electrochemical Performance of Lithium-Excess Layered Oxide  $\text{Li}_{1.13}\text{Ni}_{0.3}\text{Mn}_{0.57}\text{O}_2$  Via a Facile Nanoscale Surface Modification. *Journal of The Electrochemical Society* **2016**, *163*, A971-A973.

(36) Mohanty, D.; Kalnaus, S.; Meisner, R. A.; Safat, A. S.; Li, J.; Payzant, E. A.; Rhodes, K.; Wood, I. I. I. D. L.; Daniel, C. Structural Transformation in a  $\text{Li}_{1.2}\text{Co}_{0.1}\text{Mn}_{0.55}\text{Ni}_{0.15}\text{O}_2$  Lithium-Ion Battery Cathode During High-Voltage Hold. *RSC Advances* **2013**, *3*, 7479-7485.

## Chapter 5. Low-cost Si Anode with Enhanced Cycling Performance via Sn Doping by High Energy Ball Milling and Post Annealing

### 5.1. Introduction

Si has the highest theoretical specific capacity of  $\sim 4000 \text{ mA h g}^{-1}$  among all anode materials (except Li metal), and a moderate working voltage  $\sim 0.4 \text{ V}$  for lithium-ion batteries.<sup>1</sup> However, volumetric expansion up to  $\sim 400 \%$  and anisotropic volumetric expansion of Si crystal during lithiation leads to poor cycling stability and poor conductivity of electrodes.<sup>2,3</sup> In addition, the unstable solid-electrolyte interface (SEI) can introduce serious Si loss and lead to a low coulombic efficiency.<sup>4</sup> Although cycling stability has been improved significantly by the design and synthesis of nanostructured Si materials, other issues raised in the nanostructured Si materials, such as low coulombic efficiency resulting from the irreversible by-reactions due to large surface area, limited rate capability, low energy density etc. Porous structures<sup>5</sup> with robust frames and core-shell<sup>6</sup> structures are promising ways to develop new generation Si anodes which can supply free space for volume expansion without direct contact with electrolytes. For example, a Si nanotube synthesized by sol-gel method combining with electrospinning and CVD can give a discharge capacity of  $600 \text{ mAh g}^{-1}$  at  $\sim 6\text{C}$  after 6000 cycles.<sup>7</sup> Porous Si nanowires fabricated by etching can give a discharge capacity of  $2000 \text{ mAh g}^{-1}$  at  $0.5\text{C}$  after 200 cycles.<sup>8</sup> A core-shell structured Si/C composite made from template had a discharge capacity of  $1110 \text{ mAh g}^{-1}$  at  $0.1\text{C}$  after 1000 cycles.<sup>6</sup> However, the nanotechnology methods were

limited by disadvantages of high cost and limited feasibility to develop scalable synthetic methods.

High-energy ball milling as a facile and low-cost method was reported to synthesize alloy anode materials for lithium ion batteries,<sup>9</sup> but the specific capacities of these alloys were generally much lower than those of nanostructured anode materials. Recently, a high-energy ball milled Si anode materials was reported, a capacity of 1170 mAh g<sup>-1</sup> at ~0.1C after 600 cycles was achieved, which was comparable to the nanostructured Si materials.<sup>10</sup> It was suggested that the reasons for the enhanced cycling stability were the formation of nanosized Si crystalline region ~10 nm and grain boundaries for fast lithium diffusion. Furthermore, a molecule dynamic calculation result of also suggested that the amorphous intergranular films based on V<sub>2</sub>O<sub>5</sub> crystal bulk could play a role of fast lithium ion diffusion path.<sup>11</sup> Actually, the amorphous intergranular films could be taken as 2-D material phases<sup>12-16</sup>, and can be utilized as a facile method to thermodynamically control and modify the surface/interface properties and significantly enhance electrochemical performances. Specifically, in this case the amorphous intergranular films could play a role of fast lithium ion diffusion channel, which can facilitate lithium ion reach the inside of the Si particle and promote the simultaneous lithiation/delithiation of the inner nanosized crystalline regions. Consequently, a uniform and isotropic volumetric change could be expected.

Furthermore, Si-Sn is a miscible system ( $\Delta H_{mix}^{liq}(0K) = 25.4kJ \cdot mol^{-1}$ ) which allows Sn to exist as a second phase. The solid solubility of Sn is  $6.9 \times 10^{-4}$

(750 °C) and  $1.6 \times 10^{-3}$  (1210 °C) in Si bulk;  $6.9 \times 10^{-2}$  (750 °C) and  $1.6 \times 10^{-1}$  (1210 °C) in grain boundary respectively. The Sn particles or crystalline region should exist independently and Sn (or Sn-rich) islet could be expected.

Herein, we use a facile method of high-energy ball milling to mix the as-received microsized Si with nanosized Sn particles followed by post annealing under Ar to form a porous secondary structure with the formation of intergranular films promoted by the existence of Sn, where an improved cycling stability could be achieved as anode materials for lithium ion batteries.

## 5.2. Experimental

### 5.2.1. Materials synthesis

As-received Si microsized powder (Alfa Aesar, 99.999 %, 325 mesh) and Sn nanosized powder (US Research Nanomaterials, 99.9%, 60 – 80 nm) was weighted and placed in a round-ended hardened steel grinding vial set (SPEX SamplePrep, hardness 5.5 – 6 Mohs) with two harden steel balls and sealed in a Ar-filled glovebox to prevent the powder from oxidation. High-energy ball milling was carried out using a SPEX 8000D mill for a duration of 1 h, followed by a 0.5 h resting interval; this milling process was repeated for 20 times. Four ball milled specimens were acquired:  $\text{Si}_{0.95}\text{Sn}_{0.05}$ ,  $\text{Si}_{0.90}\text{Sn}_{0.10}$ ,  $\text{Si}_{0.85}\text{Sn}_{0.15}$  and  $\text{Si}_{0.80}\text{Sn}_{0.20}$  with ball milling yield > 96 %. The ball milled powder was placed in an alumina tray, isothermally annealed at 750 °C for 20 h in a quartz tube with Ar flow and quenched by taking the tube out of furnace and keeping Ar flow. As a reference, Si powder was prepared with the same ball milling and annealing procedure

described above without adding Sn. Furthermore, the specimen of  $\text{Si}_{0.90}\text{Sn}_{0.10}$  was annealed at various temperature 131 - 850 °C for 20 h.

### **5.2.2. Material characterization**

X-ray diffraction (XRD) was carried out on a Bruker D2 diffractometer using  $\text{Cu K}\alpha$  radiation ( $\lambda = 1.5418 \text{ \AA}$ ) operating at 40 kV and 40 mA with a step size of  $0.02^\circ$  and a step time of 1 s. Particle sizes and morphologies were characterized using a FEI XL30 scanning electron microscope (SEM). The cross section of secondary particles and EDX mapping was acquired by FEI Scios Dual Beam FIB/SEM.

Particle surfaces were characterized by high-resolution transmission electron microscopy (HRTEM) using a FEI Titan 300 kV microscope. HRTEM specimens were prepared by dispersing powders ultrasonically in acetone and dropping a small amount of the suspension onto carbon coated copper grids; the specimens were then dried overnight in a desiccator. Minimum exposure was used during HRTEM to reduce electron beam damage. The lattice spacing was measured by the software DigitalMicrograph with FFT and inverse FFT transition of dm3 files. The measured spacing result was an average of 5 – 11 lattices.

### **5.2.3. Electrochemical measurement**

To prepare cathodes, 80 wt. % active materials, 15 wt. % carbon black (MTI), 5 wt. % CMC (Sigma-Aldrich,  $M_w = 90000$ ), and a buffer solution of citric acid and NaOH pH ~3 and appropriate amount of DI water were mixed in a glass vial with a zirconia ball by a vibrating mixer, followed by ultrasonic dispersion.

The final active materials on the electrode is 75 wt. %. The mixture was coated on a Cu foil, which was subsequently dried in a vacuum oven at 100 °C for 12 h. Then the anode electrodes were punched out with a diameter of 10 mm, and dried in the vacuum oven again at 120 °C for 8 h before transferring into an Ar-filled glovebox for battery construction. The area density of dried electrode coating is  $\sim 1 \text{ mg cm}^{-2}$ . Half cells were made with an anode electrode, a metal Li chip (MTI, 99.9 %) as the anode, 1M LiPF<sub>6</sub> in EC/DMC 1:1 vol. electrolyte (LP 30, BASF), C480 separator (Celgard), and 2032 coin cell cases (SS304, MTI).

Electrochemical cycling tests were carried out on an Arbin 2143 tester. The cycling performance of Si<sub>x</sub>Sn<sub>1-x</sub> specimens was tested at the charge and discharge rate of 1C (1C equates to 4200 mAh g<sup>-1</sup>) at room temperature between 0.005 V and 1.5 V at room temperature. The cyclic voltammetry (CV) was performed between 0.005 V and 1.2 V at a scan rate of 0.1 mV s<sup>-1</sup> using a Solartron 1287A/1255B analyzer.

### 5.3. Results

Particle morphologies of Si<sub>1-x</sub>Sn<sub>x</sub> (x = 0.05, 0.10, 0.15 and 0.20) are shown in Figure 5.1. Before annealing, the morphology was not influenced by the Sn molar fraction (Figure 5.1(a)-(d)). However, after annealing at 750 °C for 20 h, sphere particles appeared on the surface; and the diameter of the sphere particles increased from  $\sim 10^1$  to  $\sim 10^2$  nm with Sn increasing (Figure 5.1(e)-(h)).

Si and Sn peaks were observed in the XRD results (Figure 5.2(a) and (c)) since there is no compound between them based on the Si-Sn phase diagram.

Neither peaks of Silicon oxides or Tin oxides were found. The grain size of Si and Sn was calculated from XRD results (Figure 5.2(b) and (d)). Grain size of ball milled pure Si was ~20 nm without annealing; it increased to ~40 nm after annealing at 750 °C for 20 h. On the other side, Si grain size still maintained at ~20 nm in all specimens with Sn (Figure 5.1(b)). The Si grain size without Sn of the annealed specimen was about twice of Specimens with Sn. It demonstrated that the existence of Sn could inhibit Si grain growth (Figure 5.2(b)). In addition, Sn grain size of  $\text{Si}_{0.95}\text{Sn}_{0.05}$  and  $\text{Si}_{0.90}\text{Sn}_{0.10}$  was close ~30 nm, and increased to 100 and 120 nm by 3 and 4 times in  $\text{Si}_{0.85}\text{Sn}_{0.15}$  and  $\text{Si}_{0.80}\text{Sn}_{0.20}$ , respectively. Furthermore, the ball milled  $\text{Si}_{90}\text{Sn}_{10}$  specimen without annealing had a Si grain size of ~10 nm; it increased with the annealing temperature slightly to ~20 nm at 850 °C. Meanwhile, the Sn grain size also increased slightly from ~20 to ~30 nm with temperature increasing up to 750 °C, then increased rapidly to ~60 nm at 850 °C.

Cycling stability of specimens  $\text{Si}_{1-x}\text{Sn}_x$  ( $x = 0, 0.05, 0.10, 0.15$  and  $0.20$ ) after high energy ball milling and annealing at 750 °C for 20 h were tested at a charge and discharge rate of 1C and room temperature (Figure 5.3(a)). The specimen of pure Si and  $\text{Si}_{0.95}\text{Sn}_{0.05}$  died after 25 cycles and 114 cycles, respectively. The specimens of  $\text{Si}_{0.90}\text{Sn}_{0.10}$ ,  $\text{Si}_{0.85}\text{Sn}_{0.15}$  and  $\text{Si}_{0.80}\text{Sn}_{0.20}$  still have a discharge capacity of 431, 352 and 267 mAh  $\text{g}^{-1}$  after 200 cycles, respectively. The ball milled specimens of  $\text{Si}_{0.90}\text{Sn}_{0.10}$  annealed at various temperatures were also tested at the rate of 1C and room temperature (Figure 5.3(b)). The specimens without annealing and annealing at 650 °C died before 200 cycles.

The specimens annealing at 750 °C and 850 °C have a discharge capacity of 900 and 995 mAh g<sup>-1</sup> at 0.1C after 400 cycles, which is comparable to the performance of the materials synthesized by complex and expensive methods as reported.<sup>1</sup>

The cyclic voltammetry results were shown in Figure 5.4. In figure 5.4(a), peaks 1, 2 and 8 are related to Si lithiation and delithiation; peaks 3, 4, 5, 6 and 7 are related to Li interaction with Sn. It showed that Si<sub>0.90</sub>Sn<sub>0.10</sub> had the highest intensity of peak 1 and moderate intensity of peaks 3 – 7 comparing to Si<sub>0.95</sub>Sn<sub>0.05</sub> and Si<sub>0.85</sub>Sn<sub>0.15</sub>. It also can be found that the intensity of peak 1 was higher than peak 2 for Si<sub>0.90</sub>Sn<sub>0.10</sub>; but the intensity of peak 1 was lower than peak 2 for Si<sub>0.95</sub>Sn<sub>0.05</sub> and Si<sub>0.85</sub>Sn<sub>0.15</sub>. Furthermore, for specimen Si<sub>0.90</sub>Sn<sub>0.10</sub>, the intensity of peak 1 increased with annealing temperature from 650 to 750 °C as shown in Figure 5.4(b).

The cross section of specimen Si<sub>0.90</sub>Sn<sub>0.10</sub> without annealing or with annealing at 750 °C was characterized by FIB/SEM. For the specimen without annealing (Figure 5.5(a)-(c)), the cross section presented a porous structure with partial cold weld effect, the primary particles were partially “sintered” and form a relatively robust structure instead of a loose agglomerated secondary structure. The cross section of the annealed specimen also had a porous structure, though the porosity was obviously lower than that of specimen without annealing (Figure 5.5(d)-(f)). Furthermore, it is interesting that bright regions distributed on the cross section uniformly with a particle size on the order of 10<sup>1</sup> nm (Figure 5.5(f)).

Sn element was detected on the cross section of both specimens with or without annealing by EDX as shown in Figure 5.6. The atomic fraction of Si/Sn from EDX results was  $\sim 10/1$  for both specimens, which was close to the stoichiometry ratio 9/1.

Figure 5.7 showed the HRTEM results of specimen  $\text{Si}_{0.90}\text{Sn}_{0.10}$  without annealing and specimen annealing at 750 °C. The specimen without annealing had a  $\sim 10$  nm crystalline regions in the bulk phase (Figure 5.7(a)) which was similar to the reported structure.<sup>10</sup> After annealing (Figure 5.7(b)),  $\sim 20 - 30$  nm crystalline particles on the surface were observed with arising of amorphous intergranular films  $\sim 3 - 5$  nm between the surface particle and the bulk, as well as between the grains in the bulk. Specifically, the lattice spacing labeled with blue parallel lines is  $\sim 0.31 - 0.33$  nm coinciding with the d spacing of (111) of Si (PDF#4-012-0806). The lattice spacing labeled with red parallel lines is  $\sim 0.28 - 0.29$  nm corresponding to Sn (002) lattice spacing (PDF#04-0673). It is worth to note that the Sn islets were distributed around the surficial particle, and between the Si crystalline and intergranular films (IGFs).

#### 5.4. Discussion

It appears that a minimum Sn atomic fraction of  $\sim 0.1$  is required on the behalf of optimization of cycling stability (Figure 5.3(a)). The distinct difference of cycling stability can be seen between the specimens  $\text{Si}_{0.90}\text{Sn}_{0.10}$  and  $\text{Si}_{0.95}\text{Sn}_{0.05}$ . When  $x < 0.1$ , the cycling stability was poor; when  $x \geq 0.1$ , they had similar improved long cycling stabilities, but the discharge capacity decreased with

increasing of Sn molar fraction. The CV results imply that the optimized cycling stability of specimen with ~ 0.1 Sn atomic fraction could correlate to the increased intensity of peak 1. It appears that 0.1 atomic fraction Sn could enhance the Si and Li interaction at the potential of ~0.4 V. On the other side, excess amount of Sn over 0.1 decrease cycling stability. As shown in the CV results, the specimen  $\text{Si}_{0.85}\text{Sn}_{0.15}$  had a lower peak 1 but higher Sn peaks 3 – 7 than that of  $\text{Si}_{0.90}\text{Sn}_{0.10}$  (Figure 5.4(a)). Sn has higher oxidation potential ~0.4 and ~0.65 V than that of Si ~ 0.15 V. The lithiation of Sn was obviously enhanced with the increasing of Sn amount and decrease lithiation of Si, which implies that over amount of Sn might weaken the interaction of Li with Si, especially influences interaction at 0.4 V.

Beside the influence of Sn atomic ratio, the posting annealing can also significantly enhance cycling stability (Figure 5.3(b)). When annealing at 650 °C or without annealing, the cycling stability was poor; when annealing at 750 and 850 °C, better cycling stabilities can be achieved. The distinct difference of cycling stability can be seen between the specimens annealed at 650 and 750 °C. The intensity of peak 1 of 750 °C annealed specimen was larger than that of specimen annealed at 650 °C as shown in CV results(Figure 5.4(b)), which is coincident with the improved cycling stability. Hence, the intensity of peak 1 was correlated to the cycling stability based on the comparison of specimens annealed at different temperatures, and was consistent with the findings based on varying Sn molar fraction: higher peak 1 intensity corresponds to better cycling stability.

It is suggested that the peak 1 in CV results indicated the process of  $\text{Si} + x\text{Li} \rightarrow a\text{Li}_x\text{Si}$  which only exists in the nanosized Si materials and play a role of reducing anisotropic expansion. A larger intensity of peak 1 could imply less anisotropic expansion during lithiation. A proper amount of Sn might have synergetic effects during electrochemical process and play an important role on the structure stability of Si.

The porosity should not be the critical factor. Both specimens with or without annealing had second porous structure. Such structure can improve Si cycling stability by supplying free space for expansion without contact with electrolyte. However, it also brings a lithium diffusion problem. The lithiation of internal Si particles could not occur until the lithium ion diffuse into the inner bulk, which will induce large stress on the joint of outer and internal particles due to the ~400 % volumetric expansion during lithiation, and lead to pulverization of the second structure. Though the porosity of specimen without annealing was higher than that of annealed specimen which can give more free space for the expansion (Figure 5.5), it had worse cycling stability than that of annealed specimens (Figure 5.3(b)). The porous second structure could facilitate the free volumetric expansion, but cannot solve the cycling stability issue correlated to the anisotropic expansion.

The anisotropic expansion can also result in particle pulverization and electrode composite disconnection losing electron conduction. From the results shown in Figure 5.5 and 5.6, the bright regions in the cross section of annealed specimen could be the Sn or Sn-rich regions. The uniform distribution of

nanosized Sn among Si grains Sn are ductile and can tolerate partial deformation due to Si anisotropic expansion. Furthermore, the formation of amorphous intergranular films (Figure 5.7(b)) close to the surface region can play a role of fast lithium paths, allowing the lithium ion diffuse into Si nanosized grains from all directions. It is also proposed that the nanosized Sn or Sn-rich islets in the bulk might promote the formation of IGFs upon post annealing and rapid quenching. Observation of more different locations is necessary for a statistic results in the future work to prove this speculation.

In addition, the lithiation potential difference of Si and Sn could raise a synergetic effect which would benefit the cycling stability too. All of the speculations can be proved by characterization of cycled specimens in the follow-up work. The cycling stability could be enhanced further by combining improved electrolyte which will benefit a stable SEI.

## 5.5. Conclusions

The cycling stability of Si anode was improved obviously by Sn doping and post annealing. It was found that  $\text{Si}_{0.90}\text{Sn}_{0.10}$  showed the best cycling stability among  $\text{Si}_{1-x}\text{Sn}_x$  ( $x = 0, 0.05, 0.10, 0.15$  and  $0.20$ ). After handled by high energy ball milling and post annealing at  $850\text{ }^\circ\text{C}$ , the discharge capacity of  $\text{Si}_{0.90}\text{Sn}_{0.10}$  was achieved  $995\text{ mAh g}^{-1}$  at  $0.1\text{C}$  after 400 cycles. The cross section of the second Si particles showed a porous structure with the Sn distributed on the section after post annealing. The Sn doping can promote the formation of amorphous intergranular films. The coexistence of porous second structure and

the amorphous intergranular films was suggested as the reason of benefiting the cycling stability by alleviating stress introduced by volumetric expansion and anisotropic expansion. The high-energy ball milling and post annealing as well as Sn doping is a low-cost method and easy to realize industry scale-up.

**Chapter 5**, in part, is a reprint of the manuscript “Intergranular Films and Secondary Structures on Cycling Stability of  $\text{Si}_{1-x}\text{Sn}_x$  Anode for Lithium Ion Batteries” in preparation, Jijia Huang, Bing Jiang, Tao Hu, J. Luo. Part of specimens were prepared by Dr. Bing Jiang. HRTEM images were taken by Dr. Tao Hu.

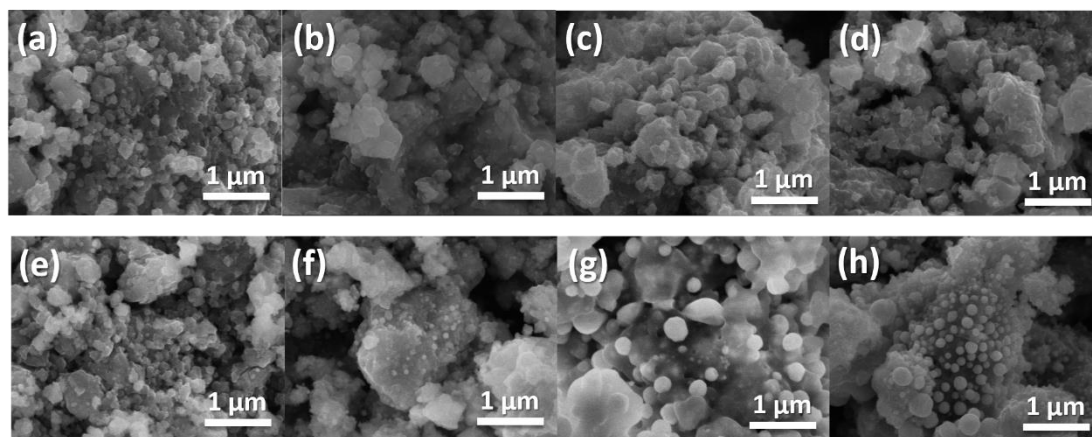


Figure 5.1 The particle morphology of  $\text{Si}_{1-x}\text{Sn}_x$  with  $x$  of (a) (e) 0.05, (b) (f) 0.10, (c) (g) 0.15 and (d) (h) 0.20. Specifically, (a), (b), (c), and (c) is for ball milled specimens without annealing and (e), (f), (g), and (h) for with annealing at 750 °C for 20 h, respectively.

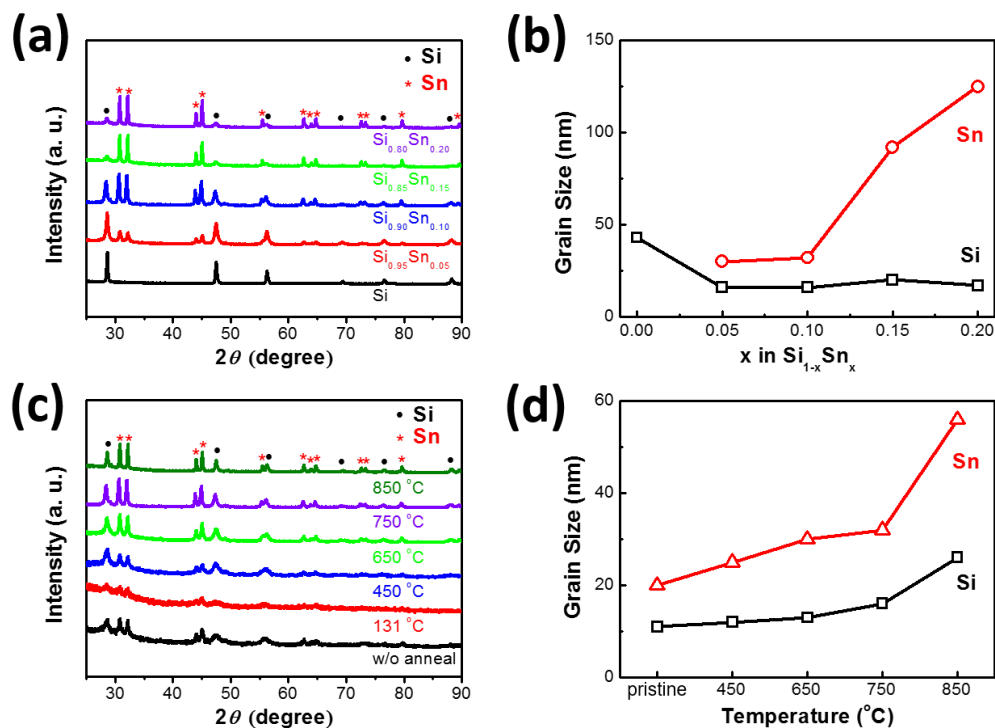


Figure 5.2 (a) X-ray diffraction pattern of high-energy ball milled  $\text{Si}_{1-x}\text{Sn}_x$  without annealing, with  $x$  of 0, 0.05, 0.10, 0.15, and 0.20. (b) calculated particle size of Si and Sn from XRD results in (a). (c) X-ray diffraction pattern of high-energy ball milled  $\text{Si}_{0.90}\text{Sn}_{0.10}$  annealed at 131, 450, 650, 750 and 850 °C for 20 h, respectively. (d) Calculated particle size of Si and Sn from XRD results in (c).

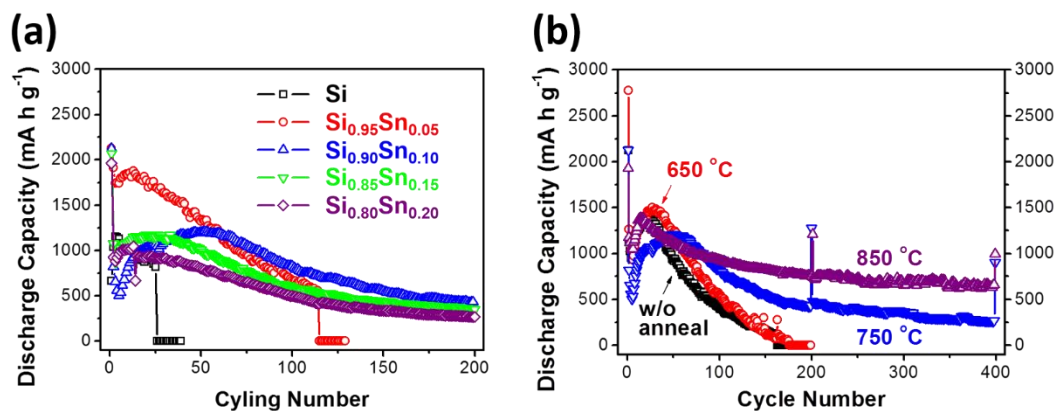


Figure 5.3 The cycling performance of (a) Si<sub>1-x</sub>Sn<sub>x</sub> after high energy ball milling 20 h with x of 0, 0.05, 0.10, 0.15, and 0.20. All specimens were annealed at 750 °C for 20 h; (b) high-energy ball milled Si<sub>0.90</sub>Sn<sub>0.10</sub> annealed at 650, 750 and 850 °C for 20 h. The high-energy ball milled specimen without annealing was also presented (black square) for comparison. The initial charge/discharge curves tested at C/10 (1C = 4200 mAh g<sup>-1</sup>) and then charged and discharged at 1C in the voltage window of 0.005 – 1.5 V at room temperature.

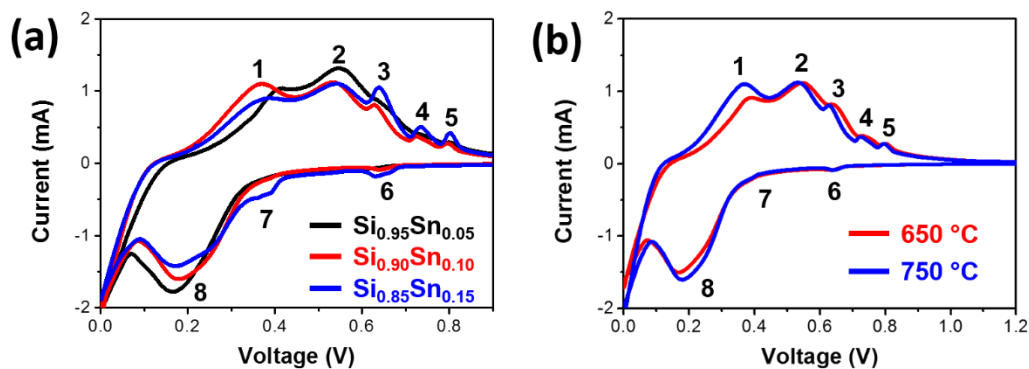


Figure 5.4 The cyclic voltammetry (CV) of (a) Si<sub>1-x</sub>Sn<sub>x</sub> after high energy ball milling 20 h with x of 0.05, 0.10, and 0.15. All specimens were annealed at 750 °C for 20 h; (b) high-energy ball milled Si<sub>0.90</sub>Sn<sub>0.10</sub> annealed at 650 and 750 °C for 20 h, respectively. The CV test was performed between 0.005 V and 1.2 V at a scan rate of 0.1 mV s<sup>-1</sup> at room temperature.

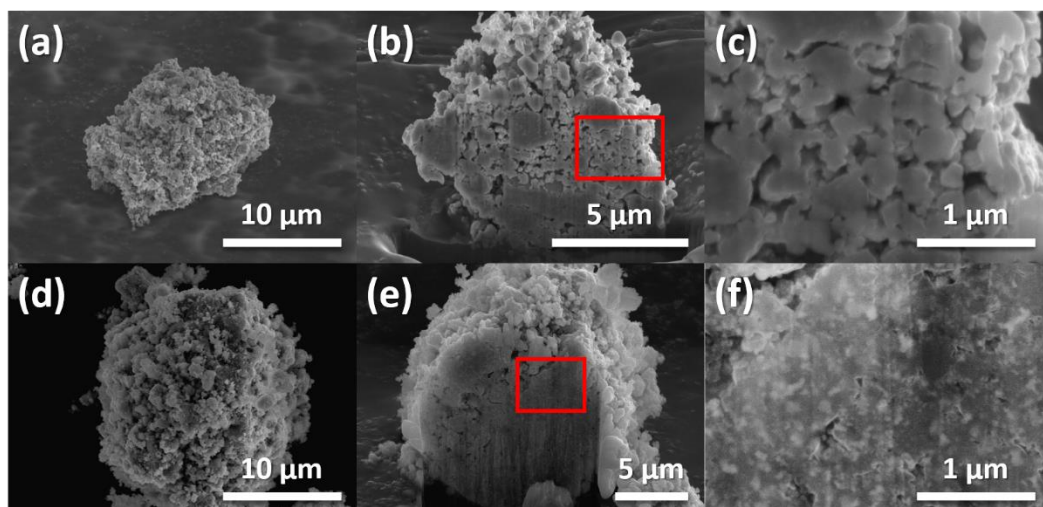


Figure 5.5 The secondary particle and cross section of high-energy ball milled  $\text{Si}_{0.90}\text{Sn}_{0.10}$  (a-c) without annealing and (d-f) annealed at  $750\text{ }^{\circ}\text{C}$  for 20 h.

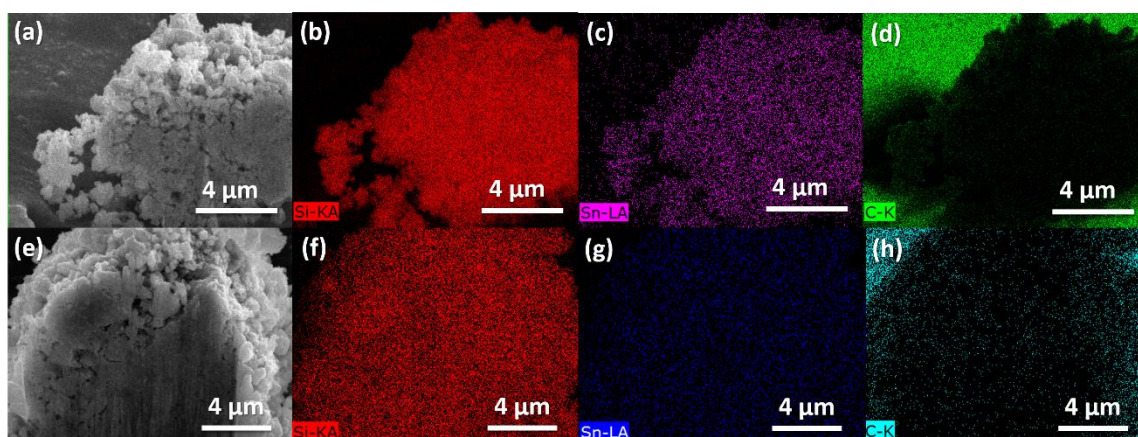


Figure 5.6 EDX of cross section of high-energy ball milled  $\text{Si}_{0.90}\text{Sn}_{0.10}$  (a-d) without annealing and (e-h) annealed at  $750\text{ }^{\circ}\text{C}$  for 20 h.

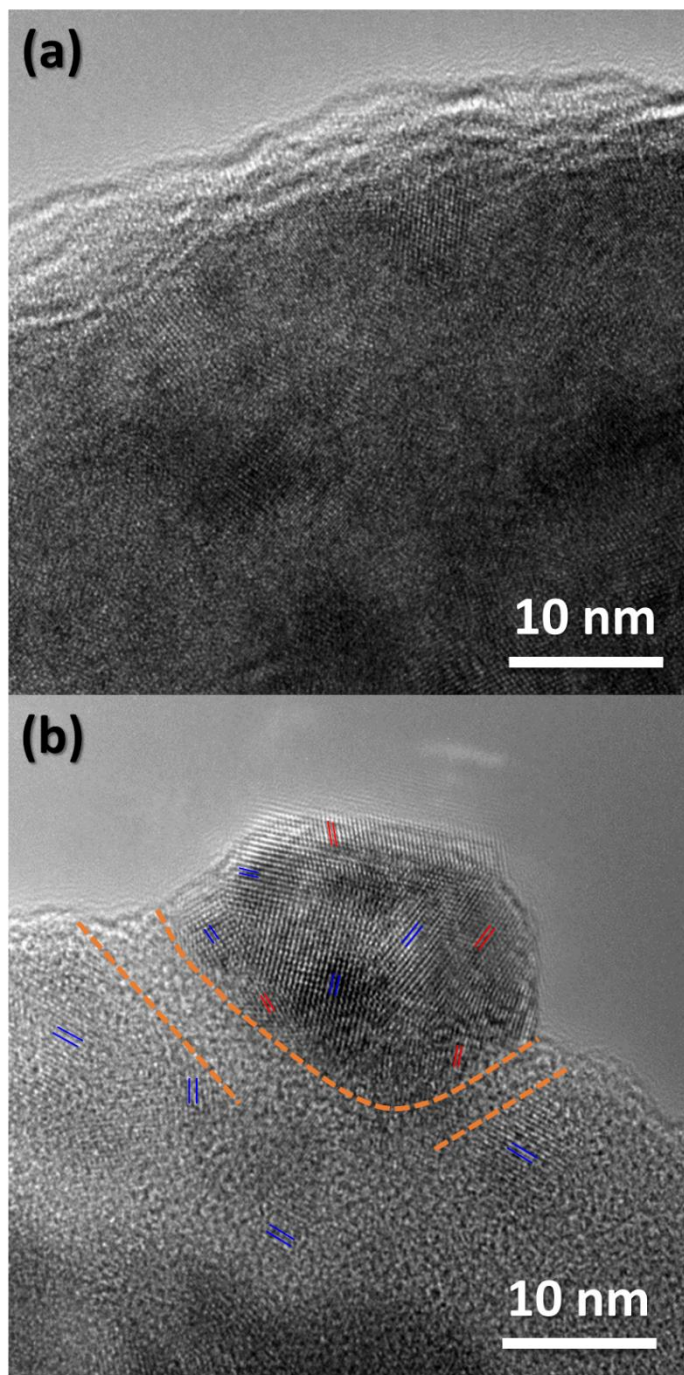


Figure 5.7 HRTEM images of (a) high-energy ball milled  $\text{Si}_{0.90}\text{Sn}_{0.10}$  without annealing and (b) annealed at  $750\text{ }^\circ\text{C}$  for 20 h.

## References

- (1) Zuo, X.; Zhu, J.; Müller-Buschbaum, P.; Cheng, Y.-J. Silicon Based Lithium-Ion Battery Anodes: A Chronicle Perspective Review. *Nano Energy* **2017**, *31*, 113-143.
- (2) Lee, S. W.; McDowell, M. T.; Choi, J. W.; Cui, Y. Anomalous Shape Changes of Silicon Nanopillars by Electrochemical Lithiation. *Nano Letters* **2011**, *11*, 3034-3039.
- (3) Liu, X. H.; Zhong, L.; Huang, S.; Mao, S. X.; Zhu, T.; Huang, J. Y. Size-Dependent Fracture of Silicon Nanoparticles During Lithiation. *ACS Nano* **2012**, *6*, 1522-1531.
- (4) Cho, J.-H.; Picraux, S. T. Silicon Nanowire Degradation and Stabilization During Lithium Cycling by Sei Layer Formation. *Nano Letters* **2014**, *14*, 3088-3095.
- (5) Ge, M.; Fang, X.; Rong, J.; Zhou, C. Review of Porous Silicon Preparation and Its Application for Lithium-Ion Battery Anodes. *Nanotechnology* **2013**, *24*, 422001.
- (6) Liu, N.; Wu, H.; McDowell, M. T.; Yao, Y.; Wang, C.; Cui, Y. A Yolk-Shell Design for Stabilized and Scalable Li-Ion Battery Alloy Anodes. *Nano Letters* **2012**, *12*, 3315-3321.
- (7) Wu, H.; Chan, G.; Choi, J. W.; Ryu, I.; Yao, Y.; McDowell, M. T.; Lee, S. W.; Jackson, A.; Yang, Y.; Hu, L.; Cui, Y. Stable Cycling of Double-Walled Silicon Nanotube Battery Anodes through Solid-Electrolyte Interphase Control. *Nat Nano* **2012**, *7*, 310-315.
- (8) Ge, M.; Rong, J.; Fang, X.; Zhou, C. Porous Doped Silicon Nanowires for Lithium Ion Battery Anode with Long Cycle Life. *Nano Letters* **2012**, *12*, 2318-2323.
- (9) Zhang, W.-J. A Review of the Electrochemical Performance of Alloy Anodes for Lithium-Ion Batteries. *Journal of Power Sources* **2011**, *196*, 13-24.
- (10) Gauthier, M.; Mazouzi, D.; Reyter, D.; Lestriez, B.; Moreau, P.; Guyomard, D.; Roue, L. A Low-Cost and High Performance Ball-Milled Si-Based Negative Electrode for High-Energy Li-Ion Batteries. *Energy & Environmental Science* **2013**, *6*, 2145-2155.
- (11) Li, W.; Garofalini, S. H. Molecular Dynamics Simulations of Li Insertion in a Nanocrystalline  $V_2O_5$  Thin Film Cathode. *Journal of the Electrochemical Society* **2005**, *152*, A364-A369.
- (12) Huang, J.; Luo, J. A Facile and Generic Method to Improve Cathode Materials for Lithium-Ion Batteries Via Utilizing Nanoscale Surface Amorphous Films of Self-Regulating Thickness. *Physical Chemistry Chemical Physics* **2014**, *16*, 7786-7798.
- (13) Kayyar, A.; Qian, H. J.; Luo, J. Surface Adsorption and Disorder in  $LiFePO_4$  Based Battery Cathodes. *Applied Physics Letters* **2009**, *95*, 221905.

(14) Luo, J.; Chiang, Y.-M. Wetting and Prewetting on Ceramic Surfaces. *Annual Review of Materials Research* **2008**, *38*, 227-249.

(15) Kang, B.; Ceder, G. Battery Materials for Ultrafast Charging and Discharging. *Nature* **2009**, *458*, 190-193.

(16) Samiee, M.; Luo, J. A Facile Nitridation Method to Improve the Rate Capability of  $\text{TiO}_2$  for Lithium-Ion Batteries. *Journal of Power Sources* **2014**, *245*, 594-598.

## Chapter 6. Effects of Secondary Structure Morphology and Surface Nitridation on TiO<sub>2</sub> Anode Materials of Sodium-ion Batteries

### 6.1. Introduction

One of the most outstanding advantages of sodium-ion batteries is lower cost comparing to lithium-ion batteries. Nanostructured TiO<sub>2</sub> as an anode material for lithium-ion batteries have been well studied and is also taken as a promising anode material for sodium-ion batteries.<sup>1,2</sup> The electrochemical performance was improved significantly in recent reports. However, the nanostructure introduced a lot problems. Firstly, the low packing density and the use of large amount of carbon or other electron conductive auxiliary materials led to a low volumetric energy density. Secondly, most of synthesis methods were complex and expensive, hindering the low-cost advantage and scale-up.<sup>3</sup> A secondary structure with nanosized primary particles is expected to meet both of high performance and high volumetric energy density.<sup>4</sup> In addition, application of large amount of carbon source on the electrode to improve the electronic conductivity will inevitably lead to decrease of energy density.<sup>5,6</sup>

Nanocrystalline anatase TiO<sub>2</sub> is active for sodium ion intercalation.<sup>7</sup> But its low electronic conductivity results in the low rate performance. The nanosized particles also have large surface area leading to low cycling stability and low volumetric energy density. The secondary structure could benefit the cycling stability by decreasing surface area contacting directly with the electrolyte. However, reducing contact between active material and electrolyte and electron

conductive additives will decrease the rate performance. Fortunately, the surface nitridation is an effective way to compensate for the disadvantage of secondary structure reported for lithium ion batteries.<sup>8</sup> It was reported that the nitridation could promote the formation of surface amorphous films which can benefit ion conduction on the surface and improve the rate performance.<sup>9-11</sup>

In this work, a commercial anatase TiO<sub>2</sub> was modified by a facile and low-cost method of high energy ball milling followed by post annealing and nitridation to improve the electrochemical performance. Meanwhile, the energy density could be maintained at an acceptable level due to the existence of microsized secondary particles of high packing density.

## 6.2. Experimental

As-received TiO<sub>2</sub> powder (anatase, 99.5%, 30 nm, US Research Nanomaterials) was placed in a Si<sub>3</sub>N<sub>4</sub> vial set (SPEX SamplePrep) with two Si<sub>3</sub>N<sub>4</sub> balls and a proper amount of ethanol. The vial was sealed in a Ar-filled glovebox to prevent the powder from oxidation. High-energy ball milling was carried out using a SPEX 8000D mill for a duration of 10 min, followed by a 15-min resting interval; this milling process was repeated for 6 times. The mixture was dried in an oven isothermally at around 60 °C. The dried powder was placed in an alumina tray, isothermally annealed at 600, 700 or 800 °C for 10 h in a box furnace with a heating rate of 5 °C/min; subsequently, the specimens were furnace quenched. The nitridation was carried out by placing the powder that was high-energy ball milled and 600 °C annealed in an alumina tray in a quartz tube

furnace, with  $\text{NH}_3$  gas flow for 1 h at 600 °C. The nitridated specimen was quenched by taking the tube out of furnace and keeping the  $\text{NH}_3$  flow until the tube cooled to room temperature.

X-ray diffraction (XRD) was carried out on a Bruker D2 diffractometer using  $\text{Cu K}\alpha$  radiation ( $\lambda = 1.5418 \text{ \AA}$ ) operating at 40 kV and 40 mA with a step size of  $0.02^\circ$  and a step time of 1 s. Particle sizes and morphologies were characterized using a FEI XL30 scanning electron microscope (SEM). The cross section of secondary particles and EDX mapping was acquired by FEI Scios Dual Beam FIB/SEM.

To prepare cathodes, 80 wt. % active materials, 15 wt. % carbon black (MTI), 5 wt. % PVDF (MTI), and an appropriate amount of NMP (Alfa Aesar, anhydrous, 99.5 %) were mixed in a glass vial by a vibrating mixer, followed by ultrasonic dispersion. The mixture was coated on a copper foil, which was subsequently dried in a vacuum oven at 90 °C for 6 h. Anode electrodes with a diameter of 10 mm were punched out, pressed at  $\sim 187 \text{ MPa}$ , and dried in a vacuum oven at 120 °C for 8 h before transferring into an Ar-filled glovebox for battery construction. The area density of dried electrode coating is  $\sim 1.5 \text{ mg cm}^{-2}$ . Half cells were made with a cathode electrode, a metal Na chip (MTI, 99.9 %) as the reference electrode, 1M  $\text{NaPF}_6$  in PC electrolyte (), glass fiber (), and 2032 coin cell cases (SS304, MTI).

Electrochemical tests were carried out on an Arbin 2143 tester. The rate performance of  $\text{LiMn}_{1.5}\text{Ni}_{0.5}\text{O}_4$  specimens was tested at the charge and discharge rates of C/50, C/10, C/5, C/2, 1C, 2C, 5C, 10C, 20C, and C/50 sequentially (1C

equates to 336 mAh g<sup>-1</sup>; 1 - 3 cycles at each rate). The cycling stabilities were measured at a constant charge and discharge rate of C/50 for the first 10 cycles and then at 1C between 0.01 V and 2.5 V at room temperature.

### 6.3. Results

The as-received anatase TiO<sub>2</sub> had an irregular secondary agglomerated structure with a primary particle size of ~20 nm (Figure 6.1(a)(e)). It is interesting that the ball milled specimens following by annealing at various temperature showed a regular sphere-like secondary structure with primary particle size of ~30 nm (Figure 6.1(b)(f)), ~50 nm (Figure 6.1(c)(g)) and ~130 nm (Figure 6.1(d)(h)) annealed at 600, 700 and 800 °C, respectively. The secondary sphere-like particles have a particle size from 1 – 20 μm for all annealed specimens.

The XRD results shown in Figure 6.2 indicated that the main phase of as-received TiO<sub>2</sub> was anatase with minor amount of rutile phase. The peak intensity of rutile phase increased with increasing annealing temperature from 600 to 800 °C. No contamination was detected in all specimens from the XRD results. The phase percentage and particle size calculated from XRD fitting by the Jade software was shown in table 6.1. The rutile phase percentage was slightly increased after annealing at 600 °C and increased ~ 10 % annealing at 700 °C. The main phase changed from anatase to rutile (~97 %) when annealed at 800 °C for 10 h. Meanwhile, the particle size of anatase phase of ball milled and annealed at 600 °C was increased but still close to that of as-received specimen,

and was double after annealing at 700 °C comparing to as-received specimen, which was close to the results observed in SEM images.

Rate capabilities and cycling stabilities of the as-received, ball milled and followed by annealing at 600, 700 and 800 °C specimens were shown in Figure 6.3. As-received specimen and ball milled with 600 °C annealed specimen had similar charge capacity  $182 \pm 2 \text{ mAh g}^{-1}$  and  $185 \pm 1 \text{ mAh g}^{-1}$ , which was much higher than that of specimens 700 and 800 °C annealed  $112 \pm 5 \text{ mAh g}^{-1}$  and  $81 \pm 6 \text{ mAh g}^{-1}$  at low rate of 0.02C (Figure 6.3(a)). Comparing the rate performance of as-received specimen and the specimen ball milled with 600 °C annealing, the later had better rate performance; and the difference of charge capacity increased with increasing rate from 0.02C to 1C. The specimen ball milled with 600 °C annealing had a higher charge capacity of  $101 \pm 1 \text{ mAh g}^{-1}$  which was 1.5 times of as-received specimen at the rate of 1C. The rate performance of the specimens that ball milled followed by annealing at 700 and 800 °C were worse than the as-received specimen due to the low charge capacity. For the cycling stability, as-received specimen and ball milled with 600 °C annealing specimen had charge capacity of 91 and 58  $\text{mAh g}^{-1}$ , corresponding to a capacity retention of 81.5 % and 93.5 % after 100 cycles, respectively, tested at charge and discharge rate of 1C at room temperature.

The Figure 6.4(a) of ball milled  $\text{TiO}_2$  without post annealing showed the regular spherical secondary structure. However, the 600 °C annealed specimen without ball milling retained the irregular secondary structure from as-received specimen (Figure 6.4(b)). It is interesting that ball milled specimen without

annealing had lower charge capacity than that of as-received specimen as shown in Figure 6.5. After annealing at 700 °C for 10 h, the peak intensity of rutile phase increased in both specimens with or without ball milling; the specimen with ball milling had a higher intensity than the specimen without ball milling (Figure 6.6(b)). There was no obvious difference between specimens with or without ball milling annealed at 600 °C for 10 h (Figure 6.6(a)).

The specimen handled by ball milling and post annealing was nitrided at 600 °C 1 h. The morphology of the N-doped specimen was not changed (Figure 6.7). The primary particle size was similar with undoped specimen ~26 nm calculated from XRD results. The phase change from anatase to rutile was not observed neither (Figure 6.8). The charge capacity of N-doped specimen was  $192 \pm 2$  mAh g<sup>-1</sup> and  $117 \pm 1$  mAh g<sup>-1</sup> at rate of 0.02C and 1C, respectively. It had a charge capacity of 60 mAh g<sup>-1</sup> at high rate 10C, which comparable to some reported results which used a large amount of electron conductive additives. Both the initial charge capacity and rate performance were improved by N-doping.

#### **6.4. Discussion**

The phase transition from anatase to rutile led to the decrease of charge capacity at low tested rate since the anatase TiO<sub>2</sub> has a higher specific capacity than that of rutile phase. The phase transition was correlated to particle size due to the rutile phase had larger surface energy than that of anatase. High temperature post annealing resulted in an increase of primary particle size as

well as phase transition from anatase to rutile and decreased the electrochemical performance.

The rate capability of specimen was improved by post annealed at 600 °C after ball milling, comparing to the as-received specimen and the ball milled specimen without annealing (Figure 6.5). Neither phase composition or primary particle size changed obviously annealing at 600 °C. The reason of the improvement could be the morphology change of the secondary particle. The regular spherical secondary particle might lead to a uniform distribution and enhance the path of electron conduction, which is one of the most critical factors limiting the rate performance as well as the cycling stability of TiO<sub>2</sub> nanomaterials.

It is worth to note that though the secondary particle morphology of the ball milled specimen without post annealing was the same to the specimen ball milled with post annealing, the rate performance of the former was still worse than that of the as-received specimen. The high-energy ball milling process would inevitably introduce defects mainly on the surface of TiO<sub>2</sub> and create oxygen vacancy, thereby decreasing the activity of Ti<sup>4+</sup> on the surface of lithiation. The post annealing at proper temperature 600 °C can repair the surface since a slightly increase of primary particle size was observed, which implied a moderate atomic mobility on the nanoparticle surface at this temperature, without introducing a dramatic increase of primary particle size or phase change to rutile. Hence, the combination of high energy ball milling and post annealing at

moderate temperature promotes an increase of rate capability and cycling stability.

Furthermore, surface nitridation can improve the rate performance further without worsen cycling stability (Figure 6.9). The formation of surface amorphous film on the surface of  $\text{TiO}_2$  by nitridation was approve in an earlier report on anode material of lithium-ion batteries. The rate performance results indicated that the surface amorphous films on the surface formed by surface nitridation also benefits the rate performance of anatase  $\text{TiO}_2$  as an anode material for the sodium-ion batteries.

## 6.5. Conclusions

The rate performance and cycling stability of a commercial nanosized  $\text{TiO}_2$  with irregular secondary structure was improved as anode materials for sodium-ion batteries. Facile method of high energy ball milling following with annealing and surface nitridation was used to modify the structure features of pristine  $\text{TiO}_2$ . It was found that the irregular secondary structure was changed to a regular sphere-like morphology by high energy ball milling. After annealing at 600 °C, the primary particle size was maintained ~ 30 nm with improved rate capability of 101 mAh  $\text{g}^{-1}$  at 1C. The rate capability can be improved further by surface nitridation and reach 118 and 78 mAh  $\text{g}^{-1}$  at 1C and 5C, respectively. It was suggested that the nitrated nanosized  $\text{TiO}_2$  with regular spherical secondary structure morphology. In addition, existence of minor rutile phase appears not influence the electrochemical performance of the anatase  $\text{TiO}_2$ .

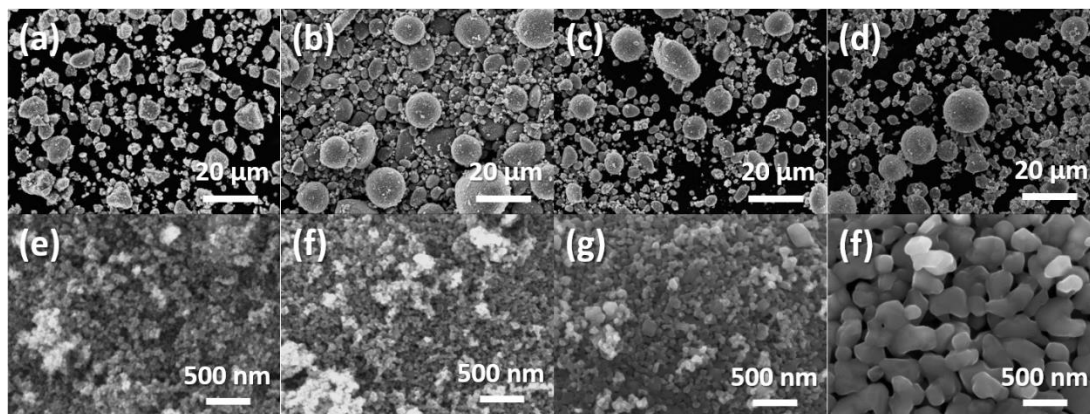


Figure 6.1 The particle morphology of four TiO<sub>2</sub> specimens: (a) and (e) as received; high-energy ball milled followed with annealing (b) and (f) at 600 °C, (c) and (g) at 700 °C, (d) and (h) at 800 °C, respectively.

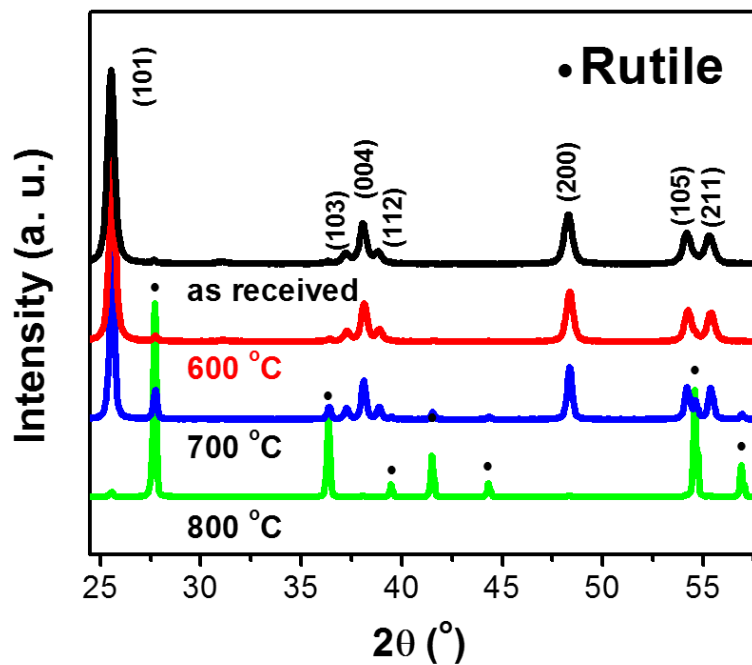


Figure 6.2 The X-ray diffraction results of as received specimen (black), and specimens high-energy ball milled following with annealed at 600 (red), 700 (blue) and 800 °C (green), respectively. The main phase was anatase with minor rutile phase labeled with black dots.

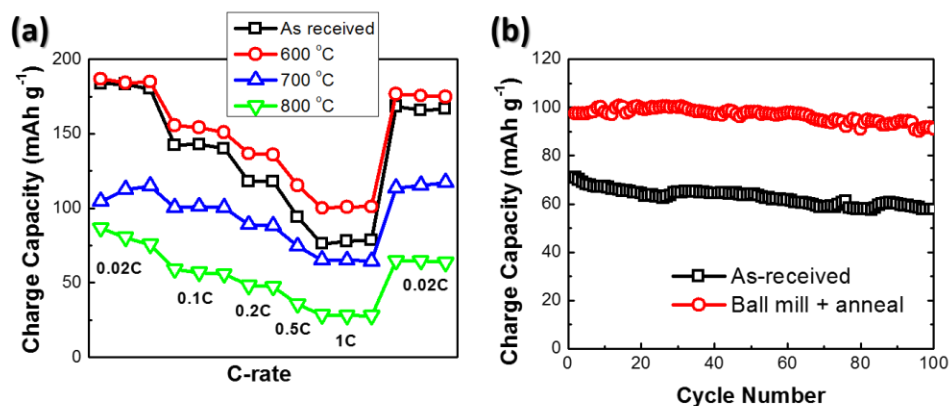


Figure 6.3 (a) Rate performance of  $\text{TiO}_2$  specimens as received (black square), and high-energy ball milled following with annealed at 600 (red circle), 700 (blue upper triangle) and 800 °C (green lower triangle), respectively. The specimens were charged and discharged at the rates of 0.02C, 0.1C, 0.2C, 0.5C, 1C and 0.02C, 0.1C, and 1C; 2 cycles for 0.2C and 1 cycle for 0.5C). (b) cycling stability of as-received (black square) and high-energy ball milled following with annealed at 600 °C (red circle) tested at charge and discharge rate of 1C and room temperature.

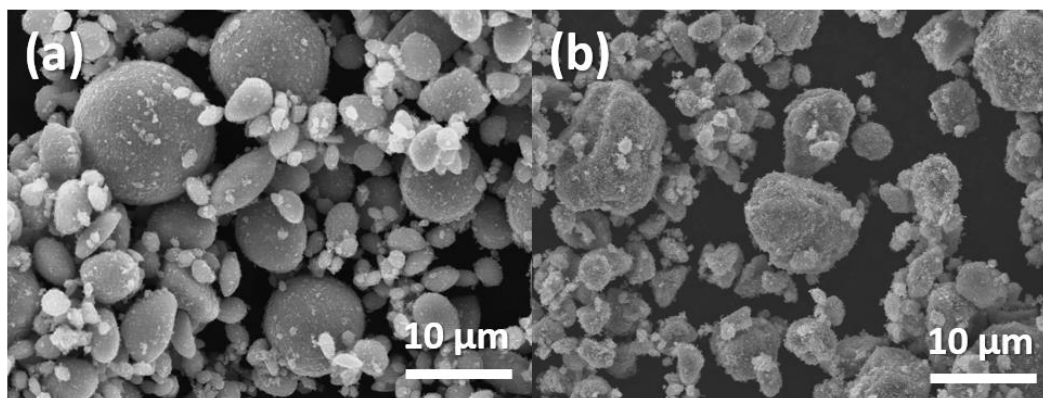


Figure 6.4 SEM images of  $\text{TiO}_2$  (a) after high-energy ball milling and (b) 600 °C annealing without high-energy ball milling.

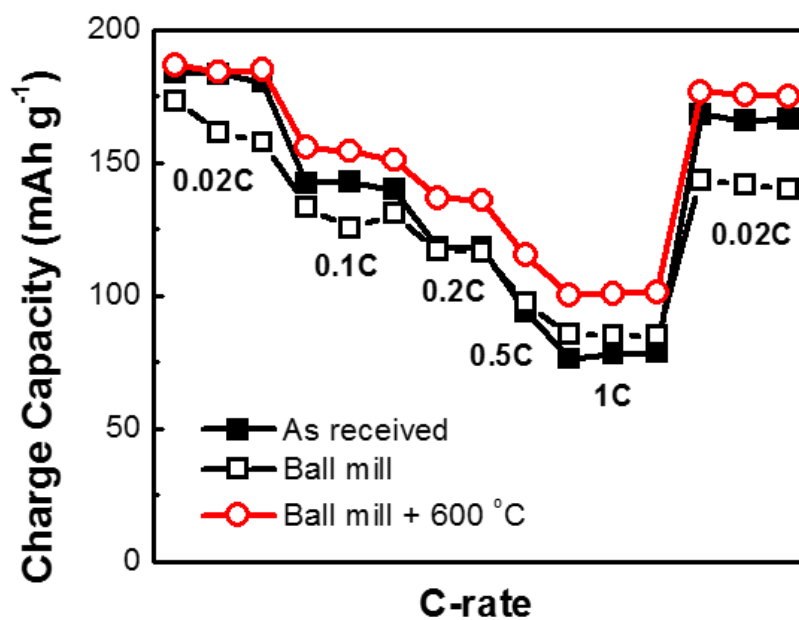


Figure 6.5 Rate performance of as-received TiO<sub>2</sub> (solid black square), ball milled TiO<sub>2</sub> (hollow black square) and ball milled TiO<sub>2</sub> followed with annealing at 600 °C (red circle). The specimens were charged and discharged at the rates of 0.02C, 0.1C, 0.2C, 0.5C, 1C and 0.02C at room temperature (3 cycles for 0.02C, 0.1C, and 1C; 2 cycles for 0.2C and 1 cycle for 0.5C).

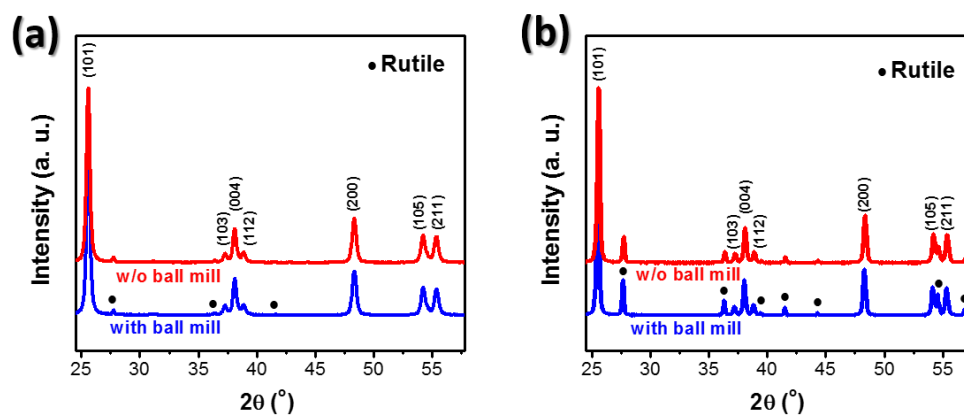


Figure 6.6 Comparison of X-ray diffraction results of anatase  $\text{TiO}_2$  for rutile phase change influenced by high-energy ball milling. (a) Specimens annealed at 600  $^\circ\text{C}$  with (blue line) or without (red line) high-energy ball milling; (b) specimens annealed at 700  $^\circ\text{C}$  with or without high-energy ball milling. The rutile phase was labeled with black dots.

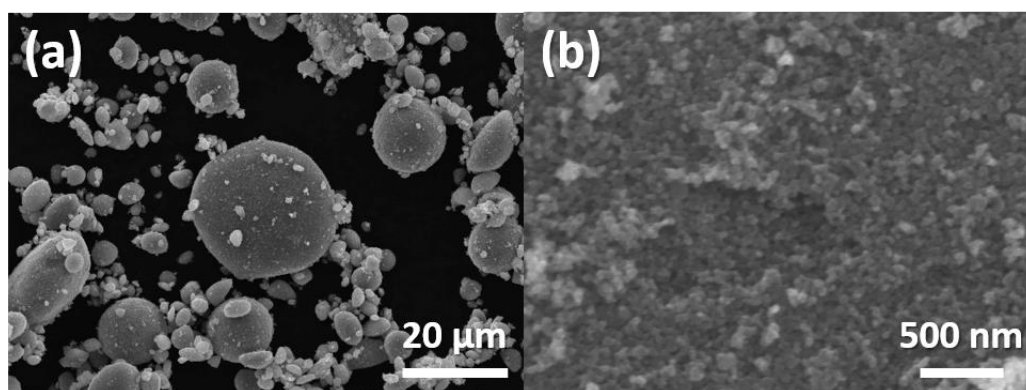


Figure 6.7 Morphology of nitrated  $\text{TiO}_2$ . The specimen was firstly fabricated by high-energy ball milling as-received  $\text{TiO}_2$  following by annealing at 600  $^\circ\text{C}$  for 10 h in air. The product was cooled down and transferred into tube furnace for annealing in  $\text{NH}_3$  gas at 600  $^\circ\text{C}$  for 1 h.

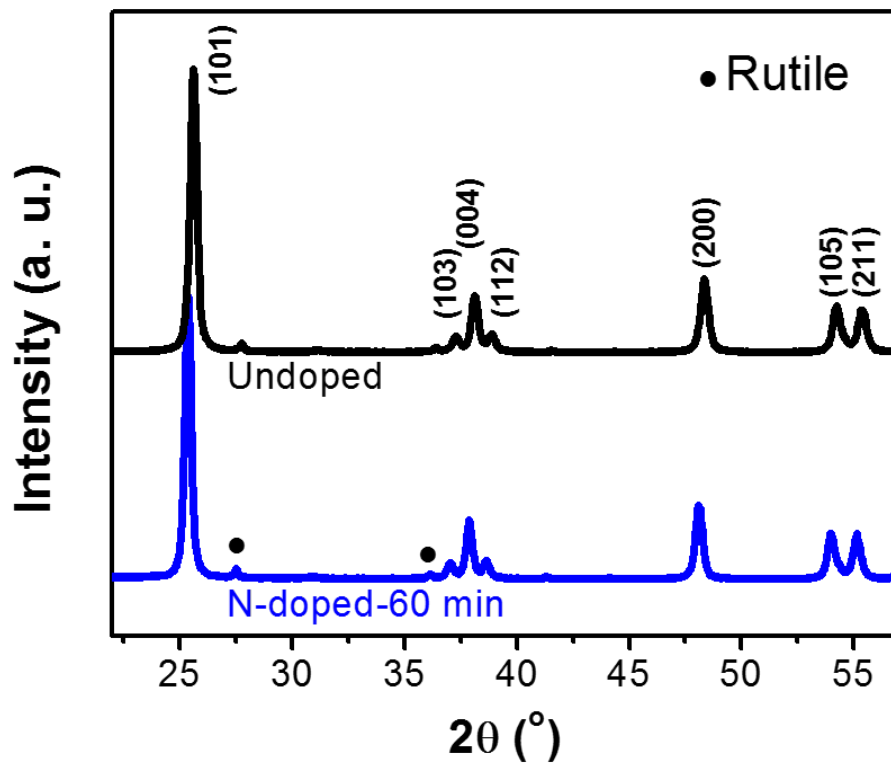


Figure 6.8 The X-ray diffraction results of undoped (black) and 1 h (blue) nitridation specimens. All specimens were high-energy ball milled followed by 600 °C for 10 h before nitridation in  $\text{NH}_3$  gas for 1 h. The main phase was anatase. Rutile phase was labeled with black dots.

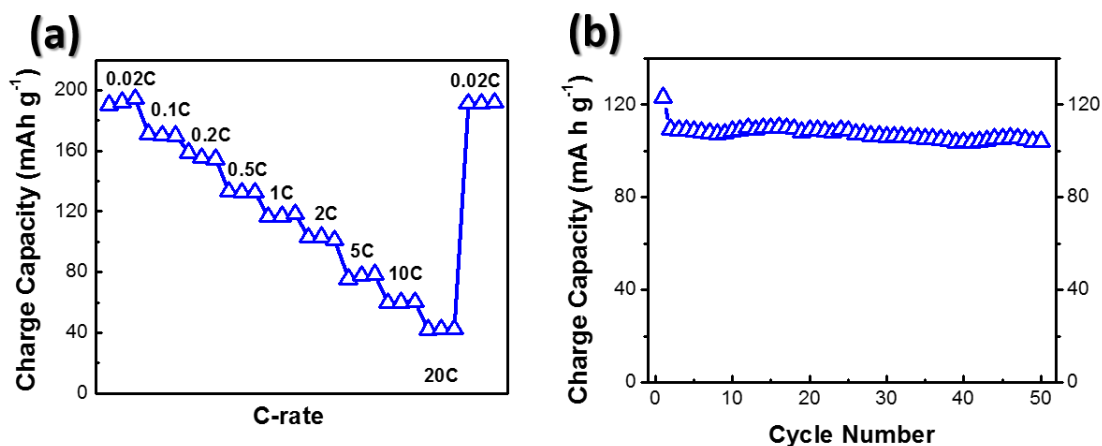


Figure 6.9 (a) Rate performance of nitrided TiO<sub>2</sub> specimens for 1 h under NH<sub>3</sub> gas flow at 600 °C. Before nitridation, the specimens were high-energy ball milled following with annealed at 600 °C. The test was carried out at the rate of 0.02C, 0.1C, 0.2C, 0.5C, 1C, 2C, 5C, 10C, 20C and 0.02C at room temperature (3 cycles for each rate). (b) Cycling stability of nitrided specimen for 1 h was tested at charge and discharge rate of 1C and room temperature for 50 cycles.

Table 6.1 Anatase phase percentage and primary particle size

Specimen	Anatase percentage (%)	Primary particle size (nm)
As-received	$99.6 \pm 0.9$	$20.7 \pm 1.5$ (anatase)
HEBM + 600 °C	$98.8 \pm 0.9$	$24.3 \pm 0.7$ (anatase)
HEBM + 700 °C	$89.4 \pm 0.8$	$38.5 \pm 1.4$ (anatase)
HEBM + 800 °C	$2.8 \pm 0.2$	190.1 (rutile)
N-doped, 600 °C	$98.7 \pm 0.5$	$26.2 \pm 2.3$ (anatase)

## References

- (1) Su, H.; Jaffer, S.; Yu, H. J. Transition Metal Oxides for Sodium-Ion Batteries. *Energy Storage Materials* **2016**, *5*, 116-131.
- (2) Mei, Y. N.; Huang, Y. H.; Hu, X. L. Nanostructured Ti-Based Anode Materials for Na-Ion Batteries. *Journal of Materials Chemistry A* **2016**, *4*, 12001-12013.
- (3) Liang, J. C.; Wang, Z. Y.; Li, Z. S.; Wang, X. F.; Yu, K. F. Fabrication of Nanostructured TiO<sub>2</sub> Using a Solvothermal Reaction for Lithium-Ion Batteries. *Nanomaterials and Nanotechnology* **2016**, *6*, 8.
- (4) Gribb, A. A.; Banfield, J. F. Particle Size Effects on Transformation Kinetics and Phase Stability in Nanocrystalline TiO<sub>2</sub>. *American Mineralogist* **1997**, *82*, 717-728.
- (5) Xu, Y.; Memarzadeh Lotfabad, E.; Wang, H.; Farbod, B.; Xu, Z.; Kohandehghan, A.; Mitlin, D. Nanocrystalline Anatase TiO<sub>2</sub>: A New Anode Material for Rechargeable Sodium Ion Batteries. *Chemical Communications* **2013**, *49*, 8973-8975.
- (6) Kim, K.-T.; Ali, G.; Chung, K. Y.; Yoon, C. S.; Yashiro, H.; Sun, Y.-K.; Lu, J.; Amine, K.; Myung, S.-T. Anatase Titania Nanorods as an Intercalation Anode Material for Rechargeable Sodium Batteries. *Nano Letters* **2014**, *14*, 416-422.
- (7) Wu, L. M.; Bresser, D.; Buchholz, D.; Giffin, G. A.; Castro, C. R.; Ochel, A.; Passerini, S. Unfolding the Mechanism of Sodium Insertion in Anatase TiO<sub>2</sub> Nanoparticles. *Advanced Energy Materials* **2015**, *5*, 11.
- (8) Samiee, M.; Luo, J. A Facile Nitridation Method to Improve the Rate Capability of TiO<sub>2</sub> for Lithium-Ion Batteries. *Journal of Power Sources* **2014**, *245*, 594-598.
- (9) Zhao, X.; Yan, C.; Gu, X.; Li, L.; Dai, P.; Li, D.; Zhang, H. Ultrafine TiO<sub>2</sub> Nanoparticles Confined in N-Doped Porous Carbon Networks as Anodes of High-Performance Sodium-Ion Batteries. *ChemElectroChem* **2017**, n/a-n/a.
- (10) Zhang, Y.; Wang, C.; Hou, H.; Zou, G.; Ji, X. Nitrogen Doped/Carbon Tuning Yolk-Like TiO<sub>2</sub> and Its Remarkable Impact on Sodium Storage Performances. *Advanced Energy Materials* **2017**, *7*, 1600173-n/a.
- (11) Liu, S. A.; Cai, Z. Y.; Zhou, J.; Pan, A. Q.; Liang, S. Q. Nitrogen-Doped TiO<sub>2</sub> Nanospheres for Advanced Sodium-Ion Battery and Sodium-Ion Capacitor Applications. *Journal of Materials Chemistry A* **2016**, *4*, 18278-18283.

## Chapter 7. Composites of Sodium Manganese Oxides with Enhanced Electrochemical Performance for Sodium-ion Batteries: Tailoring Properties via Controlling Microstructure

### 7.1. Introduction

Recently, sodium-ion batteries have attracted great research interest due to the abundance of sodium and their potential for large-scale applications. Specifically,  $\text{Na}_x\text{MnO}_2$  has been investigated as cathode materials for non-aqueous sodium-ion batteries since Mn is a low-cost and environmentally-friendly resource <sup>1</sup>. The electrochemical performance of  $\text{Na}_x\text{MnO}_2$  depends on the Na content and several different phases can form. For example, tunnel-structured  $\text{Na}_{0.44}\text{MnO}_2$  can provide relatively good rate capability and cycling stability <sup>2-4</sup>, although its theoretical capacity is relatively low ( $\sim 120 \text{ mA h g}^{-1}$ ). In contrast, layer-structured phases, such as  $\text{Na}_{0.7}\text{MnO}_2$  ( $\sim 160 \text{ mA h g}^{-1}$ ) and  $\text{NaMnO}_2$  ( $\sim 180 \text{ mA h g}^{-1}$ ), have relatively high specific capacities, but they generally exhibit poor cycling stability <sup>5-7</sup>. Thus, composite electrodes of different phases can be made to achieve better or desirable overall performance. Furthermore, a composite of P-type and O-type layer-structured phases exhibited enhanced electrochemical properties that outperformed either component phases, which was called a “synergetic effect” <sup>8,9</sup>.

In addition to the Na content, the electrochemical performance of  $\text{Na}_x\text{MnO}_2$  depends on synthesis methods and experimental conditions <sup>1</sup>, suggesting that the performance of the electrode generally depends on the

morphology and microstructure.  $\text{Na}_x\text{MnO}_2$  synthesized by solid-state reactions generally showed poor performance comparing to other wet chemical synthesis routes such as sol-gel and hydrothermal methods, where better morphological controls and crystallization can often be achieved. However, solid-state reactions remain as a prime option to synthesize  $\text{Na}_x\text{MnO}_2$  based cathode materials because they are cost-effective, scalable, and facile.

A prior study also reported that a composite of tunnel-structured  $\text{Na}_{0.44}\text{MnO}_2$  and layered  $\text{Na}_{0.67}\text{MnO}_2$  and  $\text{Na}_{0.91}\text{MnO}_2$  phases exhibited excellent electrochemical performance<sup>10</sup>. That study<sup>10</sup> further suggested that the morphology of the electrode material could play an important role in the initial stage of electrochemical cycling, where the microstructure (morphology) of the composite electrode was tailored by controlling the morphology of  $\text{Mn}_2\text{O}_3$  used in the solid-state reaction at 600 °C. In this study, we further showed that the morphology and microstructure of the composite electrode can be changed dramatically via facile and cost-effective ball milling and heat treatments, which subsequently affect not only the initial-stage<sup>10</sup> but also the long-term cycling stability and rate performance.

Specifically, we adopted high-energy ball milling before the solid-state reaction, leading to the formation of a unique microstructure with hierarchical porosities and excellent cycling stability (*e.g.*, achieving a discharge capacity of  $\sim 126 \text{ mA h g}^{-1}$  after 100 cycles) over a large electrochemical window between 2 V and 3.8 V with good rate capabilities. Moreover, we made a specimen of totally-different morphology that was made up of irregular rods after an additional

round of ball milling and reannealing, and this specimen exhibited exceptional rate performance. For example, the discharge capacity was improved by more than 230% to achieve  $\sim 53 \text{ mA h g}^{-1}$  at a particularly high rate of 50C.

## 7.2. Experimental

$\text{Na}_x\text{MnO}_2$  specimens were synthesized by a solid-state reaction route. First,  $\text{Na}_2\text{CO}_3$  (purchased from Alfa Aesar, 99.997 %),  $\text{Mn}_2\text{O}_3$  (Aldrich, 99.9 %), and acetone were added into a silicon nitride grinding vial with two silicon nitride balls. Before sealing the jar, gasket (corprene, SpexCorp) was taped by Teflon to prevent corrosion by acetone and contamination of the precursors. High-energy ball milling was carried out using a SPEX 8000D mill for a duration of 10 min followed by a 15 min resting interval; this milling process was repeated for 3 times. The ball milled mixture was dried in an oven at  $\sim 80^\circ\text{C}$ . Subsequently, the dried powder was placed in a covered alumina crucible, isothermally annealed at  $700^\circ\text{C}$  for 10 h in a box furnace (MTI Corp, XLS-1100) with a heating rate of  $5^\circ\text{C}/\text{min}$ , followed by furnace quenching, to obtain “Specimen A” (that exhibits a “meatball-like” hierarchical porous microstructure, as we will show subsequently).

Subsequently, Specimen A was ball milled again and reannealed at  $700^\circ\text{C}$  for 4 h to obtain “Specimen B” (that is made up of irregular rods, as we will show subsequently). Both Specimen A and Specimen B have the same Na/Mn atomic ratio of  $\sim 0.60$  (identical within the measurement errors, which were measured by inductively coupled plasma-optically emission spectroscopy using a PerkinElmer 3700 optical emission spectrometer), indicating that any loss of Na

(or Mn) species during the additional ball milling and reannealing is negligibly small.

X-ray diffraction (XRD) was carried out on a Bruker D8 diffractometer using Cu K $\alpha$  radiation ( $\lambda = 1.5418 \text{ \AA}$ ) with a step size of  $0.02^\circ$  and a step time of 1 s. Particle morphology was characterized using a FEI XL30 scanning electron microscope (SEM).

To prepare cathodes, 80 wt. % of the active material, 15 wt. % carbon black (MTI), 5 wt. % PVDF (MTI), and an appropriate amount of NMP (Alfa Aesar, anhydrous, 99.5 %) were mixed in a glass vial by a vibrating mixer, followed by further ultrasonic dispersion. The mixture was coated on an aluminum foil, which was subsequently dried in a vacuum oven at  $90^\circ\text{C}$  for 6 h. Cathode electrodes with a diameter of 10 mm were punched out, pressed at  $\sim 187 \text{ MPa}$ , and dried again in a vacuum oven at  $120^\circ\text{C}$  for 8 h before transferring into an Ar-filled glovebox for battery construction. The density of the dried electrode coating is  $2.5 - 3.0 \text{ mg cm}^{-2}$ . Half cells were made with a cathode electrode, a metal Na chip (MTI, 99.9 %) as the anode, 1M NaPF<sub>6</sub> in PC electrolyte, C480 separator (Celgard), and 2032 coin cell cases (SS304, MTI).

Electrochemical cycling tests were carried out on an Arbin 2143 tester. The rate performances of various specimens were tested at the discharge rates of C/10, C/5, 1C, 2C, 5C, 10C, 20C, 30C, 40C, 50C and 60C sequentially (4 cycles at C/5 and 1 cycle for other discharge rate) with a constant charge rate of C/5. The cycling stabilities were measured at a constant charge and discharge rate of 0.1C between 2 V and 3.8 V at room temperature.

Electrochemical impedance spectroscopy (EIS) and cyclic voltammetry (CV) and were performed using a Solartron 1287A/1255B analyzer.

Electrochemical impedance was measured from 1 MHz to 1 Hz at 30 mV. Before the impedance measurement, fresh cells with Na metal as the counter electrode were charged to a cut-off voltage of 3.8 V at a rate of 0.1C and were kept for 10 h after the charging to reach steady states. Cyclic voltammetry (CV) of fresh cells was performed between 2 V and 3.8 V at a scan rate of 0.1 mV s<sup>-1</sup>.

### 7.3. Results and Discussion

SEM images shown in Figure 7.1 clearly illustrate the different morphologies and microstructures of the two specimens with virtually identical composition (measured Na/Mn ratio = 0.60 for both cases). Specifically, Specimen A (*i.e.*, the as-synthesized specimen made by solid-state reaction of a high-energy ball milled mixture of precursor powders, without additional post-synthesis ball milling or reannealing) exhibits a hierarchical porous microstructure, with secondary (meatball-like) particles of sizes on the order of 10 μm, which are composed of (smaller) primary particles of < 1 μm in sizes, as shown in Figure 7.1(a). This unique microstructure was presumably formed during the solid-state reaction (noting that the precursor powders were mixed by high-energy ball milling before the 10 h solid-state reaction at 700 °C). In contrast, Specimen B (*i.e.*, the specimen resulted from an additional round of ball milling and reannealing at 700 °C of the as-synthesized Specimen A) is made up of irregular rods (Figure 7.1(b)). Figure 7.1(a') and Figure 7.1(b'), respectively,

are SEM images taken at a high magnification to show the detailed “meatball-like” and “irregular rods” microstructures, respectively. It is known that well-crystallized  $\text{Na}_{0.44}\text{MnO}_2$  particles typically exhibit a rod-like morphology since  $\text{Na}_{0.44}\text{MnO}_2$  crystals grow faster along the [001] direction, as reported in prior studies <sup>11</sup>. Therefore, the morphology change is likely due to anisotropic growth of  $\text{Na}_{0.44}\text{MnO}_2$  crystals during the re-annealing.

As shown in Figure 7.2, XRD characterization shows that both specimens have a major phase of  $\text{Na}_{0.44}\text{MnO}_2$ , since the majority of the XRD peaks are consistent with those reported in Ref. <sup>12</sup> and standard powder diffraction library (PDF#00-027-0750) for the  $\text{Na}_{0.44}\text{MnO}_2$  phase. The phase diagram <sup>13</sup> suggests that the layered  $\text{Na}_{0.7}\text{MnO}_2$  phase and the tunnel-structured  $\text{Na}_{0.44}\text{MnO}_2$  phase coexist at an equilibrium when the Na/Mn ratio is between 0.44 and 0.7. In the current case, however, two minor phases, both the equilibrium secondary phase of  $\text{Na}_{0.7}\text{MnO}_{2.05}$  (PDF#00-027-0751) and the non-equilibrium secondary phase of  $\text{Na}_{0.91}\text{MnO}_2$  (PDF#00-038-0965), were present in both specimens. The coexistence of three phases ( $\text{Na}_{0.67}\text{MnO}_2$ ,  $\text{Na}_{0.91}\text{MnO}_2$  and  $\text{Na}_{0.44}\text{MnO}_2$ ) was reported previously, which enhanced the performance of as a cathode material for sodium-ion batteries <sup>10</sup>; the coexistence of  $\text{Na}_{0.7}\text{MnO}_2$  and  $\text{Na}_{0.91}\text{MnO}_2$  phases was also observed in prior study of supercapacitors <sup>14</sup>. In this work, the  $\text{Na}_{0.44}\text{MnO}_2$  phase is clearly the majority phase for both specimens (Figure 7.2), whereas the excess amounts of Na (since the Na/Mn ratios were measured to be 0.60 for both specimens) lead to the formation of secondary layer-structured phases with higher Na contents, which may affect the electrochemical

performance of the composite electrodes as discussed subsequently. It is also possible that some Na-rich amorphous phases may form during the high-energy ball milling and heat treatments, either as bulk secondary phases or as 2-D interfacial phases (nanoscale surface<sup>15-20</sup> or intergranular<sup>16,19,21</sup> “amorphous” films), as shown in prior studies of lithium-ion battery materials that were made by similar ball milling and annealing processes<sup>16-20</sup>.

The cycling stabilities measured with a constant charge and discharge rate of 0.1C at room temperature in the voltage window 2.0 – 3.8 V (corresponding to the Na contents of 0.18 to 0.64<sup>12</sup>) were displayed in Figure 7.3. An initial discharge capacity of ~140 mA h g<sup>-1</sup> for the composite material, which is higher than the theoretical capacity of 121 mA h g<sup>-1</sup> for the main Na<sub>0.44</sub>MnO<sub>2</sub> phase due to the contributions of secondary layered phases that have higher theoretical capacities, was reached in both specimens. The initial discharge capacity of ~140 mA h g<sup>-1</sup> is comparable with some of the best reported results of similar materials, *e.g.*, ~124 mA h g<sup>-1</sup> for the best reported single-phase Na<sub>0.44</sub>MnO<sub>2</sub><sup>3</sup> and ~150 mA h g<sup>-1</sup> for a composite of P-type and O-type layer-structured Na<sub>x</sub>MnO<sub>2</sub><sup>8,9</sup>. Subsequently, the discharge capacity decayed to ~126 mA h g<sup>-1</sup> after ~15 cycles, which might be attributed to the decaying of the contributions from layered phases due to the Mn<sup>2+</sup> dissolution as well as formation and stabilization of solid-electrolyte interphase (SEI) layers.

Specimen A (with a hierarchical porous microstructure with primary and secondary particles; see Figure. 1(a) and (a')) exhibited stable cycling performance with virtually no decaying in the capacity after ~15 cycles; the

discharge capacity retained at  $\sim 126 \text{ mA h g}^{-1}$  after 100 cycles, representing virtually 100 % retention from 15 to 100 cycles (Figure 7.3(a)). This performance is on par with or exceeds with some of the best recorded results in the most recent literature <sup>2,3,8-10</sup>, most of which used specimens made by wet chemistry methods. In contrast, Specimen B (that is made up of irregular rods; see Figure 7.1(b) and (b')) displayed a discharge capacity of  $108 \text{ mA h g}^{-1}$  after 100 cycles, implying  $\sim 15\%$  capacity loss that is presumably due to the dissolution of Mn (Figure 7.3(b)). The stable cycling stability of Specimen A was attributed to specific hierarchical porous microstructure. As shown in Figure 7.3(a) and (a'), Specimen A was composed of secondary particles of  $> \sim 10 \mu\text{m}$  that were composed of primary particles of  $< \sim 1 \mu\text{m}$ , along with hierarchical porosities. A prior study already suggested that such a hierarchical porous composite structure could improve the cycling stability for sodium-ion batteries <sup>22</sup>. Several possible mechanisms are proposed and discussed below.

First, the microstructure with hierarchical porosities can help to reduce the capacity fading due to the volume changes during cycling by reducing the possibility of cracking imitation and growth. Specifically, the volume change of  $\text{Na}_{0.44}\text{MnO}_2$  during Na-ion intercalation and deintercalation is  $\sim 7.2 \%$ , which would introduce some stresses during cycling that could lead to pulverization <sup>12</sup>. In addition, the anisotropic expansion could be another important factor. Specifically, for  $\text{Na}_x\text{MnO}_2$ , the change of lattice parameters is about 1% along *a* and *c* directions, but about 5 % along *b* axis. Moreover, the increase along the *b* axis with intercalation almost stops after *x* is increased to  $\sim 0.5$  in  $\text{Na}_x\text{MnO}_2$ ,

whereas expansions in  $a$  and  $c$  axes start to accelerate <sup>12</sup>. These might lead to complex stress and strain fields that change substantially during the electrochemical cycling to promote cracking and pulverization, which could be alleviated with a microstructure with hierarchical porosities (Figure 7.1(a)).

Second, the  $\text{Mn}^{2+}$  formation (from the reduction) and dissolution during electrochemical cycling is considered as another main reason of poor cycling stability. The hierarchical porous microstructure in Specimen A might reduce the effective surface areas (as compared with the morphology shown in Figure 7.1 (b) for Specimen B), thereby reducing the dissolution rates. Moreover, the formation of  $\text{Mn}^{2+}$  on the surface layer of  $\sim 10$  nm was observed when the cathode is discharged to a less than 2.6 V (thus, the cycling stability can be improved by setting a higher cutoff voltage of 3 V to avoid the formation of  $\text{Mn}^{2+}$ , which would reduce the capacity <sup>3</sup>). We further noticed that the change of expansion mode at  $x = \sim 0.5$  in  $\text{Na}_x\text{MnO}_2$  (discussed above <sup>12</sup>) is coincident with the formation of  $\text{Mn}^{2+}$  at  $\sim 2.6$  V<sup>3</sup> (noting that 2.6 V corresponds to  $x = \sim 0.5$ ). Thus, it is possible that the lattice distortion associated with changing of the stress mode is related to the formation of surface layers enriched in  $\text{Mn}^{2+}$  and the consequently poor cycling stability due to the dissolution of  $\text{Mn}^{2+}$  cations. If this hypothesis is true, the hierarchical porous microstructure might provide an additional mechanism of alleviating the formation and dissolution of  $\text{Mn}^{2+}$  cations via suppressing the stress-induced distortion; thus, it becomes possible to suppress the Mn dissolution and the consumption of active materials without setting a higher cut-off voltage that would reduce the capacity.

In a broader context, we note that sodium cathode materials typically exhibit large (and often anisotropic) volume changes during cycling, as well as multiple stages of electrochemical phase transformations, which are usually much more complex than their lithium counterparts, due to the larger size of Na<sup>+</sup> (1.2 Å for Na<sup>+</sup> vs. 0.9 Å for Li<sup>+</sup>). The subsequent larger and more anisotropic lattice distortions are detrimental to the cycling stability. Thus, we believe that “meatball-like” microstructures with hierarchical porosities can be generally useful to improve the cycling life of many sodium electrodes.

The electrochemical impedance spectra (EIS) are shown in Figure 7.4. The measured spectra were fitted with an equivalent circuit model shown in inset of Figure 7.4. In this model,  $R_o$  refers to the Ohmic resistance that is a sum of resistance of electrolyte, battery construction, separator and cell cases;  $R_{SEI}$  and  $C_{SEI}$  are the resistance and capacitance of solid-electrolyte interphase (SEI), respectively, which produce the high-frequency semicircle in the spectra;  $R_{ct}$  and  $C_{dl}$  refer to the charge transfer resistance and the double layer capacitance, which produce the middle-frequency semicircle. The fitting results show that both specimens have similar charge transfer resistance of 137  $\Omega$  and 143  $\Omega$ , respectively, with a characteristic frequency of 2.2 Hz and 2.0 Hz, respectively, for specimen A (with a hierarchical porous microstructure with primary and secondary particles) and specimen B (with irregular rods), respectively. There are also similar features in charge transfer resistance. However, the SEI resistance of Specimen B with irregular rods is 42.5  $\Omega$ , which is significantly higher than the SEI resistance of 27.4  $\Omega$  of Specimen A with a hierarchical

porous microstructure. The lower SEI resistance in Specimen A indicates less interfacial reaction and presumably less dissolution of  $\text{Mn}^{2+}$  in the electrolyte. This is consistent with a better cycling performance of Specimen A as shown in Figure 7.3, which is presumably a merit as a result of the hierarchical porosities.

The phase transformations of the two specimens were compared through CV (cyclic voltammogram) measurements shown in Figure 7.5. Peaks  $a_1$  to  $a_5$  represent the phase transitions of the tunnel-structured  $\text{Na}_{0.44}\text{MnO}_2$ , while peaks  $b_1$  to  $b_3$  correspond to the phase transitions from layered phases<sup>12</sup>. The CV results demonstrated that the intensities of most redox peaks for Specimen A with the hierarchical porous microstructure with primary and secondary particles are lower than those of Specimen B with rod-like morphology (with the exception of peak  $b_1$  and  $a_5$ ). The reduced peak intensities imply the suppression of phase transition in Specimen A with the hierarchical porous microstructure, which is consistent with the observed enhancement in the cycling performance (Figure 7.3).

Figure 7.6 displays the rate performances of both specimens. Specifically, at a low rate of 0.1C, both specimens achieved a high specific discharge capacity of  $\sim 140 \text{ mA h g}^{-1}$ , consistent with those shown in Figure 7.3. The excess contributions to the capacity (beyond the theoretical capacity of  $\text{Na}_{0.44}\text{MnO}_2$ ) from the two layered phases ( $\text{Na}_{0.7}\text{MnO}_{2.05}$  and/or  $\text{Na}_{0.91}\text{MnO}_2$ ) in the composites were confirmed by CV measurements shown in Figure 7.5.

At high rates, Specimen A already exhibited good rate capabilities (Figure 7.6(a)). Yet, Specimen B exhibited superior rate capabilities (Figure 7.6(b)) that

were substantially better. For example, at a high rate of 1C, the discharge capacity of Specimen B was increased by more than ~13% as compared with Specimen A (~110 mA h g<sup>-1</sup> for Specimen B vs. 97 mA h g<sup>-1</sup> for Specimen A, which exceeded all other prior studies of similar materials systems<sup>2,8,9</sup> and was on par with the best recorded capacity of 118 mA h g<sup>-1</sup> at 1C for a Na<sub>0.44</sub>MnO<sub>2</sub> specimen of well-controlled needle-like crystals made by a wet chemistry process<sup>3</sup>); at a particularly high rate of 50C, the discharge capacity of Specimen B was increased by more than 230% to 53 mA h g<sup>-1</sup>. The high rate capabilities of Specimen B represented another example of the so-called “synergistic effect” that was observed in layered P- and O- type composites<sup>8,9</sup>. It is also possible that rate capabilities were improved by the formation of amorphous-like 2-D surface phases that often form spontaneously in ball-milled and annealed materials<sup>16-20</sup>. Future investigation should be conducted to probe the exact mechanisms for the improved rate capabilities.

#### **7.4. Conclusions**

A multi-phase composite of Na<sub>x</sub>MnO<sub>2</sub> phases with a (“meatball-like”) the hierarchical porous microstructure with primary and secondary particles was synthesized by a facile high-energy ball milling and solid-state reaction method. Excellent capacity and cycling performance as a cathode material of sodium-ion batteries (*i.e.*, a discharge capacity of ~126 mA h g<sup>-1</sup> after 100 cycles) were achieved. The rate performance was further enhanced drastically by an additional round of high-energy ball milling and reannealing, which changed the

morphology to irregular rods. For example, the discharge capacity was improved by more than 13% to achieve  $\sim 110 \text{ mA h g}^{-1}$  at a high rate of 1C; furthermore, the capacity was improved by more than 230% to achieve  $\sim 53 \text{ mA h g}^{-1}$  at a particularly high rate of 50C. The relevant underlying mechanisms have been discussed.

In a broader context, this study demonstrated the feasibility of drastically changing electrochemical properties of the electrode materials for solid-ion batteries by controlling and modifying the morphology and microstructure of the composite electrodes via facile ball milling and heat treatments. Additional opportunities exist via utilizing nanometer-thick, amorphous-like, 2-D interfacial phases (that may form spontaneously after ball milling and annealing at surfaces<sup>15-20</sup> and grain boundaries<sup>16,19,21</sup>) to improve cycling stability or enhance the rate capabilities. Such strategies have been demonstrated successfully for many electrode materials for lithium-ion batteries<sup>16-21</sup> and we expect more opportunities exist for sodium-ion batteries to improve and tailor the electrochemical performance via controllably altering microstructures and interfaces, particularly for composite electrodes.

**Chapter 7**, in part, is a reprint of the material “Composites of Sodium Manganese Oxides with Enhanced Electrochemical Performance for Sodium-ion Batteries: Tailoring Properties via Controlling Microstructure” as it appears in the Science China Technological Sciences, Jiajia Huang and Jian Luo, 2016, 59, 1042.

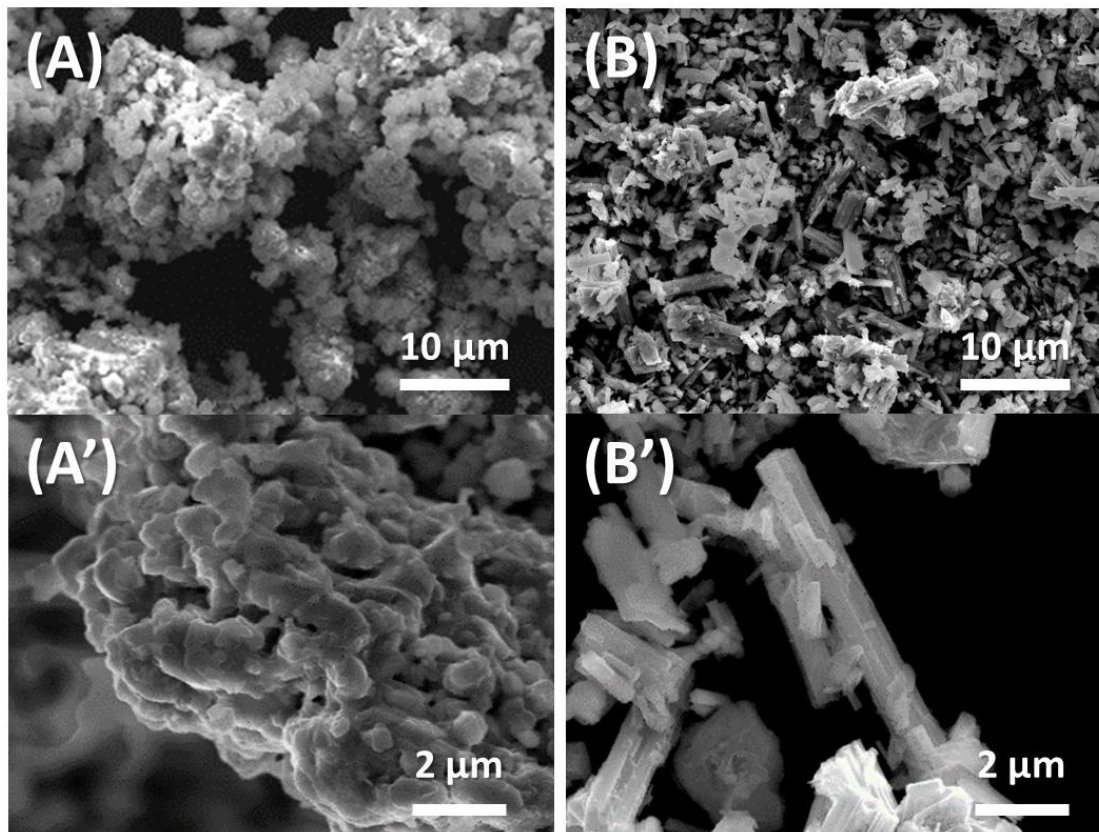


Figure 7.1 SEM images of (a and a') Specimen A that has a “meatball-like” hierarchical porous microstructure with primary and secondary particles (without extra ball milling or reannealing) and (b and b') Specimen B that is made up of irregular rods (after extra ball milling and reannealing at 700 °C). Panels (a') and (b') are SEM images taken at a high magnification to show the detailed “meatball-like” and “irregular rods” microstructures, respectively.

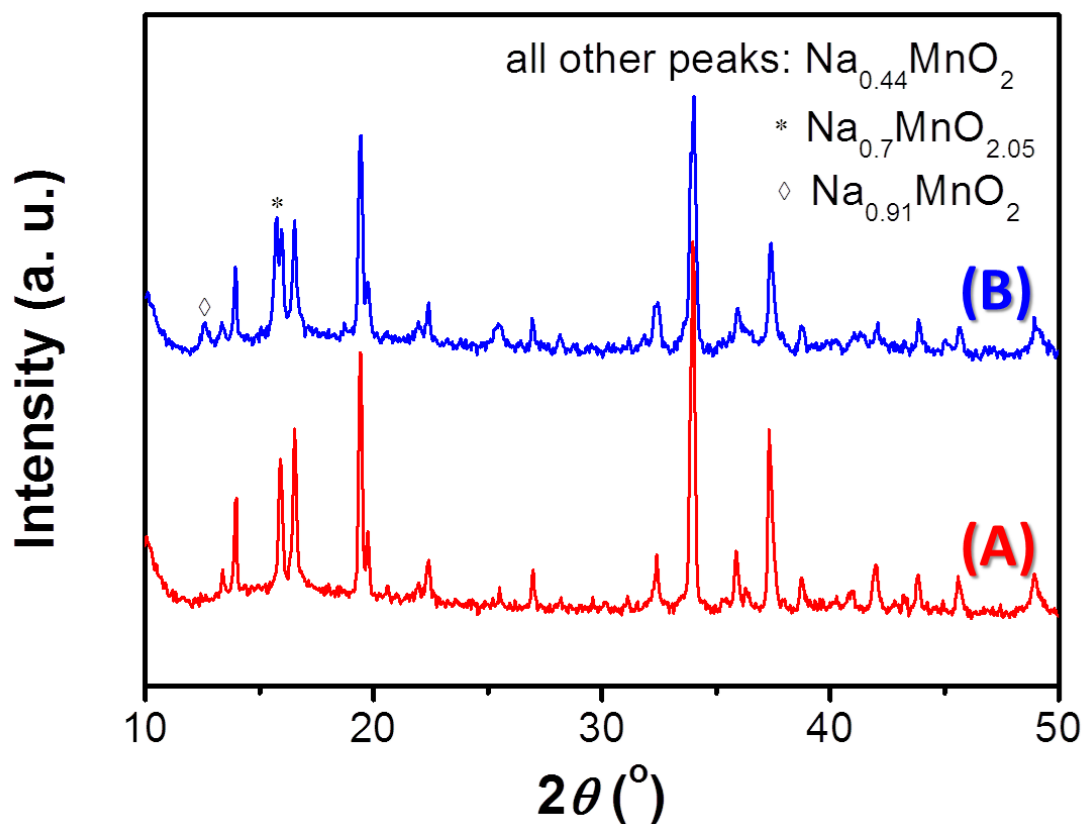


Figure 7.2 XRD patterns of the  $\text{Na}_x\text{MnO}_2$  composites of (a) Specimen A and (b) Specimen B. The peaks for the layered  $\text{Na}_{0.7}\text{MnO}_{2.05}$  and  $\text{Na}_{0.91}\text{MnO}_2$  phases are represented by the symbol \* and  $\diamond$ , respectively. In both cases,  $\text{Na}_{0.44}\text{MnO}_2$  is the dominating phase.

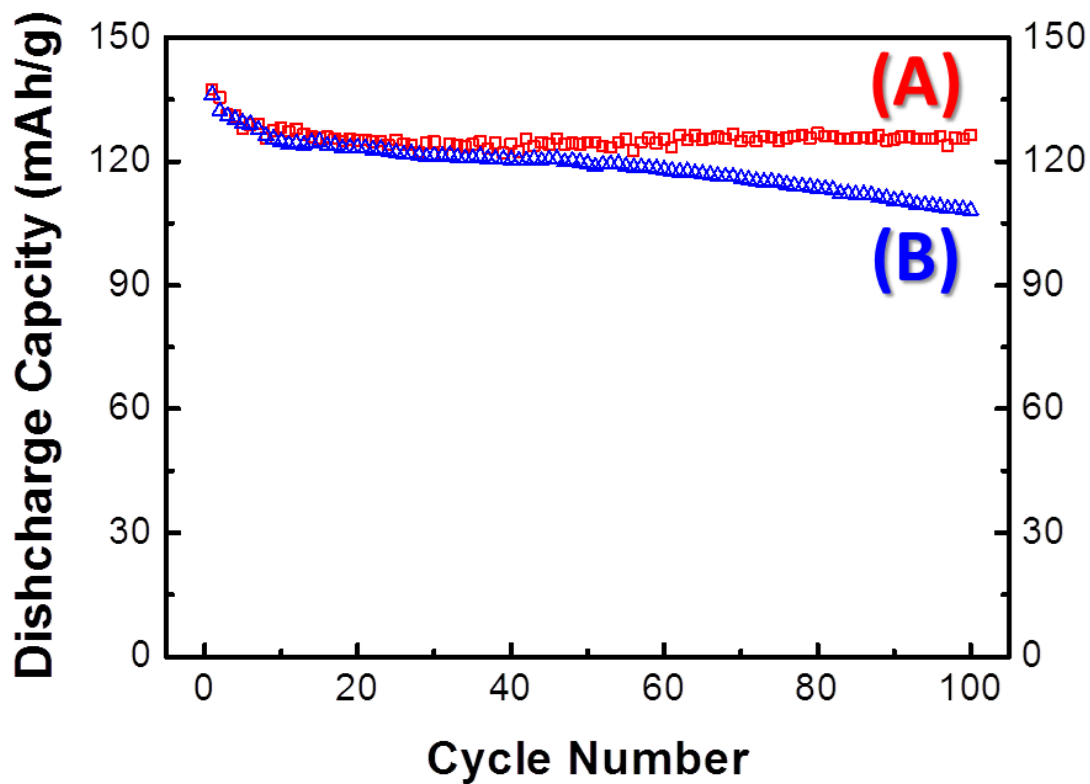


Figure 7.3 Cycling performance of (a) Specimen A (hierarchical porous microstructure with primary and secondary particles) and (b) Specimen B (irregular rods). Both specimens were charged and discharged at a constant rate of 0.1C at room temperature.

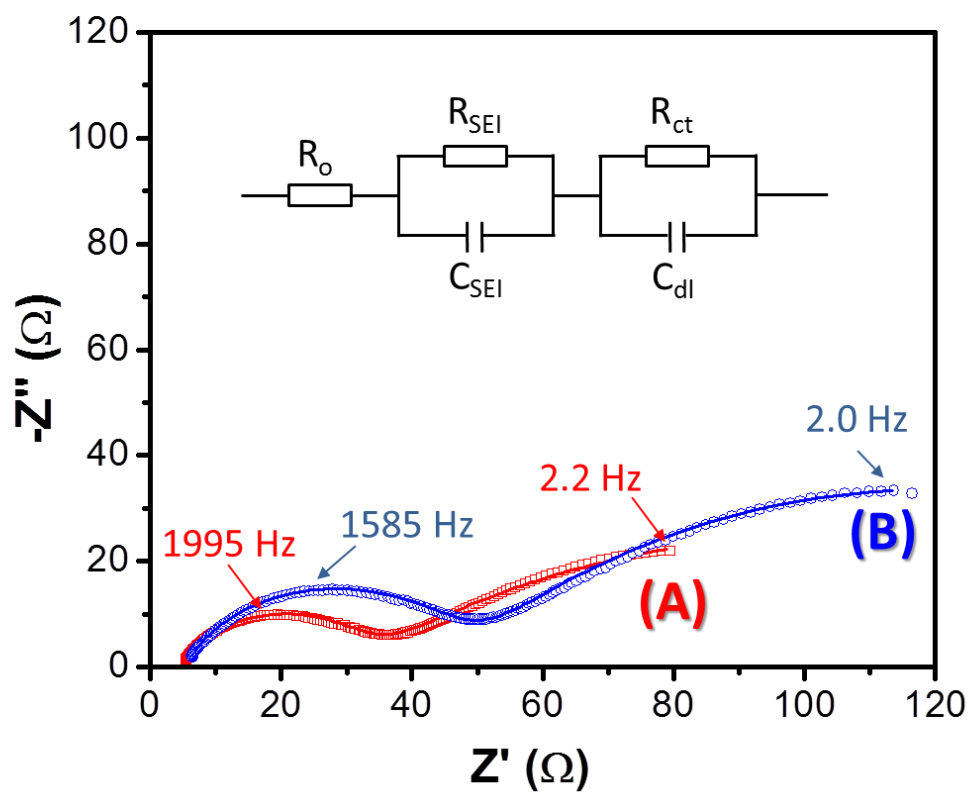


Figure 7.4 Electrochemical impedance spectra of the  $\text{Na}_{0.7}\text{MnO}_2$  of specimen A (hierarchical porous microstructure with primary and secondary particles) and specimen B (irregular rods). Dots are experimental data and solid lines represent fitting curves using the equivalent circuit model shown in the inset.

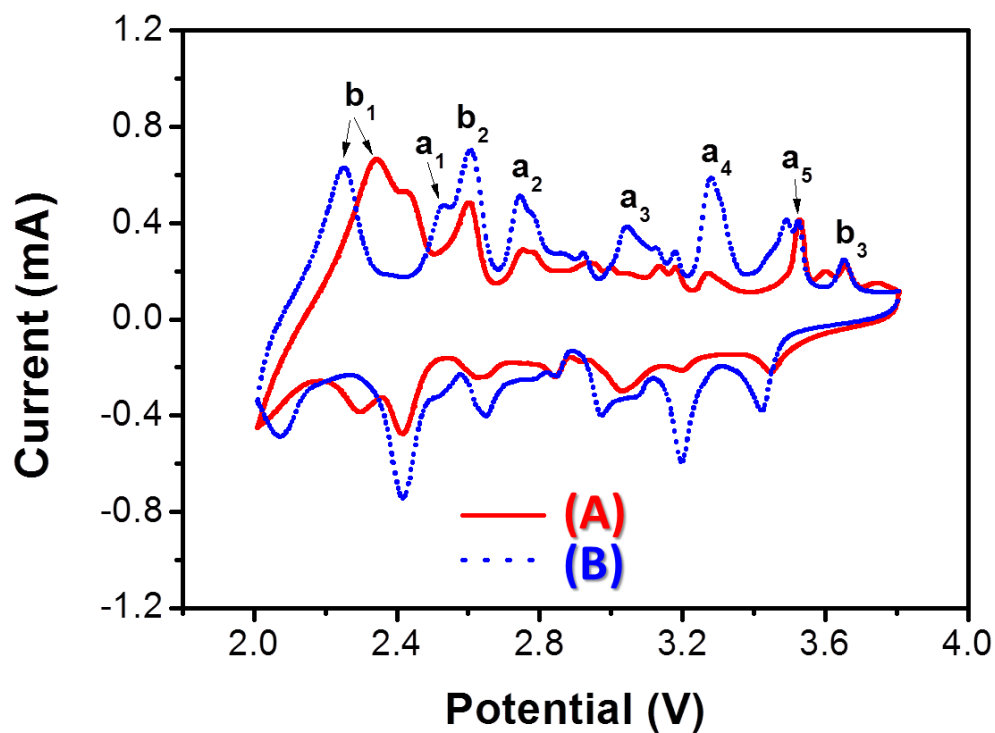


Figure 7.5 Comparison of cyclic voltammograms of the 5<sup>th</sup> cyclic sweep of (a) Specimen A (hierarchical porous microstructure with primary and secondary particles) and (b) Specimen B (irregular rods), which were measured at a scan rate of 0.1 mV s<sup>-1</sup> from 2.0 V to 3.8 V at room temperature. The a<sub>1</sub>-a<sub>5</sub> peaks represent the redox reactions from the Na<sub>0.44</sub>MnO<sub>2</sub> phase, while the b<sub>1</sub>-b<sub>3</sub> peaks represent the redox reactions from layered phases. The tests were carried out using coin cells with sodium metal as reference electrode.

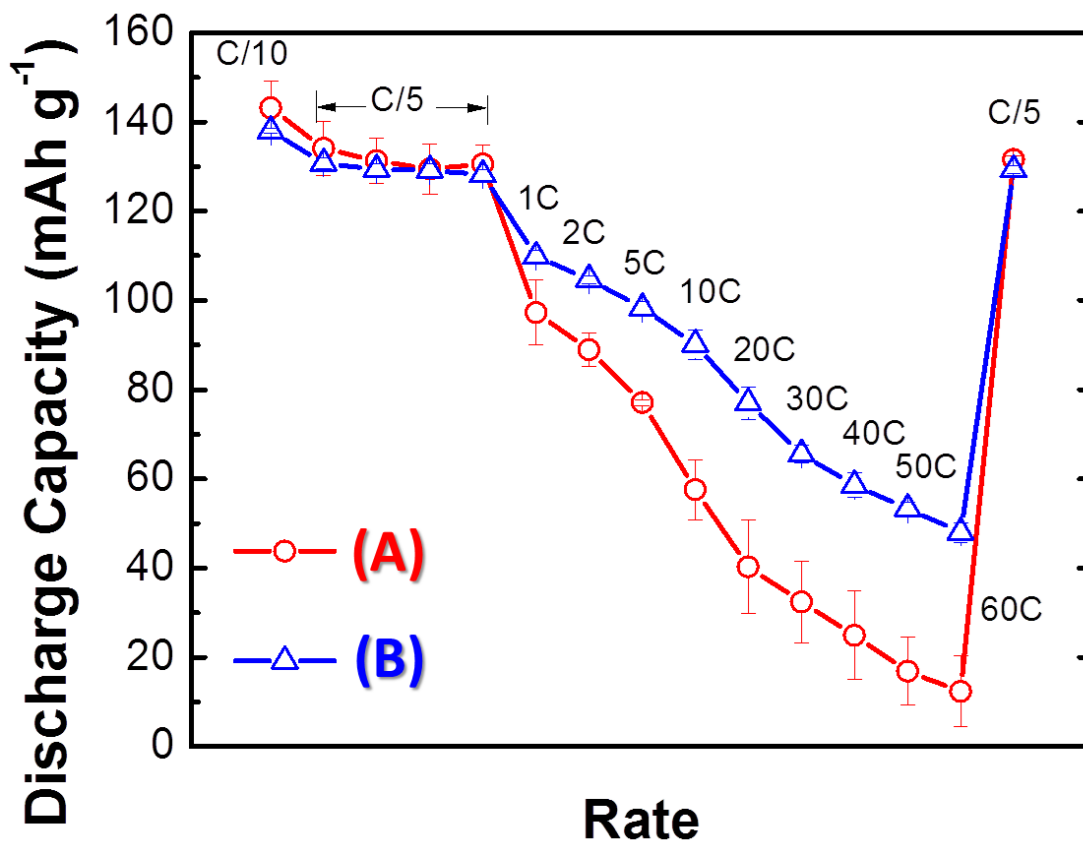


Figure 7.6 The rate performances of (a) Specimen A (hierarchical porous microstructure with primary and secondary particles) and (b) Specimen B (irregular rods). Three coin cells were made for each case. The means are plotted in the graphs, while the error bars represent  $\pm$  one standard deviations. All cells were charged at C/5 and discharged at various rates (labeled in the graphs) at room temperature.

## References

- (1) Xiang, X.; Zhang, K.; Chen, J. Recent Advances and Prospects of Cathode Materials for Sodium - Ion Batteries. *Advanced Materials* **2015**, *27*, 5343-5364.
- (2) Cao, Y.; Xiao, L.; Wang, W.; Choi, D.; Nie, Z.; Yu, J.; Saraf, L. V.; Yang, Z.; Liu, J. Reversible Sodium Ion Insertion in Single Crystalline Manganese Oxide Nanowires with Long Cycle Life. *Advanced Materials* **2011**, *23*, 3155-3160.
- (3) Qiao, R.; Dai, K.; Mao, J.; Weng, T.-C.; Sokaras, D.; Nordlund, D.; Song, X.; Battaglia, V. S.; Hussain, Z.; Liu, G. Revealing and Suppressing Surface Mn (II) Formation of Na<sub>0.44</sub>MnO<sub>2</sub> Electrodes for Na-Ion Batteries. *Nano Energy* **2015**, *16*, 186-195.
- (4) Zhao, L.; Ni, J.; Wang, H.; Gao, L. Na<sub>0.44</sub>MnO<sub>2</sub>-Cnt Electrodes for Non-Aqueous Sodium Batteries. *Rsc Advances* **2013**, *3*, 6650-6655.
- (5) Su, D.; Wang, C.; Ahn, H. j.; Wang, G. Single Crystalline Na<sub>0.7</sub>MnO<sub>2</sub> Nanoplates as Cathode Materials for Sodium - Ion Batteries with Enhanced Performance. *Chemistry-A European Journal* **2013**, *19*, 10884-10889.
- (6) Ma, X.; Chen, H.; Ceder, G. Electrochemical Properties of Monoclinic NaMnO<sub>2</sub>. *Journal of the Electrochemical Society* **2011**, *158*, A1307-A1312.
- (7) Caballero, A.; Hernan, L.; Morales, J.; Sanchez, L.; Pena, J. S.; Aranda, M. Synthesis and Characterization of High-Temperature Hexagonal P2-Na<sub>0.6</sub>MnO<sub>2</sub> and Its Electrochemical Behaviour as Cathode in Sodium Cells. *Journal of Materials Chemistry* **2002**, *12*, 1142-1147.
- (8) Guo, S.; Liu, P.; Yu, H.; Zhu, Y.; Chen, M.; Ishida, M.; Zhou, H. A Layered P2 - and O3 - Type Composite as a High - Energy Cathode for Rechargeable Sodium - Ion Batteries. *Angewandte Chemie* **2015**, *127*, 5992-5997.
- (9) Keller, M.; Buchholz, D.; Passerini, S. Layered Na - Ion Cathodes with Outstanding Performance Resulting from the Synergetic Effect of Mixed P - and O - Type Phases. *Advanced Energy Materials* **2015**, in press.
- (10) Xu, M.; Niu, Y.; Li, Y.; Bao, S.; Li, C. M. Synthesis of Sodium Manganese Oxides with Tailored Multi-Morphologies and Their Application in Lithium/Sodium Ion Batteries. *RSC Advances* **2014**, *4*, 30340-30345.
- (11) Mo, M.; Hui, K. S.; Hong, X.; Guo, J.; Ye, C.; Li, A.; Hu, N.; Huang, Z.; Jiang, J.; Liang, J.; Chen, H. Improved Cycling and Rate Performance of Sm-Doped LiNi<sub>0.5</sub>Mn<sub>1.5</sub>O<sub>4</sub> Cathode Materials for 5 V Lithium Ion Batteries. *Applied Surface Science* **2014**, *290*, 412-418.

- (12) Sauvage, F.; Laffont, L.; Tarascon, J.-M.; Baudrin, E. Study of the Insertion/Deinsertion Mechanism of Sodium into  $\text{Na}_0.44\text{MnO}_2$ . *Inorganic Chemistry* **2007**, *46*, 3289-3294.
- (13) Parant, J.-P.; Olazcuaga, R.; Devalette, M.; Fouassier, C.; Hagenmuller, P. Sur Quelques Nouvelles Phases De Formule  $\text{Na}_x\text{MnO}_2$  ( $x \leq 1$ ). *Journal of Solid State Chemistry* **1971**, *3*, 1-11.
- (14) Mai, L.; Li, H.; Zhao, Y.; Xu, L.; Xu, X.; Luo, Y.; Zhang, Z.; Ke, W.; Niu, C.; Zhang, Q. Fast Ionic Diffusion-Enabled Nanoflake Electrode by Spontaneous Electrochemical Pre-Intercalation for High-Performance Supercapacitor. *Scientific reports* **2013**, *3*, 1718.
- (15) Luo, J.; Chiang, Y.-M. Wetting and Prewetting on Ceramic Surfaces. *Annual Review of Materials Research* **2008**, *38*, 227-249.
- (16) Kayyar, A.; Qian, H. J.; Luo, J. Surface Adsorption and Disordering in  $\text{LiFePO}_4$  Based Battery Cathodes. *Applied Physics Letters* **2009**, *95*, 221905.
- (17) Huang, J.; Luo, J. A Facile and Generic Method to Improve Cathode Materials for Lithium-Ion Batteries Via Utilizing Nanoscale Surface Amorphous Films of Self-Regulating Thickness. *Physical Chemistry Chemical Physics* **2014**, *16*, 7786-7798.
- (18) Kang, B.; Ceder, G. Battery Materials for Ultrafast Charging and Discharging. *Nature* **2009**, *458*, 190-193.
- (19) Chong, J.; Xun, S. D.; Song, X. Y.; Ridgway, P.; Liu, G.; Battaglia, V. S. Towards the Understanding of Coatings on Rate Performance of  $\text{LiFePO}_4$ . *Journal of Power Sources* **2012**, *200*, 67-76.
- (20) Sun, K.; Dillon, S. J. A Mechanism for the Improved Rate Capability of Cathodes by Lithium Phosphate Surficial Films. *Electrochemistry Communications* **2011**, *13*, 200-202.
- (21) Luo, J. Interfacial Engineering of Solid Electrolytes. *Journal of Materiomics* **2015**, *1*, 22-32.
- (22) Hwang, J.-Y.; Oh, S.-M.; Myung, S.-T.; Chung, K. Y.; Belharouak, I.; Sun, Y.-K. Radially Aligned Hierarchical Columnar Structure as a Cathode Material for High Energy Density Sodium-Ion Batteries. *Nature communications* **2015**, *6*, 6865.

## Chapter 8. Future Work and Preliminary Results: Cold Sintering of Solid State Electrolyte for the All-solid-state Lithium-ion Batteries

### 8.1. Introduction

Safety issue is a major concern for current lithium-ion batteries besides the capacity insufficiency. The liquid electrolyte with flammable organic solvents would lead to damage of the battery and even a serious explosion when overheat or short circuit occurs. Hence, the all-solid-state battery will be one of the most promising options as an alternative of the traditional ion batteries. Employing a sort of nonflammable solid-state electrolyte instead of liquid electrolyte, the all-solid-state batteries could completely solve the safety problems that the current commercial batteries meet.<sup>1</sup>

After decades of study, the ion conductivity of solid state electrolytes is close to that of liquid electrolytes ( $10^{-2}$  S  $\text{cm}^{-1}$ , room temperature).<sup>2</sup> For example, the garnet<sup>3-6</sup>, perovskite<sup>7-9</sup> and NASICON-like<sup>10-13</sup> solid electrolyte has an optimized total lithium ion conductivity of  $\sim 10^{-3} - 10^{-4}$  S  $\text{cm}^{-1}$ ; the LISICON-like electrolyte has the most highest lithium ion conductivity  $\sim 10^{-2}$  S  $\text{cm}^{-1}$ .<sup>14</sup>

To consider a full battery with high energy density, Li metal has to be used as anode for all-solid-state lithium batteries. Hence, it is required that the solid electrolyte should be stable with contact with Li metal at a potential  $\sim 0$  V during electrochemical cycling. Among various solid state electrolytes, the garnet is the most stable against Li metal.<sup>15</sup> Furthermore, the electrolyte has to be prepared as a thin film with  $\sim 20$   $\mu\text{m}$  thickness to meet a feasible range of battery internal

resistance as well as a high relative density for good mechanical property. Generally, a high temperature  $> 1200\text{ }^{\circ}\text{C}$  is necessary for high relative density. However, the high temperature sintering will inevitably lead to a serious Li loss and consequent phase changes which will result in serious decrease of ion conductivity. Therefore, it will be critical for the all-solid-state lithium-ion battery application that the fabrication method sintering at low temperature with dense microstructure.

Recently, cold sintering as a low temperature ( $< 200\text{ }^{\circ}\text{C}$ , with pressing  $\sim 10^2\text{ MPa}$  assisted by water) sintering method with relatively high density  $\sim 90\%$  was reported by Randall group.<sup>16-28</sup> The feature of cold sintering method could meet the requirement of solid state electrolyte fabrication.

In this work, we successfully synthesized a garnet material  $\text{Li}_{6.4}\text{Ga}_{0.2}\text{La}_3\text{Zr}_2\text{O}_{12}$  and proved that it can be cold sintered, and could be a promising method for all-solid-state battery fabrication.

## 8.2. Experimental

$\text{Na}_x\text{MnO}_2$  specimens were synthesized by a solid-state reaction route. First,  $\text{Na}_2\text{CO}_3$  (purchased from Alfa Aesar, 99.997 %),  $\text{Mn}_2\text{O}_3$  (Aldrich, 99.9 %), and acetone were added into a silicon nitride grinding vial with two silicon nitride balls. Before sealing the jar, gasket (corprene, SpexCorp) was taped by Teflon to prevent corrosion by acetone and contamination of the precursors. High-energy ball milling was carried out using a SPEX 8000D mill for a duration of 10 min followed by a 15 min resting interval; this milling process was repeated for 3

times. The ball milled mixture was dried in an oven at  $\sim 80$  °C. Subsequently, the dried powder was placed in a covered alumina crucible, isothermally annealed at 700 °C for 10 h in a box furnace (MTI Corp, XLS-1100) with a heating rate of 5 °C/min, followed by furnace quenching, to obtain “Specimen A” (that exhibits a “meatball-like” hierarchical porous microstructure, as we will show subsequently).

Subsequently, Specimen A was ball milled again and reannealed at 700 °C for 4 h to obtain “Specimen B” (that is made up of irregular rods, as we will show subsequently). Both Specimen A and Specimen B have the same Na/Mn atomic ratio of  $\sim 0.60$  (identical within the measurement errors, which were measured by inductively coupled plasma-optically emission spectroscopy using a PerkinElmer 3700 optical emission spectrometer), indicating that any loss of Na (or Mn) species during the additional ball milling and reannealing is negligibly small.

X-ray diffraction (XRD) was carried out on a Bruker D8 diffractometer using Cu K $\alpha$  radiation ( $\lambda = 1.5418$  Å) with a step size of  $0.02^\circ$  and a step time of 1 s. Particle morphology was characterized using a FEI XL30 scanning electron microscope (SEM).

To prepare cathodes, 80 wt. % of the active material, 15 wt. % carbon black (MTI), 5 wt. % PVDF (MTI), and an appropriate amount of NMP (Alfa Aesar, anhydrous, 99.5 %) were mixed in a glass vial by a vibrating mixer, followed by further ultrasonic dispersion. The mixture was coated on an aluminum foil, which was subsequently dried in a vacuum oven at 90 °C for 6 h. Cathode electrodes with a diameter of 10 mm were punched out, pressed at

~187 MPa, and dried again in a vacuum oven at 120 °C for 8 h before transferring into an Ar-filled glovebox for battery construction. The density of the dried electrode coating is 2.5 – 3.0 mg cm<sup>-2</sup>. Half cells were made with a cathode electrode, a metal Na chip (MTI, 99.9 %) as the anode, 1M NaPF<sub>6</sub> in PC electrolyte, C480 separator (Celgard), and 2032 coin cell cases (SS304, MTI).

Electrochemical cycling tests were carried out on an Arbin 2143 tester. The rate performances of various specimens were tested at the discharge rates of C/10, C/5, 1C, 2C, 5C, 10C, 20C, 30C, 40C, 50C and 60C sequentially (4 cycles at C/5 and 1 cycle for other discharge rate) with a constant charge rate of C/5. The cycling stabilities were measured at a constant charge and discharge rate of 0.1C between 2 V and 3.8 V at room temperature.

Electrochemical impedance spectroscopy (EIS) and cyclic voltammetry (CV) and were performed using a Solartron 1287A/1255B analyzer. Electrochemical impedance was measured from 1 MHz to 1 Hz at 30 mV. Before the impedance measurement, fresh cells with Na metal as the counter electrode were charged to a cut-off voltage of 3.8 V at a rate of 0.1C and were kept for 10 h after the charging to reach steady states. Cyclic voltammetry (CV) of fresh cells was performed between 2 V and 3.8 V at a scan rate of 0.1 mV s<sup>-1</sup>.

### 8.3. Results and Discussion

The particle size of synthesized Li<sub>6.4</sub>Ga<sub>0.2</sub>La<sub>3</sub>Zr<sub>2</sub>O<sub>12</sub> is ~2 μm with a narrow particle size distribution (Figure 8.1(a)). The XRD result (Figure 8.2(a)) showed that the synthesized powder has a pure phase (PDF #01-080-4947, cubic).

Hence a pure cubic phase was synthesized at relatively lower temperature by Ga doping. The cubic phase has higher ion conductivity than the tetragonal phase. The Ga can stable the cubic phase at lower temperature from tetragonal phase.<sup>5</sup>

The relative density of the pellet reached ~83 % by cold sintering at 200 °C for 1 h with 1.2 GPa pressure, much higher than that of the pellet before cold sintering ~59 %. The Figure 8.1(b) and 8.1(c) clearly presented that the particle sintering occurred. The main phase after cold sintering is consistent with the pure phase. There were unknown minor peaks in the cold sintered specimen as shown in Figure 8.2(b). The unknown phase(s) disappeared by post annealing at 1100 °C for 2 h.

Figure 8.3 showed the comparison of specimen with (Figure 8.3(a) and 8.3(b)) or without (Figure 8.3(c) and 8.3(d)) cold sintering followed with post annealing at 1100 °C for 2 h. The first specimen reached a relative density of 82.3 %; the second specimen has a higher relative density of 89.1 %. It is obvious that cold sintering benefits the sintering by decreasing the micro-sized pores (~1 – 5 μm) during post annealing. It is suggested that the relatively higher initial density could facilitate the high-temperature sintering.

#### **8.4. Conclusions**

A novel method to fabricate lithium solid state electrolyte was addressed. Pure cubic phase of  $\text{Li}_{6.4}\text{Ga}_{0.2}\text{La}_3\text{Zr}_2\text{O}_{12}$  was synthesized at relatively low synthesis temperature 1150 °C.  $\text{Li}_{6.4}\text{Ga}_{0.2}\text{La}_3\text{Zr}_2\text{O}_{12}$  was proved can be cold sintered at 200 °C and 83 % relative density was achieved, thereby an

improvement of ~40 % comparing to the green pellet without cold sintering. Furthermore, the higher initial density improved by cold sintering can further facilitate the post annealing at 1100 °C for a higher density of ~89 %.

### **8.5. Future work**

The cold sintering was proved to be an effective method to acquire relatively dense solid-state electrolyte  $\text{Li}_{6.4}\text{Ga}_{0.2}\text{La}_3\text{Zr}_2\text{O}_{12}$  at very low sintering temperature ~200 °C. For the future work, on one side, it will be worth to explore the cold sintering method to more solid-state electrolyte systems for a wide screen based on the final sintering features and lithium ion conductivities. On another side, the mechanism of cold sintering is still not clear. By clarifying the mechanism, the density after cold sintering could be improved further and benefit facilitate method to the real world. The precipitation is one of the speculation that influenced by pH range of the suspension. It could be a promising way to tailoring the pH value to accelerate the reaction and benefit cold sintering process.

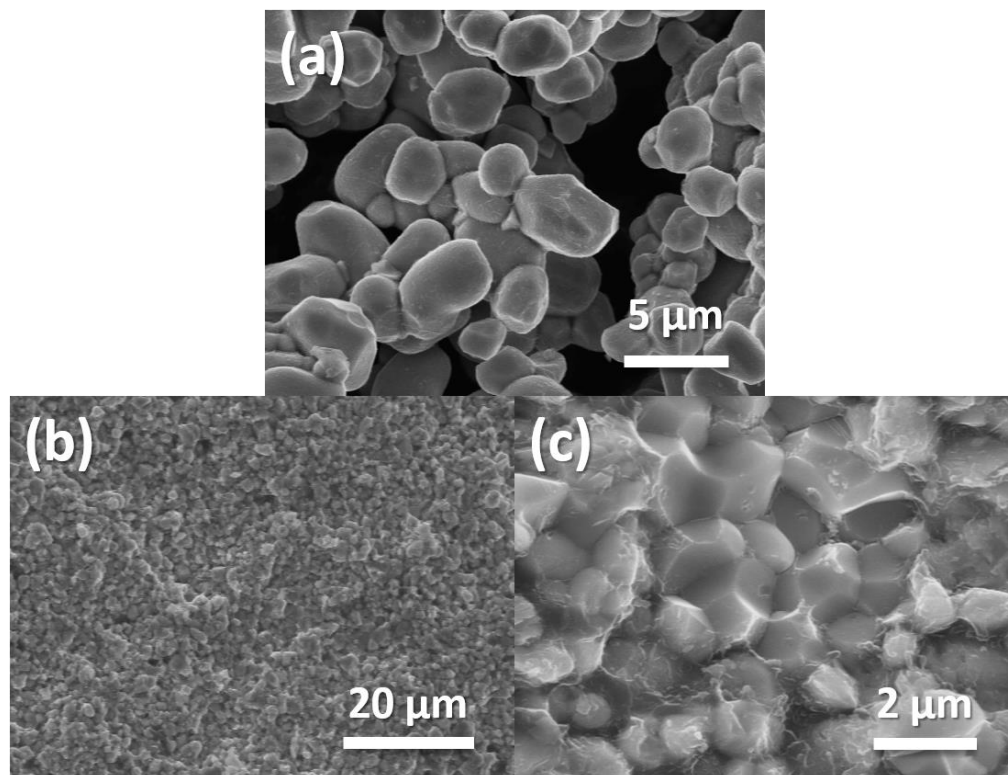


Figure 8.1 SEM images of  $\text{Li}_{6.4}\text{Ga}_{0.2}\text{La}_3\text{Zr}_2\text{O}_{12}$  (a) powder synthesized at 1150 °C for 2 h; (b) and (c) pellet of cold sintered at 200 °C for 1 h under pressure of 1.2 GPa.

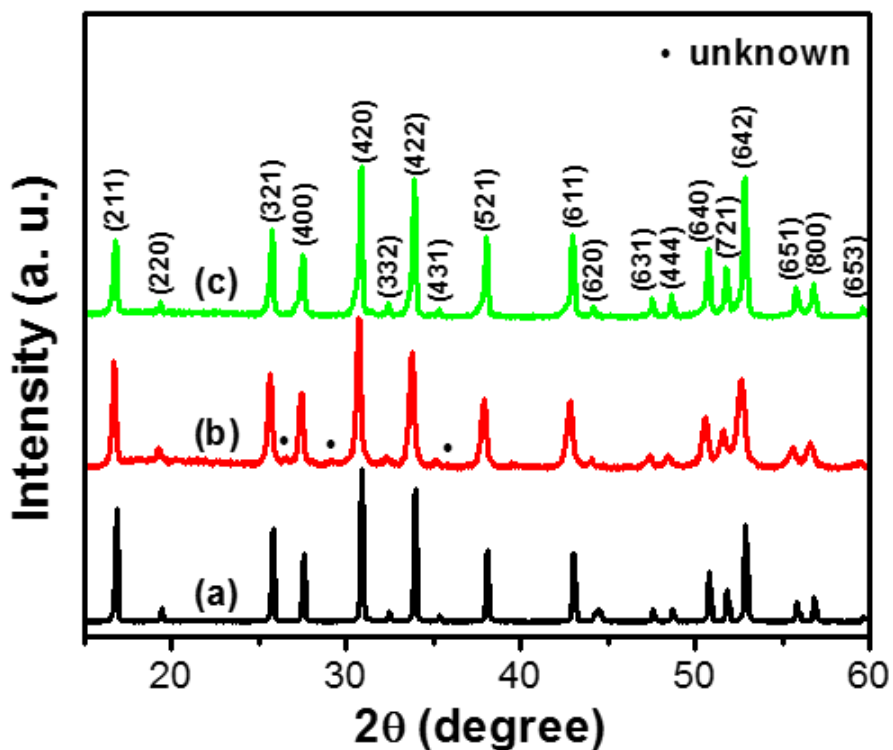


Figure 8.2 XRD patterns of  $\text{Li}_{6.4}\text{Ga}_{0.2}\text{La}_3\text{Zr}_2\text{O}_{12}$  (a) sintered at 1100 °C for 2 h in box furnace without cold sintering; (b) cold sintered at 200 °C for 1 h under pressure of 1.2 GPa; (c) cold sintering at 200 °C for 1 h under pressure of 1.2 GPa followed by sintering at 1100 °C for 2 h in box furnace.

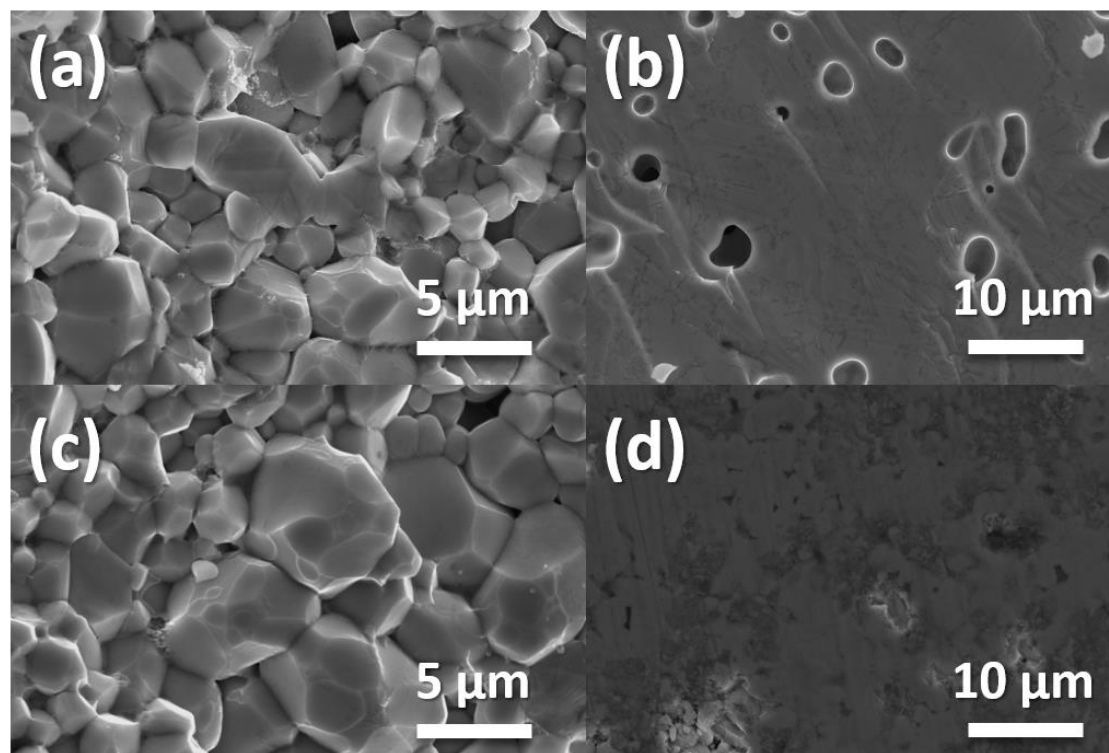


Figure 8.3 Cycling performance of (a) Specimen A (hierarchical porous microstructure with primary and secondary particles) and (b) Specimen B (irregular rods). Both specimens were charged and discharged at a constant rate of 0.1C at room temperature.

## References

- (1) Braga, M. H.; Grundish, N. S.; Murchison, A. J.; Goodenough, J. B. Alternative Strategy for a Safe Rechargeable Battery. *Energy & Environmental Science* **2017**, *10*, 331-336.
- (2) Bachman, J. C.; Muy, S.; Grimaud, A.; Chang, H.-H.; Pour, N.; Lux, S. F.; Paschos, O.; Maglia, F.; Lupart, S.; Lamp, P.; Giordano, L.; Shao-Horn, Y. Inorganic Solid-State Electrolytes for Lithium Batteries: Mechanisms and Properties Governing Ion Conduction. *Chemical Reviews* **2016**, *116*, 140-162.
- (3) Bernuy-Lopez, C.; Manalastas, W.; Lopez del Amo, J. M.; Aguadero, A.; Aguesse, F.; Kilner, J. A. Atmosphere Controlled Processing of Ga-Substituted Garnets for High Li-Ion Conductivity Ceramics. *Chemistry of Materials* **2014**, *26*, 3610-3617.
- (4) Buschmann, H.; Dolle, J.; Berendts, S.; Kuhn, A.; Bottke, P.; Wilkening, M.; Heitjans, P.; Senyshyn, A.; Ehrenberg, H.; Lotnyk, A.; Duppel, V.; Kienle, L.; Janek, J. Structure and Dynamics of the Fast Lithium Ion Conductor "Li<sub>7</sub>La<sub>3</sub>Zr<sub>2</sub>O<sub>12</sub>". *Physical Chemistry Chemical Physics* **2011**, *13*, 19378-19392.
- (5) Peng, H.; Wu, Q.; Xiao, L. Low Temperature Synthesis of Li<sub>5</sub>La<sub>3</sub>Nb<sub>2</sub>O<sub>12</sub> with Cubic Garnet-Type Structure by Sol–Gel Process. *Journal of Sol-Gel Science and Technology* **2013**, *66*, 175-179.
- (6) Thangadurai, V.; Weppner, W. Li<sub>6</sub>Aa<sub>2</sub>Ta<sub>2</sub>O<sub>12</sub> (a = Sr, Ba): Novel Garnet-Like Oxides for Fast Lithium Ion Conduction. *Advanced Functional Materials* **2005**, *15*, 107-112.
- (7) Ma, C.; Chen, K.; Liang, C.; Nan, C.-W.; Ishikawa, R.; More, K.; Chi, M. Atomic-Scale Origin of the Large Grain-Boundary Resistance in Perovskite Li-Ion-Conducting Solid Electrolytes. *Energy & Environmental Science* **2014**, *7*, 1638-1642.
- (8) Mei, A.; Wang, X.-L.; Feng, Y.-C.; Zhao, S.-J.; Li, G.-J.; Geng, H.-X.; Lin, Y.-H.; Nan, C.-W. Enhanced Ionic Transport in Lithium Lanthanum Titanium Oxide Solid State Electrolyte by Introducing Silica. *Solid State Ionics* **2008**, *179*, 2255-2259.
- (9) Mei, A.; Wang, X.-L.; Lan, J.-L.; Feng, Y.-C.; Geng, H.-X.; Lin, Y.-H.; Nan, C.-W. Role of Amorphous Boundary Layer in Enhancing Ionic Conductivity of Lithium–Lanthanum–Titanate Electrolyte. *Electrochimica Acta* **2010**, *55*, 2958-2963.
- (10) Lang, B.; Ziebarth, B.; Elsässer, C. Lithium Ion Conduction in Li<sub>2</sub>(PO<sub>4</sub>)<sub>3</sub> and Related Compounds Based on the Nasicon Structure: A First-Principles Study. *Chemistry of Materials* **2015**, *27*, 5040-5048.
- (11) Aono, H.; Sugimoto, E.; Sadaoka, Y.; Imanaka, N.; Adachi, G. y. Ionic Conductivity of Solid Electrolytes Based on Lithium Titanium Phosphate. *Journal of the Electrochemical Society* **1990**, *137*, 1023-1027.

- (12) Aono, H.; Sugimoto, E.; Sadaoka, Y.; Imanaka, N.; Adachi, G. y. The Electrical Properties of Ceramic Electrolytes for  $\text{Li}_m \text{X Ti}_2 - \text{X} (\text{Po}_4)_3 + \text{YLi}_2 \text{O}$ ,  $\text{M} = \text{Ge}, \text{Sn}, \text{Hf}$ , and  $\text{Zr}$  Systems. *Journal of the Electrochemical Society* **1993**, *140*, 1827-1833.
- (13) Kuwano, J.; Sato, N.; Kato, M.; Takano, K. Ionic Conductivity of  $\text{Li}_m(\text{Po}_4)_3$  ( $\text{M}=\text{Ti}, \text{Zr}, \text{Hf}$ ) and Related Compositions. *Solid State Ionics* **1994**, *70*, 332-336.
- (14) Kato, Y.; Hori, S.; Saito, T.; Suzuki, K.; Hirayama, M.; Mitsui, A.; Yonemura, M.; Iba, H.; Kanno, R. High-Power All-Solid-State Batteries Using Sulfide Superionic Conductors. *Nature Energy* **2016**, *1*, 16030.
- (15) Zhu, Y.; He, X.; Mo, Y. Origin of Outstanding Stability in the Lithium Solid Electrolyte Materials: Insights from Thermodynamic Analyses Based on First-Principles Calculations. *ACS Applied Materials & Interfaces* **2015**, *7*, 23685-23693.
- (16) Guo, J.; Guo, H.; Heidary, D. S. B.; Funahashi, S.; Randall, C. A. Semiconducting Properties of Cold Sintered  $\text{V}_2\text{o}_5$  Ceramics and Co-Sintered  $\text{V}_2\text{o}_5$ -Pedot:Pss Composites. *Journal of the European Ceramic Society*.
- (17) Guo, J.; Guo, H.; Baker, A. L.; Lanagan, M. T.; Kupp, E. R.; Messing, G. L.; Randall, C. A. Cold Sintering: A Paradigm Shift for Processing and Integration of Ceramics. *Angewandte Chemie* **2016**, *128*, 11629-11633.
- (18) Guo, J.; Berbano, S. S.; Guo, H.; Baker, A. L.; Lanagan, M. T.; Randall, C. A. Cold Sintering Process of Composites: Bridging the Processing Temperature Gap of Ceramic and Polymer Materials. *Advanced Functional Materials* **2016**, *26*, 7115-7121.
- (19) Guo, J.; Baker, A. L.; Guo, H.; Lanagan, M.; Randall, C. A. Cold Sintering Process: A New Era for Ceramic Packaging and Microwave Device Development. *Journal of the American Ceramic Society*, n/a-n/a.
- (20) Guo, H.; Guo, J.; Baker, A.; Randall, C. A. Cold Sintering Process for  $\text{ZrO}_2$ -Based Ceramics: Significantly Enhanced Densification Evolution in Ytria-Doped  $\text{ZrO}_2$ . *Journal of the American Ceramic Society* **2016**, n/a-n/a.
- (21) Guo, H.; Guo, J.; Baker, A.; Randall, C. A. Hydrothermal-Assisted Cold Sintering Process: A New Guidance for Low-Temperature Ceramic Sintering. *ACS Applied Materials & Interfaces* **2016**, *8*, 20909-20915.
- (22) Guo, H.; Bayer, T. J. M.; Guo, J.; Baker, A.; Randall, C. A. Current Progress and Perspectives of Applying Cold Sintering Process to  $\text{ZrO}_2$ -Based Ceramics. *Scripta Materialia* **2017**, *136*, 141-148.
- (23) Guo, H.; Bayer, T. J. M.; Guo, J.; Baker, A.; Randall, C. A. Cold Sintering Process for 8 Mol%  $\text{Y}_2\text{o}_3$ -Stabilized  $\text{ZrO}_2$  Ceramics. *Journal of the European Ceramic Society*.

- (24) Guo, H.; Baker, A.; Guo, J.; Randall, C. A. Protocol for Ultralow-Temperature Ceramic Sintering: An Integration of Nanotechnology and the Cold Sintering Process. *ACS Nano* **2016**, *10*, 10606-10614.
- (25) Guo, H.; Baker, A.; Guo, J.; Randall, C. A. Cold Sintering Process: A Novel Technique for Low-Temperature Ceramic Processing of Ferroelectrics. *Journal of the American Ceramic Society* **2016**, *99*, 3489-3507.
- (26) Funahashi, S.; Guo, J.; Guo, H.; Wang, K.; Baker, A. L.; Shiratsuyu, K.; Randall, C. A. Demonstration of the Cold Sintering Process Study for the Densification and Grain Growth of ZnO Ceramics. *Journal of the American Ceramic Society*, n/a-n/a.
- (27) Berbano, S. S.; Guo, J.; Guo, H.; Lanagan, M. T.; Randall, C. A. Cold Sintering Process of  $\text{Li}_{1.5}\text{Al}_{0.5}\text{Ge}_{1.5}(\text{PO}_4)_3$  Solid Electrolyte. *Journal of the American Ceramic Society* **2017**, *100*, 2123-2135.
- (28) Baker, A.; Guo, H.; Guo, J.; Randall, C. Utilizing the Cold Sintering Process for Flexible-Printable Electroceramic Device Fabrication. *Journal of the American Ceramic Society* **2016**, *99*, 3202-3204.